Imaging Major Canadian Sedimentary Basins and Their Adjacent Structures Using Ambient Seismic Noise (and Other Applications of Seismic Noise)

by

Ayodeji Paul Kuponiyi

B.Sc. (Honours), University of Lagos, 2001
M.Sc., University of Lagos, 2008
M.Sc., North Carolina Central University, 2012

A Dissertation Submitted in Partial Fulfillment of the

Requirements for the Degree of

DOCTOR OF PHILOSOPHY

in the School of Earth and Ocean Sciences

©Ayodeji Paul Kuponiyi, 2021
University of Victoria

All rights reserved. This dissertation may not be reproduced in whole or in part, by photocopy or other means, without the permission of the author.

Imaging Major Canadian Sedimentary Basins and Their Adjacent Structures Using Ambient Seismic Noise (and Other Applications of Seismic Noise)

by

Ayodeji Paul Kuponiyi

B.Sc. (Honours), University of Lagos, 2001
M.Sc., University of Lagos, 2008
M.Sc., North Carolina Central University, 2012

Supervisory Committee

Dr. Honn Kao (School of Earth and Ocean Science)
Co-Supervisor

Dr. George Spence (School of Earth and Ocean Science)
Co-Supervisor

Dr. Stan Dosso (School of Earth and Ocean Science)
Departmental Member

Dr. John Cassidy (School of Earth and Ocean Science)
Departmental Member

Dr. Pan Agathoklis (Department of Electrical and Computer Engineering)
Outside Member

Abstract

Supervisory Committee

Dr. Honn Kao (School of Earth and Ocean Science)
Co-Supervisor

Dr. George Spence (School of Earth and Ocean Science)
Co-Supervisor

Dr. Stan Dosso (School of Earth and Ocean Science)
Departmental Member

Dr. John Cassidy (School of Earth and Ocean Science)
Departmental Member

Dr. Pan Agathoklis (Department of Electrical Engineering)
Outside Member

Over a decade ago, it was discovered that the earth's natural seismic wavefields, propagating as seismic noise, can be processed using correlation methods to produce surface waves, similar to those generated by earthquakes. This discovery represents a paradigm shift in seismology and has led to several tomographic studies of earth structures, at different scales and resolutions, in previously difficult-to-study areas around the world. This PhD dissertation presents research results on multi-scale and multi-purpose applications of ambient seismic noise wavefields under three topics: (1) Imaging of sedimentary basins and sub-basin structures in eastern and western Canada using ambient seismic noise, (2) Combining measurements from ambient seismic noise with earthquake datasets for imaging crustal and mantle structures, and (3) Temporal variation in cultural seismic noise and noise correlation functions (NCFs) during the COVID-19 lockdown in Canada.

The first topic involved imaging the sedimentary basins in eastern and western Canada using shear wave velocities derived from ambient noise group velocities. The results show that the

basins are characterized by varying depths, with maximums along the studied cross-sections in excess of 10 km, in eastern and western Canada. Characteristics of accreted terranes in eastern and western Canada are also revealed in the results. A seismically distinct basement is imaged in eastern Canada and is interpreted to be a vestige of the western African crust trapped beneath eastern Canada at the opening of the Atlantic Ocean. In western Canada, the 3D variation of the Moho and sedimentary basin depths is imaged. The thickest sediments in eastern Canada are found beneath the Queen Charlotte, Williston and the Alberta Deep basins, while the Moho is the deepest beneath the Williston basin and parts of Alberta basin and northern British Columbia.

For the second topic, I worked on improving the seismological methodology to construct broadband (period from 2 to 220 s) dispersion curves by combining the dispersion measurements derived from ambient seismic noise with those from earthquakes. The broadband dispersion curves allow for imaging earth structures spanning the shallow crust to the upper mantle.

For the third topic, I used ambient seismic data from the earlier stages of the COVID-19 pandemic to study the temporal variation of seismic power spectra and the potential impacts of COVID-19 lockdown on ambient NCFs in four cities in eastern and western Canada. The results show mean seismic power drops of 24% and 17% during the lockdown in eastern Canada, near Montreal and Ottawa respectively and reductions of 27% and 17% near Victoria and Sidney respectively. NCF signal quality within the secondary microseism band reached maximum before the lockdown, minimum during lockdown and at intermediate levels during the gradual reopening phase for the western Canada station pair.

Table of Contents

Supervisory Committee ii
Abstract iii
Table of Contents v
List of Tables viii
List of Figures ix
Acknowledgement xii
Dedication xiv
Chapter 1. Introduction 1
1.1 Overview 1
1.2 Outline of Thesis 1
Table of Abbreviations 3
Chapter 2. Imaging of Sedimentary Basins and Sub-basin Structures in Eastern Canada Using Ambient Seismic Noise 2
2.1 Article Information 2
2.1.1 Author and Coauthor Contributions 2
2.1.2 Citation 2
2.1.3 Author's Names and Affiliations 3
2.1.4 Article Format 3
2.1.5 Data and Resources 3
2.2 Upper Crustal Investigation of the Gulf of Saint Lawrence Region, Eastern Canada Using Ambient Noise Tomography 5
2.2.1 Abstract 5
2.2.2 Introduction 6
2.2.3 Geological Setting 8
2.2.4 Data and Analysis 14
2.2.5 Results 22
2.2.6 Interpretation and Implications 41
2.2.7 Discussion 51
2.2.8 Summary and Conclusion 52
2.2.9 Acknowledgements 54
2.3 Supplemental Materials 54
Chapter 3. Imaging of Sedimentary Basins and Sub-basin Structures in Western Canada Using Ambient Seismic Noise 55

3.1 Article Information 55
3.1.1 Author and Coauthor Contributions 55
3.1.2 Article Format 55
3.1.3 Data and Resources 56
3.2 3-D Geometry of Sedimentary Basins and Moho Beneath Western Canada from Ambient Seismic Noise Tomography 57
3.2.1 Abstract 57
3.2.2 Introduction 58
3.2.3 Geological Setting 63
3.2.4 Data and Methods 68
3.2.5 Results and Interpretation 72
3.2.6 Implication and Discussion 122
3.2.7 Summary and Conclusions 141
3.2.8 Acknowledgements 142
3.3 Supplemental Materials 143
Chapter 4. Combining Measurements from Ambient Seismic Noise with Earthquake Datasets for Imaging Crustal and Mantle Structures 145
4.1 Article Information 145
4.1.1 Author and Coauthor Contributions 145
4.1.2 Citation 145
4.1.3 Author's Names and Affiliations 146
4.1.4 Article Format 146
4.1.5 Data and Resources 146
4.2 Construction of Broadband Dispersion Curves by Reconciling Ambient Seismic Noise and Earthquake Surface Wave Data 147
4.2.1 Abstract 147
4.2.2 Introduction 148
4.2.3 Discrepancies Between Dispersion Curves Derived from Earthquake and Ambient Noise Data…… 150
4.2.4 A Framework for the Construction of Broadband Dispersion Curves 154
4.2.5 Main Drawbacks of Traditional ANT Phase Velocity Dispersion Measurement 158
4.2.6 Determining the Optimal Corner Periods for Phase Velocity Dispersion Measurement Using SNR Analyses 159
4.2.7 Combining Dispersion Measurements from Ambient Seismic Noise and Earthquake Datasets to Construct a Broadband Phase Velocity Dispersion Curve 162
4.2.8 Broader Advantage of Band-pass Filtering Based on Period-dependent SNR 163
4.2.9 Discussion and Conclusion 168

4.2.10 Acknowledgements 175
Chapter 5. Temporal Variation in Cultural Seismic Noise and Noise Correlation Functions During COVID-19 Lockdown in Canada 176
5.1 Article Information 176
5.1.1 Author and Coauthor Contributions 176
5.1.2 Citation 176
5.1.3 Author's Names and Affiliations 176
5.1.4 Article Format 177
5.1.5 Data and Resources 177
5.2 Temporal Variation in Cultural Seismic Noise and Noise Correlation Functions During COVID-19 Lockdown in Canada 178
5.2.1 Abstract 178
5.2.2 Introduction 179
5.2.3 Data and Analysis 183
5.2.4 Results 186
5.2.5 Discussion and Conclusion 199
5.2.6 Acknowledgements 203
Chapter 6. Conclusions 204
6.1 Summary 204
6.2 Recommendations for Future Work 209
Bibliography 211

List of Tables

Table 3.1 Description of network and association with colour-codes 69

Table 4.1 Percentage of Station Pairs with Improvement in Waveform Signal-to-Noise Ratio 169

Table 5.1 COVID-19 Timeline for Canadian Provinces and Seismograph Stations used in this Study. 183

List of Figures

Figure 2. 1 Map of the GSL region showing the locations of the selected cross-sections (A-E) as well as major geological and tectonic features 9

Figure 2. 2 Map of the GSL region showing the locations of the selected cross-sections (A-E) as well the location and geometry of major sedimentary basins in the GSL 10

Figure 2. 3 Distribution of seismograph stations used in the GSL and the corresponding ray path and coverage 15

Figure 2. 4 Cross correlogram and group velocity measurement for station pair DRLN and BATG 18

Figure 2. 5 Group velocity maps for selected periods in the range 2-20 s 25

Figure 2. 6 1-D V_s results (a) near station *MADG* within Magdalen Basin; (b) offshore western Newfoundland, near the edge of Magdalen Basin. 28

Figure 2. 7 Depth slices of *Vs* shown in left and right panels respectively for (a) 2 km (b) 5 km (c) 10 (d) 20 km 30

Figure 2. 8 Depth slices of uncertainty distribution associated with Figure 2.7 are shown in the left and right panels respectively for (a) 2 km (b) 5 km (c) 10 (d) 20 km 31

Figure 2. 9 Potential Field Data – (a) Bouguer and (b) Free-Air gravity anomalies for the Gulf of St. Lawrence 34

Figure 2. 10 Potential Field Data –Residual Total Magnetic Field for the Gulf of St. Lawrence. Data source 35

Figure 2. 11 Cross-sections showing the *Vs* and uncertainty distributions 37

Figure 2. 12 Co-linear cross-sections from our 3-D model compared with Lithoprobe vintage deep seismic reflection lines 86-1 and 86-2 50

Figure 3. 1 Geological and tectonic map of western Canada 59

Figure 3. 2 Map showing station distribution used in this study and simplified propagation paths..... 67

Figure 3. 3 Surface wave tomography results 74

Figure 3. 4 The probability distribution of *Vs* plotted with depth derived from the trans-D inversion of grid dispersion curves 78

Figure 3. 5 Three-dimension *Vs* distribution for western Canada at depths 83

Figure 3. 6 Cross-sections taken along the Offshore basins..... 93

Figure 3. 7 Lithoprobe line 10 taken from southern cordillera (Intermontane belt)…. 99

Figure 3. 8 Lithoprobe line 11b taken from Central Alberta 109

Figure 3. 9 3-D sediment thickness across western Canada..... 124

Figure 3. 10 Cartoon illustration of two velocity models showing the types of crust-mantle boundaries 126

Figure 3. 11 Depth variation at the base of the crust (referenced in the text as $Z_{0\%}$) and the top of the mantle 127

Figure 3. 12 Distribution of *Vs* at the base of the crust (referenced in the text as $V_{0\%}$); and the top of the mantle (referenced as $V_{100\%}$) 129

Figure 3. 13 Percentage change of depth (a) and *Vs* (b) from the base of the crust to the top of the mantle 130

Figure 3. 14 Plot of CRUST1.0 Moho depths for western Canada..... 132

Figure 3. 15 Intermediate depths between base of the crust and the top of the mantle..... 135

Figure 3. 16 *Vs* and uncertainty estimates across a segment of the shallow high-*Vs* structure. 138

Figure 3. 17 1-D *Vs* model (solid red line) and associated uncertainty estimates..... 139

Figure 3. 18 Depths to the base of the crust and the top of the mantle, similar to Figure 3.11, however, areas with unreliable estimates are covered by the gray and black dashed masks… 140

Figure 4. 1 Map showing the seismic stations used in this study..... 151

Figure 4. 2 Results of time-frequency analysis of two representative station pairs..... 153

Figure 4. 3 Schematic summary of data processing steps to construct a broadband dispersion curve 155

Figure 4. 4 Two representative examples showing the determination of minimum and maximum resolvable periods (red dots) with the SNR thresholds 161

Figure 4. 5 Phase velocity curves correctly determined within the optimal threshold window for station pairs..... 164

Figure 4. 6 Broadband phase velocity curves (dashed black line) for station pairs 167

Figure 4. 7 Example showing SNR improvement above typical dispersion quality thresholds…….. 171

Figure 4. 8 Analyses of SNR improvement for CNSN and USArray stations…..... 172

Figure 5. 1 Map showing CNSN seismic stations used in this study..... 180

Figure 5. 2 Seismic power calculated over 12-hour (gray solid lines) and 48-hour (black open circles) moving windows for stations..... 188

Figure 5. 3 Probability density functions of seismic noise for stations..... 191

Figure 5. 4 Mean of seismic noise in the three temporal windows under consideration for stations..... 194

Figure 5. 5 Symmetric ambient noise cross-correlation functions for station-pairs 195

Figure 5. 6 Spectral SNR for the period band of 1-10 s..... 196

Acknowledgement

Firstly, I would like to thank my PhD supervisor, Dr. Honn Kao for his guidance and mentorship throughout my PhD studies. His patience and unrelenting support helped me cross the finish line.

I would also like to thank the rest of my PhD supervisory committee – Drs. George Spence, John Cassidy, Stan Dosso and Pan Agathoklis, for dedicating their time in providing guidance, which broadened the scope of my research.

Outside of my supervisory committee, many of whom I collaborated with, I thank my other collaborators for their contribution to my research experience, among them, Cees van Staal, Cuilin Li, Pierre Arroucau, Eric Brandamyr, Fiona Darbyshire. I appreciate.

I benefited immensely from contributions from Robert Kung, Ryan Visser, co-op students (Connor Gaudreau and Jeremiah Wilbur), and scientists: Drs. Jiangheng He, Andrew Schaeffer, Ramin Dohkt, Kelin Wang and Roy Hyndman, all at PGC. I acknowledge all the great contributions and insights from the weekly research seminars at PGC.

My research was partly funded through NSERC Discovery grants to HK, GS and JC.

Miles Warner (GSC, Ottawa) provided (converted) Potential Field data used in my Gulf of Saint Lawrence project. Steve Grasby and Jacek Majorowicz contributed heat flow data to my western Canada project.

I acknowledge the use of the following software packages: Python (and modules included), Observational Seismology Python modules (ObsPy, Beyreuther et al., 2010), Generic Mapping Tools (GMT, Wessel et al., 2013), Fast Marching Surface Wave Tomography (FMST, Rawlinson

and Sambridge (2003)) package and Trans-dimensional inversion code (trans-D, Dosso et al., 2014), Seismic Analysis Code (SAC), Computer Programs in Seismology (CPS, Herrmann, 2013).

Dedication

Firstly, I dedicate this PhD Dissertation to God, who makes all things beautiful in His time.

Dad and Mom, you are my first teachers, you raised me with love and gave up everything for the scholarship of your children. I thank you for your encouragement and prayers that got me this far. And to my brothers, you were always there when I needed you.

To my wife, my love and jewel of inestimable treasure. It has been just the two of us balancing between family, graduate school, and full-time jobs, how could I have done all these without your support and encouragement?

I take this paragraph to thank my kids for providing consistent support and immense inspiration. Kemi, you were my PhD admission gift, one of the kindest people I know. Tobi, you were my PhD Candidacy qualifying gift, you never back down until you achieve success. Dara, you are my graduation gift, the sweetest baby I know. Thank you all for your sacrifice and support through this program, I hope I inspire you to greatness as much as you all do to me daily.

To my family friends in Victoria who were so generous with their time and support, among whom are Subbarao Yelisetti, Romina Gehrmann, Angela Schlesinger, Jesse Hutchinson, Tian Sun, Lucinda Leonard, Ryan Visser, Ramin Dokht, Ali Mahani, Amir Farahbod, Jeremy Gosselin, Dawei Gao, Carlos Herrera, PGC seismology lab group (past and current) and my church family.

I appreciate the professional support of Robert White (Emergency Management of BC), Jaklyn Vervynck and Ben Driver (both of the Ministry of Transportation and Infrastructure, BC).

Outside of Canada, I thank Henry Ochije, Pierre Arroucau and Femi Giwa for their encouragement when I was deciding to pursue a PhD.

To mentors, supervisors, and administrative staff at the SEOS and PGC. Honn, I appreciate your wisdom, patience, and kindness. Thank you for providing me the atmosphere to thrive and grow as a scientist, I have learnt a lot from you. John, you are kind and caring, an advocate, a calm and encouraging voice as I balance research, with family and a full-time job. Thank you for all your support. George, you made my coming to UVic possible and provided all the necessary support to make me settle into life in Victoria, thank you for welcoming and guiding my learning. Stan, thank you for your support, you were always available to answer my questions, no matter how long it took. To the administrative staff, at the SEOS – Allison Rose, Kimberly Smith-Jones (retired), Terry Russell and Kalisa Valenzuela and at the PGC – Barbara Anderson (retired), Nina Parry and Ann Smith (Commissionaires), thank you all for what you do, without you, I could not have done this.

Finally, I take this paragraph to recognize that the world today is diametrically different, in many aspects, from when I started my PhD. Changes in technology have made me rewrite my computer codes in several different languages over these few years to keep up with technological advancements. However, the most profound and far-reaching of these changes, has to be the one brought about by the 2019/2020 COVID-19 pandemic. Lives and livelihood have been lost and homes decimated by the pandemic. My prayer is for things to get better.

Chapter 1. Introduction

1.1 Overview

The main objective of my PhD is to study the shear wave velocity characteristics in the crust and, where possible, the uppermost mantle of eastern and western Canada, using the non-invasive ambient seismic noise tomography method. This work also leverages the availability of large ambient seismic noise datasets to further propose an improved method for constructing broadband dispersion data and study seismic noise propagation.

1.2 Outline of Thesis

The body of this thesis consists of four manuscripts that are either published, submitted or in preparation, each presented as a Chapter. Each Chapter fully describes the unique scientific questions being addressed in the paper, data and methods used, the results, interpretations and contributions associated with the article. Because each chapter is a stand-alone project, it is therefore expected that parts of the introductions and methods may be repeated.

Chapter 2 presents the results of studying the upper- and mid-crustal structure beneath the Gulf of St. Lawrence in eastern Canada. Results of this work have implications for the tectonic evolution of the northern Appalachian belt, the potential of hydrocarbon accumulation and seismic hazard in the region.

Chapter 3 presents the results of studying the velocity structure of the western Canadian crust and uppermost mantle. Because the geographic scope extends across most of western Canada, results of this work may have several implications including geohazard (induced seismicity –

fracking and ground water studies), tectonic (including the state of subducted slabs at depth, the Moho topography across western Canada) and energy resources (geometry, thickness and evolution of sedimentary basins in western Canada).

Chapter 4 presents an improvement to the ambient seismic noise processing methods, which allows for proper determination of ambient seismic noise phase velocities and further develops a framework for constructing truly broadband phase velocity dispersion curves by combining ambient noise (period range 2 – 30 s) and earthquake data (period range 30 – 200 s).

Chapter 5 presents the impacts of the COVID-19-related restrictions of human activities on seismic power and the signal quality of ambient seismic noise correlation functions in four Canadian cities – Ottawa, Quebec, Victoria, and Sidney. The lockdown presents a rare opportunity to make observations that would be impossible to make otherwise.

Chapter 6 is a summary of the contributions of the four research projects presented in this dissertation and provides some conclusions and recommendations for future work.

Table of Abbreviations

AB	Alberta
AI	Anticosti Island
ANT	Ambient Noise Tomography
ASF	Appalachian Structural Front
ASN	Ambient Seismic Noise
BBF	Bramford Brook Fault
BC	British Columbia
BSB	Bowser/Sustut Basin
BVBL	Baie Verte – Brompton Line
CanMB	Canadian Maritimes Basin
CCF	Cobequid-Chedabucto Fault
CCHF	Caledonia-Clover Hill Fault,
CDF	Cordillera Deformation Front
CDF	Cordillera Deformation Front
CMA	Collector Magnetic Anomaly
CNSN	Canadian National Seismic Network
COCORP	Consortium for Continental Reflection Profiling
CSZ	Cascadia Subduction Zone
DHF	Dover-Hermitage Bay Fault
ECF	Earthquake Correlation Function
EGF	Empirical Green's Function
Exp	Explorer
FTAN	Frequency-Time Analysis
GB	Georgia Basin
GF	Green’s Function
GSC	Geological Survey of Canada
GSL	Gulf of Saint Lawrence
HVZ	High-velocity Zone
IGRF	International Geomagnetic Reference Field
IMB	Intermontane Basin
IRIS	Incorporated Research Institution for Seismology
JdF	Juan de Fuca
LVZ	Low-velocity Zone
MB	Manitoba
MBF	Macintosh Brook Fault
NA	North America
NACP	North America Central Plain
NB	Nechako Basin
NB	New Brunswick
NCF	Noise Correlation Function
NCVP	Northern Cordillera Volcanic Province
NDA	Notre Dame Arc
NL	Newfoundland and Labrador
NS	Nova Scotia
NWT	Northwest Territory
OSB	Offshore Basins
PEI	Prince Edward Island
PPD	Posterior Probability Density
PPSD	Probabilistic Power Spectral Density
QC	Quebec
QCB	Queen Charlotte Basin
QCF	Queen Charlotte – Fairweather
RIL	Red Indian Line
RMT	Rocky Mountain Trench
Sask	Saskatchewan
SEED	Standard for Exchange of Seismic Data
SNR	Signal-to-Noise-Ratio
TF	Tintina Fault
Trans-D	Transdimensional
Vs	Shear Wave Velocity
WCSB	Western Canada Sedimentary Basin
YT	Yukon Territory

Chapter 2. Imaging of Sedimentary Basins and Sub-basin Structures in Eastern Canada Using Ambient Seismic Noise

2.1 Article Information

2.1.1 Author and Coauthor Contributions

The article presented in this Chapter was published in the *Journal of Geophysical Research: Solid Earth* but reformatted and adapted for this dissertation. The author of this dissertation, APK, carried out the data preprocessing and cross-correlations, surface wave tomography, 1-D trans-dimensional (transD) inversion and the pseudo 3-D tomography. APK wrote the manuscript under the guidance and supervision of coauthor HK. CRvS contributed immensely to the interpretation section of the article. SED wrote the transD inversion code. JFC contributed to the experiment design and provided literature review materials, GDS contributed to the style and result presentation. All coauthors contributed to the thorough review of the manuscript before submission.

2.1.2 Citation

Kuponiyi, A. P., Kao, H., van Staal, C. R., Dosso, S. E., Cassidy, J. F., and Spence, G. D. (2017), Upper crustal investigation of the Gulf of Saint Lawrence region, Eastern Canada using ambient noise tomography, *J. Geophys. Res. Solid Earth*, 122, 5208– 5227, doi:10.1002/2016JB013865

2.1.3 Author's Names and Affiliations

Ayodeji Paul Kuponiyi[1, 2*], Honn Kao[1, 2], Cees R. van Staal[3], Stan E. Dosso[1], John F. Cassidy[1, 2], George D. Spence[1]

[1]School of Earth and Ocean Sciences, University of Victoria, Victoria, BC V8P 5C2, Canada
[2]Geological Survey of Canada, Pacific Geoscience Centre, Sidney, BC V8L 4B2, Canada
[3]Geological Survey of Canada, 605 Robson Street, Vancouver, BC V6B 5J3, Canada

* Corresponding Author: ayodejik@uvic.ca; ayodeji.kuponiyi@gmail.com

2.1.4 Article Format

The text and figures included in the article are taken from the JGR publication. Supplementary materials that are a part of the publication are presented in Section 2.3. Sections, Figures, and Tables in the original article have been renumbered to conform with the dissertation style. References cited in the publication are included in the bibliography of this dissertation.

2.1.5 Data and Resources

This research is jointly supported by a CSEGF award (sponsored by Arcis Seismic Solutions—a TGS company) to A.P.K, the Induced Seismicity Research Project of Natural Resources Canada (NRCan), Natural Sciences and Engineering Research Council (NSERC) of Canada grants to H. K., J.F.C., G.D.S., and S.E.D. Seismic data were obtained from Canadian National Seismic Network data center (http://www.earthquakescanada.nrcan.gc.ca/stndon/CNSN-RNSC/stnbook-cahierstn/index-en.php). Potential field data were obtained from Geoscience Data Repository for Geophysical Data at the NRCan's website (http://gdr.agg.nrcan.gc.ca/gdrdap/dap/search-eng.php) and converted with help from Miles

Warner. Most of the figures were plotted by the Generic Mapping Tools (GMT). This is NRCan contribution 20170080.

Codes for the project are available on GitLab online repository upon request at https://gitlab.com/qnoise/Gulf-of-StLawrence-ANT-Project (last accessed December 31, 2020)

2.2 Upper Crustal Investigation of the Gulf of Saint Lawrence Region, Eastern Canada Using Ambient Noise Tomography

2.2.1 Abstract

This Chapter presents 3-D shear-wave velocity (V_s) structure in the Gulf of St. Lawrence (GSL) and adjacent onshore areas to 20 km depth by inverting Rayleigh-wave dispersion extracted from the vertical components of continuous ambient seismic noise waveforms. The region is divided into three broad zones based on their V_s characteristics. In the northwest, the Grenville Province (i.e., the exposed edge of predominantly Middle-Proterozoic Laurentian crust) is dominated by high-V_s, except for well-known anorthosite sites, which are characterized by relatively lower-V_s. In contrast, the central segment of the GSL region corresponds to a belt with generally low-V_s at upper-crustal levels. In the southeastern part of the GSL, prominent low-V_s values in the uppermost-crust are found to coincide with locations of subsidiary basins of the Canadian Maritime Basin, while higher-V_s values characterize the accreted Appalachian terranes where they are exposed on land. The Grenville Province is wedged out at depth by the Red Indian Line, which is the suture between composite-Laurentia and peri-Godwanan Ganderia in the Canadian Appalachians. The geometry and V_s characteristics of the southeasternmost peri-Gondwanan terranes of Avalonia and Meguma, suggest that they may be fully or partially structurally overlying a basement with distinct seismic characteristics, which could be a vestige of the West-African craton that was under-thrust beneath composite-Laurentia during the terminal Alleghenian continent-continent collision. In the middle of the GSL, the 3-D geometry of the Canadian Maritimes sedimentary basins overlying the Appalachian terranes shows that the depth to the top of basement is in excess of 8 km.

2.2.2 Introduction

The Gulf of St. Lawrence (GSL) region in eastern Canada has been an important focus of geophysical and geological studies due to its significance in understanding the tectonic evolution of the northern Appalachian belt and the potential of hydrocarbon accumulation (Dietrich et al., 2011). Large parts of the GSL (Figure 2.1), which is located within and north of the southwest-northeast trending Appalachian mountain belt, have been interpreted to be underlain by Middle to Late Paleozoic basins formed during rifting associated with orogen-parallel transcurrent faulting (Waldron et al., 2015; Williams, 1979). Potential field analyses have been carried out for parts of the region using gravity and magnetic anomaly data (Dehler & Roest, 1998; Lefort & Haworth, 1978; Oakey & Dehler, 1998). The methods are largely sensitive to the average of the crustal structure, and thus are insufficient to constrain the details of the evolution, geometry, and structure of the GSL region (Jackson, 2002). Petrological investigations revealed that extensive bodies of Mississippian age volcanic rocks cover the thick column of Paleozoic sedimentary rocks (Barr et al., 1985; Giles, 2009; Keen & Williams, 1990). The capping volcanic rocks are associated with local salt tectonism at depth (Barr et al., 1985) and they conceal the deeper sedimentary and crustal structures from active seismic profiling such as the reflection and refraction surveys conducted by the oil and gas industry and the Lithoprobe project (e.g., Keen et al., 1986, 1987; Voogd and Keen, 1987; Marillier and Verhoef, 1989; Marillier et al., 1989; Hall et al., 1995, 1998). As a result, exactly how the sediment thickness varies across the basins, the geometry and location of the Appalachian structural wedge northwest of the Baie Verte-Brompton line (BVBL) (Williams & Julien, 1982) – conventionally referred to as the Appalachian Structural Front (ASF), and the geometry of the successive Appalachian terranes at depth, are yet to be fully resolved.

To address these important issues, the Geological Survey of Canada (GSC), with support from the Portable Observatories for Lithospheric Analysis and Research Investigating Seismicity (POLARIS), deployed an array of 10 temporary broadband seismic stations in the GSL region between October 2005 and October 2008. These stations, combined with 14 permanent stations of the Canadian National Seismograph Network (CNSN) in the region, provide a station density sufficient for detailed studies of velocity structures using passive seismic sources (Figure 2.3).

Ambient seismic noise tomography is one of the most successful passive seismic methods (e.g., Campillo and Paul, 2003; Sabra et al., 2005; Shapiro et al., 2005). It provides detailed velocity structures, with a velocity-depth trade-off, but with no dependence on active seismic sources. The method has been applied at the continental scale to constrain crustal and upper mantle structures in North America (e.g., Ritzwoller et al., 2005; Lin et al., 2007; Kao et al., 2013). It was also applied at the regional scale in Canada, around Hudson Bay (Pawlak et al., 2011) and the Nechako basin, BC (Idowu et al., 2011), and at the localized scale in studies of mineral deposits in Manitoba, Canada (Cheraghi et al., 2015).

The main goal of this study is to obtain a comprehensive seismic velocity model using ambient noise seismic tomography in the GSL region to provide unprecedented data coverage and spatial resolution. Specifically, we process the vertical component of continuous seismic waveforms recorded by the temporary and permanent seismic stations in the region. Following well-established ambient noise processing procedures (e.g., Bensen et al., 2007; Arroucau et al., 2010), we determine surface wave dispersion curves (group velocity of the fundamental mode of the Rayleigh wave) for periods between 2 and 20 s. These dispersion curves were then inverted to constrain the 3-D distribution of velocity anomalies. In addition to conventional surface wave tomography, a pseudo 3-D shear-wave velocity (V_s) model is obtained with an innovative trans-

dimensional (trans-D) inversion scheme (Bodin et al., 2012; Dettmer et al., 2010; Dosso et al., 2014). Finally, the newly derived high-resolution tomography images are used to address key tectonic issues related to the evolution and sedimentary structures of the GSL region.

2.2.3 Geological Setting

The eastern margin of North America has been shaped by multiple tectonic events throughout geological time, including those responsible for forming the Grenville orogen (~1.3-0.98 Ga) and the Appalachian mountain belt during the Paleozoic (480-270 Ma) (van Staal et al., 2009; van Staal & Barr, 2012). The Grenville Province stretches from Texas, through Tennessee in the USA to Labrador, Canada (Brandmayr et al., 2016; Tollo et al., 2004). As a result of Grenville orogenesis and subsequent erosion, deep-lying crystalline basement rocks of the Grenville Province (Rivers, 2008; Wiener et al., 1984; Williams, 1979) (Figure 2.1), primarily comprising of ortho- and para- gneisses, diabase, gabbro, mangerite and anorthosites, were exhumed along the eastern edge of the North American craton prior to the Paleozoic. Adjacent to the Grenville Province, the main phases of Appalachian mountain belt include the Taconic, Salinic, Acadian, Neoacadian and terminal Alleghenian orogenies. These orogenic events were due to episodes of terrane accretion and terminated with continent (Gondwana)-continent (composite Laurentia) collision during the Alleghenian. Uplift, erosion, extension, subsidence and sediment deposition were generally associated with these orogenic events, most of which had some impact on the GSL region and associated basins.

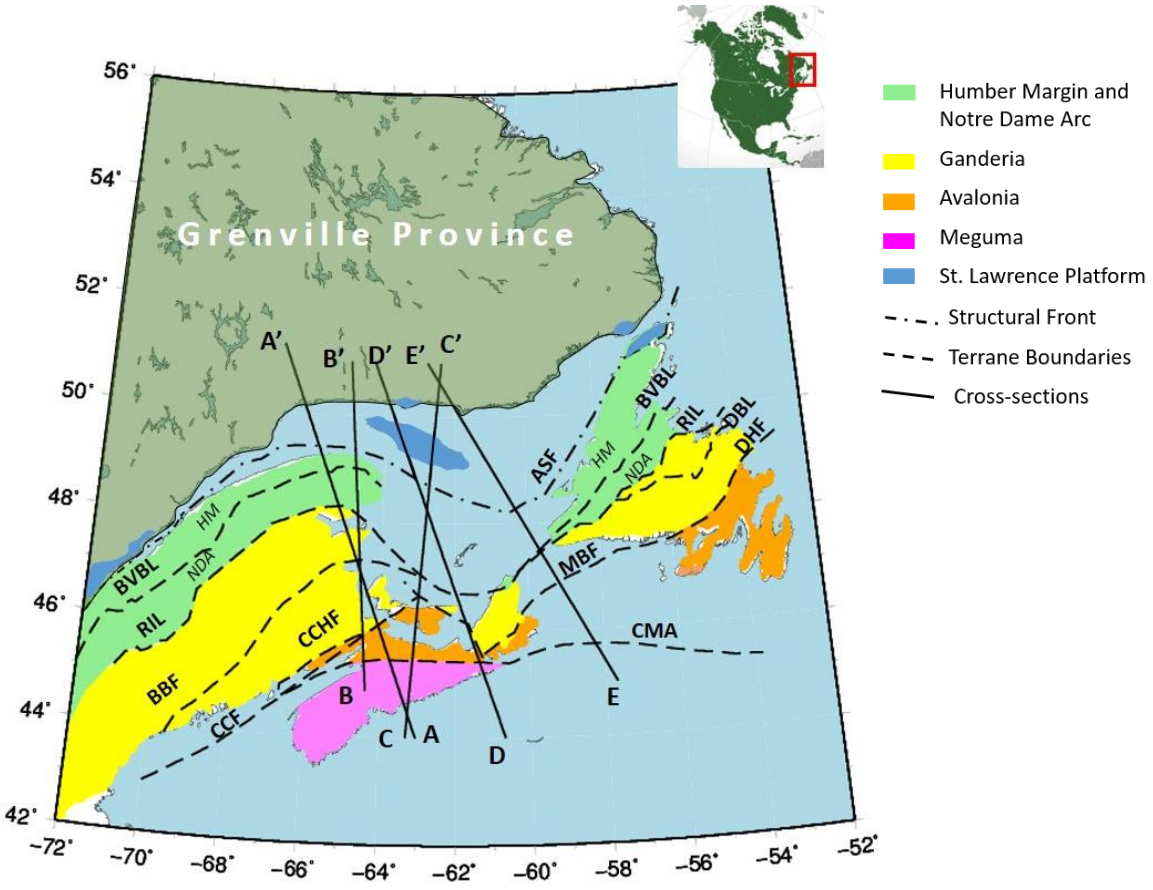

Figure 2. 1 Map of the GSL region showing the locations of the selected cross-sections (A-E) as well as major geological and tectonic features (after van Staal and Barr (2012)). Paleo margins: HM – Humber Margin, NDA – Notre Dame Arc. Structural Lines: ASF – Appalachian Structural Front, BBF – Bamford Brook Fault, BVBL – Baie Verte – Brompton Line, CCF – Cobequid-Chedabucto Fault, CCHF – Caledonia-Clover Hill Fault, CMA – Collector Magnetic Anomaly, DBL – Dog Bay Line, DHF – Dover-Hermitage Bay Fault, MBF – MacIntosh Brook Fault, RIL – Red Indian Line. Inset is the map of North America with the location of the GSL in eastern Canada marked by a red box.

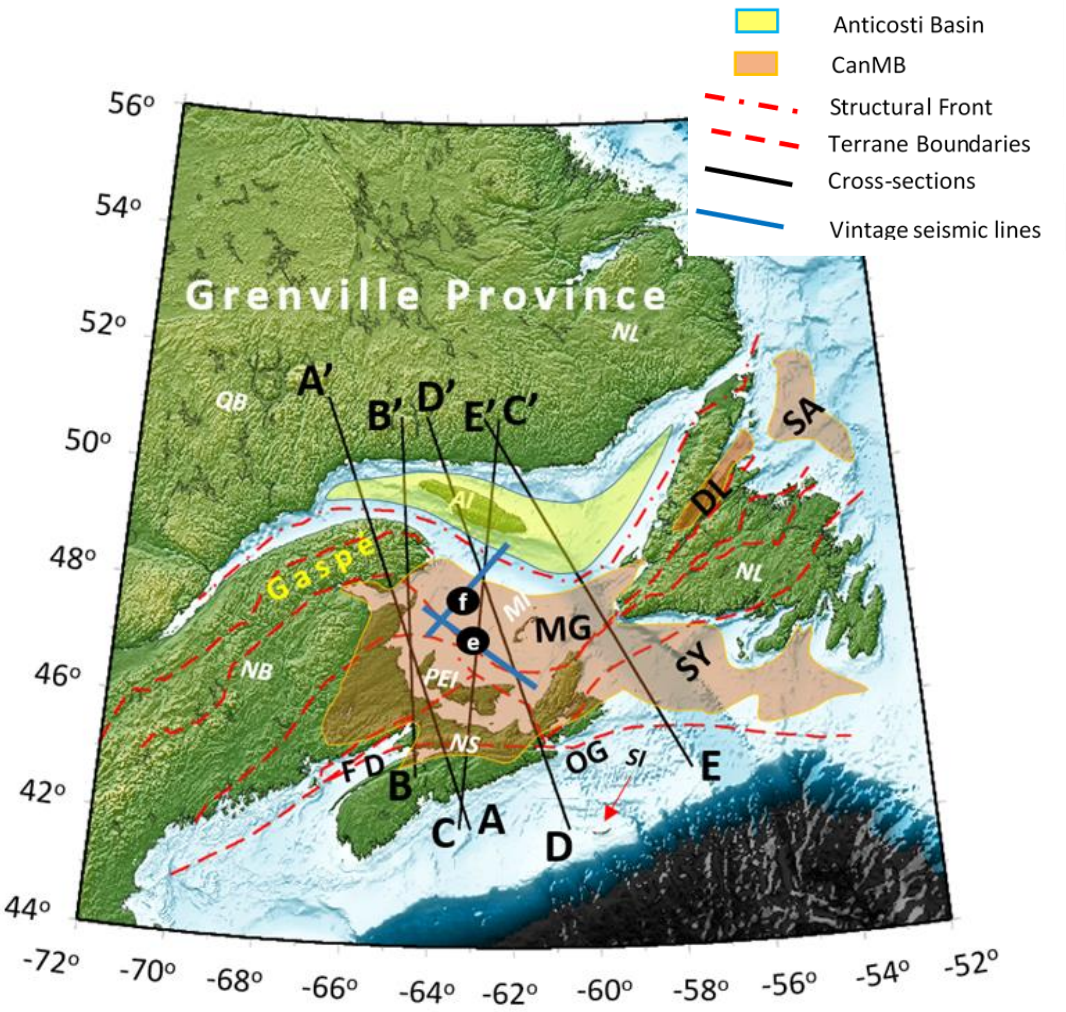

Figure 2. 2 Map of the GSL region showing the locations of the selected cross-sections (A-E) as well the location and geometry of major sedimentary basins in the GSL, modified after Dietrich et al. (2011), Chi et al. (2010), Peter (1993) and Marillier and Reid (1990). Blue lines and black circles with letters inside mark the location of vintage wide-angle seismic reflection lines 86-1 ("e") and 86-2 ("f"), adopted from Keen et al. (1986) and Marillier et al. (1989). Basins: CanMB – Canadian Maritimes Basin, DL – Deer Lake Basin, FD – Fundy Basin, MG – Magdalen Basin, SA – St. Anthony Basin, SY – Sydney Basin; OG – Orpheus Graben. Provinces and Islands: QC – Quebec, NB – New Brunswick, NS – Nova Scotia, NL – Newfoundland and Labrador, PEI – Prince Edward Island, SI – Sable Island, AI – Anticosti Island, MI – Magdalen Island.

The Appalachian mountain belt was previously divided into five major tectono-stratigraphic zones or terranes identified in as the Humber, Dunnage, Gander, Avalon and Meguma terranes, each with unique geological characteristics (Williams, 1995). The Gander, Avalon and Meguma terranes represent separated and isolated Gondwanan-derived micro-continental fragments, referred to herein as Ganderia, Avalonia and Meguma (Figure 2.1). The Gondwanan-derived terranes accreted independently and sequentially and were responsible for the Salinic, Acadian and Neoacadian orogenic cycles respectively (van Staal et al., 2009; van Staal & Barr, 2012). Large parts of the former Dunnage zone were shown to have formed on Gander zone (Exploits subzone of Williams et al., 1988) and its basement (van Staal, 1987; Williams & Piasecki, 1990), whereas the Ordovician arc-related rocks of the western part of the Dunnage zone (Notre Dame subzone) were largely built upon Laurentian-derived basement (van Staal et al., 2007; Waldron & van Staal, 2001; Williams et al., 1988). Hence, the tectono-stratigraphic concept became obsolete and was replaced by a new nomenclature used herein (e.g. Hibbard et al., 2006; van Staal and Barr, 2012).

The former Notre Dame subzone comprises multiple, closely related arc terranes (van Staal et al., 2007; Zagorevski & van Staal, 2011), which for the sake of simplicity are referred to herein as the Notre Dame arc (NDA, Figure 2.1). The boundary between the two Dunnage subzones is the Red Indian Line (RIL), which is the fundamental suture in the Appalachian mountain belt, separating rocks that formed in the peri-Laurentian domain from those that originated near the Gondwanan margin of Iapetus (peri-Gondwanan domain) (Hibbard et al., 2006). The RIL is exposed in Newfoundland and Maine and was previously imaged geophysically at depth (Hall et al., 1998; van der Velden et al., 2004). It is buried beneath successor basin strata in the GSL region and New Brunswick (van Staal & Barr, 2012). Peri-Godwanan-derived Ganderia comprises two

major tectonic blocks that accreted independently: the leading Popelogan-Victoria arc and the trailing Gander margin (van Staal, 1994). The latter mainly comprises of Cambrian to Silurian siliciclastic sedimentary rocks (van Staal & Barr, 2012). The Popelogan-Victoria arc and the Gander margin became separated by the oceanic Tetagouche-Exploits back-arc basin during the Middle Ordovician, which in turn was closed during the predominantly Silurian Salinic orogenic cycle (van Staal, 1994; van Staal & Barr, 2012).

The Popelogan-Victoria arc accreted to the leading edge of composite Laurentia during the Late Ordovician (ca. 455 Ma) along the RIL, whereas the trailing Gander margin sutured to a progressively expanding and hence, composite Laurentia at approximately 430 Ma along the Dog Bay Line (DBL) - Bramford Brook Fault (BBF) system (Williams et al., 1993; van Staal et al., 2008, 2009; Reusch and van Staal, 2011). Southeast of the DBL-BBF fault system, Ganderia and Avalonia are separated by a generally steeply northwest-dipping tectonic boundary, known as the Caledonia-Clover Hill Fault (CCHF) in New Brunswick, Macintosh-Brook Fault (MBF) in Nova Scotia and Dover-Hermitage Fault (DHF) in Newfoundland (van Staal & Barr, 2012). The southeasternmost peri-Gondwanan Meguma terrane, which represents an isolated crustal block with a probable West African provenance, is separated from Avalonia by the Cobequid-Chedabucto Fault (CCF) in Nova Scotia and Collector Magnetic Anomaly (CMA) offshore to the east (Figure 2.1).

The three main geological phenomena associated with the GSL region are the Lower Paleozoic and older strata of the Iapetan passive margin of eastern Laurentia, younger Paleozoic strata of the Gaspe Belt and the Canadian Maritime Basin (CanMB) (Figure 2.2). The latter two basins represent successor basins deposited on accreted and deformed older rocks. The deformed Lower Paleozoic rocks of the Humber Zone mark the westernmost extent of allochthonous rocks

in the Canadian Appalachian mountain belt. It consists mainly of carbonate and siliciclastic sedimentary rocks and corresponds to the bulk of the Iapetan passive margin of eastern Laurentia, hence is referred to as the Humber margin (van Staal et al., 2007) (Figure 2.1). The Humber margin is bounded by a narrow zone of ophiolitic- and arc-related rocks of the NDA (van Staal et al., 2007) southeast of the BVBL (Williams & Julien, 1982). The Appalachian Structural Front (ASF; Figure 2.1) marks the contact between un-deformed rocks of the St. Lawrence Platform (SLP; Figure 2.1) and rocks folded and imbricated during the various orogenic phases that created the Appalachian mountain belt, including the Appalachian structural wedge situated northwest of the BVBL (Pinet et al., 2014).

In western Newfoundland, the ASF coincides with the boundary (Logan's Line) between the allochthonous Humber margin and the SLP (Figure 2.1). Further southwest, the ASF is located within a strip of SLP involved in Appalachian deformation (Pinet et al., 2014). Locally in the GSL, the ASF is truncated at surface by younger sedimentary rocks of the CanMB (Figure 2.2), which unconformably overlie the Appalachian structural wedge (Haworth, 1978; Jackson et al., 1998; Pinet et al., 2014). The middle Paleozoic Gaspé Belt (Figure 2.2), found mostly in eastern Quebec and northern New Brunswick, consists of shallow to deep marine clastic sedimentary rocks, volcanic flows and volcaniclastic rocks (Wilson et al., 2004). It overlies the Humber margin and is partly overlain unconformably by the Upper Paleozoic rocks of the CanMB (Dietrich et al., 2011; Waldron et al., 2015). The Upper Paleozoic CanMB, covers a total area of about 250,000 km^2 (Dietrich et al., 2011). It is a basin system comprising four major sub-basins (mainly Carboniferous and younger rocks): Magdalen, Deer Lake, Sydney and St. Anthony (Figure 2.2). Although the basin thickness and geometry are not clearly known, general estimates from active

source seismic studies suggest the top of the basement locally may be over 12 km deep (Gibling et al., 2008; Howie, 1988).

2.2.4 Data and Analysis

In this section, I describe the seismic noise data used in our analysis and our data processing routine. The analysis procedures include waveform preprocessing and cross-correlation, determination of group velocities and surface wave tomography, and 1-D trans-dimensional Bayesian inversion. Finally, the 1-D velocity profiles at all grid points are combined to produce a pseudo 3-D shear wave velocity model for the region.

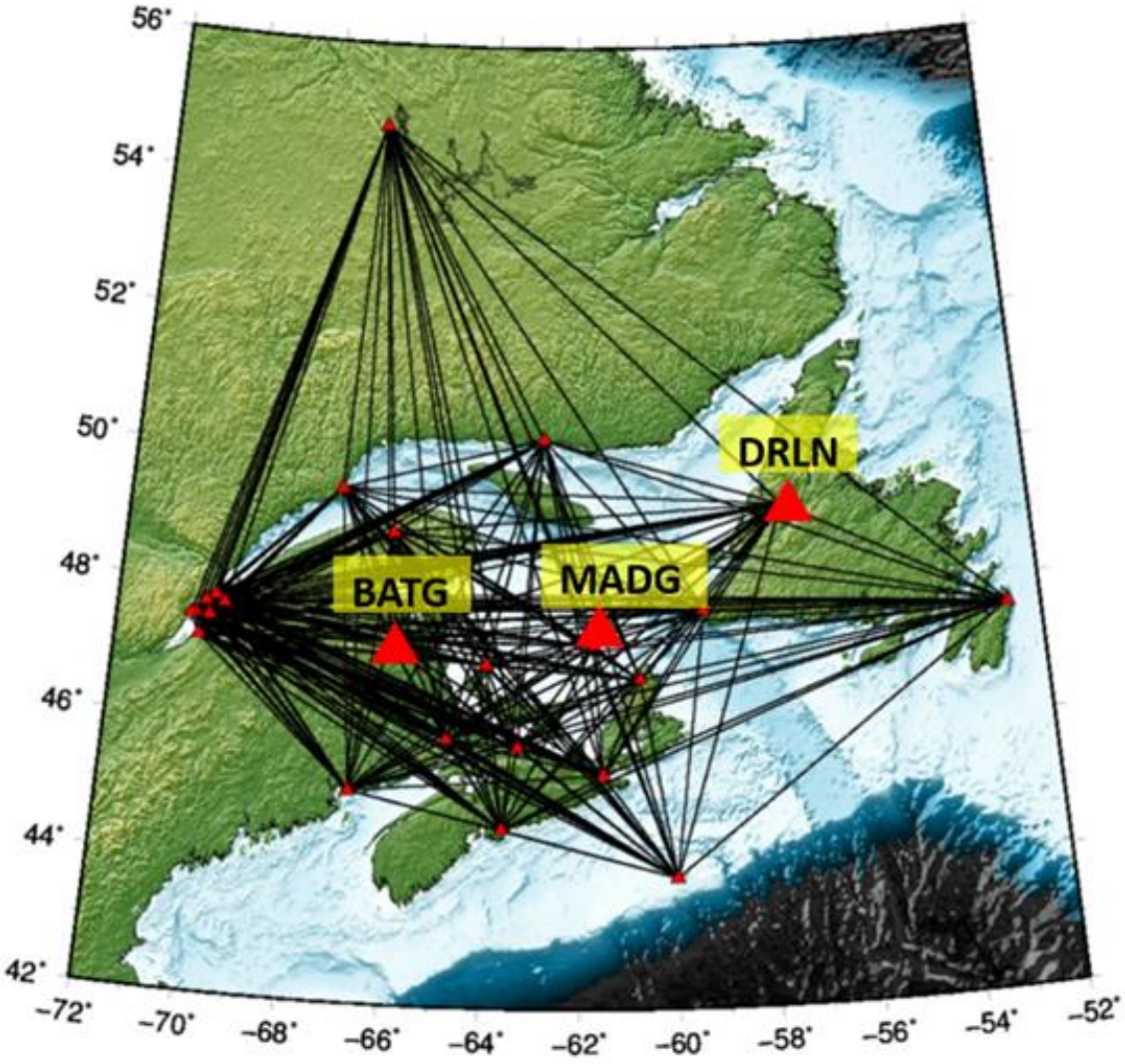

Figure 2. 3 Distribution of seismograph stations used in the GSL and the corresponding ray path and coverage. Red triangles are station locations, the larger (named) ones are the stations referenced in the text.

2.2.4.1 Ambient Noise Data

Continuous ambient noise waveform data were recorded at 24 CNSN and POLARIS seismic stations. The primary noise source is the microseism energy propagating from the GSL and the adjacent Atlantic Ocean. The stations were mostly deployed between October 2005 and October 2008. Six stations were set to record at 40 samples per second (sps), while the rest recorded at 100 sps. The station density and distribution allow for adequate coverage of the basin structure (Figure 2.3). With the exception of probable instrument malfunction and/or deployment/maintenance schedules, most of the stations used in this study recorded about 3 years of continuous noise data. These data, archived in the CNSN database in the Standard for Exchange of Seismic Data (SEED) format, were retrieved and processed following the standard ambient noise scheme proposed by Bensen et al. (2007), except for the spectral whitening step, which sometimes introduce spectral contamination (Arroucau et al., 2010; Brandmayr et al., 2016). Only the vertical components of the waveforms from simultaneously recording stations were considered and processed for this study. A total of 27,185 SEED files were systematically converted to Seismic Analysis Code (SAC) format and cut into segments with a uniform length of 24 hours. Our final dataset consists of 24,791 day-long records. About 9% of the original files were lost in the conversion process because of incomplete daily records and bad file formats.

2.2.4.2 Pre-processing and Cross-Correlations

The initial steps adopted in the preprocessing scheme involved removing the mean and linear trend of the waveform data recorded at individual stations. Since different instruments were used in data acquisition, instrument responses were removed from the data to convert all traces to ground velocity. The data were then down-sampled to 1 sps for storage space and computational

efficiency. One-bit time domain normalization and spectral whitening were subsequently applied to remove high-amplitude signals such as earthquakes and spurious signals from instrumental irregularities and to also improve spectral resolution. Each one-day segment of the data was cross-correlated for every available pair of stations. A total of 265,334 daily cross-correlograms were produced at this stage; one example is shown in Figure 2.4. Only datasets with pairs of complete daily records were considered for cross-correlation. Each noise correlation function (NCF) corresponds to the elastic response of the earth along the path between the station pair under consideration. The low signal-to-noise-ratio (SNR) of the resultant waveform is improved by stacking the NCF over the days for which the pair of records exists. Depending on the operational status of individual stations, the number of available days for stacking ranges from 750 to 1083 with an average of 962 days. The resulting waveforms show a remarkable improvement in the SNR, as both the causal and acausal parts of the signals are clearly identifiable in most cases (Figure 2.4a – *middle panel*). Symmetrization of the stacked traces was achieved by taking an average of the waveform and its time-reversed component (Figure 2.4a – *bottom panel*). I achieved these steps by writing several Linux shell scripts to execute commends and functions included in the Seismic Analysis Code (SAC), which is written in the C language.

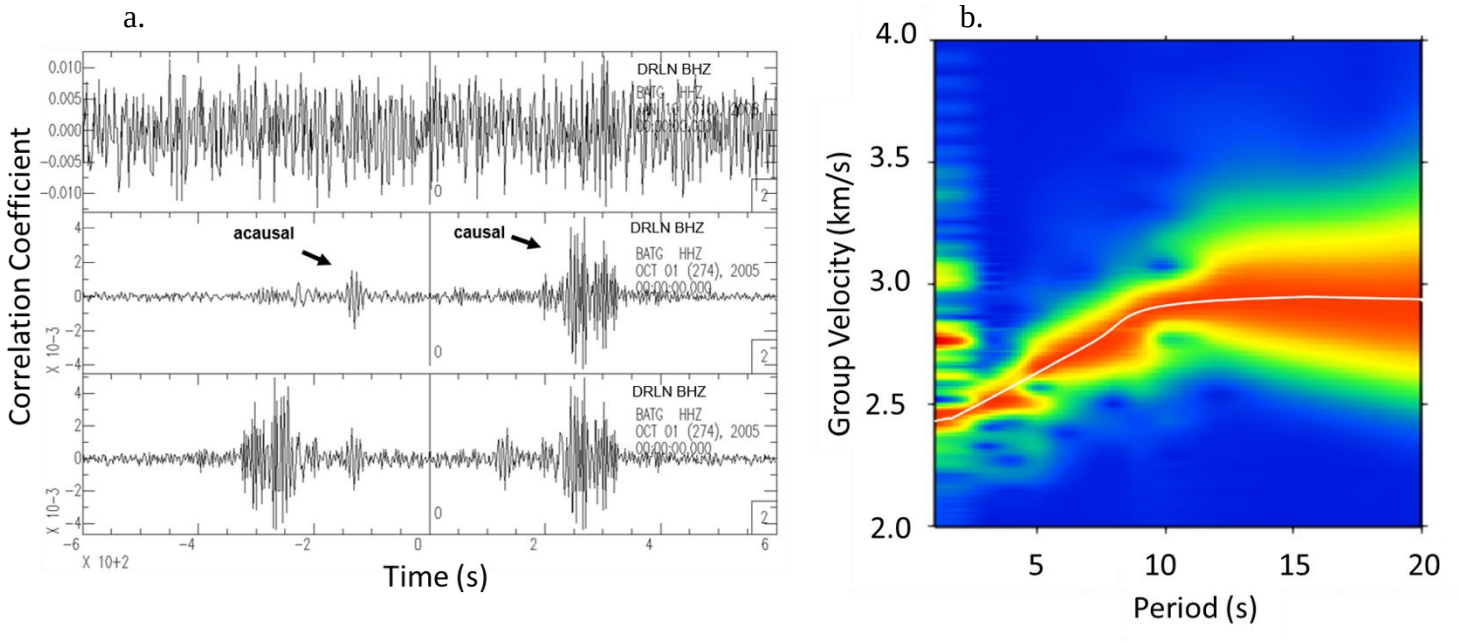

Figure 2. 4 Cross correlogram and group velocity measurement for station pair DRLN and BATG. (a) top panel: 1-day cross correlogram; middle panel: stacked cross-correlogram; bottom panel: stacked and symmetrized cross-correlogram. (b) Group velocity dispersion distribution for station pair DRLN and BATG. Gray line indicates dispersion curve. BHZ and HHZ represent the vertical component of a broadband sensor.

2.2.4.3 Group Velocity Dispersion and Surface Wave Tomography

Group velocities of the fundamental mode of the Rayleigh wave were measured from the stacked symmetric traces for periods between 2 and 20 s using the frequency-time analysis method (FTAN) (Bensen et al., 2007; Dziewonski et al., 1969). The FTAN method was implemented by combining functionalities in SAC, Computer Programs in Seismology (CPS; Herrmann, 2013) and some self-developed FORTRAN codes, all implemented through Linux shell scripts that I wrote. Dispersion plots of period-dependent group velocities were obtained for every station-pair propagation path; an example is shown in Figure 2.4b. The spatial distribution of group velocity anomalies for each period considered was obtained by implementing the iterative non-linear fast marching surface wave tomography with the computer code provided by Nick Rawlinson (Rawlinson and Sambridge, 2003) and Linux shell sripts written by myself. It combines a forward calculation using the fast marching method of Sethian and Popovic (1999) with a regularized iterative subspace inversion step (Kennett et al., 1988; Sambridge, 1990). The forward step calculates seismic waves arrival times by tracking the wavefront propagation, while the inversion step estimates several models that fit the data. The final model selection is guided by a pair of regularization parameters referred to as the damping and smoothing parameters, which provide a trade-off between the data fit and model smoothness. A synthetic checkerboard resolution test is adopted in this study to test spatial resolution across the period range considered.

2.2.4.4 Trans-dimensional Bayesian Inversion and Pseudo-3D Tomography

The final step of our data processing is to convert the surface wave tomography results to a 3-D shear wave velocity model. We followed the steps described in Kao et al. (2013) to define a grid system for the study region (45–50.5ºN, 55–68ºW, 0.5º grid spacing). At each grid point, a

new dispersion curve was constructed by taking values from the surface wave tomography maps at successive periods. This dispersion curve was then inverted to obtain a 1-D velocity profile using a non-linear trans-dimensional (trans-D) Bayesian inversion scheme (Dettmer et al., 2010; Dosso et al., 2014; Malinverno, 2002; Sambridge et al., 2006). Bayesian inversion is based on estimating the posterior probability density (PPD) which combines data information (through the likelihood function) with prior information (here taken to be a bounded uniform distribution). Trans-D inversion addresses the problem of model selection within parameter/uncertainty estimation. In the present problem, the number of layers in the 1-D *Vs* profile which is consistent with the resolving power of the dispersion data is not known *a priori*. Under-parameterizing the model (choosing too few layers) can under-fit the data and leave model structure unresolved. Conversely, over-parameterizing the model (too many layers) can over-fit the data, leaving the structure unconstrained. Regularized (linearized) inversion typically over-parameterizes the model but constrains the result by explicitly minimizing roughness, subject to fitting the data to a statistically appropriate level, to produce the simplest (smoothest) model (Constable et al., 1987). However, regularization and linearization generally preclude meaningful uncertainty estimates of the solution (a point estimate). In contrast, trans-D Bayesian inversion provides a fully nonlinear ensemble of solutions by sampling probabilistically over the number of layers to let the data determine the appropriate parameterization (with the uncertainty in the number of layers included in the parameter uncertainty estimates).

Trans-D inversion constructs an estimate of the PPD which spans multiple dimensions using a birth–death reversible-jump Markov Chain Monte Carlo (rjMCMC) algorithm (Green, 1995) to add and delete layers during sampling. The rjMCMC algorithm is implemented using a scheme in which perturbation, birth and death moves are proposed with equal probabilities. A perturbation move perturbs the values of model parameters (e.g., interface depths, shear-wave

velocities) without changing the number of layers. A birth move proposes to add an interface to the model at a randomly chosen depth; a death move proposes to remove a randomly-chosen interface. All moves from the current model to the proposed model are either accepted or rejected based on the Metropolis-Hastings-Green criterion. To improve the acceptance rate of birth and death moves and ensure complete sampling, parallel tempering is applied based on a set of interacting Markov-chain samplers in which the likelihood is successively relaxed (Dosso et al., 2012; Sambridge, 2014). (For details on the particular trans-D algorithm used here, readers are referred to Dosso et al. (2014)). Due to the variable parameterizations in trans-D inversion, results are typically considered in terms of marginal probability profiles. Here, the collection of model samples is binned onto a depth-V_s grid to produce marginal profiles. A representative model can be selected from the samples using a variety of statistical operations. Examples of representative models applied in previous studies include: the mean (e.g. Pilia et al., 2015), median (e.g. Gehrmann et al., 2015) and maximum *a posteriori* (MAP) model for the most-probable number of layers (e.g. Steininger et al., 2013). The trans-D inversion scheme was implemented using a FORTRAN code written by Stan Dosso (Dosso et al., 2014), while model sample binning, selection and plotting were achieved by a few MATLAB scripts I wrote.

For this work, the inversion starts with an initial model of 3 layers above a mantle half space with the thickness and V_s of each layer arbitrarily fixed. The input dispersion data for each grid point consists of 12 group velocity data points over the frequency range of 0.05–0.5 Hz with an estimated standard deviation of 0.05 km/s. We set the *a priori* range of V_s at 2–5 km/s and the number of interfaces is allowed to vary between 1 and 10. P-wave velocity (V_p) and density values were scaled to the *Vs*. An ensemble of 700,000 models was drawn from the PPD, and the ensemble examined to ensure stationary sampling in likelihood and convergent results for the model parameters. The data residuals (difference between measured and modeled data) were found to be

consistent with the assumption of Gaussian errors of the specified standard deviation. Marginal probability of model ensembles was obtained by considering the entire model samples drawn from the PPD for each inverted grid dispersion curve in the GSL. Representative 1-D V_s models, corresponding to the median of the distribution, together with the associated uncertainty estimates were then extracted and interpolated from grid to grid, over the whole region. In principle, the depth inversion of Rayleigh wave group velocities also depends weakly on V_p and density. These models were estimated in the inversion but were poorly constrained and as a result, excluded from subsequent analysis.

2.2.5 Results

In this section, we present three sets of results obtained from the processing stages that follow our dispersion measurements. The first set includes frequency-dependent 2-D group velocity maps obtained by applying regularized 2-D surface wave tomographic inversion methods to our dispersion measurements. The second is 1-D V_s models obtained by trans-D inversion of group velocities at specific grid locations of the study area. The last set shows the *pseudo* 3-D tomography model (with uncertainty distribution) obtained by combining 1-D V_s models at all grid points. Vertical cross sections passing through various parts of the GSL are also presented to show the regional sub-surface velocity heterogeneity. For the surface wave tomography, low- and high-velocity anomalies are defined as regions with group velocities < 2.95 km/s and > 3.05 km/s, respectively. For the *pseudo* 3-D tomography, we define a crustal low-velocity zone (LVZ) and a high-velocity zone (HVZ) to be places where the corresponding V_s is below and above 5% of the mean value, respectively. In addition to the V_s tomography results, regional potential field datasets (distributions of Bouguer, free-air, and magnetic anomalies), derived from a compilation of surveys since 1944, are incorporated to provide an integrated interpretation framework in section

2.5. The potential field datasets are available through the Geoscience Data Repository for Geophysical Data on the Natural Resource Canada's website (http://gdr.agg.nrcan.gc.ca/gdrdap/dap/search-eng.php). The magnetic residuals data are obtained by subtracting the International Geomagnetic Reference Field (IGRF) from the total field, with the regional field also accounted for (Teskey et al., 1982).

2.2.5.1 Surface Wave Tomography and 1-D Vs Results

2-D Group Velocity Maps

Group velocity maps for periods from 2 to 20 s were produced by applying linearized and regularized surface wave inversion methods on composite dispersion data obtained from processing the GSL ambient seismic noise dataset. The selection of group velocity maps for each period was guided by analyzing the "L-curve", which compares the data misfit to the model damping and smoothness. A trade-off between the data fit and the damping and smoothness parameters was established for each group velocity map. The optimum group velocity model (map) is the one for which there is little to no improvement in the data fit for a large change in the model perturbation (damping level) and smoothness. Figure 2.5 shows the distribution of Rayleigh wave group velocities for the periods of 2, 5, 8, 10, 18 and 20 s, together with sample results of the checkerboard resolution test and the corresponding ray-path coverage. The 2 s map is characterized by an isolated relatively high-velocity anomaly (~3.2 km/s) in the middle of the Magdalen sub-basin (a) (centered at ~47.0ºN, ~62.5ºW), surrounded by low-velocity anomalies (Figure 2.5a). The low-velocity anomalies extend landward of the Magdalen sub-basin but transition sharply to high-velocity anomalies (>3.0 km/s) farther north of GSL (i.e., the Grenville Province, Figure 2.1). Close to the middle of the CanMB, the observed low-velocity anomaly becomes prominent and

extensive at the 5 s period, covering the entire GSL and the adjacent lands (Newfoundland, Nova Scotia, and New Brunswick). It also extends as far south as Sable Island (at ~44.2ºN, 60ºW) near the southern edge of our model (Figure 2.5b). The signature of relatively higher group velocities of the Grenville orogen north of the GSL remains unchanged. At the period of 8 s, the prominent low-velocity anomaly shrinks toward the center of the GSL, with a minor expression across parts of the Humber Zone and Gaspé Belt (Figure 2.2) to the west and Sable Island to the south (Figure 2.5c). Higher group velocity structures are observed everywhere else on this map. At 10 s, the low-velocity anomaly is visible only in the Magdalen Basin (Figure 2.5d). At periods longer than 15 s, the prominent low-velocity anomaly typically associated with shorter periods starts to vanish. There is some expression of low velocity at the center of the GSL and to its west. The signature of low group velocity anomaly is minimal at the period of 20 s (Figure 2.5f).

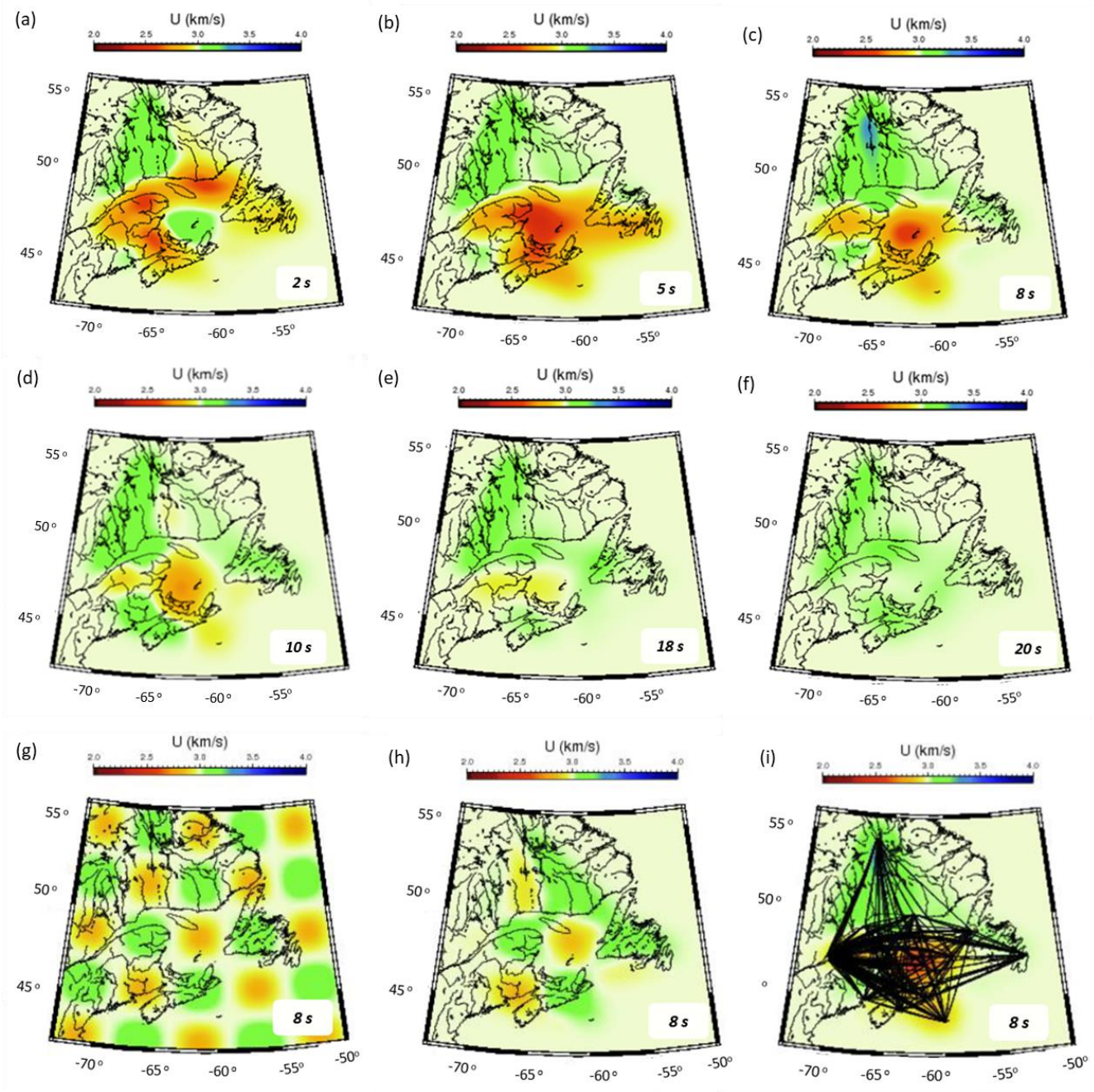

Figure 2. 5 Group velocity maps for selected periods in the range 2-20 s (a-f). Example of checkerboard resolution analyses for 8 s period: (g) synthetic positive and negative velocity anomaly field; (h) recovered velocity anomaly; (i) group velocity results for 8 s from observed datasets with the available interstation ray path coverage used in the inversion.

The checkerboard resolution test, typically implemented in many tomography studies using synthetic datasets, is adopted here to evaluate the structural resolution our ray coverage could provide across the range of specified periods. Figures 2.5g-i show the representative example of applying the checkerboard test to the synthetic dataset of 8-s period at resolutions of 2°. After trying different cell sizes for our checkerboard test, we found that our station spacing and distribution allows for a lateral resolution of 80–100 km in areas of good ray coverage. The same routines used in the inversion of the observed data are applied to the synthetic data and the result obtained is typical for periods between 2 and 20 s. Figure 2.5g shows the input velocity field with alternating high and low-velocity anomalies, while the result in Figure 2.5h is obtained with the corresponding ray coverage shown in Figure 2.5i. This test indicates that velocity anomalies within the GSL and the adjacent land can be adequately resolved by our ray coverage.

1-D *Vs* Profiles

A total of 567 1-D V_s models were constructed for the region, spanning latitudes 43° –53° N and longitudes 68° – 55° W (Figure 2.3). The 1-D models were combined to produce cross-sections of lateral velocity distribution within the basin structures, similar to what is shown on seismic sections of active seismic surveys. Our study considers depths to 20 km, due to limitations presented by the resolution beyond these depths. As a result, we focus on the upper crustal, mid-crustal and the top part of the lower crustal structures associated with the Paleozoic cover. Two examples of 1-D V_s probability distributions together with their representative models and uncertainties are shown in Figure 2.6. Near station *MADG*, on Magdalen Island, the model depicts a shallow ($\leq$ 2 km thick) high V_s structure overlying a thick column of low V_s layers (Figure 2.6a). This type of velocity structure constitutes a velocity reversal at the interface between two structural units and is atypical of the characteristic Earth model that usually shows an increase in seismic

velocity with depth. Outside this location (e.g. offshore southwestern Newfoundland), the velocity model is characterized by thick layers of low V_s materials atop higher V_s structures (Figure 2.6b).

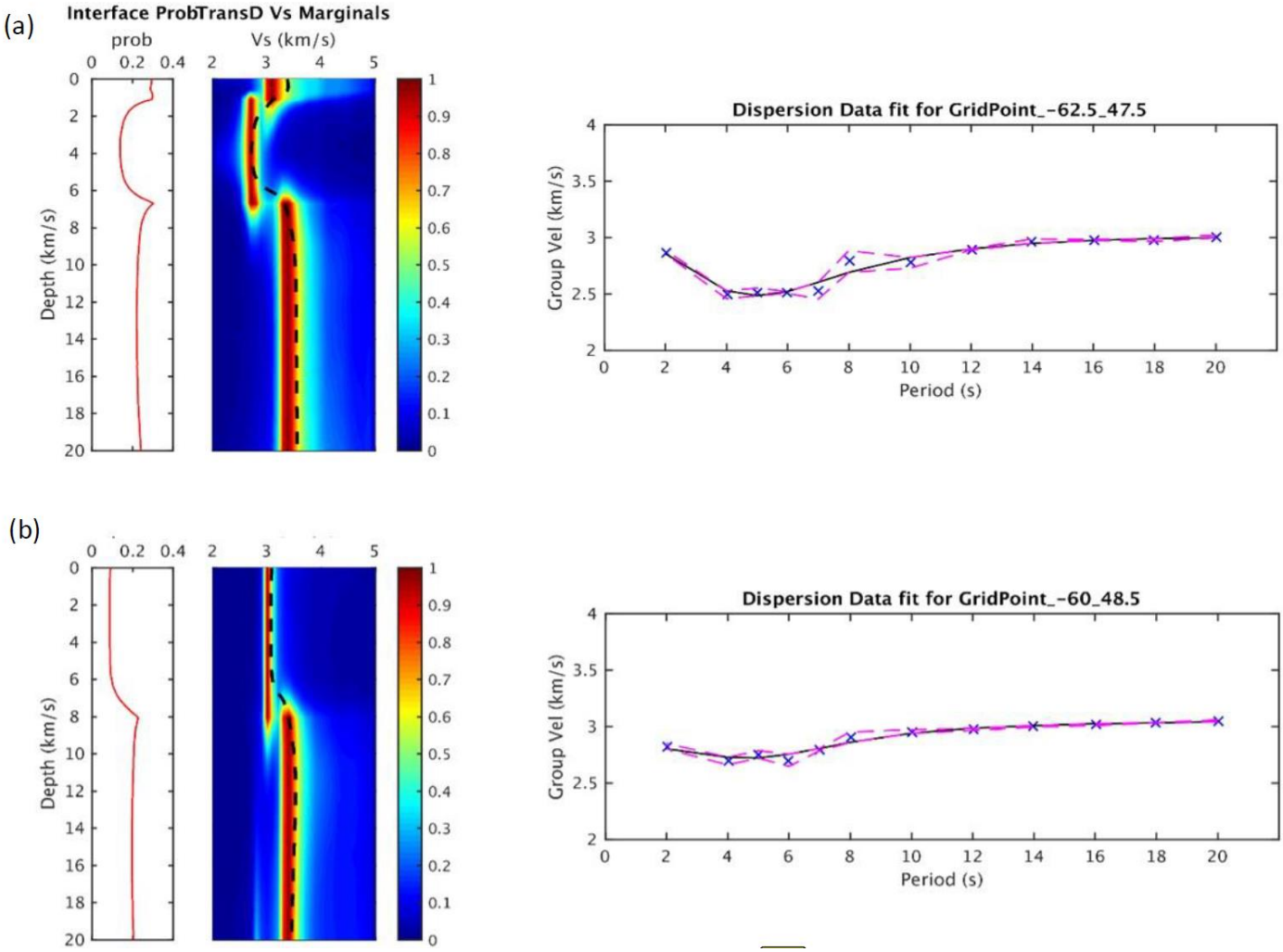

Figure 2. 6 1-D V_s results (a) near station *MADG* within Magdalen Basin; (b) offshore western Newfoundland, near the edge of Magdalen Basin. *Left panel:* Interface probability and probability marginals of V_s near station *MADG* within Magdalen Basin, red-blue colors mark high-low probabilities while dashed black line represents the 1-D representative model. Marginal probability profiles are normalized independently at every depth for display purposes. *Right panel*: Data fit for the inversion results: the asterisks are dispersion data; black continuous line is the mean of model-derived dispersion data and the magenta broken lines represent the standard deviation of the data

2.2.5.2 3-D Vs Results

Pseudo 3-D Tomography

We obtained the 3-D distribution of V_s by combining individual trans-D inversion results (Figures 2.7 and 2.8). Generally, the quality of 1-D V_s profiles obtained from the trans-D Bayesian inversion scheme used in this work strongly relies on data availability and quality. Inconsistencies in the inversion process can arise from sparse or low-quality data. These may be carried over to the 3-D tomography maps (including 2-D cross-sections) and presented as single-node anomalies. Hence, it is difficult to determine if isolated, short-wavelength anomalies actually correspond to significant geological features associated with local heterogeneities in the tectonically complex GSL region. For this reason, it is important to consider the uncertainty estimates provided with the V_s results when interpreting the features on our tomography results. In this study, we take a more conservative approach by focusing more on the long-wavelength features.

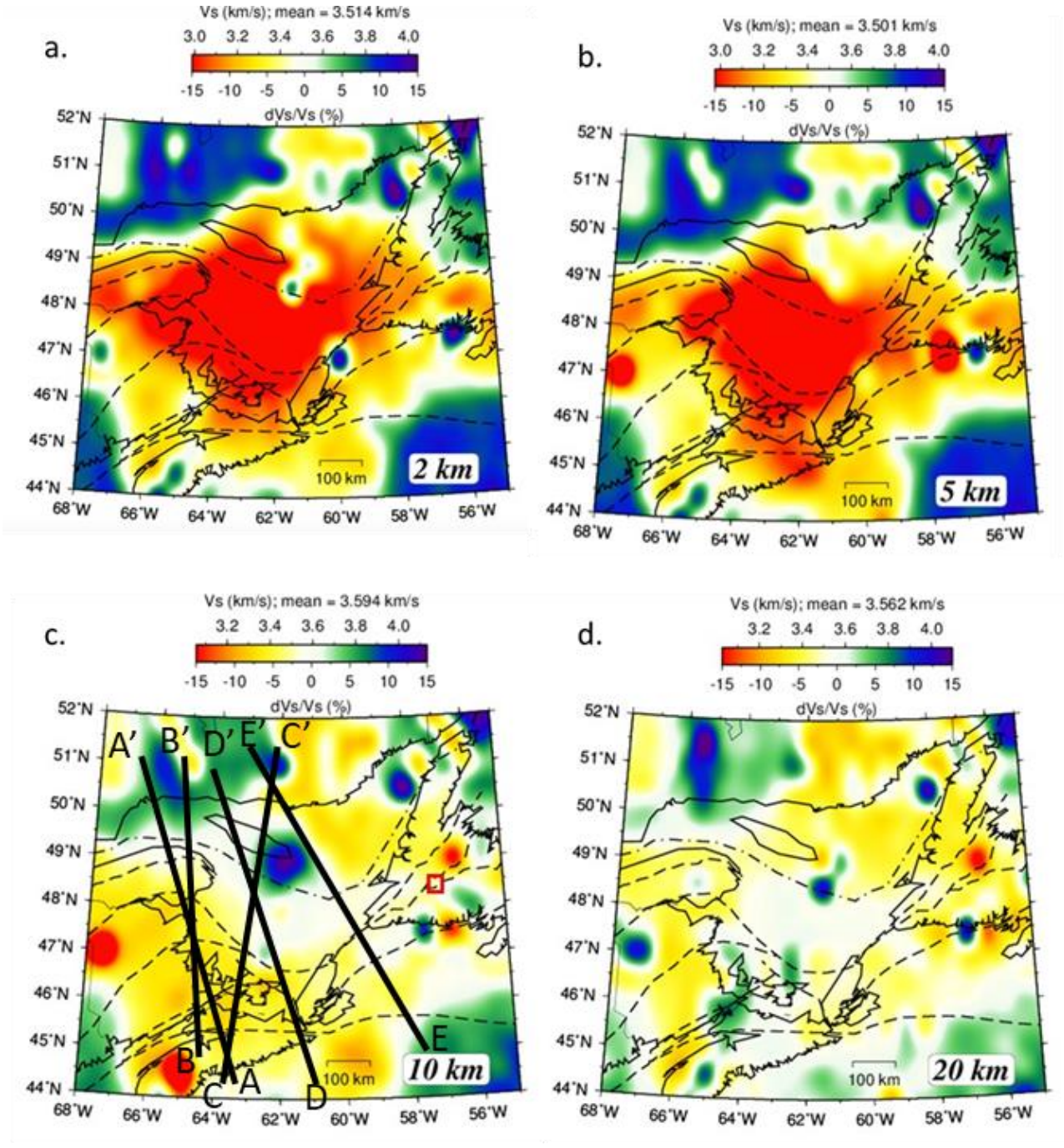

Figure 2. 7 Depth slices of *Vs* shown in left and right panels respectively for (a) 2 km (b) 5 km (c) 10 (d) 20 km. Black dashed lines on the *Vs* maps are faults and terrane boundaries labelled in Figure 2.1. Black solid lines on (c) indicate the location of the cross-sections

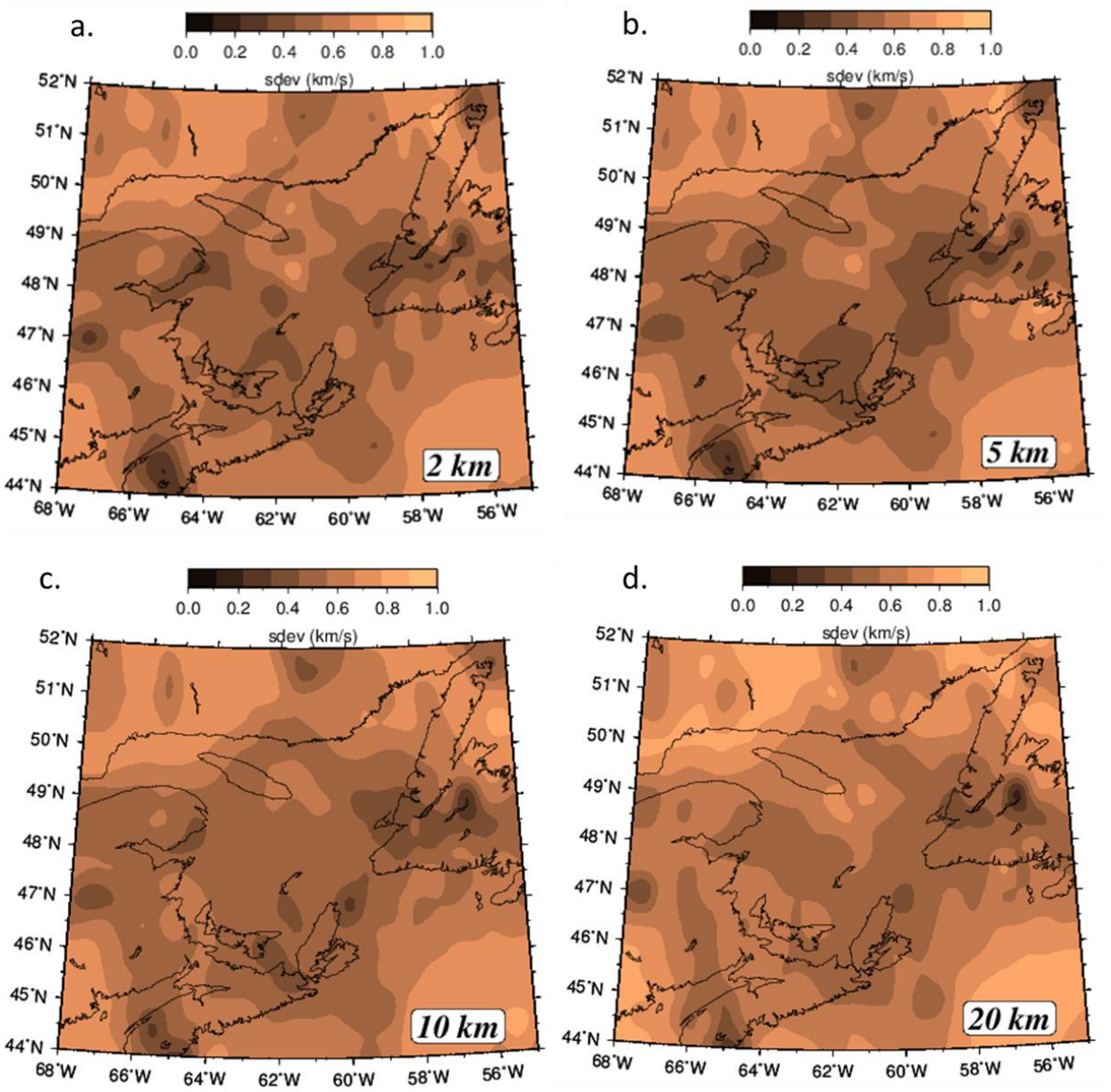

Figure 2. 8 Depth slices of uncertainty distribution associated with Figure 2.7 are shown in the left and right panels respectively for (a) 2 km (b) 5 km (c) 10 (d) 20 km; right panel corresponding standard deviation maps.

The uppermost structure of the GSL and the adjacent regions is shown in Figure 2.7a and b. The mean V_s found at the depth of 2 and 5 km are 3.51 and 3.50 km/s, respectively. In general, the velocity distribution highlights three important features. First, there is an expression of a northern HVZ that stretches southward from the Grenville province and tapers toward the Anticosti basin. Within this region, a relatively low velocity zone separates two blocks of high velocity to the east and west. The near-surface structures of the HVZ, between 50°N and 52°N, are characterized by an average V_s perturbation of > 5%. Second, an extensive LVZ ($dV_s/V_s < -12\%$) is found south of the northern HVZ between 44°N and 49.5°N, covering most of Anticosti and Magdalen Basins. The third important feature in Figure 2.7a is the emergence of high velocity structures south of 46°N. Southwest of New Brunswick, the westernmost HVZ extends to Nova Scotia and is bounded by a major LVZ near Fundy Basin (centered at 45°N, 64°W). It is also separated by the HVZ in the southeastern corner of the study area by a region of relatively low velocity near the location of the Orpheus Graben around 60°W (see Figure 2.2 for location). The associated uncertainty distribution for the 2 and 5 km depth slices are shown in Figure 2.8a and b, respectively.

Figure 2.7(c) shows the V_s structure at 10 km depth, with a mean V_s of 3.59 km/s. North of 49.5°N, the GSL is characterized by intercalated low and high V_s. South of 49.5°N, a quasi-detached HVZ, bounded mostly by low-velocity structures, is found beneath Anticosti and Magdalen Islands. Most of the prominent LVZs over the main central portion of the study area, identified on the shallower slices, are not well preserved at this depth. Lastly, the main features observed south of 47°N, at shallower depths (described above), are also present at 10 km depth. Figure 2.8c shows the corresponding uncertainty distribution.

The velocity structure at 20 km depth represents the deepest structures imaged in our study (Figure 2.7d). The mean V_s at this depth is ~3.56 km/s. The general features observed at mid-

crustal depths (i.e., 10–20 km) are preserved at this depth. Prominent but localized HVZs are found in the northern, central and southern portions of the depth slice. The HVZ identified to the south of Anticosti Island appears to have diminished, whereas new HVZ structures appear near Magdalen and Prince Edward Islands. The southwestern high velocity structure becomes more extensive, replacing the low velocities found at 10 km depth near the location of the Orpheus Graben. Maps of the potential field data show low gravity and predominantly high magnetic (with patches of lows) anomalies at the edge of the Grenville Province. On the other hand, the middle of the GSL is dominated by higher gravity (and relatively higher magnetic) anomalies with bands of lows, while the southernmost edge of the maps is characterized by a mix of prominently high and low gravity and magnetic anomalies (Figures 2.9 and 2.10). The corresponding uncertainties are presented in Figure 2.8d.

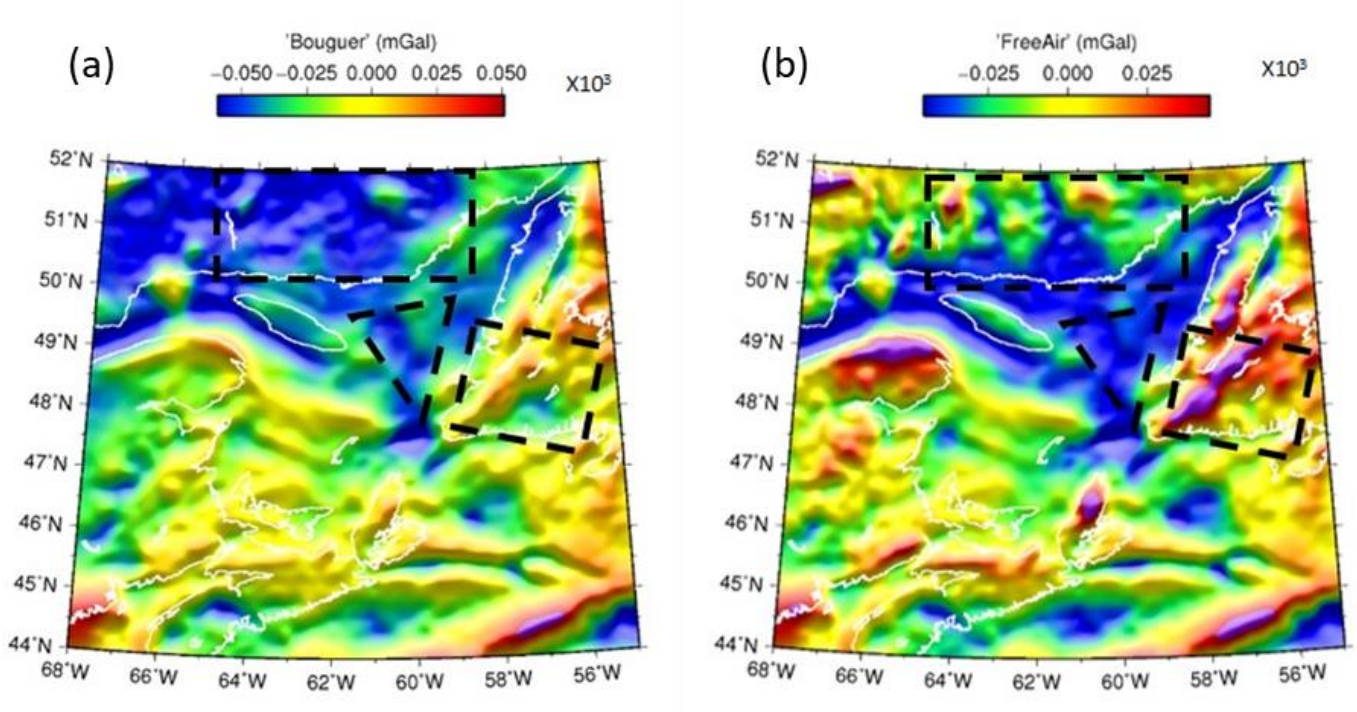

Figure 2. 9 Potential Field Data – (a) Bouguer and (b) Free-Air gravity anomalies for the Gulf of St. Lawrence. Data source: Geoscience Data Repository for Geophysical Data (http://gdr.agg.nrcan.gc.ca/gdrdap/dap/search-eng.php). Polygons with black broken lines show locations of previously studies anorthosite intrusions corresponding to local gravity- lows: Murthy and Rao (1976) – square (near 48.5°N, 58.5°W); Haworth (1978) - rectangle and square; V-shaped zone of Hayward et al. (2001) – triangle.

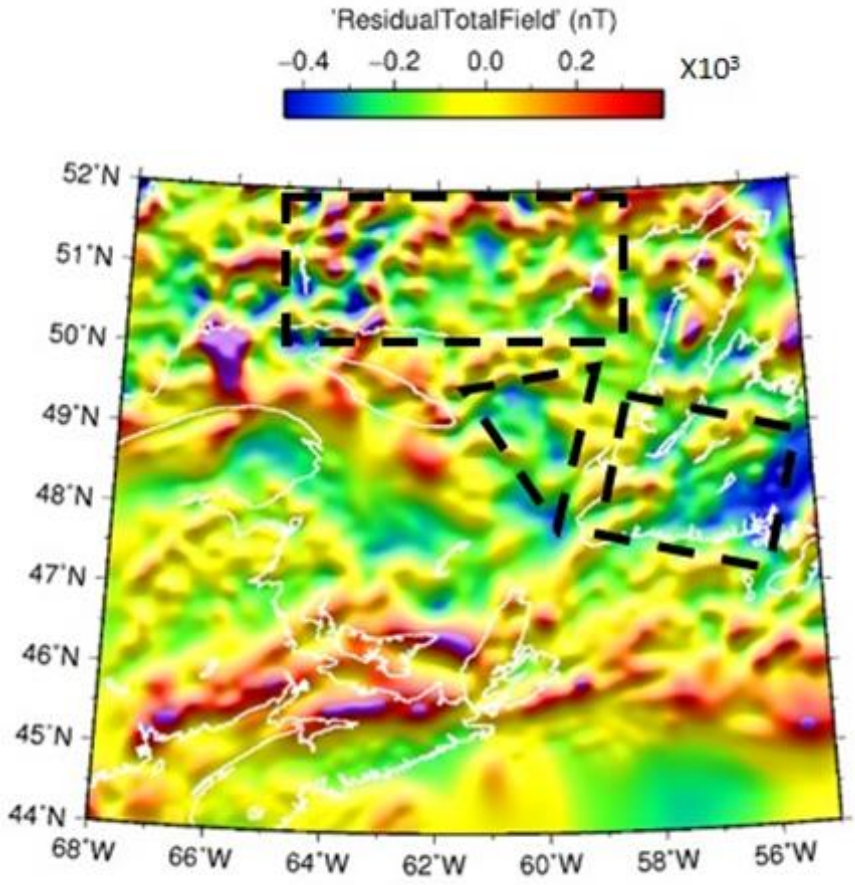

Figure 2. 10 Potential Field Data –Residual Total Magnetic Field for the Gulf of St. Lawrence. Data source: Geoscience Data Repository for Geophysical Data (**http://gdr.agg.nrcan.gc.ca/gdrdap/dap/search-eng.php**). Polygons with black broken lines show locations of previously studies anorthosite intrusions corresponding to local magnetic-lows: Murthy and Rao (1976) – square (near 48.5°N, 58.5°W); Haworth (1978) - rectangle and square; V-shaped zone of Hayward et al. (2001) – triangle.

2-D *Vs* Cross Sections

We present five approximately N-S trending V_s cross-sections (A-A', B-B', C-C', D-D' and E-E'), chosen along paths that cross all the major terranes, faults and tectonic sutures at high angles to their strike, in order to properly image their geometries at depth (Figure 2.11). The locations of the lines are marked in Figure 2.1. All the profiles run from offshore Nova Scotia in the south to Quebec in the north. Profiles A-A' and B-B' runs mostly through on-shore New Brunswick, while C-C', D-D' and E-E' mainly cover the GSL. Profile E-E' is the closest to Newfoundland. Cross-sections on land in Newfoundland were excluded from our interpretations, since these were already covered during Lithoprobe (Hall et al., 1998; van der Velden et al., 2004).

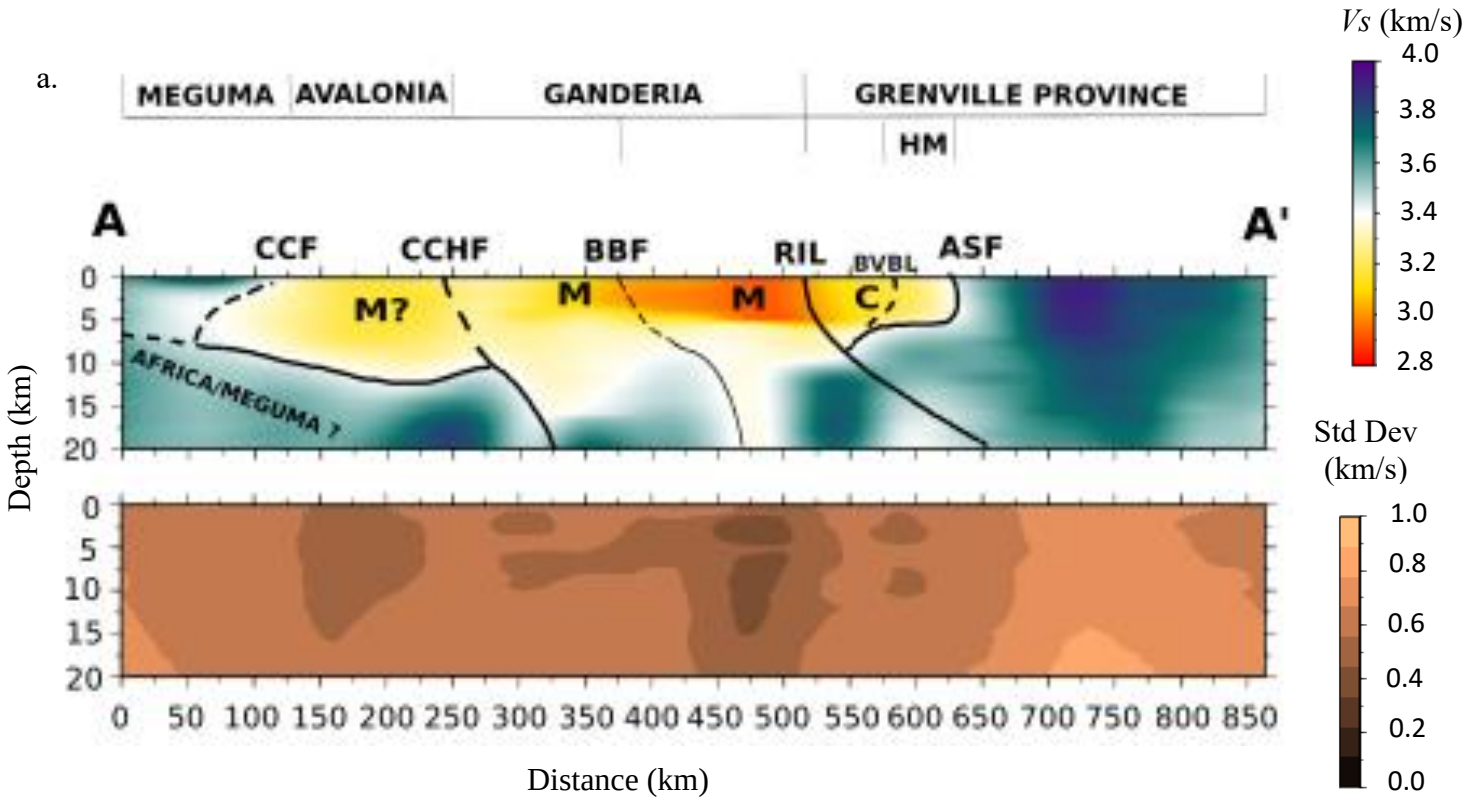

Figure 2. 11 Cross-sections showing the *Vs* and uncertainty distributions (top and bottom panel respectively) along (a) A-A', (b) B-B', (c) C-C', (d) D-D', and (e) E-E'. ASF – Appalachian Structural Front, BBF – Bamford Brook Fault, BVBL – Baie Verte – Brompton Line, CCF – Cobequid-Chedabucto Fault, CCHF – Caledonia-Clover Hill Fault, CMA – Collector Magnetic Anomaly, DHF – Dover-Hermitage Bay Fault, MBF – MacIntosh Brook Fault, RIL – Red Indian Line. Locations of sedimentary basins (after Dietrich et al. [2011]): A – Anticosti Basin, M – Magdalen Basin, S – Sydney Basin; P (in red) is the transition from high-Vs anomalies of the Grenville Province to relatively lower-Vs anomalies of the SLP. Solid lines are known faults or tectonic boundaries with clear seismic signatures, whereas dashed lines are inferred/alternative boundaries.

Figure 2.11 (continued).

b.

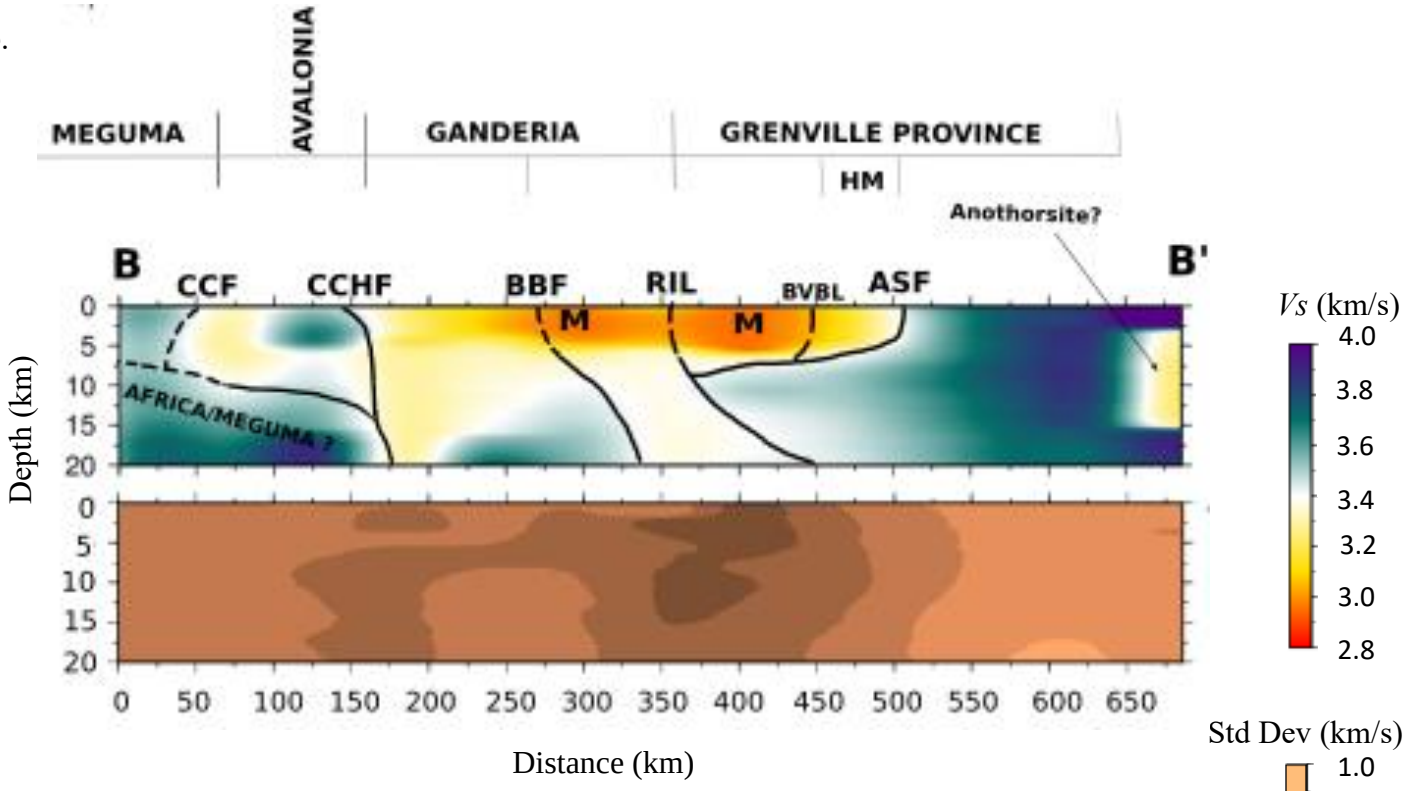

c.

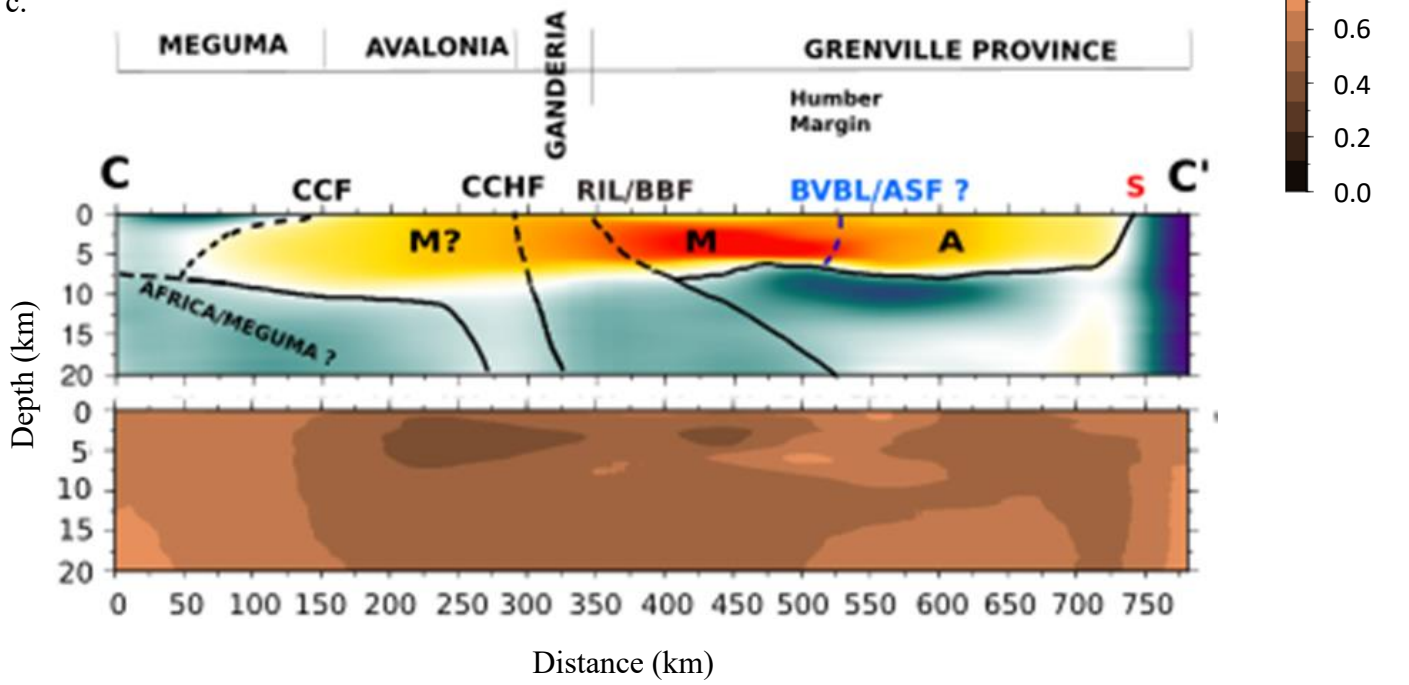

Figure 2.11 (continued).

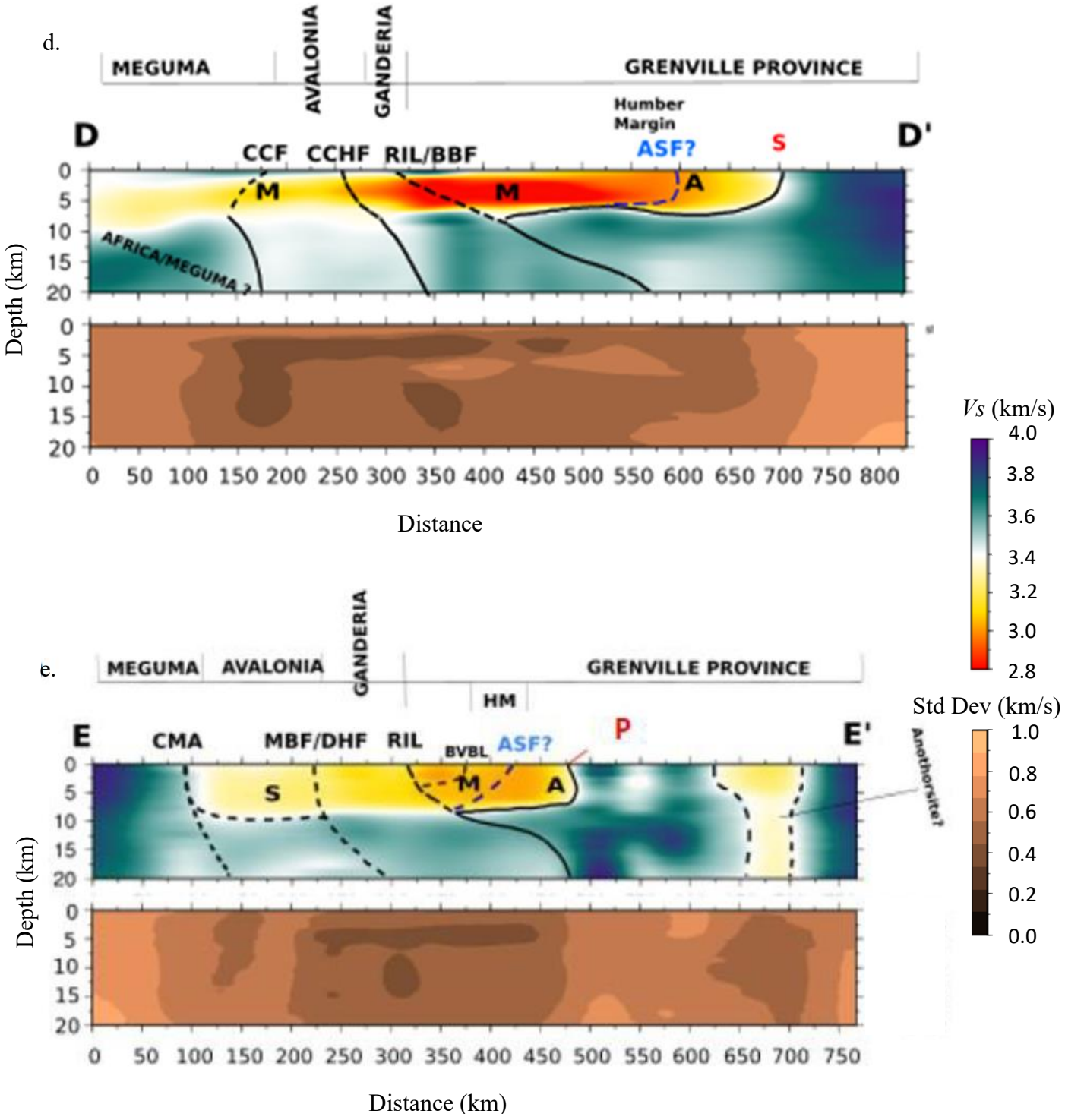

Transect A-A’ (Figure 2.11a) consists of HVZs in the southern- and northern-most edges of the cross-section but is separated by a generally lower-V_s mid-section overlying basement with V_s > 3.4 km/s. Transitions to lower V_s from the southern- and northern- most high-V_s structures correspond to the surface locations of the CCF and ASF respectively on the profile. The most prominent low-V_s is located in the top 6-7 km between the surface locations of BBF and RIL. An important observation along this line is the separation between the shallow and deep high-V_s structures at the southeasternmost edge of the profile. Cross-sections A-A’ and B-B’ are co-incident between BBF and CCHF. Both the northern and southern edge of profile B-B’ are characterized by HVZs, with a relatively lower-V_s anomaly found between the depths of 5 and 15 km at distances greater than 650 km (Figure 2.11b). The mid-section structure of B-B’ is similar to A-A’ at depth, except for a shallow high-V_s structure bounded to the northwest by the CCHF, centered at the distance of 125 km. Relatively low-V_s are found in the southeast near the boundary between Avalonia and Meguma. While the southeastern- and northwestern-most HVZs are preserved along C-C’, the low-V_s in the mid-section is more extensive, and the high-V_s basement structure appears to vary less. A moderately to steeply south-dipping CCF markedly truncates the shallow high-*Vs* that characterizes the northern margin of Meguma on profiles A-A’, B-B’ and C-C’. However, the band of shallow high-*Vs* is poorly preserved or absent along D-D’, which may be related to structures and strata associated with formation of the Late Paleozoic Orpheus graben (Marillier et al., 1989). Hence, the CCF is poorly imaged at shallow depth on this transect. Instead, the band of low-V_s structure that characterizes most of the Magdalen basin merges with the one situated across the CCF, such that it completely conceals the high-V_s basement underneath. Offshore Nova Scotia, the easternmost Meguma is separated from Avalonia by the steeply dipping CMA along profile E-E’. A notable feature along E-E’ is the sub-vertically dipping low-V_s band

within the Grenville Province centered at the distance of 675 km. We speculate that it may be the manifestation of anothorsite intrusion.

2.2.6 Interpretation and Implications

Our results represent a 3-D view of the seismic velocity structures beneath the GSL region and adjacent land areas, obtained by combining ambient seismic noise imaging techniques with a fully non-linear 1-D trans-D Bayesian inversion scheme. The results are presented with the corresponding uncertainty distributions and compared with other available seismic and potential field studies. Although ambient seismic noise tomography may be inherently incapable of resolving fine stratigraphic details at depth, it provides the opportunity for a full-coverage study of the seismic characteristics of the structure beneath the GSL and at least first-order features are well constrained. In general, we have been careful not to emphasize the lithological interpretation of the V_s results, given the highly non-linear relationship between seismic velocity and lithology, owing to a number of factors (e.g. depth of rock units and pore spaces within the rock) (Fountain & Christensen, 1989; Hughes et al., 1994). Nevertheless, to make our interpretations as reliable as possible, we compare our results with other geological and geophysical datasets, as well as with interpretations from previous studies in the region if they are available. For example, our results are consistent with the V_s (≈ 3.55 km/s) estimated at depth of 10 km from active-source seismic studies in central Newfoundland (48.52^{o}N, 56.8^{o}W; Figure 2.7c), assuming a Poisson's ratio of ~0.24. This Poisson's ratio is consistent with the 0.23-0.24 ratio estimated for the same location and depth by Hughes et al. (1994).

2.2.6.1 Vs characteristics of the Grenville Province

The high-V_s ($\geq$ 3.5 km/s) widely observed in the Grenville Province is a prominent feature of our tomography result. Similarly high velocities have been reported by geophysical studies carried out at other Laurentian and peri-Laurentian domains in Canada and northeastern USA (Musacchio et al., 1997; Petrescu et al., 2016; Boyce et al., 2016). The high V_s is characteristic of the presence of crystalline basement rocks exposed within the Grenville Province (Musacchio et al., 1997). The observed shallow-depth high-velocity anomalies in north-western Newfoundland (Figure 2.7a and b) coincide with the allochthonous Long Range inlier (Rivers, 1997; Williams, 1979, 1995), which represents an important exposure constraining the southeastern extent of the Grenville Province that was originally attached to the Humber margin. At depth, our tomographic cross-sections indicate that the Grenville Province extends further southeastward beneath the para-autochthonous, shallowly south-east-dipping Humber margin and wedges out at depth at a location which coincides with the inferred projection of the Red Indian Line (RIL) from the surface. This is consistent with the seismic interpretations of van der Velden et al. (2004) in central Newfoundland. The north-west-dipping RIL represents the fundamental suture in the northern Appalachians (van Staal et al., 1998; Hibbard et al., 2006), separating (peri) Laurentian elements involved in Appalachian orogenesis (Humber margin and NDA) from Gondwana-derived Ganderia (van Staal et al., 1998; Williams, 1995). It appears to be shallower dipping in the middle of the GSL (along profiles C-C', D-D', and E-E') than onshore (along A-A' and B-B') where the RIL, BBF and BVBL converge and/or merge, at least on surface, due to strong structural attenuation and/or excision of the Popelogan-Victoria arc (leading edge of Ganderia) and NDA (peri-Laurentia) associated with dextral strike-slip movements along the southern edge of the St. Lawrence promontory. Our tomographic cross-sections show that the RIL appears to be steeper in

the west (e.g., along A-A') than in the east (e.g., along E-E'). The basement-cover structure beneath the Humber margin and SLP is more listric on the eastern profiles with the width of the autochthonous SLP, which still overlies its original Grenville basement, varying along strike (Pinet et al., 2014). The relatively lower V_s observed at both shallow and mid-crustal depths within the Grenville Province (Figures 2.7a and 2.7e) coincides with prominent low-gravity anomalies and a characteristic magnetic signature (Figures 2.9 and 2.10) typically associated with known anorthosite suites (Haworth, 1978; Hayward et al., 2001; Murthy & Rao, 1976).

2.2.6.2 Appalachian Terranes

The V_s characteristics of the Appalachian structure are better revealed on the cross-sections (Figure 2.11) and are largely consistent with interpretations from previous studies (Dietrich et al., 2011; van Staal & Barr, 2012).

Humber Margin and the Appalachian Structural Front

The allochthonous Humber margin (e.g. *Waldron and Stockmal*, 1994) and coeval strata of the SLP are located immediately adjacent to exposed basement of the Grenville Province. In general, they are characterized by prominently low-V_s, corresponding up to ~7-9 km thick sediments, structurally underlain by Grenville basement. The transition point between the high-V_s Grenville structure and the lower-V_s structure of the Humber margin and SLP coincides approximately with the conventional location of the ASF along the western profiles (e.g. A-A' and B-B'), but is offset with respect to the ASF to the north, by 200, 100 and 50 km along profiles C-C', D-D' and E-E' respectively (marked by "P" on Figure 2.11c-e). In this region, the northern extent of the allochthonous Humber margin and the ASF do not appear to coincide. Rather, the ASF lies further to the north because part of the SLP strata are also involved in the Appalachian

structural wedge (Pinet et al., 2014). The Humber margin is bounded by the BVBL to the southeast. The zone between the BVBL and the RIL west and east of the GSL is occupied by the NDA, which is either severely attenuated or excised beneath most of the GSL. The RIL is covered by the Matapedia cover sequence in New Brunswick and inferred to occur at depth (Wilson et al., 2004) but reappears at the surface in Maine (van Staal et al., 1998; van Staal et al., 2009). Similarly, previous studies have shown that the BVBL is difficult to image geophysically (Keen et al., 1986; Spencer et al., 1989). Its V_s characteristics are not distinctly resolvable on profile A-A', but its location on profile B-B' coincides with the boundary between two low-V_s anomalies of different intensities. van der Velden et al. (2004) suggested that the BVBL is sub-vertical and continues into the lower crust in Newfoundland. Our results suggest that the BVBL appears to be truncated in the upper crust by the shallowly southeasterly dipping listric fault that separates Grenville basement and the structurally overlying rocks of the Humber margin. The BVBL is probably truncated by the RIL and/or BBF/DBL at shallow depth beneath most of the GSL, because all terranes strongly converge here in general, such that the wedge of NDA either becomes extremely narrow or is completely excised.

Ganderia

The leading edge of Ganderia (Popelogan-Victoria arc) is structurally juxtaposed against the NDA and its basement along the length of most of the RIL in the Canadian Appalachians (van Staal & Barr, 2012; Zagorevski et al., 2007; Zagorevski et al., 2008). Our results show that the shallow segments of this part of Ganderia cover a larger width on the western profiles (e.g. A-A' and B-B') but become progressively narrower towards the more eastern profiles. In general, the structure from the Ganderian basement to the Popelogan-Victoria arc is characterized by a relatively lower-V_s structure compared to basement situated beneath the adjacent NDA and

Humber margin on profiles A-A' and B-B', supporting the geological inference that they represent two different tectonic domains (Hibbard et al., 2006; van Staal et al., 2009; van Staal & Barr, 2012; Williams, 1995; Williams et al., 1988). This difference in V_s becomes less clear beneath the GSL, probably because the Popelogan Victoria arc, like the NDA, is structurally excised and/or strongly attenuated due to distributed strike-slip deformation along the southern edge of the St. Lawrence promontory, such that the Gander margin (trailing edge of Ganderia) may be directly juxtaposed structurally against the Humber margin along the virtually merged DBL-BBF, RIL and BVBL fault zones. The V_s structure of the basement to the Gander margin on profiles C-C' and D-D' is not markedly different from that of the Grenville basement present immediately west of the RIL, but when combined with the results of profiles B-B' and E-E', they suggest that the Gander margin overall has a slightly lower V_s structure than the Grenville basement west of the RIL.

The BBF suture between the Gander margin and the Popelogan-Victoria arc on cross sections A-A' and B-B' is obscured at shallow levels by a lack of velocity contrast, due to the presence of part of the CanMB and probably juxtaposition of similar sedimentary rocks on both sides of the suture (Reusch & van Staal, 2011) in the top 6 km. But it becomes well marked by more notable differences in V_s signature at depth. The BBF and the RIL thus are distinct recognisable structural features onshore. The generally low-V_s that characterize the southeastern margin of Ganderia along our cross-sections could be associated with sedimentary sequences, considered to have been deposited between the Lower Cambrian and the end of the Lower Ordovician (van Staal et al., 1996; van Staal & Barr, 2012). The Gander margin is bounded to the southeast by the CCHF in the uppermost crust in southern New Brunswick on profiles A-A' and B-B' and juxtaposed at depth against an apparently continuous shallowly northwest-dipping high-V_s extension of the basement present beneath Meguma. The juxtaposition of different V_s signature at depth suggests that the CCHF is steeply dipping towards the northwest through the crust in

southern New Brunswick (Figure 2.11 a, b), consistent with the potential field interpretations of King and Barr (2004).

Avalonia

Avalonia is sutured to composite Laurentia (at this stage including all of Ganderia) along the CCHF in New Brunswick, DHF in Newfoundland and MBF in Cape Breton Island (Nova Scotia) on the surface (van Staal & Barr, 2012). There is no clear velocity contrast at high crustal levels across the CCHF on profiles A-A', C-C' and D-D', but a high-V_s structure characterizes Avalonia on profile B-B' compared to the low-V_s structure of the adjacent Gander margin (Figure 2.11b). The CCHF also appears to be a steeply NW-dipping structure on profiles C-C' and D-D' using the criteria established on profiles A-A' and B-B'. The velocity contrast across the correlative structures further north (MBF & DHF) is less obvious at depth on profile E-E', but can be interpreted as steeply dipping to the northwest to be consistent with the seismic reflection results of Keen et al. (1986) and van der Velden et al. (2004) along the DHF in northern and southern Newfoundland, respectively. The low-V_s anomalies observed at shallow depths along most of the cross-sections probably relate to the Ediacaran-Ordovician supra-crustal successions that characterize Avalonia (Landing, 2004; O'Brien et al., 1996; van Staal & Barr, 2012). Continuous shallowly northwest-dipping high-V_s structure found beneath Avalonia (profiles A-A', B-B' and C-C') appears to be an extension of the lower crustal basement structure beneath Meguma, which if correct, implies that this part of Avalonia is a relatively thin allochthonous crustal slice completely detached from its lower crust. However, the basement characteristics of Avalonia to the east (along profiles D-D' and E-E') show different seismic characteristics with slightly lower V_s values than that observed on the cross-sections to the west. This could be associated with the preservation of lower crustal Avalonian basement beneath these parts, overlain by a band of lower-

V_s supra-crustal units. Either the seismically identified basement beneath Avalonia represents a complex structural geometry comprising allochthonous and autochthonous segments created during the Neoacadian accretion of Meguma and/or Alleghenian terminal collision, or Avalonia's basement was originally very heterogeneous and locally is very similar to that situated beneath Meguma.

Meguma

The transition from low- to high-velocity anomalies near the eastern edge of our cross-sections coincides with the steep, south-dipping CCF that separates the Avalonia from Meguma in Nova Scotia (Marillier et al., 1989). Offshore Nova Scotia, the CCF transitions into the CMA, which is a sub-vertical velocity boundary at high crustal levels on profile E-E'. Low-V_s crustal structures wedging out beneath a thin relatively high-V_s Meguma uppermost crust, on all cross-sections except profile E-E', probably represent Avalonian supra-crustal sequences that were originally under-thrust beneath Meguma's upper crust only at high crustal levels (Keen et al., 1991; van Staal & Barr, 2012; Wade et al., 1996). The E-W trending, west-dipping high-V_s basement structure that underlies Meguma appears to continue beneath Avalonia on profiles A-A', B-B' and C-C'. If correct, this could either be the original Meguma basement or a remnant of the leading edge of the West African craton that was under-thrust beneath Meguma during the Alleghenian continent-continent collision and left behind during Mesozoic post-orogenic rifting associated with the opening of the Atlantic Ocean (Hutchinson et al., 1988; Keen et al., 1991; van Staal & Barr, 2012). Regardless, an apparent velocity contrast separating the uppermost Meguma structure and basement, especially on the southern profiles (A-A', B-B' and C-C'), where Avalonia has a wedge-like geometry, suggests that Meguma is detached from its basement (Keen et al., 1991; Wade et al., 1996). The tomographic imaging of the basement beneath Meguma delineated by this study

seems to support the model of Keen et al. (1991) based on seismic reflection studies *(Figure 2.10b in their paper*), which proposed that Meguma could be allochthonous above Avalonia as well as over a basement with a distinct seismic characteristics, therein referred to as the "Sable block". Such an interpretation is also consistent with isotopic data (Eberz et al., 1991).

2.2.6.3 The Structure of the GSL Basins

Segments of the CanMB and Anticosti Basin (Figure 2.2) have been previously studied using a variety of geophysical methods; however, none offered the advantage of providing a detailed image of the entire 3-D structure within the upper and mid- crust. The spatial distribution of the prominent low-V_s anomalies on our tomographic maps correlate well with the spatial locations and extents of the CanMB and Anticosti Basin (Figure 2.2). Our tomographic cross-sections show the characteristics of both the basins and the underlying basement structures (Figure 2.11). Most of the locations of the low-V_s anomalies correspond to the conventional spatial locations of the basins, marked with alphabets on the figures (Figure 2.11). In general, our results compare well with deep seismic reflection data collected as part of the Lithoprobe program (Keen et al., 1986). In particular, both Lithoprobe lines image the sedimentary basin and its basement and show remarkable first-order agreement with our tomographic results. Two cross-sections drawn from our 3-D result at locations collinear with the deep seismic lines 86-1 and 86-2 (labeled "e" and "f" on Figure 2.2), show sharp reflections coinciding with the base of our low velocity layer at ~ 7 km (Figure 2.12). The slight variation between the reflection and *Vs* cross-sections may be related to the loss of resolution at depth, as suggested by the smearing observed on the tomographic resolution maps (e.g., Figure 2.5h).

Along profile A-A' (Figure 2.11a), the low-V_s unit located within the NDA (marked "C") mainly corresponds to the composite sedimentary sequences of the Humber margin, Middle-

Paleozoic Gaspé Belt cover and perhaps a part of the onshore Upper-Paleozoic Magdalen Basin. The latter two sequences locally disconformably overlie allochthonous ophiolites and volcanic rocks of poorly known thickness, which are in turn structurally underlain by under-thrust rocks of the Humber margin (Pinet, 2013). The sedimentary units were deposited above a Grenvillian basement, with the top of the basement at the depth of ~5-7 km. More prominent low-V_s anomalies found between the RIL and the apparent location of the ASF within the GSL (e.g. profiles C-C' and D-D') are probably associated with Paleozoic sediments deposited in the various basins underlying this region, mainly the Magdalen sub-basin. The thin top layer of relatively high-V_s anomaly, which characterizes the shallowest (~2 km) levels of crust on profiles C-C' and D-D' (e.g. between the distances of 300 and 400 km on profile D-D') could be associated with Late Paleozoic volcanic rocks, as identified in previous studies (Barr et al., 1985). South of the Humber margin, relatively low-V_s anomalies overlying relatively high-V_s Ganderian basement on profiles C-C' and D-D' could also be related to Late Paleozoic sediments that form part of the Magdalen sub-basin. The base of the sub-basin is located at depths ≥ ~7 km within Ganderia.

The Magdalen sub-basin also extends eastward within Avalonia as characterized by the relatively low-V_s structure in the upper 10 km. The low-V_s anomaly located north of the Humber Margin in the SLP (marked "A" in Figure 2.11) probably mainly corresponds to the sedimentary successions of the Ordovician-Silurian Anticosti foreland basin and underlying rocks of the SLP (Hibbard et al., 2006). Its depth to the top of the basement is ~6-7 km. The boundary between Anticosti and Magdalen (sub) basins are poorly discernable along our chosen cross- sections, but V_s anomalies that characterize the Anticosti Basin are generally higher than those associated with the Magdalen sub-basin. Similarly, the Sydney sub-basin, which is imaged on profile E-E' and marked with "S", also has a relatively higher low-V_s anomaly than the Magdalen sub-basin. The top of the basement is located at the depth of ~7-8 km along the cross-section. None of our selected

cross-sections passes through Deer Lake sub-basin; however, the shallow V_s maps (e.g. Figure 2.7a) show prominently low-velocity anomalies at its location to the depth of ~5 km.

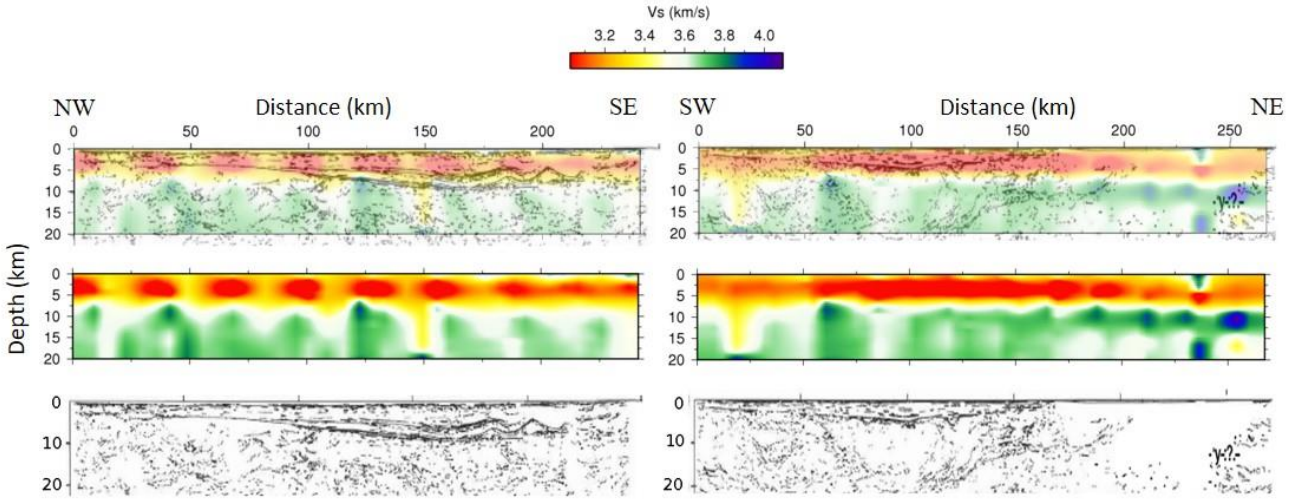

Figure 2. 12 Co-linear cross-sections from our 3-D model compared with Lithoprobe vintage deep seismic reflection lines 86-1 and 86-2 in the *top row* (marked "e" and "f" respectively on Figure 2.2); *left column* corresponds to 86-1 ("e") and *right column* corresponds to 86-2 ("f"). *Middle row:* Tomographic cross-sections displayed in top row. *Bottom row:* Vintage Seismic lines compared in the top row. The base of the low-V_s layer on our tomography cross-sections corresponds to strong reflections on the seismic profile lines at ~7 km on both lines.

2.2.7 Discussion

We interpret the results obtained from processing continuous seismic noise data recorded at 24 broadband seismic stations in the GSL region by the combining ambient noise tomography method with a fully non-linear Bayesian inversion. In general, areas within the GSL have adequate ray-path coverage and the inversion for shear wave velocities is well constrained. Consequently, the results are associated with low uncertainties. Regions with sparse station distribution and ray-path coverage (Figure 2.3) are generally associated with larger uncertainties and this was taken into consideration in our interpretations. Anomalies less than the maximum spatial resolution obtained from the surface wave tomography process might be artefacts from the inversion steps, which in most cases associated with increase in uncertainty estimates. Such short-wavelength structures are excluded from our interpretation.

The high-V_S Grenville Province is structurally wedged beneath all of the allochthonous Humber margin up to the RIL. The under-thrust Grenville wedge is thus truncated by a younger RIL. Such interpreted geometry is consistent with the seismic reflection data of the Quebec-Maine-Gulf of Maine seismic transect (Stewart et al., 1993), Gaspé (Pinet et al., 2014) and Lithoprobe transects in Newfoundland (Hall et al., 1998; van der Velden et al., 2004). East of the RIL, Ganderia is interpreted to be more or less attached to its original basement, which overall has a different velocity structure than the basement beneath adjacent Meguma and Avalonia.

Farther southeast of the Gander margin, our results can be used to test three modes of interpretations for the basement beneath Meguma's and Avalonia's upper crust: (1) It is the original, now detached basement of Meguma that was under-thrust beneath Avalonia, such that Avalonia locally became completely detached from its original basement; the latter was tectonically removed by subduction; (2) the basement is a vestige of the under-thrust leading edge

of the West-African craton (Sable block) and Meguma and parts of Avalonia represent upper crustal slices detached from their tectonically removed lower crustal basement; and (3) the basement beneath Avalonia and Meguma was originally fortuitously very similar below only some segments. We consider the third model the least likely, because we cannot find any seismic evidence for a structural boundary between Meguma and Avalonia at depth on any of the cross-sections except along profile E-E' where the steeply dipping CMA represents an observable boundary. The first and second models are both viable on the basis of our results, but we prefer model 2 for three reasons: (1) the geometry of Avalonia's upper crustal structural wedge, which separates Meguma and its basement along profiles A-A', B-B' and C-C', demands Meguma's upper crust to be structurally detached from its basement, which is consistent with the observed V_s variations (Figure 2.11a-c); (2) the V_s signature of the inferred autochthonous basement beneath Avalonia on profile D-D' and part of C-C'(Figure 2.11d) is markedly different from the allochthonous basement beneath Meguma upper crust on the same cross-section, suggesting limited under-thrusting of this basement to the northwest beneath Avalonia there; and (3) this model is most consistent with the seismic reflection data and other evidence used in the tectonic interpretations of Keen et al. (1991).

2.2.8 Summary and Conclusion

We present a comprehensive 3-D velocity model obtained from ambient noise tomography for the GSL region. The major results are as follows:

i) First order features of cross-sections drawn from our 3-D model correspond remarkably well with the co-linear Lithoprobe deep seismic reflection lines.

ii) In general, the tomographic images show a tri-band velocity structure: the prominently high-V_s Grenville Province to the northwest and the Appalachian terranes to the southeast,

separated by the low-V_s sedimentary basins overlying the uppermost Appalachian terranes in the center of the orogen.

iii) The Grenville Province is wedged out at depth due to the southeast-dipping Grenville Province being truncated by the northwest-dipping Red Indian Line, which appears to become shallowly dipping below the GSL.

iv) Low-V_s anomalies within Grenville province coincide with and hence are associated with the locations of previously known/studied anothorsites.

v) The conventional location of the Appalachian Structural Front approximately coincides with the transition from high to low V_s along some of our selected cross-sections (A-A' and B-B'). However, the same seismic distinction lies farther to the north of the ASF by as much as 200 km along other cross-sections made in the middle of the GSL, due to the presence of the Anticosti foreland basin and a more pronounced involvement of the SLP in the Appalachian structural wedge.

vi) V_s characteristics beneath Meguma's and parts of Avalonia's upper crust suggest that they could be detached from and hence, are allochthonous over a seismically distinct lower crustal basement.

vii) The allochthonous seismically distinct basement beneath Meguma and Avalonia, with the latter wedging out at depth to the southeast beneath southern Nova Scotia, could be Meguma's original basement or the West African crust under-thrust to the northwest. The latter is our preferred interpretation.

viii) Low-V_s anomalies, mostly overlying the Appalachian terranes, correspond to locations of major Canadian Maritimes sedimentary basins. These basins are characterized by varying depths and the maximum depth to the basement along our selected profiles could be up to 10 km.

2.2.9 Acknowledgements

Constructive comments from two anonymous reviewers are gratefully acknowledged. This research is jointly supported by a CSEGF award sponsored by Arcis Seismic Solutions (a TGS company) to APK, the Induced Seismicity Research Project of NRCan, Natural Sciences and Engineering Research Council (NSERC) of Canada grants to HK, JFC, GDS and SED. Seismic data was obtained from Canadian National Seismic Network data center

(http://www.earthquakescanada.nrcan.gc.ca/stndon/CNSN-RNSC/stnbook-cahierstn/index-en.php). Potential field data was obtained from Geoscience Data Repository for Geophysical Data at the Natural Resource Canada's website (http://gdr.agg.nrcan.gc.ca/gdrdap/dap/search-eng.php) and converted with help from Miles Warner. Most of the figures were plotted by the Generic Mapping Tools (GMT; Wessel and Smith (1995)).

2.3 Supplemental Materials

The supplemental materials include the results of our 3-D trans-D tomography inversion. Each line corresponds to a grid point and the values are longitude (in degrees), latitude (in degrees), depth (in km), shear velocity (in km/s) and standard deviation (in km/s). It is a 495-page document which can be found through the publishing journal's Internet link - https://agupubs-onlinelibrary-wiley-com.ezproxy.library.uvic.ca/action/downloadSupplement?doi=10.1002%2F2016JB013865&file=jgrb52146-sup-0002-2016JB013865-ts01.pdf (last accessed October 15, 2020).

Chapter 3. Imaging of Sedimentary Basins and Sub-basin Structures in Western Canada Using Ambient Seismic Noise

3.1 Article Information

3.1.1 Author and Coauthor Contributions

The article presented in this Chapter is being prepared for publication. The author of this dissertation, APK, carried out the data preprocessing and cross-correlations, surface wave tomography, 1-D trans-dimensional (transD) inversion and the pseudo 3-D tomography. APK wrote the manuscript under the supervision of coauthors HK and GS. SED wrote the transD inversion code. All coauthors contributed to the thorough review of the manuscript before submission.

3.1.2 Article Format

The text and figures included in a manuscript draft being prepared to be submitted to the Journal of Geophysical Research for publication. Figures, and Tables in the draft manuscript have been renumbered to conform with the dissertation style. References cited in the draft are included in the bibliography of this dissertation.

3.1.3 Data and Resources

This research is partly supported by the Induced Seismicity Research Project of Natural Resources Canada (NRCan), Natural Sciences and Engineering Research Council (NSERC) of Canada grants to H. K., Seismic data were obtained from Canadian National Seismic Network (http://www.earthquakescanada.nrcan.gc.ca/stndon/CNSN-RNSC/stnbook-cahierstn/index-en.php) and Incorporated Research Institution for Seismology (IRIS; http://ds.iris.edu/mda) data centers. Most of the figures were plotted by the Generic Mapping Tools (GMT).

Codes for the project are available upon request on GitLab online repository at https://gitlab.com/qnoise/WCSB-ANT-Project (last accessed December 31, 2020).

3.2 3-D Geometry of Sedimentary Basins and Moho Beneath Western Canada from Ambient Seismic Noise Tomography

3.2.1 Abstract

This Chapter presents a comprehensive 3-D shear wave velocity (*Vs*) model for western Canada with associated uncertainty estimates. In all, the characteristics of the western Canada morpho-geological belts, the geometry of the major sedimentary basins as well as the 3-D Moho structure in western Canada are inferred from our results. Within the Insular belt, the offshore basins studied here have a maximum depth in excess of 10 km and 5 km beneath the Queen Charlotte Basin (QCB) and Georgia Basin (GB) respectively. Similarly, a deeper Moho is observed beneath the QCB than GB. Within the Intermontane belt, the maximum basin depth is 7.5 and 7 km for Nechako and Bowser/Sustut Basins respectively. The shallowing of prominent high-*Vs* structure beneath the Intermontane belt along our referenced cross-sections obscures the clear observation of the Moho. The high-*Vs* structure is associated with relatively high uncertainty estimates, likely related to structural complexity at the edge of an underthrust craton. Moho depths are however well constrained by the 1-D *Vs* model in the northern and southern parts of the Intermontane belt as 34 and 33 km respectively. Within the Western Canada Sedimentary Basin, the deepest part of the Alberta Basin is located between the Montney and Duvernay Basins, with the maximum depth in excess of 6 km. At depth, the Moho is observed to have a slight southwest-ward dip, except for local variations beneath the Montney Basin. The thickest sediments estimated in this study are found beneath the QCB, Williston Basin and the Alberta Deep Basin, while the deepest Moho underlies the Williston Basin, parts of the QCB, Alberta Deep Basin, and northern British Columbia.

3.2.2 Introduction

The western Canada tectonic structure consists of the Interior Platform of ancient North America (NA) on the east and the Canadian Cordillera on the west (Figure 3.1). West of the exposed Canadian craton, the Interior Platform consists of the Western Canadian Sedimentary Basin (WCSB), a composite sedimentary wedge underlain by the westernmost extensions of Archean rocks of the Canadian craton (Hoffman, 1988). The Canadian Cordillera was formed by the successive accretion of the Intermontane and Insular superterranes onto ancient NA (Figure 3.1a). The superterranes are separated by tectonic welts corresponding to the Omineca and Coast Mountain belts within which severe deformation, regional metamorphism and granitic magmatism are engrained (Monger et al., 1982). Farther west, the ongoing subduction of the Juan de Fuca (JdF) oceanic plate beneath the North American continental plate in the south is characterized by active accretion and deformation of the Insular superterrane.

The multiple episodes of tectonic accretion in the Cordillera led to the formation of offshore and intermontane sedimentary basins within the Insular and Intermontane superterranes respectively. The Intermontane Basin (IMB) consist mainly of Nechako (NB), Bowser/Sustut (BSB), Whitehorse and other smaller basins (Figure 3.1b). The much younger offshore basins (OSB) consist mainly of Georgia (GB), Tofino, Winona, and Queen Charlotte (QCB) Basins. The WCSB is formed as an westward-thickening supracrustal wedge overlying a Precambrian basement of the Canadian craton (Price, 1994; Wright et al., 1994). It comprises the eastern Canadian Cordillera and two major sedimentary basins (i.e., the northwest-trending Alberta Basin and the intracratonic Williston Basin). Major unconventional hydrocarbon exploration in the Alberta Basin occurs within several formations and sub-basins including the Montney, Duvernay, Liard, Horn River and Alberta Deep Basins.

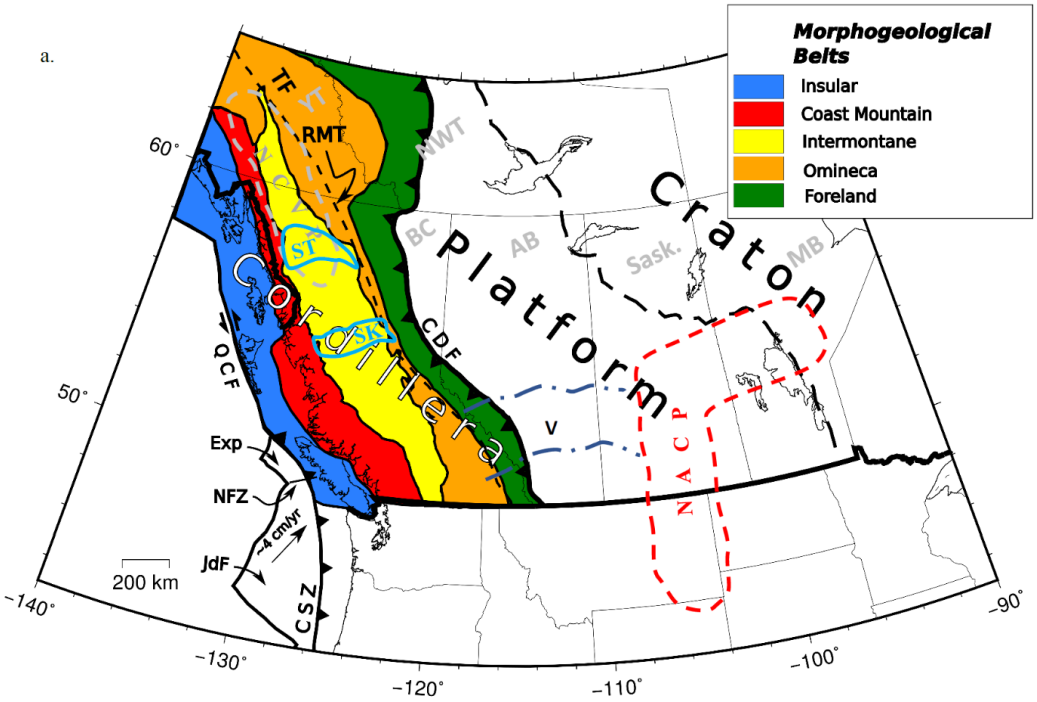

Figure 3. 1 Geological and tectonic map of western Canada showing – (a) tectonic and morpho-geological demarcations and structures; (b) prominent sedimentary basins consisting of Offshore, Intermontane, Western Canada Sedimentary Basins; (c) cross-section (purple and green lines) and 1-D *Vs* (red squares) locations. Lines: red lines – *Vs* cross-section locations with start and end positions annotated by black box with white fonts; short green lines – locations of selected *Vs* cross-sections collocated with existing Lithoprobe seismic reflection lines (marked as L10 and 11b); short purple line: location of existing COCORP seismic reflection line (marked as C) in close proximity to *Vs* cross-sections W-W' and WX-WX' (this study) within the Williston basin; thick long dashed lines – Craton-Platform demarcation; blue dash-dot lines – Vulcan Structure boundaries. Text: NACP*:* North America Central Plain Conductivity Anomalies; NCVP: Northern Cordillera Volcanic Province; CDF: Cordillera Deformation Front; RMT: Rocky Mountain Trench; CSZ: Cascadia Subduction Zone; JdF: Juan de Fuca; Exp: Explorer; QCF: Queen Charlotte – Fairweather; V: Vulcan Structure; ST: Stikine arch; SK: Skeena Arch; BC: British Columbia; AB: Alberta; Sask: Saskatchewan; MB: Manitoba; YT: Yukon Territory; NWT: Northwest Territory.

Figure 3.1 (continued).

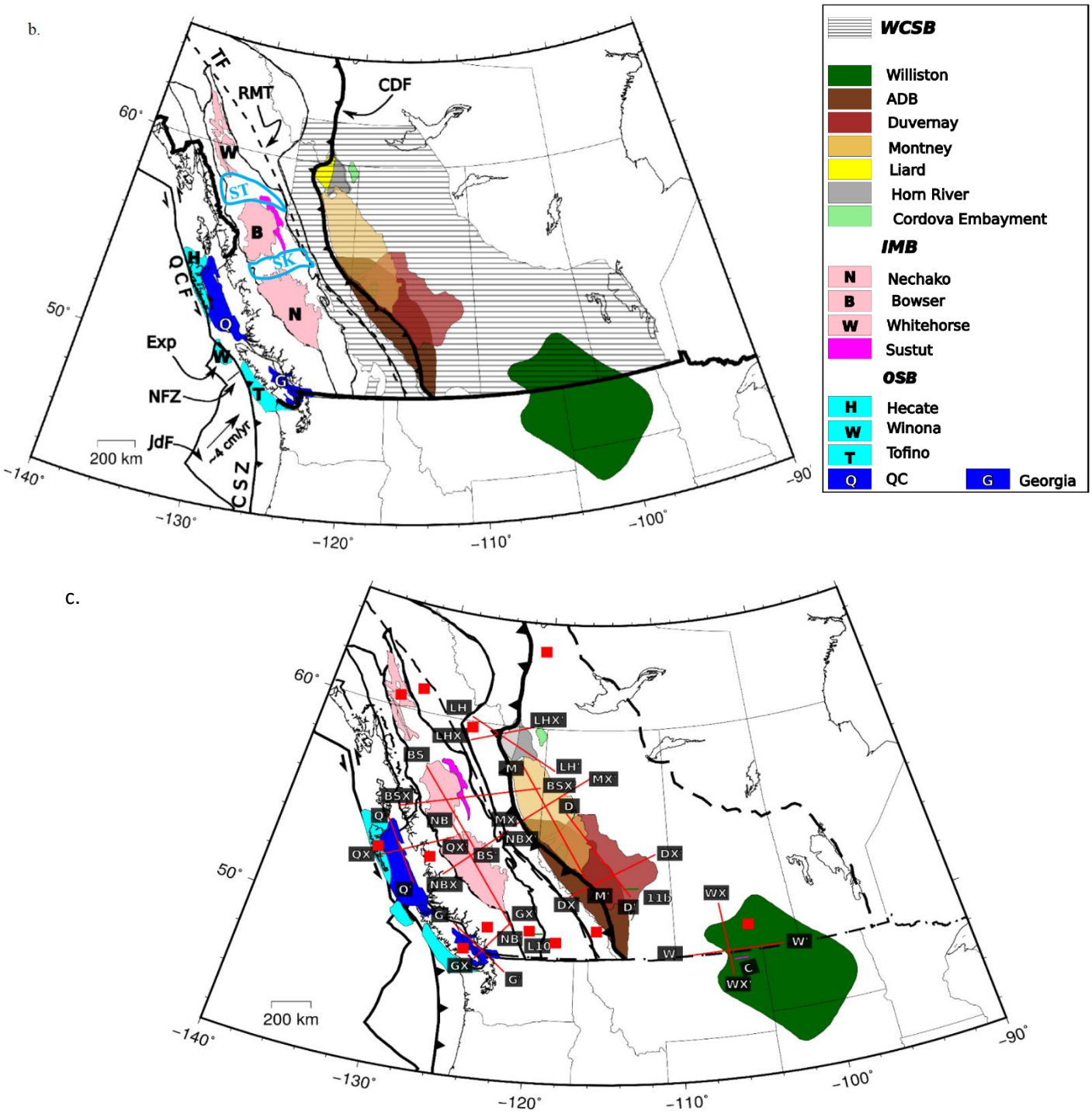

Western Canada has been an important focus of several geophysical and geological studies due to its significance in plate tectonics (Hyndman, 2010; Leonard et al., 2007; Rogers & Dragert, 2003), as well as its vast and varied energy resources (Yorath et al., 1991). The Lithoprobe project (1984-2003; Clowes et al., 1999), Canada's largest earth science study, examined the evolution of the northern North American continent and provided important insights into the tectonic structure of western Canada by combining multiple geophysical and geological techniques (Clowes et al., 1999), which include: active source seismic (e.g., Cook et al., 2010; Spence & McLean, 1998) and electromagnetic (e.g., Unsworth, 2015). Other independent studies provided further insights on the tectonic structure of western Canada using seismological methods such as: teleseismic receiver functions and earthquake surface waves (e.g., Audet et al., 2020; Cassidy, 1995; Gu et al., 2018; Mercier et al., 2009) and ambient noise tomography (e.g., Kao et al., 2013; McLellan et al., 2018). Long- and short-wavelength potential field data of the region show that basement depths and lithospheric composition, structure and thickness vary laterally in western Canada (Cook et al., 1995; Stacey, 1973; Stephenson et al., 1989). Within the Cordillera, seismic studies show the transform and transpressional tectonics of the OSB (e.g., Hannigan et al., 2001) and the severe deformation beneath the IMB. Adjacent to the Cordillera, sediment thickness in the WCSB generally tapers from west to east toward the craton (e.g., Hammer & Clowes, 2004). To the south, a deep seismic reflection survey carried out in the late 1980s by the Consortium for Continental Reflection Profiling (COCORP) in the Montana plains between the Rocky Mountains and Williston Basin suggests a thick crust beneath the Williston Basin (Latham et al., 1988) and, together with the existing Lithoprobe seismic lines, provide a good basis of comparison with our shear-wave velocity (*Vs*) cross-sections in the region (Figure 3.1c).

While these previous studies provide important constraints on the western Canada tectonic structure, they are mostly limited either by poor depth-sensitivities or inadequate spatial coverage and resolution. In many cases, the rugged terrain and extensive landmass of western Canada limits the location of studies, resulting in constraints interpolated over a large area and making it difficult to comprehensively study the 3-D geometry of the subsurface structures. As a result, exactly how the sediment thicknesses vary within the composite basins, the 3-D geometry of the crustal structure and Moho depths, as well as the along-strike characteristics of the accreted Cordilleran superterranes and suture zones in western Canada, remain poorly understood. To address these gaps, we collect continuous ambient noise seismic data recorded between 2003 and 2016 at 151 seismic stations spanning 14 Canadian, American and Global seismic networks (Figure 3.2, Table 3.1). From our knowledge, the combination of spatial and temporal coverage of the data within a regional context is the largest for this type of study in western Canada. The station distribution provides data density and temporal resolution adequate for detailed resolution of the western Canada velocity structures using ambient seismic noise methods.

For over a decade, ambient seismic noise tomography (ANT) has been leveraged as a passive source seismic imaging method to provide detailed velocity structures. The significant advantages of ANT include non-dependence on active seismic sources and, depending on the station coverage and distribution, may provide a combination of excellent spatial coverage and resolution. The method has been applied at the continental scale to constrain crustal and upper mantle structures in NA (Kao et al., 2013; Ritzwoller et al., 2005). It was also applied at the basin scale in Canada, around the Gulf of Saint Lawrence (Kuponiyi et al., 2017), Hudson Bay (Pawlak et al., 2011), NB (Idowu et al., 2011) and at the localized scale in parts of the Canadian Cordillera (Bao et al., 2016; Dalton et al., 2011; Gu & Shen, 2015). The primary objective of this study is to obtain a

comprehensive 3-D seismic velocity structure of the region using ambient noise seismic tomography. Subsequently, from the result, we estimate basin and crustal thicknesses for the entire region. This study leverages a massive combination of regional and cross-border ambient noise data to provide high resolution, wide-coverage spatiotemporal geophysical imaging of western Canada with associated uncertainty estimates. The routine involves processing the vertical component of continuous seismic waveforms recorded by the temporary and permanent seismic stations within and surrounding the region (Figure 3.2). Following processing procedures described in Kuponiyi et al. (2017) and references therein, we determined group velocity dispersion curves of the fundamental mode of the Rayleigh surface wave for periods between 1.5 and 60 s. These dispersion curves were then inverted to constrain group velocity anomalies. Comprehensive 3-D *Vs* and uncertainty distribution models for crust and upper-mantle for the region were obtained by applying a trans-dimensional (trans-D) inversion scheme (Bodin et al., 2012; Dettmer et al., 2010; Dosso et al., 2014) to grid dispersion data obtained at every 0.5^{o} x 0.5^{o} node of the surface wave tomography result. Finally, we address important issues related to the geometry of major sedimentary basins and the 3-D Moho structure beneath western Canada.

3.2.3 Geological Setting

The westward growth of NA was initialized by the opening of the Atlantic Ocean on the east around 180 – 200 Ma (Klitgord and Schouten, 1986; Sahabi et al., 2004). This resulted in the westward drift of the proto-continent and the multiple episodes of collision with, and accretion of, inbound exotic terranes onto the proto-NA continental margin to form the Canadian Cordillera (Monger et al., 1982; Monger & Price, 1979). The development of the Canadian Cordillera led to the formation of suture zones and sedimentary sequences. The Cordillera is bounded on the east along the Cordillera Deformation Front (CDF), by a stable craton which comprises several

Archean terranes amalgamated during a series of Paleoproterozoic orogenies that ended over 1 Ga (Bastow et al., 2011; Hoffman, 1988; Thompson et al., 2010). The Intermontane superterrane is a collage of already accreted smaller terranes, mainly Stikinia, Cache Creek, Quesnelia, Slide Mountain and Kootenay terranes. It collided with the ancient margin of ancestral NA, in Early-Mid Jurassic (Gabrielse et al., 1991). This led to an intensely folded miogeoclinal margin, which was detached from its crystalline basement, and upthrust onto ancestral NA to form the Foreland fold-and-thrust belt (Gabrielse & Yorath, 1991; Monger et al., 1982; Monger & Price, 1979). Meanwhile, the Omineca belt, made up of highly pressurized and fractured rocks, represents the suture zone between the Intermontane belt and proto-NA (Monger & Price, 1979). The Rocky Mountain Trench (RMT)/Tintina Fault (TF) represents the boundary between the Omineca and Foreland belts (Figure 3.1a).

In the Late Jurassic, the Insular superterrane collided with the western coastline of the Intermontane belt (now composite NA). The Coast Mountain belt, which represents the suture zone, comprises Late Cretaceous-Tertiary magmatic rocks (Cook et al., 2004). The Insular superterrane currently being accreted to modern NA comprises mainly the Wrangellia, Alexander, Pacific Rim and Crescent terranes. As a result, the western edge of the Canadian Cordillera is characterized by active tectonic systems with complex deformational processes from north to south. In the northwest, the Yakutat Block, an allochthonous terrane formed from both continental and oceanic igneous and sedimentary rocks, collides with and is being accreted to the NA plate (Hyndman et al., 2005; Plafker & Berg, 1994). South of the Yakutat block, the Pacific and NA plates interact in a relative dextral motion along the Queen Charlotte-Fairweather strike-slip fault at a rate of ~55 mm/year (DeMets & Dixon, 1999). The prevailing tectonics led to the formation of the OSB (Hannigan et al., 2001). South of the strike-slip fault system, there is a complex

transition to the Cascadia subduction zone where, the JdF and Explorer oceanic plates subduct beneath the NA at rates of ~40 mm/year and ~20 mm/year, respectively (DeMets & Dixon, 1999; Riddihough, 1984). Within the OSB (Figure 3.1b), this study focuses on QCB, which is adjacent to the Queen Charlotte Fault and GB, which straddles the Insular and Coast belts. Several models have been proposed for the formation of the QCB, with the majority supporting a complex multi-stage process involving extensions accommodated by strike-slip faults and varying degrees of oblique compression and regional/thermal subsidence (e.g. Higgs, 1991; Hole et al., 1993; Hyndman & Hamilton, 1990; Rohr & Dietrich, 1992). Another model derived from the combination of several datasets, including magnetic, gravity, and seismic, suggested that the basin was formed by the reactivation of pre-Cenozoic faults and basin subsidence in the Tertiary resulting from regional translation over a mantle hot-spot in the Neogene and an outflow of lower crustal materials onto the adjacent Coastal belt (Lyatsky, 1993, 2006). On the other hand, the GB is a forearc basin which initially developed above Wrangellia in a non-oceanic convergent-margin setting. It is located between the Late Cretaceous arc in eastern Coast Mountains and a trench or transform fault thought to be located offshore Vancouver Island (VI) (Muller, 1977).

The IMB (Figure 3.1b), largely comprising of the Whitehorse Trough (WT), NB (Idowu et al., 2011; Stephenson et al., 2011) and BSB (Evenchick, 1991), is believed to originate from the Cordillera accretion of the Intermontane superterrane (Calvert et al., 2011; Gabrielse & Yorath, 1991; Idowu et al., 2011; Stephenson et al., 2011). Within the IMB, the BSB is separated from the WT in the north by the Stikine arch and from the NB in the south by the Skeena arch. The arches are long-lived volcanic arcs that formed within the Intermontane belt. The focus of this study is on the BSB and NB. In the late stages of collision between the Quesnelia and Stikinia, thermal subsidence of the Stikinia basement in the presence of arc magmatism, coupled with crustal

loading from an obducted Cache Creek terrane, resulted in the formation of the Bowser Basin. On the other hand, the much smaller Sustut basin is the foreland basin to the Skeena fold belt (Evenchick, 1991) linked to the tectonic contraction driven by the accretion of Insular supterterrane in the west (Ricketts, 2008). The ongoing accretion of the Insular superterrane (Monger et al., 1982) is associated with the active development of the frontier (relative to WCSB) OSB (Hannigan et al., 2001), which includes the Queen Charlotte (Higgs, 1991; Hole et al., 1993; Lyatsky & Haggart, 1993), Winona (Davis & Riddihough, 1982), Tofino (Yorath, 1980) and Georgia (Katnick & Mustard, 2003; Mustard, 1994) Basins (Figure 3.1).

The WCSB (Figure 3.1b) is the easternmost basin system in western Canada. It is made up of the eastern Canadian Cordillera and two major sedimentary basins, namely: the Mesozoic-Early Cenozoic Alberta Basin and the Phanerozoic intracratonic Williston Basin. The eastern Canadian Cordillera comprises deformed sedimentary rocks derived from five terranes: the Quesnel, Slide Mountain, Selkirk, Cassiar, and Rocky Mountain terranes (Struik, 1992). The adjacent Alberta Basin was formed over a cratonic basement predominantly in a foreland setting, as a wedge between the proto-NA continent and the relatively juvenile Canadian cordillera (Porter et al., 1982). Over time, localized geological settings allowed the formation of several sub-basins including: the Liard, Horn River, Montney, Duvernay and Alberta Deep Basins. In contrast, the intracratonic Williston Basin is the easternmost basin within the WCSB, with its center in North Dakota, USA. It is formed over a structural depression which has been linked to Phanerozoic subsidence initiated by subcrustal metamorphic phase change of a mafic upper mantle material to eclogite (Baird et al., 1995; Fowler & Nisbet, 1985).

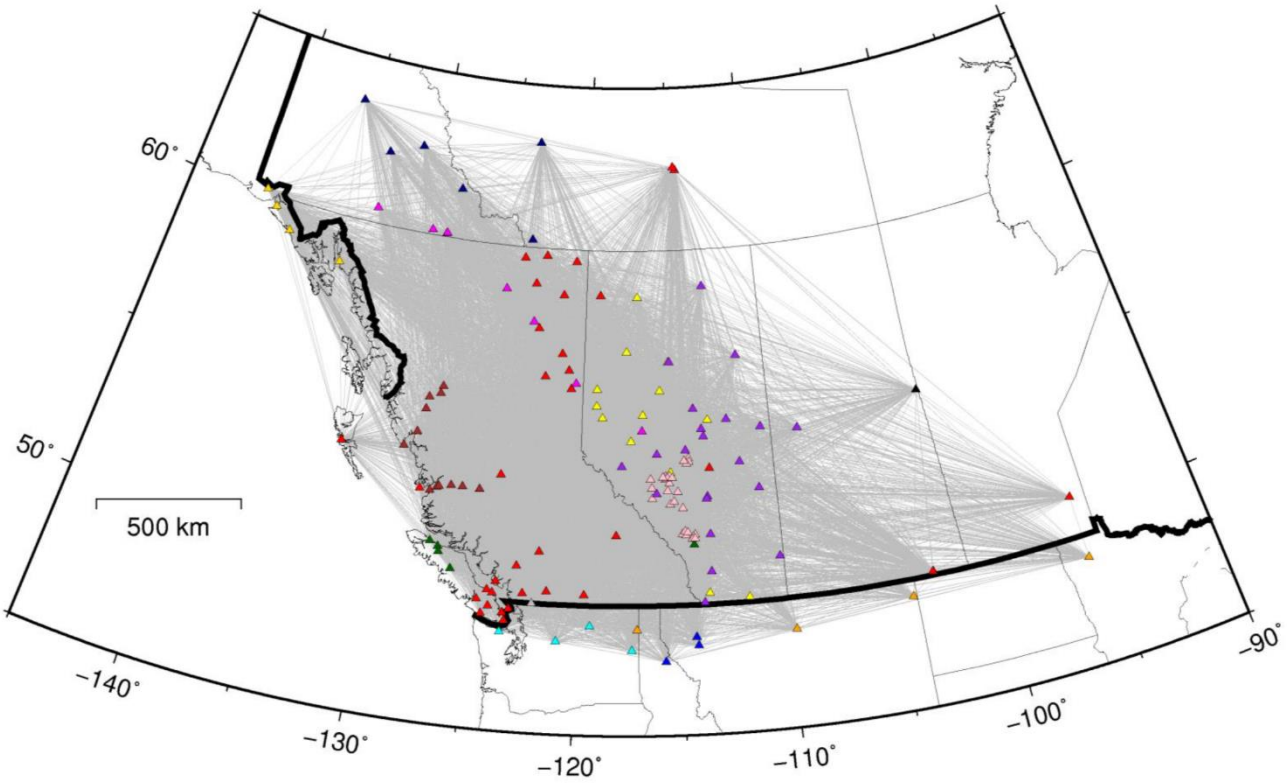

Figure 3. 2 Map showing station distribution used in this study and simplified propagation paths. Gray lines are presumptive station-station propagation paths for surface waves. Colored triangles mark locations of seismic stations used in this study. The colors represent the seismic network to which each station belongs. The stations and their associated colors are presented on Table 3.1

3.2.4 Data and Methods

We analyze continuous ambient seismic noise waveform data recorded by 151 seismic stations from 14 networks between 2003 and 2016 (Figure 3.2). Only stations with minimum data availability of 180 days were used. The station density and distribution allow for adequate coverage of western Canada. The seismic noise data were retrieved from both the Canadian National Seismic Network (CNSN) and the Incorporated Research Institution for Seismology (IRIS) database in the Standard for Exchange of Seismic Data (SEED) format.

Table 3.1 Description of network and association with color-codes

	Network	Symbol	Color	Period of Operation
1.	Batholiths Broadband	XY	Brown	2005 – 2006
2.	Canada Northwest Experiment (CANOE)	XN	Magenta	2003 – 2005
3.	Canadian Rockies and Alberta Network	Y5	Purple	2006 – 2018
4.	Alaska Regional Network	AK	Gold	1990 –
5.	Montana Regional Seismic Network	MB	Blue	1996 –
6.	United States National Seismic Network	US	Orange	1990 –
7.	Pacific Northwest Regional Seismic Network	UW	Cyan	1992 –
8.	Canadian National Seismograph Network	CN	Red	1980 –
9.	USArray Transportable Array	TA	Gray	2003 – 2016
10	Regional Alberta Observatory for Earthquake Studies Network (RAVEN)	RV	Yellow	2013 –
11	Yukon Northwest Seismic Network (YNSN)	NY	Navy Blue	2013 –
12	Trans-Alta Monitoring Network	TD	Pink	2013 –
13	Global Seismograph Network (GSN)	II	Black	1986 –
14	Portable Observatories for Lithospheric Analysis and Research Investigating Seismicity	PO	Dark	2000 –

3.2.4.1 Cross-Correlations and Group Velocity Dispersion

Following the processing steps highlighted in Kuponiyi et al. (2017), vertical components of waveforms from simultaneously recording stations were merged and cut into one-day segments. The mean, linear trend and instrument response of the data from each station were removed and the data were converted to ground velocity. The data were then down-sampled to 2 samples per second and one-bit time-domain normalization was applied to remove high-amplitude signals, such as earthquakes. Each one-day segment of the data was filtered in the band 1.5 – 60 s and cross-correlated with simultaneously recorded data from every available pair of stations. Over three million daily noise correlation functions (NCFs) were calculated at this stage. Only station pairs with data overlapping for a minimum of 180 days were used in the cross-correlation. In theory, the extraction of the Green's function (GF) requires a symmetric distribution of sources. For asymmetric distribution of seismic noise sources, however, stacking of several NCFs from a station pair results in an approximate GF (Ermert et al., 2016). The resulting daily NCFs from the multi-stage processing were stacked over the duration of data availability and GFs with remarkably improved signal-to-noise ratios (SNRs) emerged. Subsequently, symmetric components were obtained by averaging the waveforms with their time-reversed components. A total of 5,246 stacked and symmetrized NCFs were obtained at this stage. Group velocities of the fundamental mode of the Rayleigh wave were measured from the stacked symmetric traces for periods between 1.5 and 60 s following the frequency-time analysis method (FTAN). I wrote a software in the Python language based on the ObsPy and other scientific modules to automate the process from data mining to dispersion measurements. Among other steps, the software searches an online station database and downloads seismic data for station pairs based on a set of options including channel, mutual data availability, and geographical location. Dispersion measurements for this

study were obtained for station pairs with interstation distances corresponding to at least two wavelengths. A phase-match filter and an SNR criterion of 10 were applied to the filtered NCF, such that the number and quality of group velocity measurements selected are significantly improved (Bensen et al., 2007; Brandmayr et al., 2016).

3.2.4.2 Surface Wave Tomography, Trans-dimensional Bayesian Inversion and 3D Tomography

The steps described here follows the implementation, and uses the same codes, presented in Chapter 2 of this dissetation. Following Rawlinson and Sambridge (2003), surface wave tomography, which represents spatially distributed group velocity anomalies for successive periods, was carried out through an iterative non-linear fast marching scheme. This scheme combines a forward calculation using the fast marching method of Sethian and Popovic (1999) with a regularized iterative subspace inversion step (Kennett et al., 1988; Sambridge, 1990). The applied regularization parameters were based on the trade-off between the data-fit and model variance as well as smoothness for successive periods. Synthetic checkerboard analysis is used to evaluate the spatial resolution of our surface wave results across the period range considered. Checkerboad test carried out for varying structure sizes revealed that resolution varies from the center of the study area to the edges of the region, depending on the ray coverage.

A three-dimensional *Vs* model for the region was obtained by dividing the study area into a grid of 0.5^{o} x 0.5^{o} interval. Based on the surface wave tomography result, a new dispersion curve for each grid point was constructed from the group velocities of successive periods. A total of 5,940 grid dispersion curves were obtained. Each newly constructed dispersion curve was then inverted to obtain a 1-D velocity model using a fully non-linear trans-dimensional (trans-D)

Bayesian inversion scheme (Dosso et al., 2014, and references therein). A summary of the implementation is given by Kuponiyi et al. (2017).

The trans-D inversion was initialized using a model of 3 layers above a mantle half space with the thickness and *Vs* of each layer randomly selected. The input dispersion data for each grid point consists of 38 group velocity data points over the frequency range of 0.02–0.5 Hz with an estimated standard deviation of 0.05 km/s. The number of interfaces is allowed to vary between 1 and 10 and an *a priori* range of *Vs* is set at 2–5 km/s. An ensemble of 500,000 models was drawn from a posterior probability distribution (PPD). Stationary sampling in likelihood and convergence of model parameters was achieved after a burn-in of the first 0.5% of the total samples drawn. The data residuals (difference between measured and modeled data) were found to be consistent with the assumption of Gaussian errors of the specified standard deviation. Marginal probability for each 0.5^{o} x 0.5^{o} grid point in western Canada was obtained by considering the entire set of model samples drawn from the PPD. The median of the distribution was determined to be the representative 1-D model for each grid point. Both the 1-D *Vs* model and the corresponding uncertainty estimates were then extracted and interpolated from one grid point to another, over the whole region to give pseudo-3-D *Vs* and uncertainty distributions.

3.2.5 Results and Interpretation

Our surface wave tomography results show the spatial distribution of group velocity anomalies from the upper crust to the uppermost mantle in western Canada (Figure 3.3). Shear wave velocity is an important physical property that is associated with the thermal and compositional states of earth structures and has implications for the history of their tectonic deformation and evolution. Our 1-D *Vs* models obtained from the transD inversion of the surface

wave tomography results show the variation of *Vs* at depth (Figure 3.4). The 3-D *Vs* model obtained by combining the relevant 1-D models show the spatial variation of *Vs* structure at depth over the region of study and the corresponding uncertainty (Figure 3.5). The internal structure beneath the major sedimentary basins in western Canada was then imaged by extracting 2-D *Vs* cross-sections and uncertainty estimates (Figures 3.6 – 3.8).

3.2.5.1 Group Velocity Maps

We present group velocity maps together with corresponding ray coverage and checkerboard results for 5 s, 15 s, 30 s, 40 s, which are periods sensitive to structures at depths from the upper crust to the uppermost mantle (Figure 3.3). For each period, low and high velocity anomalies are defined as areas with velocity changes less than –5% and greater than +5% relative to the mean, respectively. The checkerboard test (Figure 3.3 e-h) and the corresponding ray density (Figure 3.3 i-l) show that velocity anomalies with minimum sizes of 2^{o} are well resolved within the study area. Structures with sizes of 50 – 80 km could be resolved in areas with good ray coverage, especially near the center of the study area.

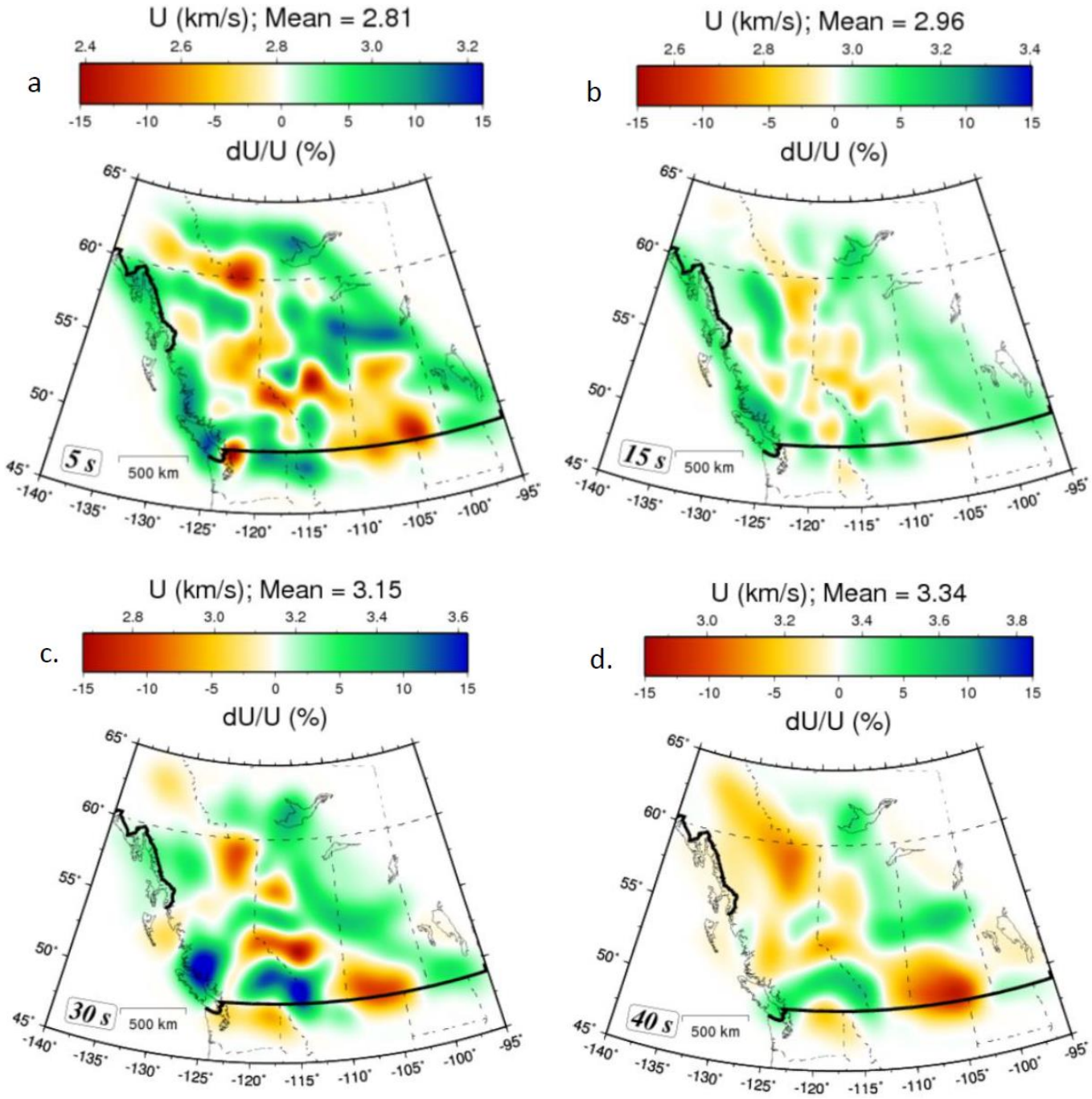

Figure 3. 3 Surface wave tomography results for periods (a) 5 s (b) 15 s (c) 30 s (d) 40 s, which are sensitive to upper (a), middle (b), lower crust (c), and uppermost mantle (d) respectively. Results of checkerboard resolution test from surface wave tomography for periods corresponding to a – d are presented in e – h. Ray densities associated with the checkerboard test are shown in i – l.

Figure 3.3 (continued).

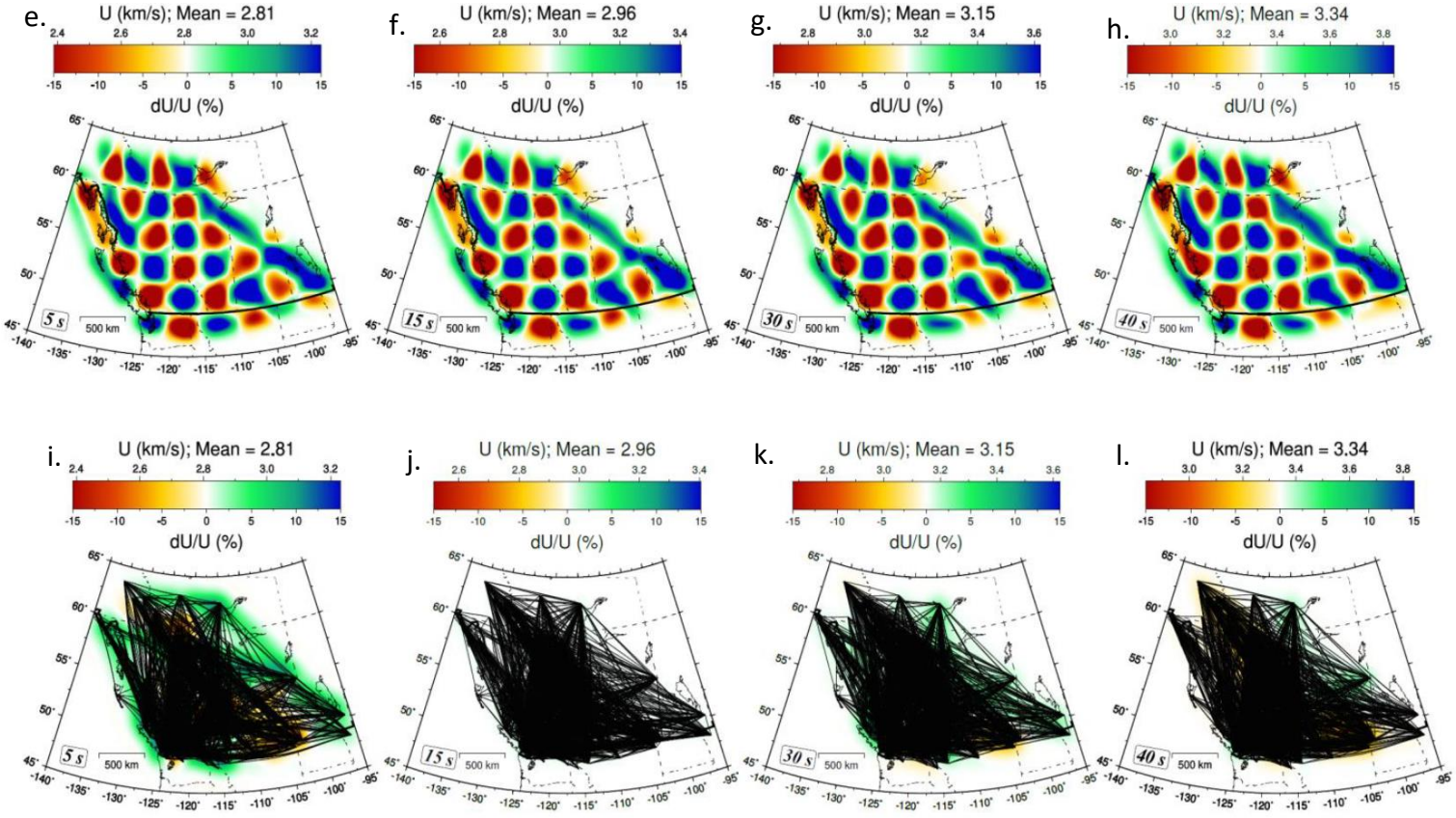

The first order feature in our results is a general tri-band velocity distribution pattern across all periods. The region is characterized by mean group velocity ranging from 2.8 – 2.96 km/s in the shallow to middle crust (Figure 3.3 a-b), 2.99 – 3.15 km/s in the lower crust (Figure 3.3c), and >3.3 km/s in the uppermost mantle (Figure 3.3d). Predominantly high velocities are observed from the western limit of the craton through the westernmost edge of the cordillera across all period ranges. The observed high velocities are divided by a variable NW-SE low-velocity trend distributed over the WCSB in the middle. The low velocities are centered at locations of known sedimentary basins across all periods.

3.2.5.2 1-D Vs Models

We obtained 5,940 1-D *Vs* profiles with their uncertainty distributions over latitudes 46.24 – 65.63^{o} N and longitudes 95.35 – 145.25^{o} W. Due to the very large area of coverage of this study, we present the general characteristics of a subset of the 2,875 1-D *Vs* results selected for the final 3D model based on the area of study interest and resolution quality. Figure 3.4 shows 12 1-D *Vs* models taken from each morpho-geological demarcation in western Canada (the locations are shown on Figure 3.1). The top row comprises *Vs* models for locations in the northern part of the region, while the bottom row is for the south. The maximum of the marginals (white line in the plots) tracks the layering and transitions in the *Vs* model better than the mean or smoother model (magenta line in the plots) and is thus referenced here. The migrated Lithoprobe seismic reflection lines offer good coverage especially within the southern cordillera and provide independent constraints of the morpho-geological divisions of the Canadian Cordillera, (https://ftp.maps.canada.ca/pub/nrcan_rncan/vector/lithoprobe/web_gis/sc/index.html#6/50.177/-114.049, last accessed on November 14, 2020). Two major features in our 1-D *Vs* results are the *Vs* jump at shallow depths (between 5 and 15 km) and a significant *Vs* increase, which may occur

either sharply or gradationally, at deeper depths (>30 km). The former may correspond to the depth to the sedimentary basement, while the latter may correspond to the change from the base of the crust to the top of the mantle (i.e., the Moho discontinuity). Aside from these, other *Vs* changes may be due to intra-crustal changes or local geological features. To validate our results, the models from the southern portion of the demarcations (Figure 3.1) were chosen near or along seismic reflection lines from the Lithoprobe and/or COCORP programs, where available. The location of the lines corresponds to areas of good spatial resolution as constrained by our surface wave tomography results. Following Welford and Clowes (2005), the reflection lines were converted from time to approximate depths using an average velocity of 6 km/s.

In the northern part of the Insular superterrane (Figure 3.4a), a prominent low *Vs* layer is observed to a depth of ~12 km, beneath which a relatively stable *Vs* is observed down to a depth of ~42 km with another large jump immediately beneath to higher *Vs*. In the south, the model is drawn near point 216 on the proximal Lithoprobe seismic line VI-2 (Yorath et al., 1985). Several *Vs* increases are observed at depths greater than 27 km. The increase at depths of 27 and 33 km correspond to a group of strong reflections on the Lithoprobe line, previously interpreted as imbricated basalts associated with the subduction of the JdF plate (Clowes et al., 1995). The last coherent reflection on line VI-2 occurs at depths between 35 and 40 km and was interpreted as the subducting oceanic Moho by previous studies (e.g. Clowes et al., 1995). Beneath the strong reflection, and similar to the northern model, the most prominent *Vs* jump occurs at ~43 – 45 km.

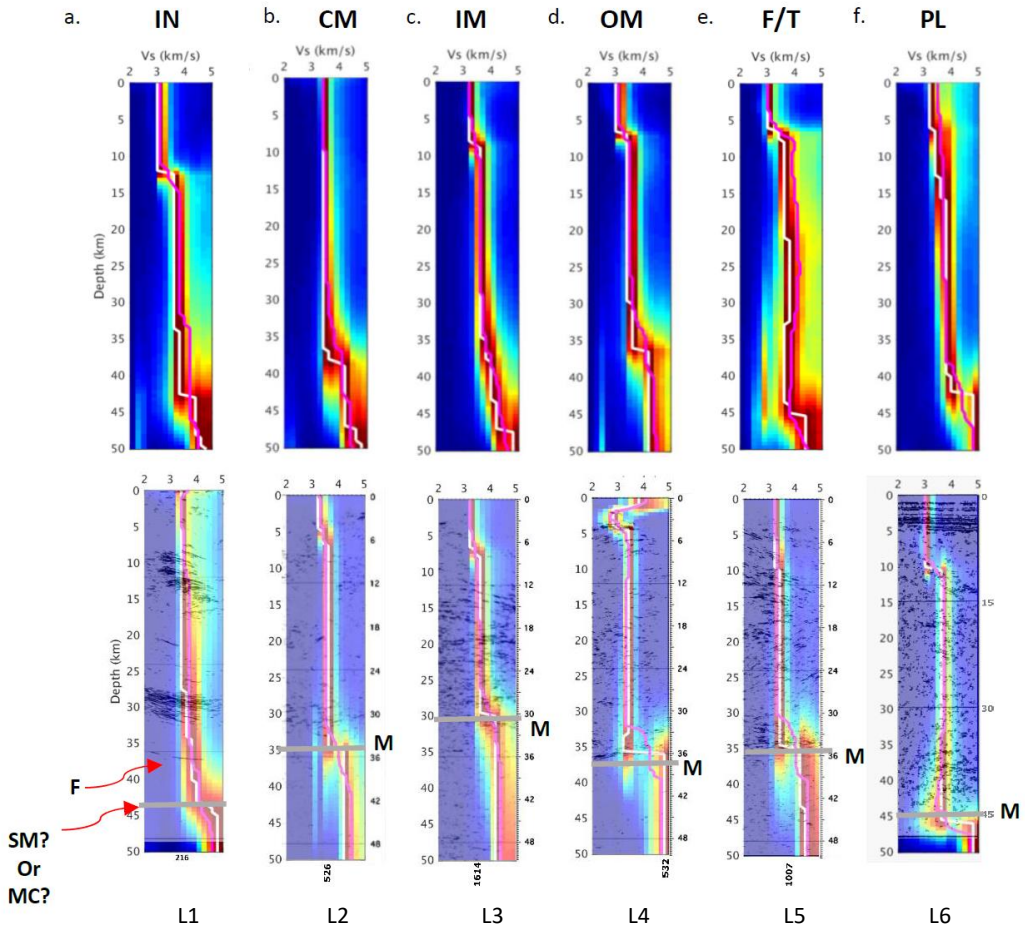

Figure 3. 4 The probability distribution of *Vs* plotted with depth derived from the trans-D inversion of grid dispersion curves (color scale from blue-red shows low-high probability). The results are for the following morpho-geological divisions in western Canada (a) Insular (IN) (b) Coast Mountain (CM) (c) Intermontane (IM) (d) Omineca (OM) terranes as well as (e) the Foreland Fold and Thrust belt (F/T) and (f) Platform (PL). Upper and lower panels show the model for the north and south of each physiographic division respectively. The locations are shown on the station map (Figure 3.1c). White and purple lines running through the middle of the distribution represent maximum and mean of the distribution respectively. Lithoprobe reflection line segments: L1 – VI-2, L2 – line 14, L3 – line 11, L4 – line 7, L5 – line 9, L6 – COCORP line 8 .Gray horizontal lines mark the base of strong lower crustal reflections, which are also close to the jump in *Vs* (Moho – "M", subducting plate Moho – "SM" or continental Moho – "MC") in our 1-D model. "F" marks the last band of reflection on the southern Insular Lithoprobe line in (a), adapted from *Clowes et al., 1995.*

In the northern Coast Mountain belt (Figure 3.4b), no significant layering is observed down to the depth of 36 km, then a large jump to higher *Vs* at the depth range of 36 – 39 km is observed and interpreted as the Moho. The model in the southern Coast Mountain belt is drawn near point *526* on Lithoprobe seismic reflection line 14 (Cook, 1995). A ~6 km thick low *Vs* is observed at shallow depths, which contrasts to the observation in the north. A large *Vs* increase, which is interpreted as the Moho, occurs at the depth range of 31 – 32 km close to the base of the strong reflections on the reflection line.

Within the Intermontane superterrane (Figure 3.4c), a shallow (6 – 8 km) low-*Vs* layer is observed on the north and south profiles. In contrast to the somewhat sharper transition to higher *Vs* observed on the other profiles, a more gradational transition is observed in the north, with velocities gradually increasing from a depth of ~34 km to ~48 km. The southern Intermontane *Vs* model is drawn near point *1614* on the Lithoprobe seismic reflection line 11 (Cook, 1995). In contrast to the northern model, a sharper transition to a high *Vs* is observed at a depth of ~33 km and is interpreted as the Moho beneath the southern Intermontane belt. This feature corresponds well with the base of the strong reflections observed on the seismic reflection line.

For the northern Omineca (Figure 3.4d), a low-*Vs* layer is constrained to the shallowest 7 km, beneath which *Vs* is relatively uniform down to the depth of ~36 km. The large *Vs* increase observed at 36 – 37 km is interpreted as the Moho beneath the northern Omineca. In the southern Omineca belt, our *Vs* model is drawn near point *526* along the Lithoprobe seismic reflection line 7 (Cook et al., 1988). A prominently high-*Vs* layer with a thickness of 2 – 3 km is observed to overlie a low-*Vs* layer with a base at the depth of 5 km. The base is marked by strong reflections on the Lithoprobe line. The high-*Vs* layer may be associated with the volcanic rocks of the Kootenay terrane overlying sedimentary rocks of the Quesnel terrane. A large *Vs* increase in the

model at the depth of ~36 km corresponds to strong reflections on the Lithoprobe line and is interpreted as the Moho.

Prominent transitions within the Foreland fold-and-thrust belt are well constrained, albeit with relatively larger uncertainties, relative to others (Figure 3.4e). In the northern part of the Foreland belt, a low-*Vs* layer is observed down to ~7 km, while a large increase occurs at the depth range of 43 – 45 km. This jump is interpreted as the Moho. The *Vs* model in the southern Foreland belt is located near point *1007* on the Lithoprobe seismic reflection line 9 (Cook et al., 1992). A relatively low-*Vs* layer is observed down to the depth of ~10 km with corresponding strong reflections on the Lithoprobe line. In the northernmost part of the Platform (Figure 3.4f), small *Vs* increases are observed in the upper 15 km. The major transition to large *Vs* occurs at the depths between 40 and 43 km. Finally, a 1-D *Vs* model is drawn from within the Williston basin in the south. The COCORP seismic reflection line 8 (Latham et al., 1988), which was recorded a short distance to the south, is overlain on and compared with our model. A clear shallow low *Vs* layer, about 10 km thick, is observed in the upper 10 km. The sharp transition to high *Vs* is observed over a narrow depth range at 45 – 46 km on this model and matches strong reflections near 15 s two-way travel time on the COCORP seismic reflection line.

The successful validation of our 1-D *Vs* results with the Lithoprobe lines provides a solid basis to combine them in producing 3-D depth slices and 2-D *Vs* cross-sections to show the general variation of structure for previously unimaged locations in western Canada where our surface wave tomography resolution is reliable.

3.2.5.3 3-D Shear Wave Velocity

A 3-D *Vs* model with uncertainty estimates was obtained for much of western Canada by combining all 2,875 1-D *Vs* results on a 0.5° x 0.5° grid (Figure 3.5). Similar to the surface wave tomography results, the 3-D *Vs* results are delineated into low- and high-velocity zones, each characterized by *Vs* changes (d*Vs*) less than –5% (LVZ) and greater than +5% (HVZ) respectively, relative to the mean *Vs* for each depth slice. The reliability of the model depends primarily on the availability and quality of input data into the Bayesian inversion. Here, we present generalized *Vs* results from the upper crust to the uppermost mantle (Figure 3.5 a – d). As expected, uncertainty estimates (Figure 3.5 e – h) increase with depth; however, first-order features are retained. In this section, we first describe the general *Vs* characteristics of the crust and uppermost mantle across the morpho-geological divisions of the Canadian Cordillera, then present the features of the major basins in western Canada.

General Vs Characteristics of the Western Canada Morpho-geological Divisions

In the upper crust (depth < 10 km, e.g. Figure 3.5a), a mean *Vs* of 3.3 km/s is observed with low velocity anomalies of $Vs \leq 3$ km/s (or $dVs \leq -10\%$) corresponding to sedimentary basins. In the middle crust (depth 11 – 20 km, e.g. Figure 3.5b), a mean *Vs* of ~3.88 km/s is observed, which represents a 5% increase relative to observation in the upper crust. A velocity range of $3 < Vs \leq 4$ km/s is observed in the middle crust. Meanwhile in the lower crust (depth 21 – 30 km, e.g. Figure 5c), the mean *Vs* further increases by ~2.4% to ~3.97 km/s and the range is 3.3 – 4 km/s. Finally, the mean *Vs* in the uppermost mantle (31 – 50 km, e.g. Figure 3.5d) jumps to 4.21 km/s, representing an increase of ~10.6% relative to the observation in the lower crust.

Near the westernmost edge of the Canadian Cordillera, the Insular belt is dominated by relatively low *Vs* (e.g. 5 km, Figure 3.5a) in the upper crust, coinciding well with the location of the OSB in western Canada (marked as O on Figure 3.5a). A relatively low $Vs \leq 3.2$ km/s is observed in the QCB. This observation is consistent with a $Vp \leq 5.5$ km/s at depths ≤ 8 km reported by previous active-source seismic studies of the basin (e.g. Clowes et al., 2005; Spence & Asudeh, 1993; Yuan et al., 1992) and interpreted as sedimentary rocks interbedded with Tertiary volcanics (Rohr & Dietrich, 1992; Spence & Asudeh, 1993). In the southeastern portion of the Insular belt, the observed LVZ, which straddles the Insular and Coast Mountains, is over 10% lower than the mean *Vs* of the upper crust and corresponds to the Upper Cretaceous Nanaimo Group and more recent sediments (Zelt et al., 2001) of the GB.

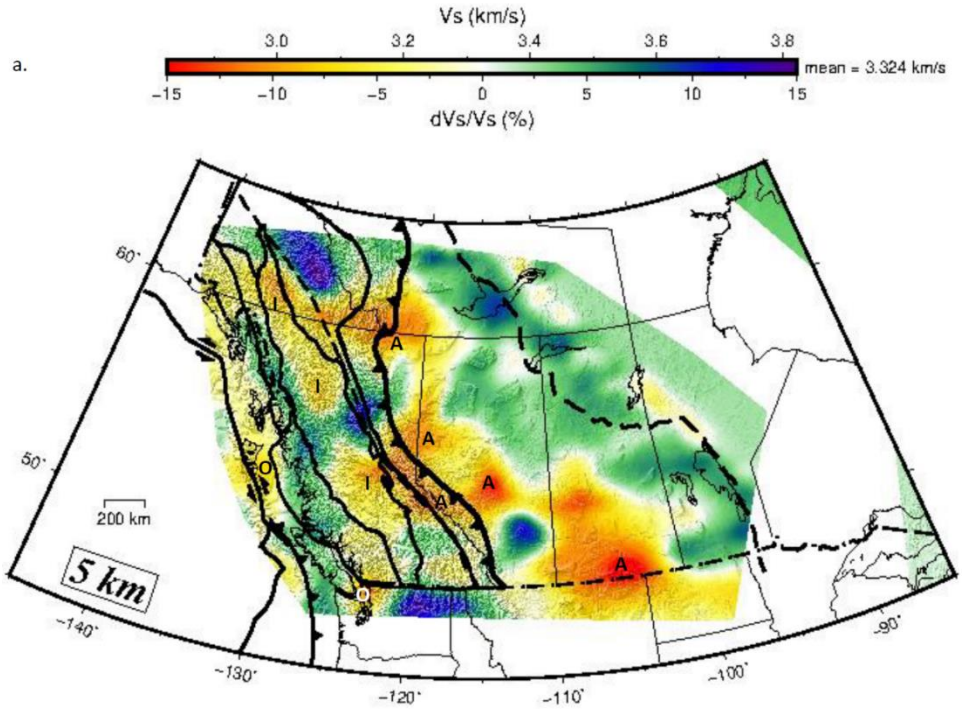

Figure 3. 5 Three-dimension *Vs* distribution for western Canada at depths of (a) 5 km (b) 15 km (c) 30 km (d) 45 km, representing uppermost, middle, lower crusts and uppermost mantle respectively; e – f correspond to uncertainty distributions associated with a – d. Thick black lines on the *Vs* plots represent the terrane demarcations; the spikey black line represents the location of the Cordillera Deformation Front and the red dashed polygon represents the location of the North American Central Plain Conductivity Anormaly. Basins (*labelled on (a)*): O – offshore, I – Intermontane, A – Alberta. Structure: V – Vulcan Structure.

Figure 3.5 (continued).

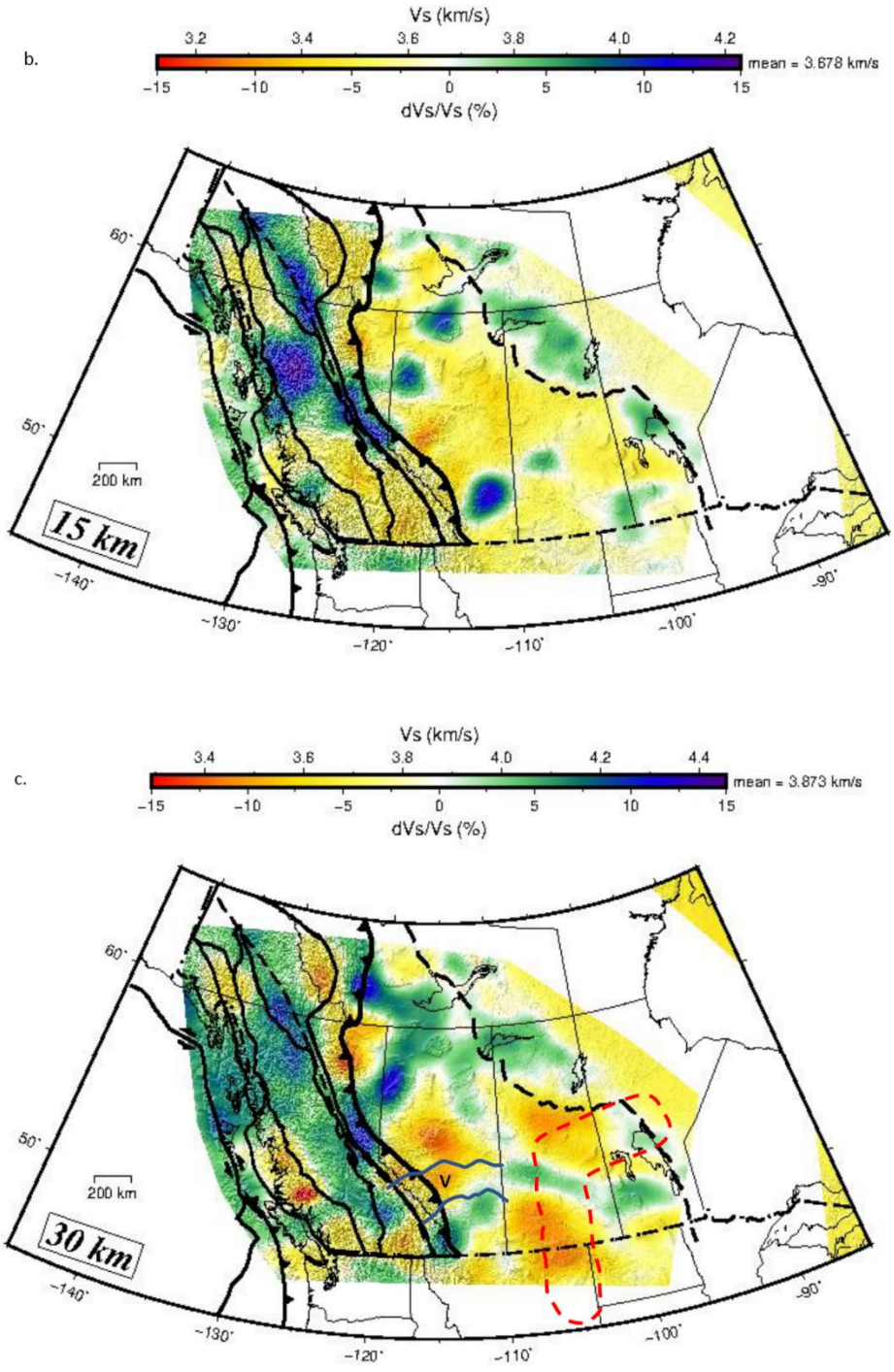

Figure 3.5 (continued).

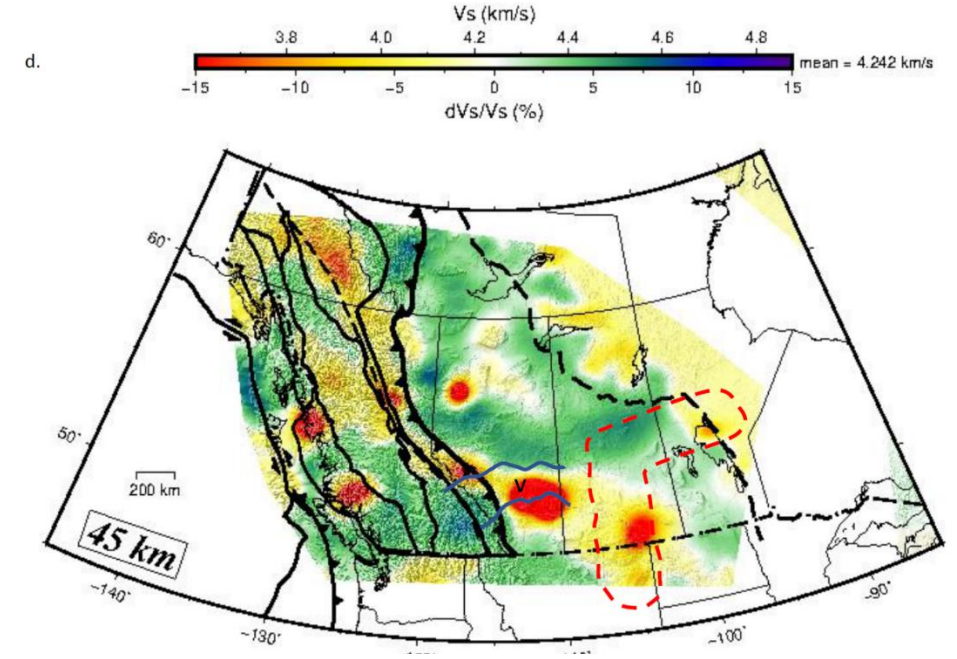

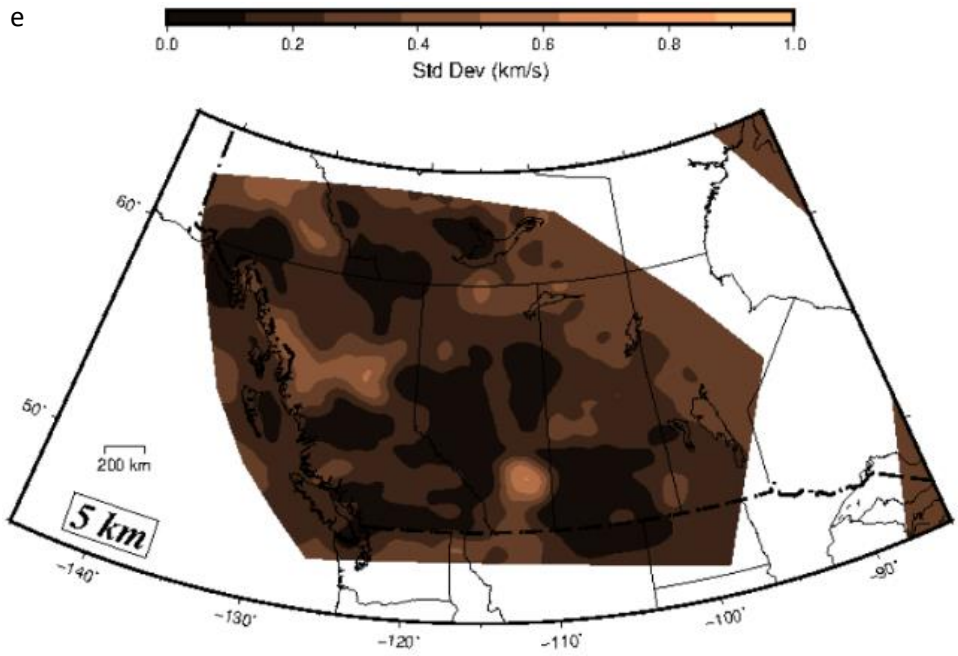

Figure 3.5 (continued).

f.

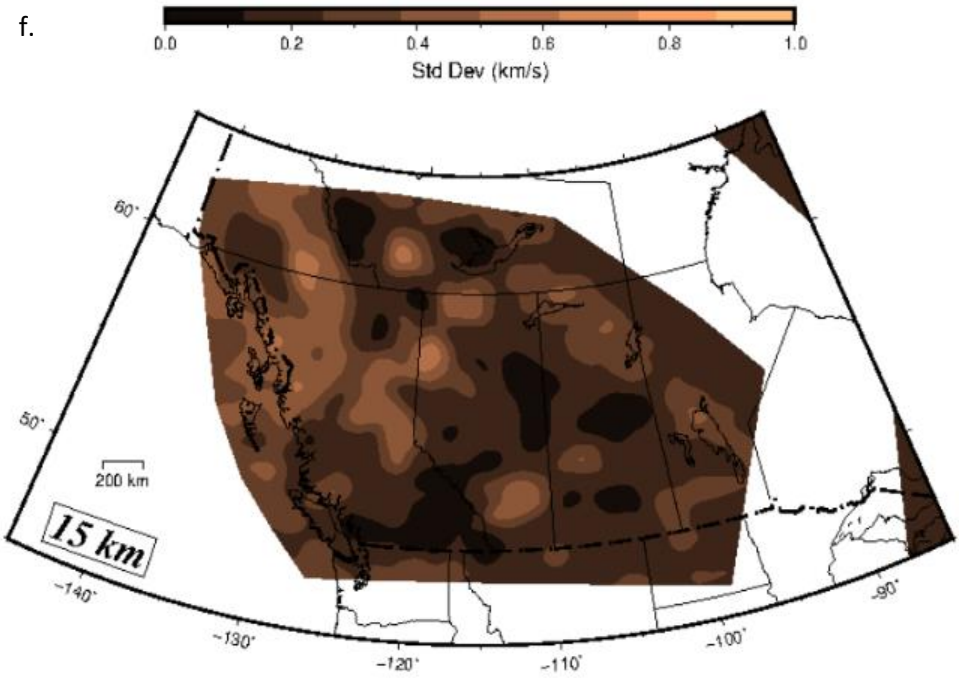

g.

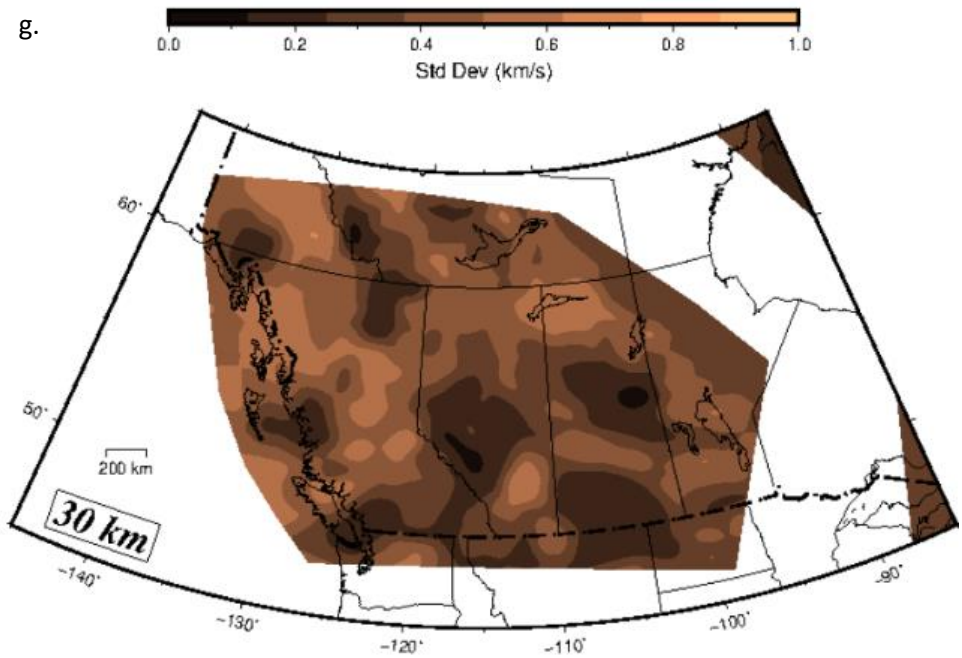

Figure 3.5 (continued).

h.

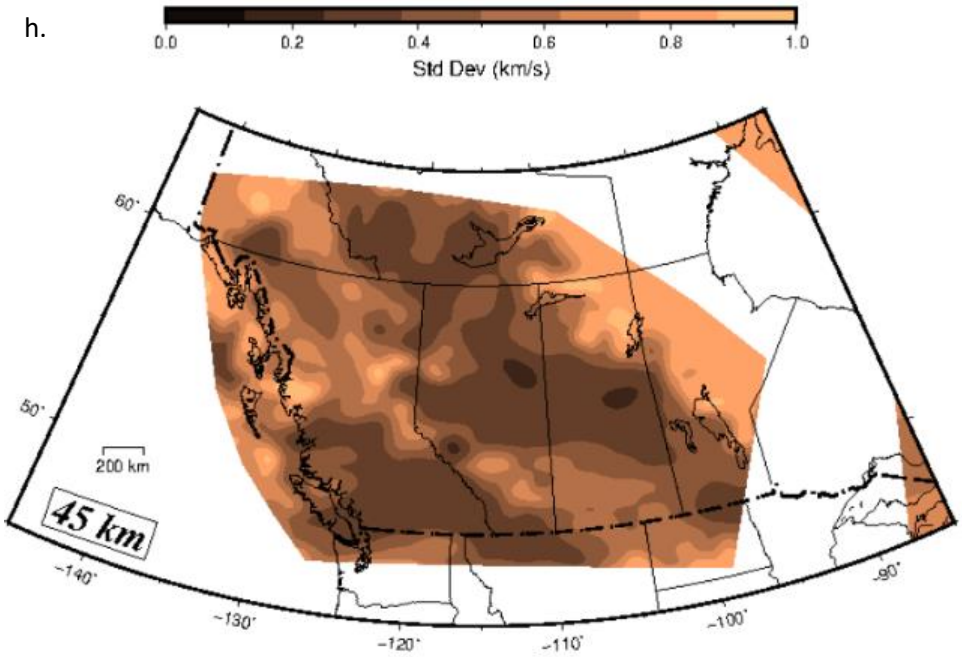

The general trend observed beneath the QCB and GB is the replacement of LVZs in the upper crust by higher *Vs* at the deeper depths of 15 and 30 km (Figure 3.5 b and c) with *Vs* ranging from 3.7 to 4.0 km. Transition to even higher *Vs* is observed at the depth of 45 km (Figure 3.5d). A relatively low-*Vs,* observed beneath the Hecate and Queen Charlotte Basins at the depth of 45 km is bounded to the north and south by higher *Vs* structures. Previous studies suggest a high heat flow in the Hecate Strait and Queen Charlotte sound (Hyndman et al., 1982). The relatively low-*Vs* may be related to the thermal regime in the area.

The Coast belt is dominated by a band of NW-SE trending HVZ in the north and lower-*Vs* in the south at depths ≤ 10 km (Figure 3.5a). At this depth range, a NW-SE trending HVZ (*dVs* ≥ 5%, or *Vs* ≥3.5 km/s) is observed. Given a Poisson's ratio of ~0.25, this *Vs* range is consistent with the crustal *Vp* of 6.6 – 6.8 km/s reported by previous seismic reflection studies (Spence & McLean, 1998), and may be attributed to the prevalence of igneous and metamorphic rocks. The provenance of these rocks is linked to long-term subduction and accretion of the Insular superterrane. *Vs* distribution patterns similar to that in the upper crust are observed in the deeper crust (Figure 3.5b and c) and the uppermost mantle (Figure 3.5d), with more pronounced and focused low *Vs* anomalies beneath the Cascades at mantle depths. The low-*Vs* anomalies may be the result of the higher temperatures beneath the Cascades.

The Intermontane belt is demarcated into northern and southern less-prominent LVZs by a prominent HVZ in the upper crust (Figure 3.5a). The LVZs have a maximum *dVs* of – 5% and are centered around the locations of known IMB. The HVZ, which is co-located with and could be the signature of the Skeena Arch, separates the NW-SE trending LVZs into two broad segments: the BSB in the north and the NB in the south (Massey et al., 2005). These basins are filled with widespread sediments overlain by Late Triassic, Early Jurassic, Late Cretaceous and Early Tertiary

volcanic rocks (Hannigan et al., 2001). At the crustal depths of 15 and 30 km (Figure 3.5b and c), the HVZ is more prominent in the north while relatively lower *Vs* are predominant in the south. The prominent HVZ associated with the Skeena Arch at shallower depths is absent at the depth of 45 km (Figure 3.5d), which suggests that the Arch is probably a crustal feature.

The Omineca belt is characterized by rapidly varying high and relatively low *Vs* structures in the upper crust in the range of 2.9 – 3.4 km/s (Figure 3.5a). This *Vs* pattern is consistent with observations by previous studies (e.g. Zelt and White, 1995) and is attributed to the presence of deformed metamorphic rocks in the suture zone between the Canadian Cordillera and eastern Laurentia (Carr, 1995). This pattern changes with depth, with a higher *Vs* dominating the northern half while relatively lower *Vs* is observed in the south (Figure 3.5b and c). To the east, the *Vs* structure of the Omineca belt abuts the RMT/TF, which separates it from the Foreland fold-and-thrust belt.

East of the Omineca, the velocity structure of the Foreland belt is characterized by prominent LVZs which correspond to the preserved sedimentary rocks of the WCSB and extend across the eastern limit of the CDF onto the Interior Platform. The LVZs in the Alberta basins are separated from the Williston Basins by a prominently high *Vs* structure observed to coincide with the location of the Bow Island Arch. In southern Alberta, the LVZ in the lower crust coincides with the Vulcan structure, a prominent gravity and magnetic feature interpreted to be linked to crustal delamination from the subduction of adjacent Archean blocks (Eaton et al., 1999). The widespread LVZ east of the Arch corresponds to the intracratonic Williston basin, straddling Saskatchewan, Manitoba and North and South Dakota. To the east, the intracratonic Williston basin and adjacent structures are underlain by relatively low-*Vs* zones in the middle and lower crust, distributed mostly in Saskatchewan and, to a lesser extent, Manitoba. This feature spatially

coincides with the North American Central Plain (NACP) conductivity anomaly (Alabi et al., 1975) and a mid-lower crust seismic low-velocity layer (Green et al., 1985; Morel-à-l'Huissier et al., 1987). The anomaly has been interpreted to be akin to the burial of ocean-type hydrous material within an ancient back-arc basin (Green et al., 1985; Nelson et al., 1993). The HVZs located east of the Williston basin are predominantly rocks that form the North American craton.

The general distribution of *Vs* in the crust in western Canada shows a pattern of widespread deformations controlled by the forces of terrane accretion. At the uppermost mantle depths, however, distinctions based on terrane characteristics are rarely observed. First order observations of the general structure in the uppermost mantle (e.g. 45 km; Figure 3.5d) show two main blocks separated by bands of low *Vs*: one is a predominant HVZ on the east, while the other on the west is characterized by a mix of HVZ (in the south) and LVZ (in the north). This pattern is similar to the structural patterns observed for the region by deeper lithospheric studies (Schaeffer & Lebedev, 2014; Zaporozan et al., 2018). The eastern HVZ trends NE-SW over much of the Platform and is roughly bounded by the CDF and corresponds to the mantle structures of the Canadian craton over which parts of the Cordillera terranes lie. LVZs within Alberta and Saskatchewan lie approximately in the locations of the Vulcan structure and the NACP anomaly respectively. Temperature is the main control of seismic velocity within the mantle (Hyndman, 2010). The widespread relatively low *Vs* observed within the western block suggests larger temperature gradients in the mantle relative to the Canadian shield on the east.

Characteristics of the Western Canada Basins from Vs Cross-Sections

In Figures 3.6-3.8, we present cross-sections extracted from our results at locations corresponding to major composite sedimentary basins within the OB, IB and WCSB. For each

composite basin, there are two orthogonal cross-sections, showing the internal *Vs* structure from the upper crust to the uppermost mantle. The first panel of each figure shows the topography, the second panel shows the *Vs* cross-sections and the third panel shows the corresponding uncertainty. Actual *Vs* values are presented together with the corresponding change in velocity (*dVs*, expressed in percentage) for each cross-section. The same *Vs* scale is maintained for all velocity cross-sections. Low *Vs* packages (≤ 3 km/s) which correspond to known sedimentary basins are highlighted by dashed lines, while thick solid lines mark the transition to higher, mantle-type *Vs* boundaries. Transition from the lower crust to the uppermost mantle across the Moho is broadly marked by *Vs* increase corresponding to ≥ 5% of the lower crust *Vs*, depending on the location in western Canada. In many cases this corresponds to velocity of *Vs* ≥ 4.2 km/s on our selected cross-sections.

Offshore Basins

Within the OB, the cross-sections are oriented in the NW-SE and NE-SW directions over the QCB (Q-Q', Figure 3.6a) and the GB (G-G', Figure 3.6c). Mean *Vs* along Q-Q' and QX-QX' are ~3.91 and ~3.9 km/s respectively, with predominantly low uncertainty for much of the cross-section. *Vs* ≤ 3.2 km/s dominate the upper 10 km of both lines. On Q-Q' beyond ~350 km toward northernmost VI, velocities in the upper 10 km start to increase and the sedimentary basement appears to be thin (Figure 3.6a). Similarly, on QX-QX' across the Coast Mountain, the sedimentary basin thins out and disappears east of ~225 km (Figure 3.6b). At depth, *Vs* >4.0 km/s dominates the deepest layers, with the top of the layers becoming shallow on the flanks beneath the Insular terrane and adjacent to northern VI on Q-Q' (Figure 3.6a). The top of the >4.0 km/s *Vs* anomaly appears to be flat at depths of >40 km on the QX-QX' line except for beneath the Coast Mountain terrane where it appears to have been displaced by a prominent low-*Vs* anomaly (Figure 3.6b).

In the QCB (Figure 3.6 a and b), on the basis of our definition, the base of the sedimentary rocks on cross-section Q-Q' (Figure 3.6a) is located at ~7 km close to the southeastern tip of Alaska in the north, ~10 km in the middle of the basin and tapers in the south, adjacent to northern VI. Sedimentary rocks within the QCB are interbedded with Tertiary volcanics (Rohr & Dietrich, 1992a; Spence & Asudeh, 1993), hence they appear to have velocities in the upper limits of the low-*Vs* range. The crust appears to thin to depths of 22-24 km near the northern and southern edges of the cross-section, close to the depth range of previous studies (e.g. Spence & Asudeh, 1993; Yuan et al., 1992). The crust thickens to ~42 km near the middle of the line, beneath the thickest part of the basin. This thickness is inconsistent with the interpretation of 22 – 29 km from previous seismic refraction studies near the location (Spence & Asudeh, 1993, Hole et al., 1993, Yuan et al., 1992). The cross-section QX-QX' crosses Q-Q' at a point where both the basin and the crust are the thickest (Figure 3.6b). The basin thickness of ~10 km is maintained across the width of the Insular belt and tapers beneath the Coast Mountain belt. Our result is consistent with $Vp \leq 5.5$ km/s at depths ≤ 8 km reported by previous active-source seismic studies of the basin (e.g. Clowes et al., 2005; Spence & Asudeh, 1993; Yuan et al., 1992). The base of the sub-basin crust is at the depth range of 42–44 km and appears to be of uniform thickness along QX-QX'. A gap in the ANT-derived Moho observed at depths >40 km at distances between 150 and 300 km marks the transition to a deep column of low *Vs* directly over which a high *Vs* structure is located. This feature lies beneath the conventional boundaries of the Coast and Intermontane belts; it is east of the refraction lines of Spence & Asudeh (1993) and could not have been detected in those studies. We do not interpret the feature due to the large uncertainties associated with the *Vs* values. Further investigation of this area with better data constraint is an interesting topic for future research.

Offshore Basins

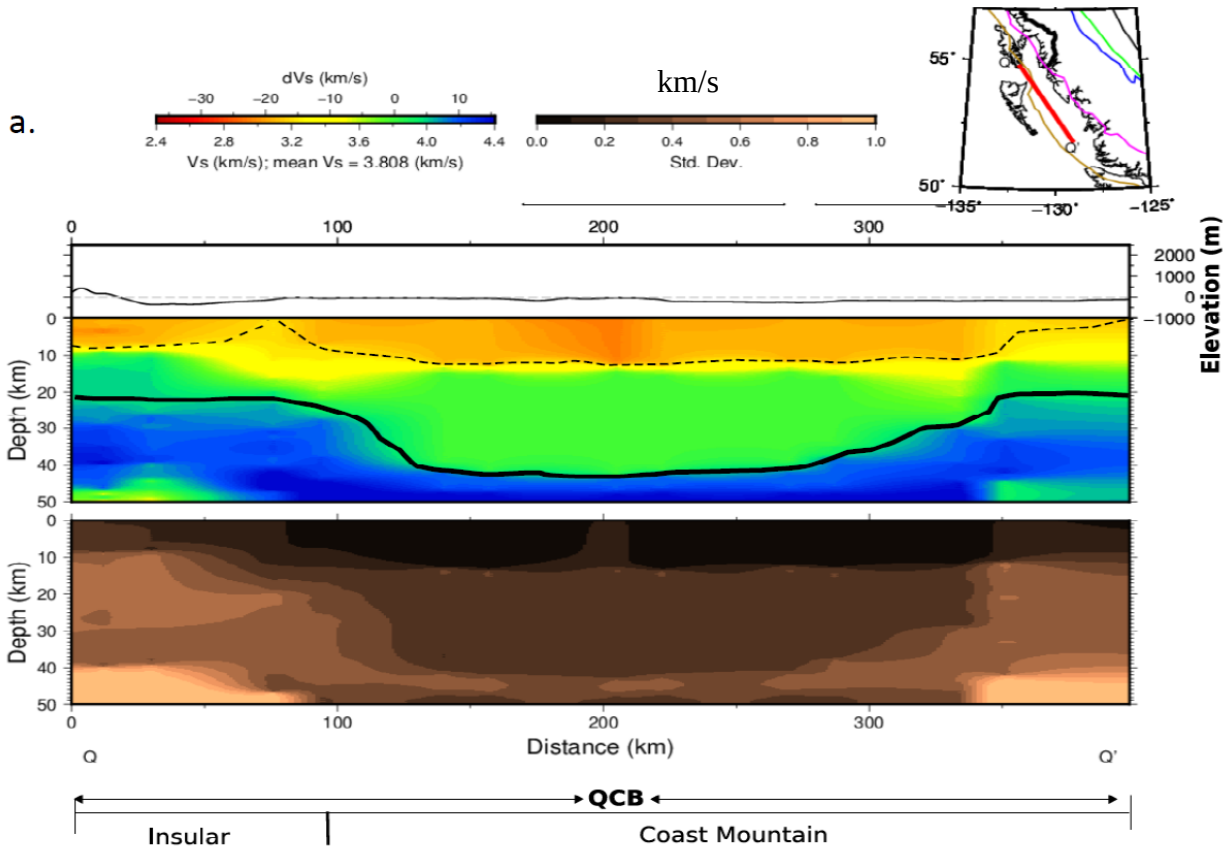

Figure 3. 6 Cross-sections taken along the Offshore basins: Queen Charlotte Basin in the NW-SE and NE-SW directions (a) and (b); Georgia Basin in the NW-SE and NE-SW directions (c) and (d). *Top panel*: topography along the cross-section; middle panel: *Vs* cross-section; bottom panel: uncertainty distribution associated with the *Vs* cross-section in the middle panel. Lines: thick black lines in the *Vs* plot are used to mark the location of the Moho; thick red line in the inset marks the actual location of the cross-section; thin dashed black lines are used to mark the basins in the shallowest depths. QCB – Queen Charlotte Basin; GB – Georgia Basin; CL – coastline.

Figure 3.6 (continued).

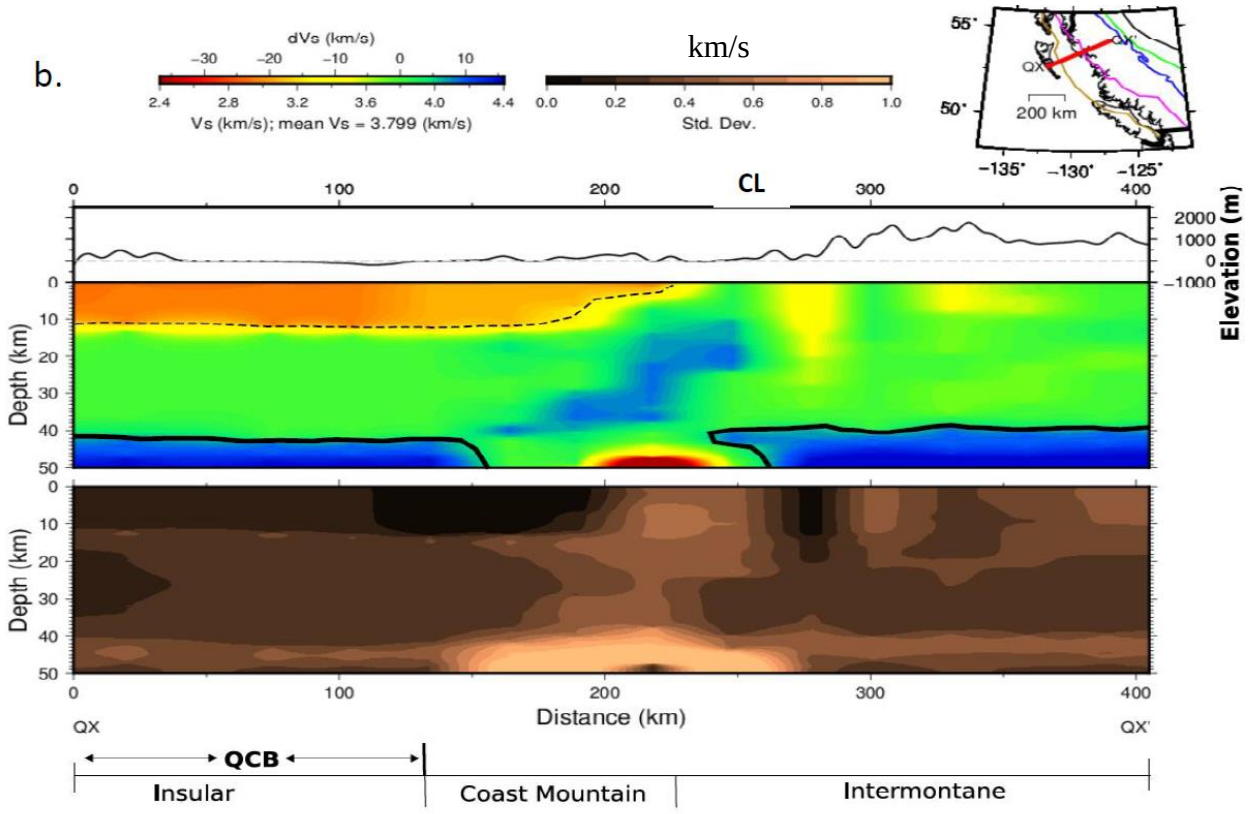

Figure 3.6 (continued).

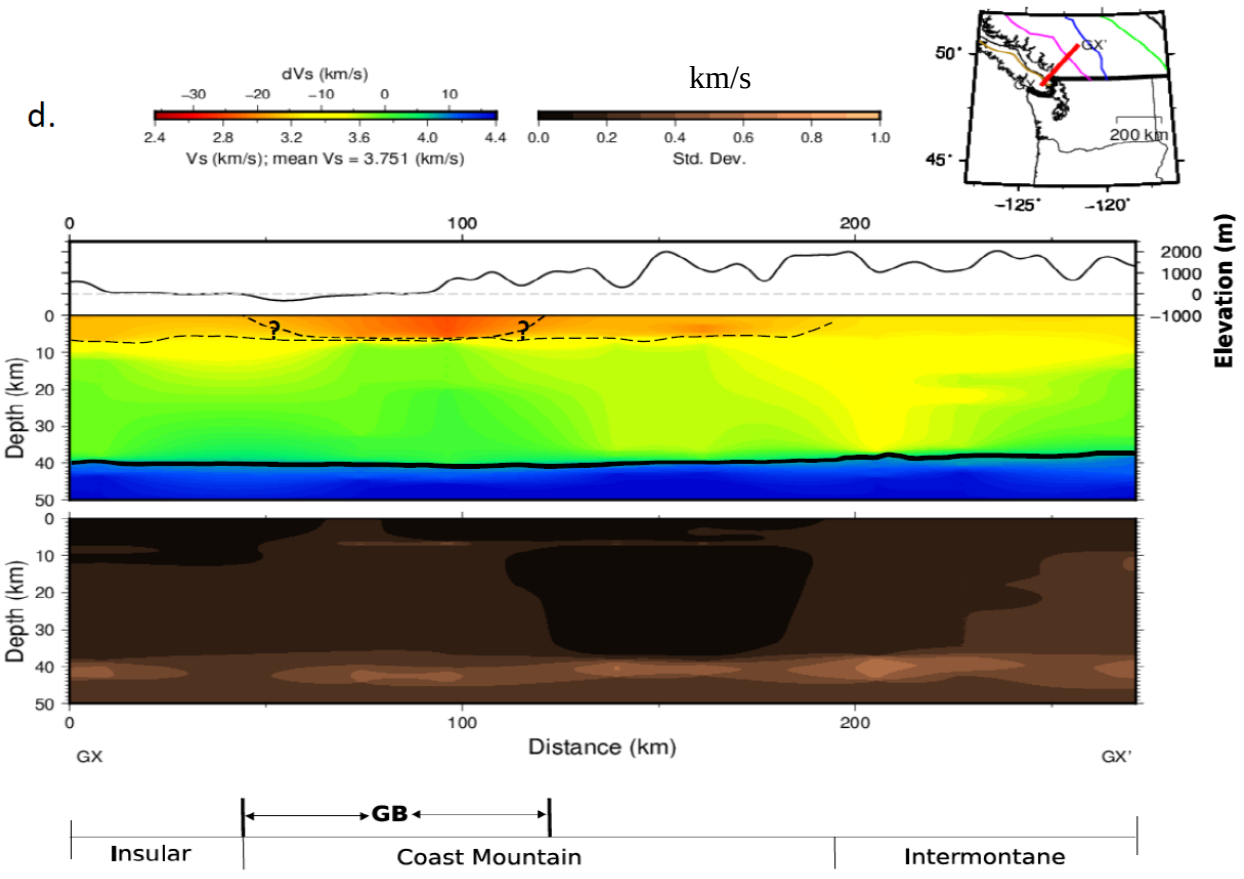

Meanwhile the GB is characterized by prominent low *Vs* anomalies in the uppermost 6 km in the southern half of the cross-section but shallower in the north (G-G', Figure 3.6c). The low-*Vs* values observed on cross-sections G-G' are divided into the northern (distance ≤ 50 km) and southern (distance ≥ 180 km) segments (Figure 3.6c). In the northern segment, the base of the sedimentary rocks is located at the depth of ~4 km in the north and at ~6 km in the southern part on the basis of our initial *Vs* definitions. Much lower *Vs* values are observed in the southern portion than is observed both in the northern portion and in the QCB. These observations fit well with results from a previous seismic reflection study of the uppermost crust, where P-wave velocities (*Vp*) are higher in the north (*Vp* ~ 4.5–6 km/s) than in the south (*Vp* ~ 3–6 km/s) (England & Bustin, 1998; Zelt et al., 2001). Zelt et al. (2001) estimated the maximum depth to basement as 8 – 9 km in the south of the basin. The low *Vs* in the north is interpreted to correspond to the Upper Cretaceous Nanaimo Group, while in the south, it is interpreted to be the result of more recent sediments, including those derived from glacial till and the Fraser river (Zelt et al., 2001). The cross-section is also characterized by prominent high-*Vs* anomalies with the top at 26-km depth in the north and 30 km in the south, but gouges to the depth of ~42 km in between (Figure 3.6c). Along GX-GX', the basin straddles the Insular and Coast Mountain belt on the west and east respectively, but its core appears between 50 and 110 km from the southwestern end (Figure 3.6d). The prominent low-*Vs* anomalies are mostly contained in the shallowest 7 km beneath the Insular and Coast Mountain terranes. The sediments to the west (distance <120 km) represent the marine Upper Cretaceous Nanaimo Group, while on the east, the basin comprises Quaternary fluvial and deltaic sands and gravels of the Fraser River delta and the non-marine Neogene sediments of the Boundary Bay Formation (England & Bustin, 1998; Zelt et al., 2001). The *Vs* characteristics of the sub-basin crust change close to the transition between the Coast Mountain and Intermontane

belts. The transition to the uppermost mantle appears to be smooth and almost flat in the NE–SW direction and this occurs at the depths of 40 and 36 km near the western and eastern edges of GX-GX' respectively. This observation is in reasonable proximity of previously interpreted Moho depths in SE Insular/SW Coast belts of 30 – 37 km depending on the location (Zelt et al., 1993; O'Leary et al., 1993).

Intermontane Basins

Prior to extracting the cross-sections over the Intermontane basins, we take advantage of one of the Lithoprobe southern cordillera surveys (Cook, 1995) for further comparison with our results. We draw a *Vs* cross-section I-I' from our 3-D model along a path that is colinear with Lithoprobe line 10 (Figure 3.7a). The path is oriented in the E–W direction, perpendicular to the strike of major Cordillera structures and located in a region of good resolution for our surface wave tomography.

The basement beneath I-I', within the Intermontane belt, is located at the depth of ~6 km and coincides largely with the strong basement reflections on line 10. Transition to the lower-crust *Vs* occurs at the depth of ~25 km and coincides remarkably with a consistent reflection on the Lithoprobe line. Similarly, the top of the prominently high-*Vs* that occurs at ~30 km marks the transition to the mantle and is ~3 km shallower than the base of the reflectivity on the Lithoprobe line. To the best of our knowledge, the basement depth was not explicitly interpreted in the literature, although Cook et al. (1992) provided a general interpretation that corresponds to the uppermost 10 – 15 km of the line to Paleozoic (meta-)sedimentary, Tertiary Volcanic and other supracrustal rocks. Meanwhile, the Moho depth along this profile was interpreted as varying from ~33 to ~31 km on the basis of truncated reflectivity (Cook, 1994). With the reasonable comparison

obtained between our results and the Lithoprobe line 10, we present *Vs* cross-sections drawn across NB and BSB within Intermontane belt.

Intermontane Basins

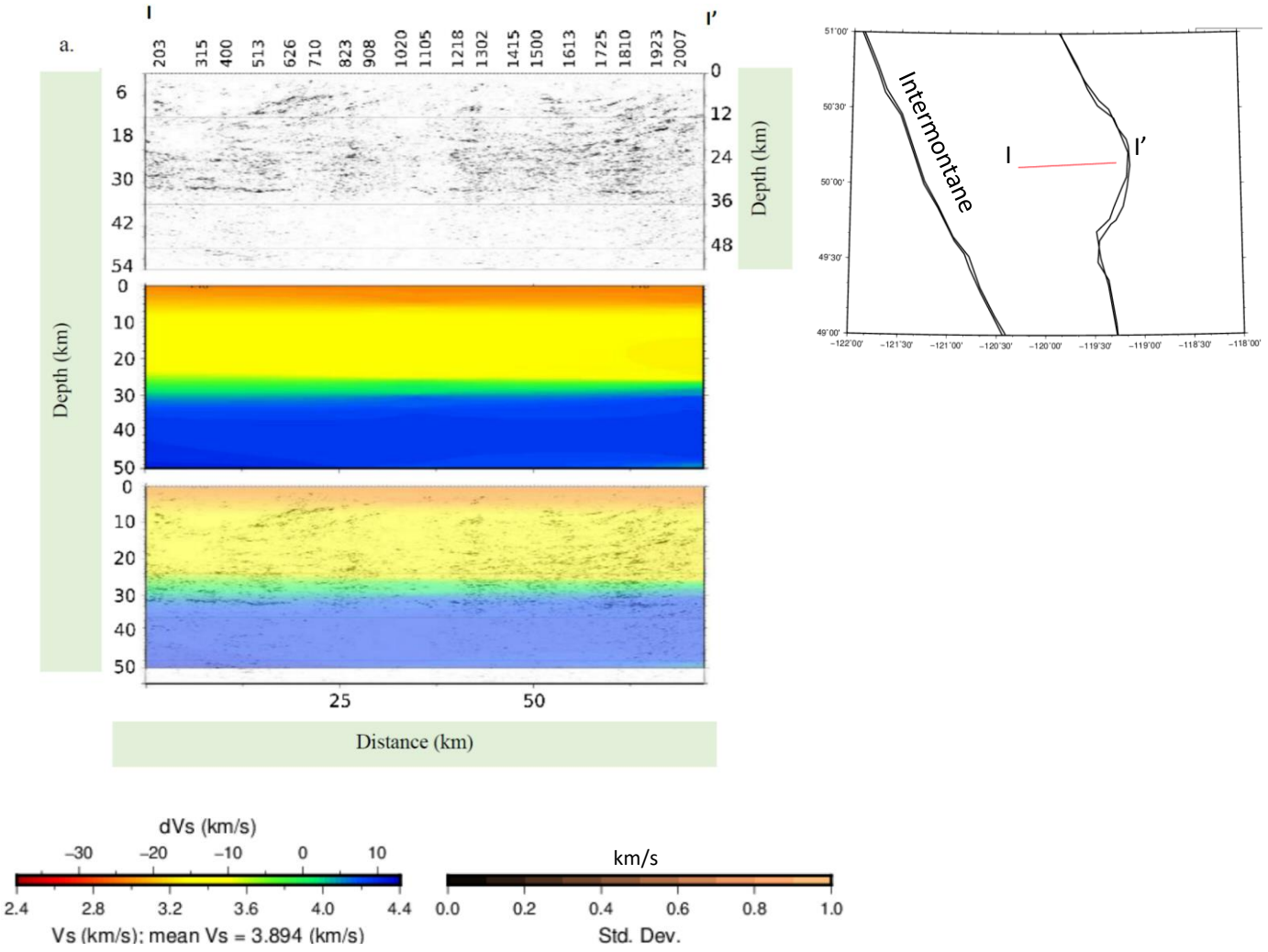

Figure 3. 7 (a) *Top row*: Lithoprobe line 10 taken from southern cordillera (Intermontane belt). *Middle row*: co-linear *Vs* cross-section corresponding to the Lithoprobe line 10. *Bottom row*: Lithoprobe line overlain on the co-linear *Vs* cross-section. The location of the line is shown in Figure 3.1c. *Cross-sections drawn over major sedimentary basins in the Intermontane belt*: Bowser/Sustut Basin in the NW-SE and NE-SW

Figure 3.7 (continued).

directions (b) and (c); Nechako Basin in the NW-SE and NE-SW directions (d) and (e). *Top panel*: topography along the cross-section; *middle panel*: *Vs* cross-section; *bottom panel*: uncertainty distribution associated with the *Vs* cross-section in the middle panel.Lines: thick black lines in the *Vs* plot are used to mark the location of the Moho; white dashed line in (b) and (c) mark the alternative Moho interpretation; thick red line in the inset mark the actual location of the cross-section; thin black lines are used to mark the basins in the shallowest depths. BSB – Bowser/Sustut Basin; NB – Nechako Basin.

Figure 3.7 (continued).

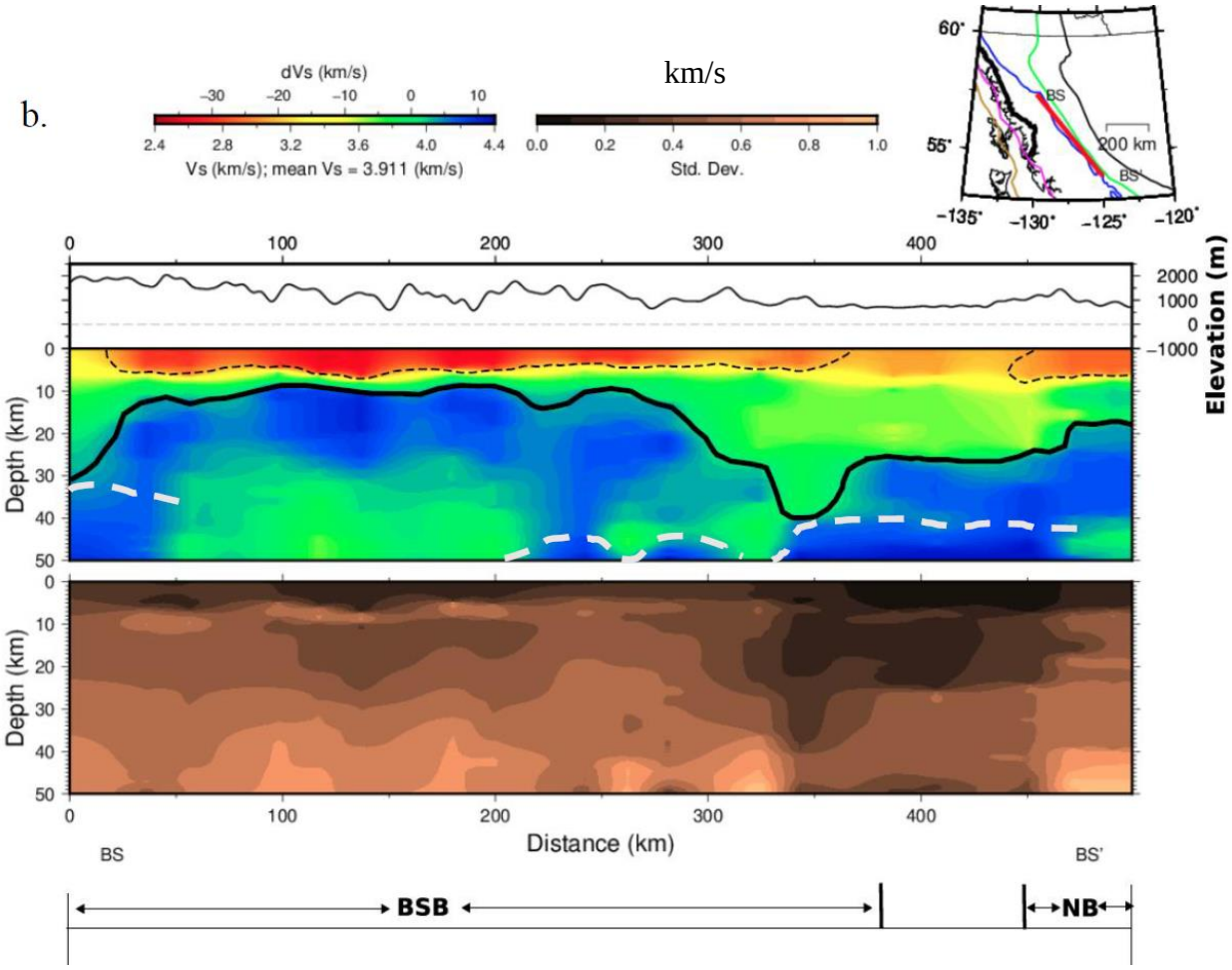

Figure 3.7 (continued).

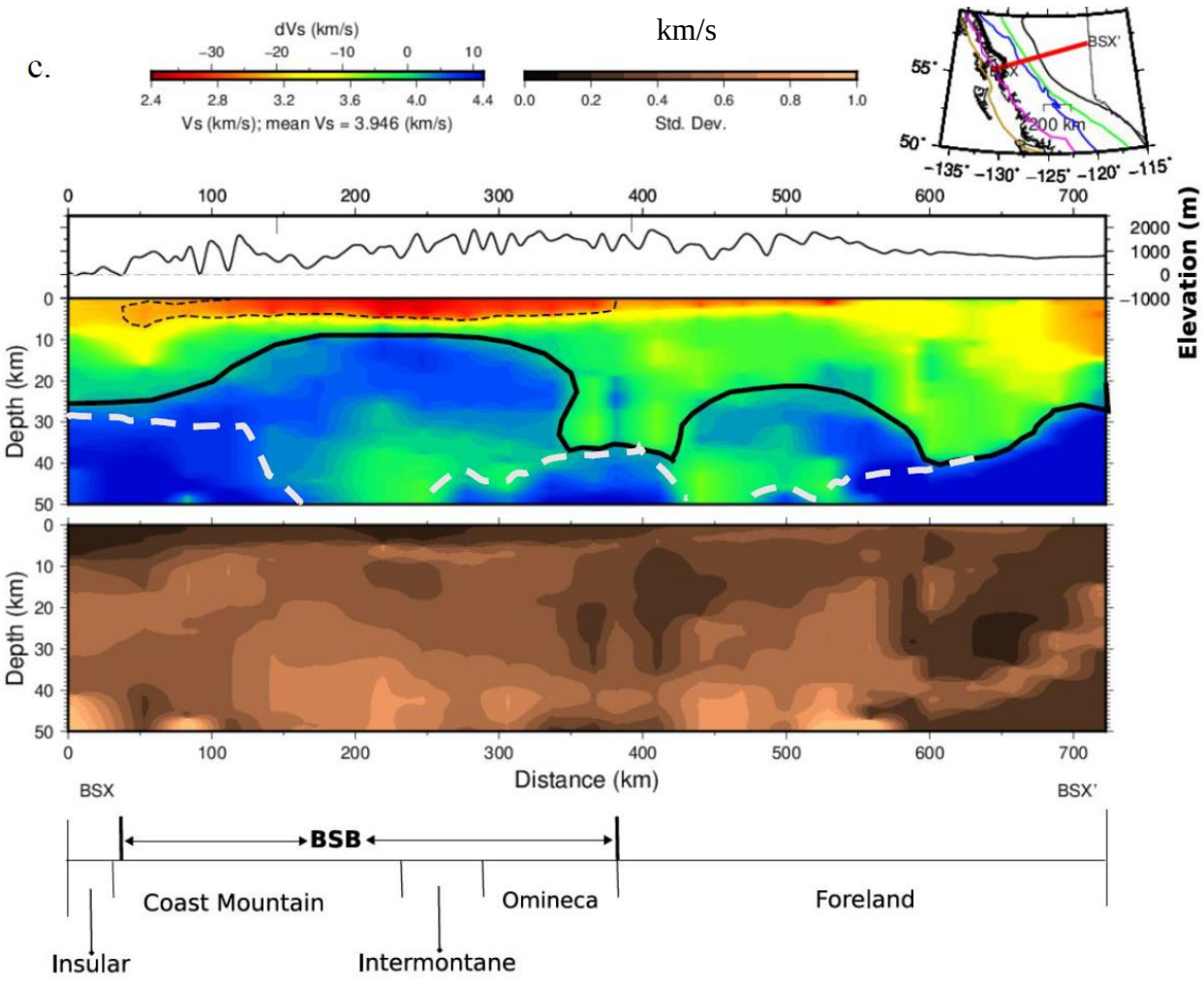

Figure 3.7 (continued).

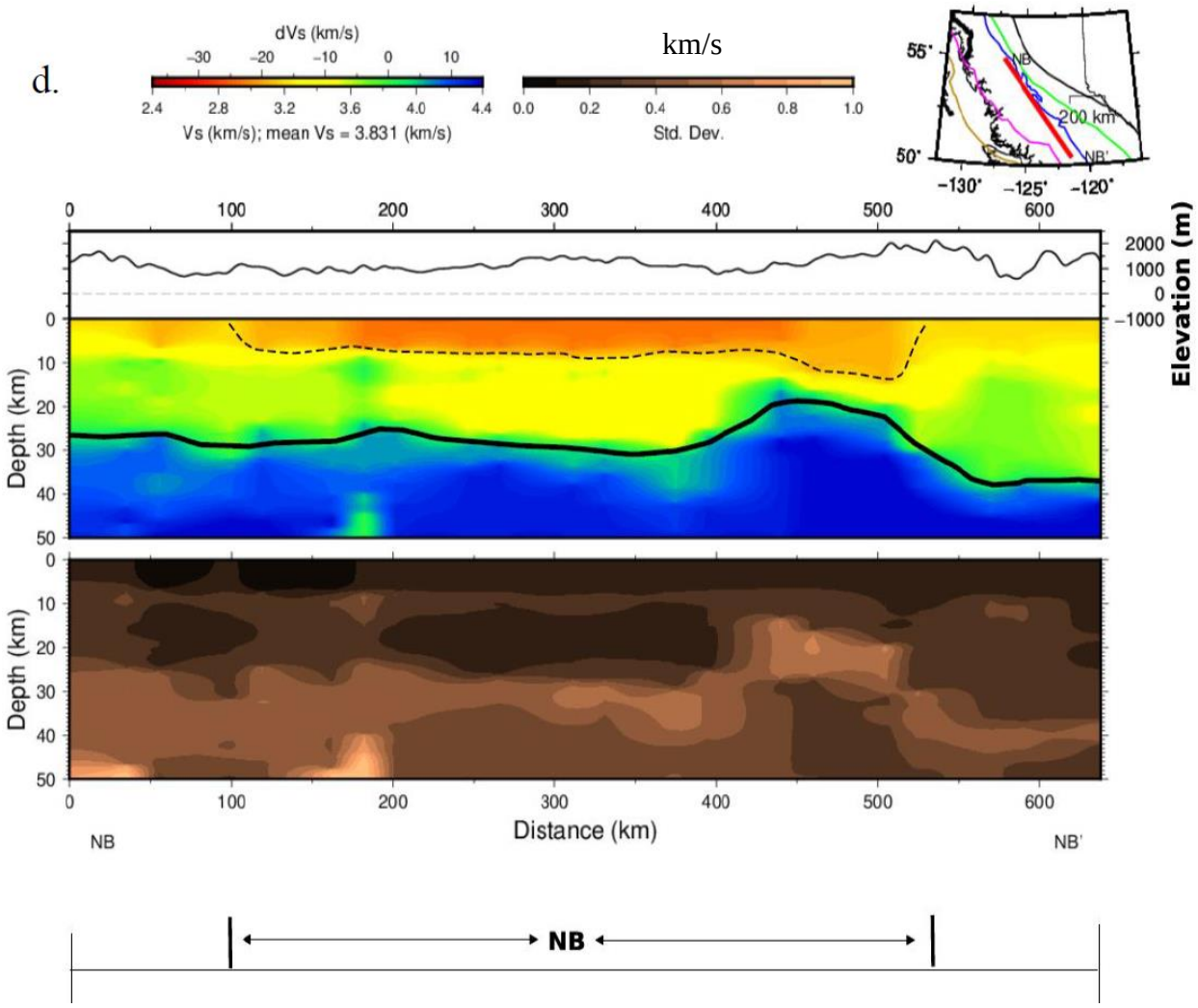

Figure 3.7 (continued).

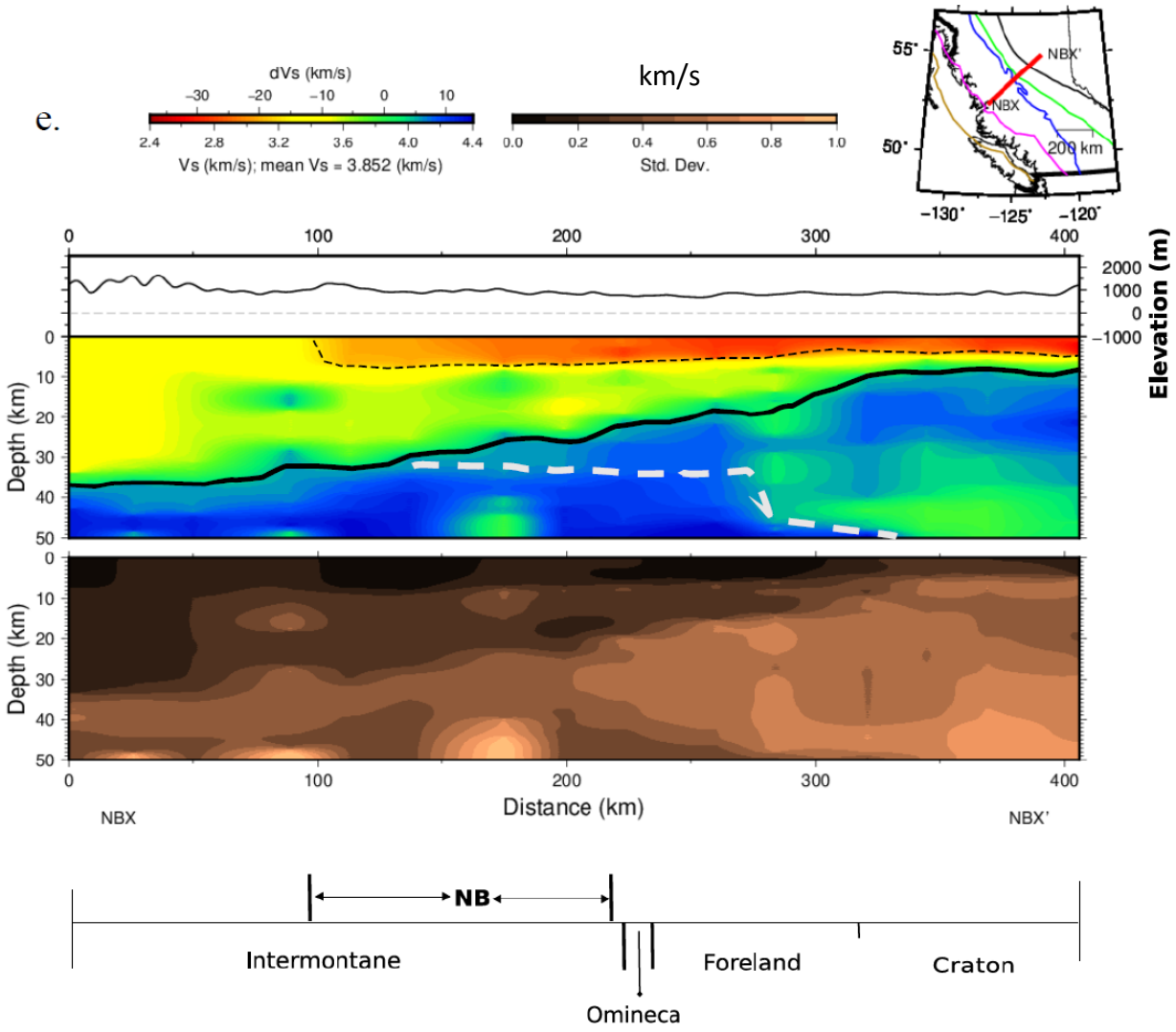

NB and the composite BSB lie in the strike direction of the Intermontane superterrane. The Bowser and Sustut are two different but spatially close basins that are inseparable on our tomography image due to limited data resolution. In general, the results obtained for BSB and NB are consistent with other studies, especially within the upper crust. As the uncertainty associated with the results appears to increase with depth in most part of BSB and NB cross-sections, the constraint on the structure at depth becomes relatively unreliable. In the NW-SE direction along BS-BS', BSB are characterized by the north-dipping low-*Vs* anomaly in the uppermost 7 km at distances from 20 to 380 km (Figure 3.7b), corresponding to the Paleozoic sedimentary rocks that are overlapped by Mesozoic assemblage rocks (Evenchick et al., 2005; Welford et al., 2001). The southernmost low-*Vs* anomaly belongs to the NB. Along BSX-BSX', the shallow low-*Vs* anomaly extends from the Insular terrane to the Foreland where the thickness of the low-velocity layer becomes small (Figure 3.7c). Beneath the sedimentary basin, the sub-basin crust is characterized by unusually high-*Vs* structures in the middle-lower crust. To our knowledge, there are no existing seismic reflection/refraction lines that are co-located with our cross-sections in this area, but previous studies of the Intermontane belt show that the Moho is located at the depths of 34 – 35 km along our studied paths (Creaser and Spence, 2004; Spence and McLean, 1998; Zelt et al., 1993). Our 1-D *Vs* results from the northern and southern part of the Intermontane belt (Figure 3.4c) show the Moho depth of 30 km in the south and a gradational increase in the north starting from the depth of 35 km. These results are close to the interpreted depths from previous seismic studies. Given the relatively high uncertainties (≥0.5 km/s) associated with structures at sub-basin depths (predominantly at distances up to ~350 km on BS-BS' and 600 km on BSX-BSX'), the results might be somewhat unreliable. If this is the case, then the relatively higher uncertainties may be due to the complexity of the structures beneath the Intermontane belt. On the other hand,

if the observations are real, then the anomalously high *Vs* may be the characteristics of the under-thrusted NA craton beneath the Canadian cordillera (Ross, 1991; Carr and Brown, 1990; Armstrong, 1988; Price, 1981). In the latter case, the Moho depths, marked by the white dashed line on the cross-sections (Figure 3.7 b and c), are consistent with previous studies and with the Moho depth of 34 km from our 1-D *Vs* model located north of these cross-sections.

South of the BSB, the NB is characterized by prominent low-*Vs* anomalies that stretch across the middle of cross-section NB-NB' (distance between 100 and 550 km from the northwestern end, Figure 3.7d), corresponding to sedimentary and volcanic rocks of the Takla and Hazelton Group (Yorath, 1991). The base of the basin is at the depth of ~7.5 km at the center of NB-NB', while the relatively low *Vs* observed at the distance from 450 – 500 km is below the 3 km/s *Vs* definition for sedimentary basin in this study and extends down to the depth of ~14 km. This feature may be associated with the prevalent volcanic rocks interbedded with older sediments (Stephenson et al., 2011). Along NBX-NBX', the basement is at the depth of ~6 km. The Moho along NB-NB' is located at the depth of ~30 km in the north, 38 km in the south but appears to shallow to the depth of ~22 km beneath the deepest part of the basin at the distance of ~450 km (Figure 3.7d). On the westernmost edge of NBX-NBX', the Moho depth is ~ 37 km but shallows to ~22 km near the middle of the profile. The uncertainty associated with the results along NBX-NBX' appears to increase with depth toward the NE mostly at distances greater than 200 km. As a result, *Vs* structures may be unreliable at depth east of the Intermontane belt. According to the refraction and wide-angle reflection studies of the southern NB (Stephenson et al., 2011), the basement and Moho depths are 3.3 km and 33.5 – 35 km, respectively along their profile. These are strikingly similar to our 1-D *Vs* results (Moho ~33 km) obtained in the southern Intermontane belt (Figure 3.4c). Furthermore, a magnetotelluric study of the Nechako basin (Spratt & Craven,

2011) shows similar correspondence to our results, especially at shallow depths. In the middle crust, the study interpreted a high-conductivity anomaly as rising magma. A *Vs* structure corresponding to this interpretation is not observed along our selected cross-sections, possibly because of the relatively increased uncertainty estimates associated with the mid-crustal *Vs* values along these cross sections.

Western Canada Sedimentary Basins (WCSB)

The availability of Lithoprobe seismic reflection lines which sample the Alberta basement (Hope et al., 1999) makes it possible to draw another comparison with our results. A *Vs* cross-section (AB-AB') from our 3-D model is extracted and compared with Lithoprobe seismic line 11b, located along a colinear path within the WCSB. Similar to seismic line 10, line 11b is oriented in the E–W direction, perpendicular to the strike of major Cordillera structures and located in a region of reasonable resolution for our surface wave tomography. At shallow depths, line AB-AB' is characterized by an ~7 km-thick low-*Vs* layer which coincides reasonably well with the strong reflections on line 11b. Previous attempts to map the depth and geometry of the basement reflection were hampered by the presence of multiple reverberations at basement depths (Hope et al., 1999). A sharp increase in *Vs* occurs at the depth of ~32 km coinciding with the top of a band of strong reflection and marking the transition to a lower crust high-velocity layer. The reflection Moho, interpreted on the basis of change in reflectivity, varies E-W at the depth between 37 and 40 km (Bouzidi et al., 2002). The Moho uplift observed on our *Vs* profile is centered at the distance of ~450 km and it corresponds to the area where the strong reflections disappear. The reflections faintly re-emerge in the east with the bottom matching the transition to the Moho on the *Vs* profile. After the further validation of our results in the WCSB, we proceed to describe the *Vs* cross-sections drawn over the major sedimentary basins and formations.

In the WCSB, we present results for the Liard/Horn River, Montney, Duvernay and Williston basins. The Liard basin to the west is separated from the Horn River basin by the Bovie fault. Both basins are jointly represented in this study due to limitations in resolution. The Liard/Horn River basins are characterized by low-*Vs* anomalies in the upper 10 km along line LH-LH' (Figure 3.8b), with a possibility of extending down to 15 km in the southeastern part of the line. The top of the prominent high *Vs* anomaly at depths is at ~34 km near the northern edge of the line but deepens to ~42 km and remains flat from the distance of 125 km till the end of the cross-section (Figure 3.8b). Along the E–W cross-section (LHX-LHX'), a 3-km-thick layer of low *Vs* is observed near the westernmost edge of the cross-section but thickens eastward to the depth of ~8 km. The top of prominent high *Vs* is located at the depth of ~44 km near the western edge of the cross-section but shallows to the depth of ~16 km in the east (Figure 3.8c). The mean *Vs* for LH-LH' and LHX-LHX' are 3.7 and 3.86 km/s, respectively, with generally low uncertainty estimates for both cross-sections.

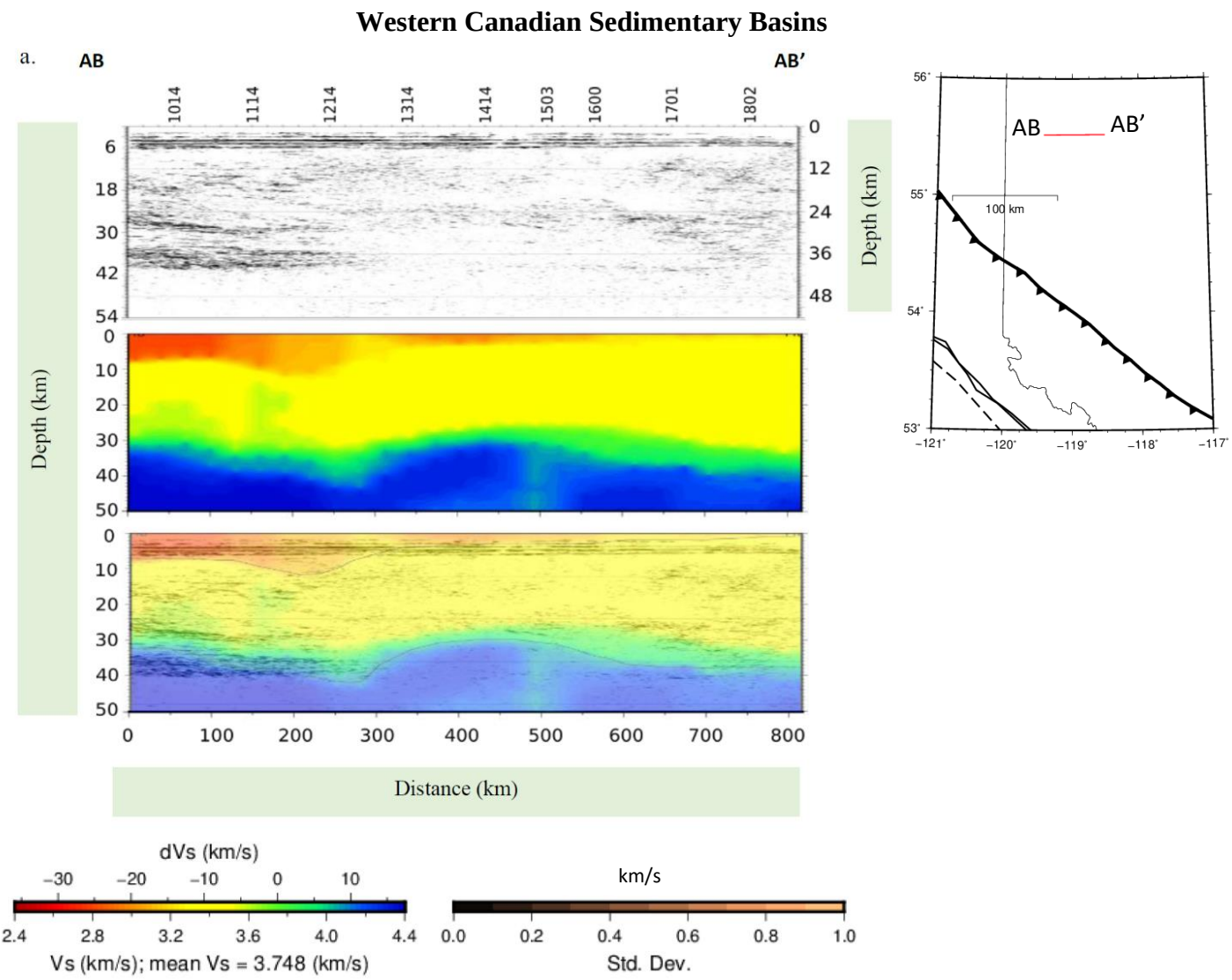

Figure 3. 8 *Top row*: Lithoprobe line 11b taken from Central Alberta. *Middle row*: co-linear *Vs* cross-section corresponding to the Lithoprobe line 11b. *Bottom row*: Lithoprobe line overlain on the co-linear *Vs* cross-section. The location of the line is shown in Figure 3.1c. *Cross-sections taken along major*

Figure 3.8 (continued).

western Canadian sedimentary basins: Liard/Horn River Basins in the NW-SE and NE-SW directions (b) and (c); Montney Basin in the NW-SE and NE-SW directions (d) and (e); Duvernay Basin in the NW-SE and NE-SW directions (f) and (g) and Williston Basin in the W-E and N-S directions (h) and (i). *Top panel*: topography along the cross-section; *middle panel*: *Vs* cross-section; *bottom panel*: uncertainty distribution associated with the *Vs* cross-section in the middle panel. Lines: thick black lines in the *Vs* plot are used to mark the location of the Moho; thick red line in the inset mark the actual location of the cross-section; thin black lines are used to mark the basins; dashed line on (h) marked "C", denotes the location of the COCORP reflection line. LHRB – Liard/Horn River; HRB – Horn River Basin; MB – Montney Basin; DB – Duvernay Basin; ADB – Alberta Deep Basin; BF – Bovie Fault (location).

Figure 3.8 (continued).

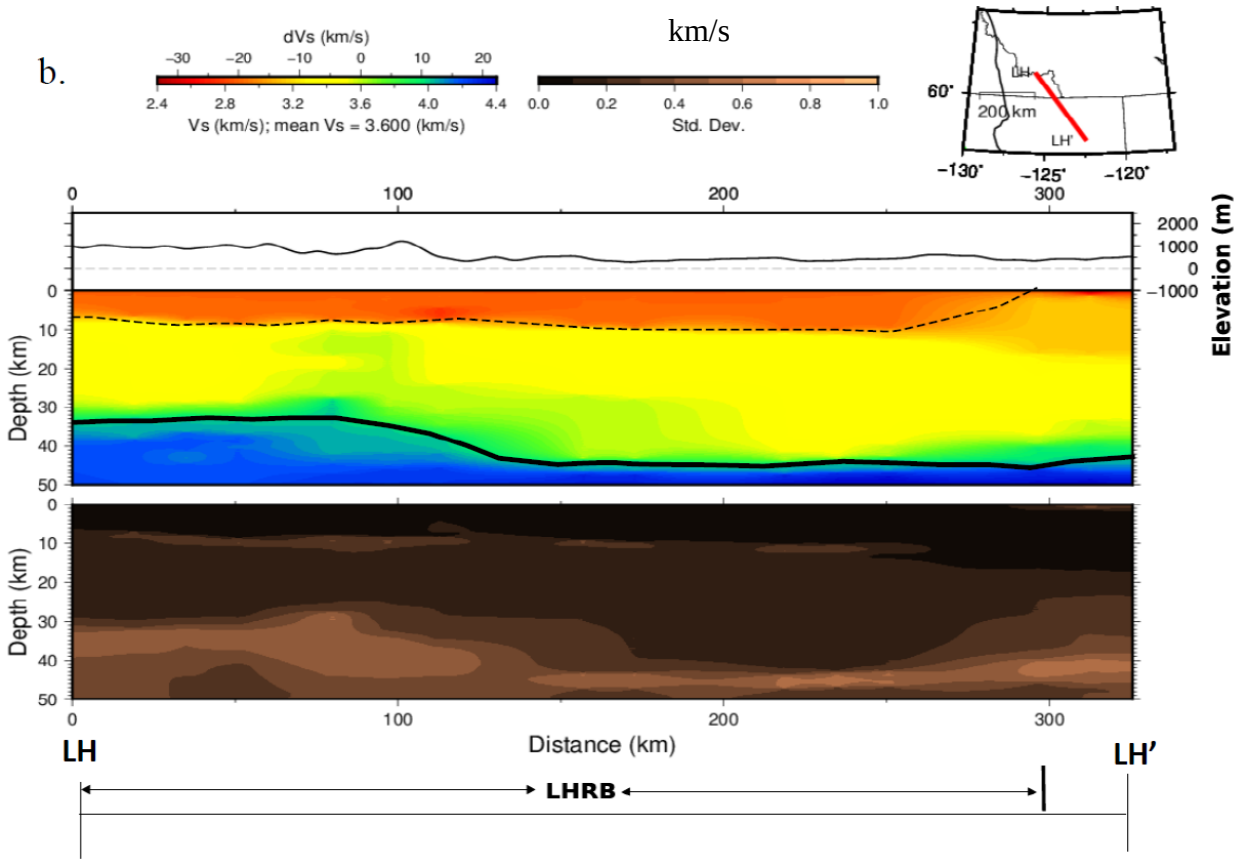

Figure 3.8 (continued).

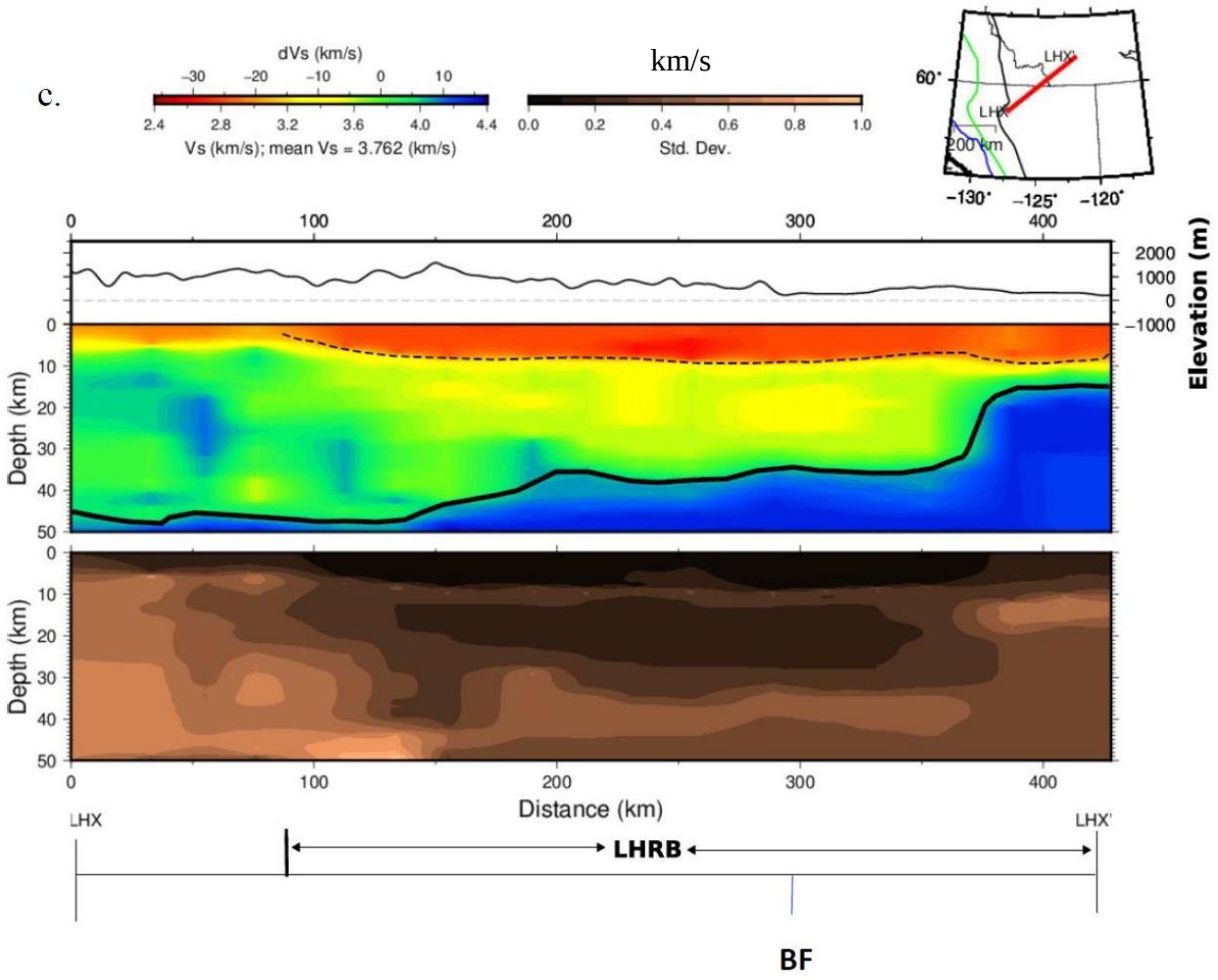

Figure 3.8 (continued).

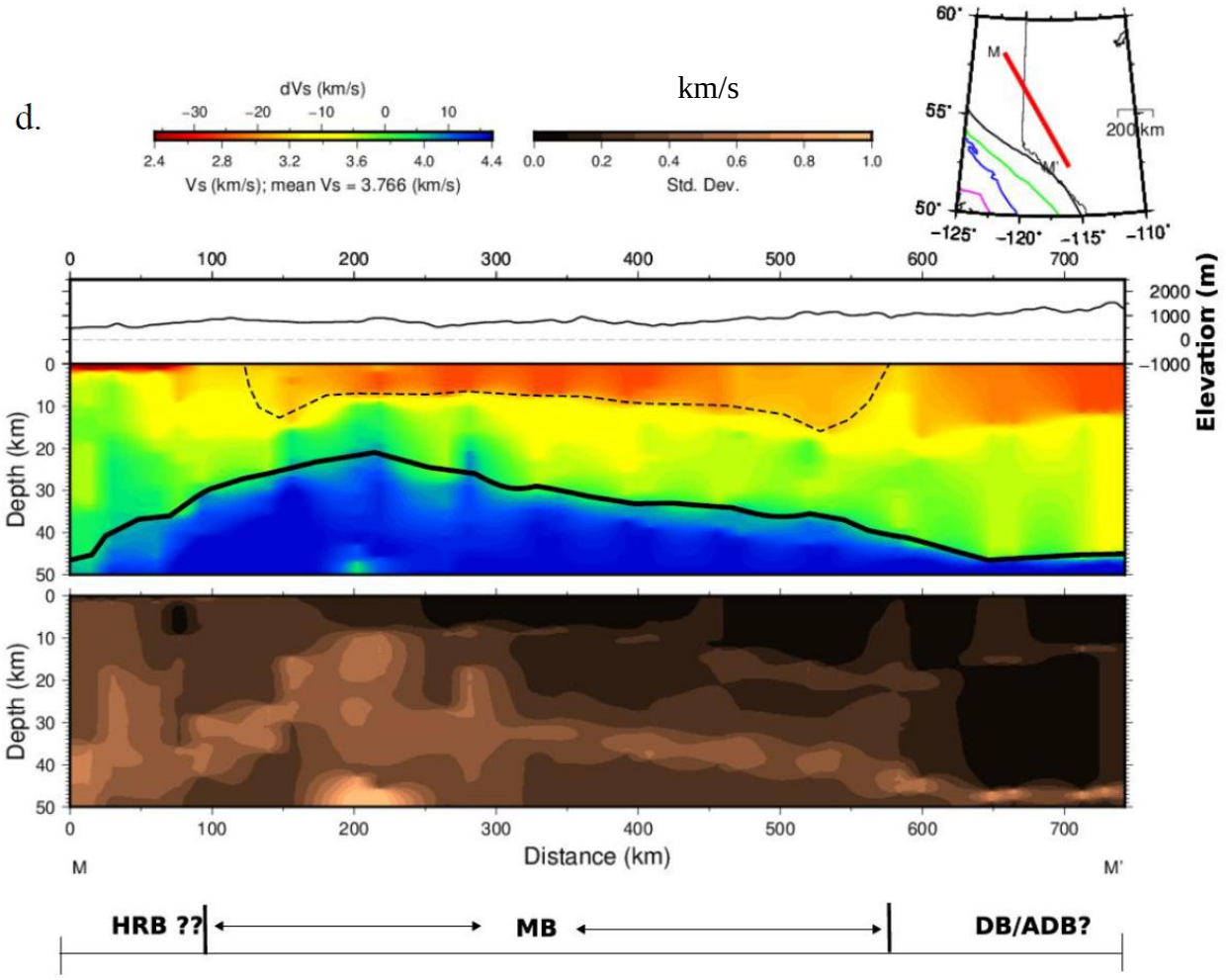

Figure 3.8 (continued).

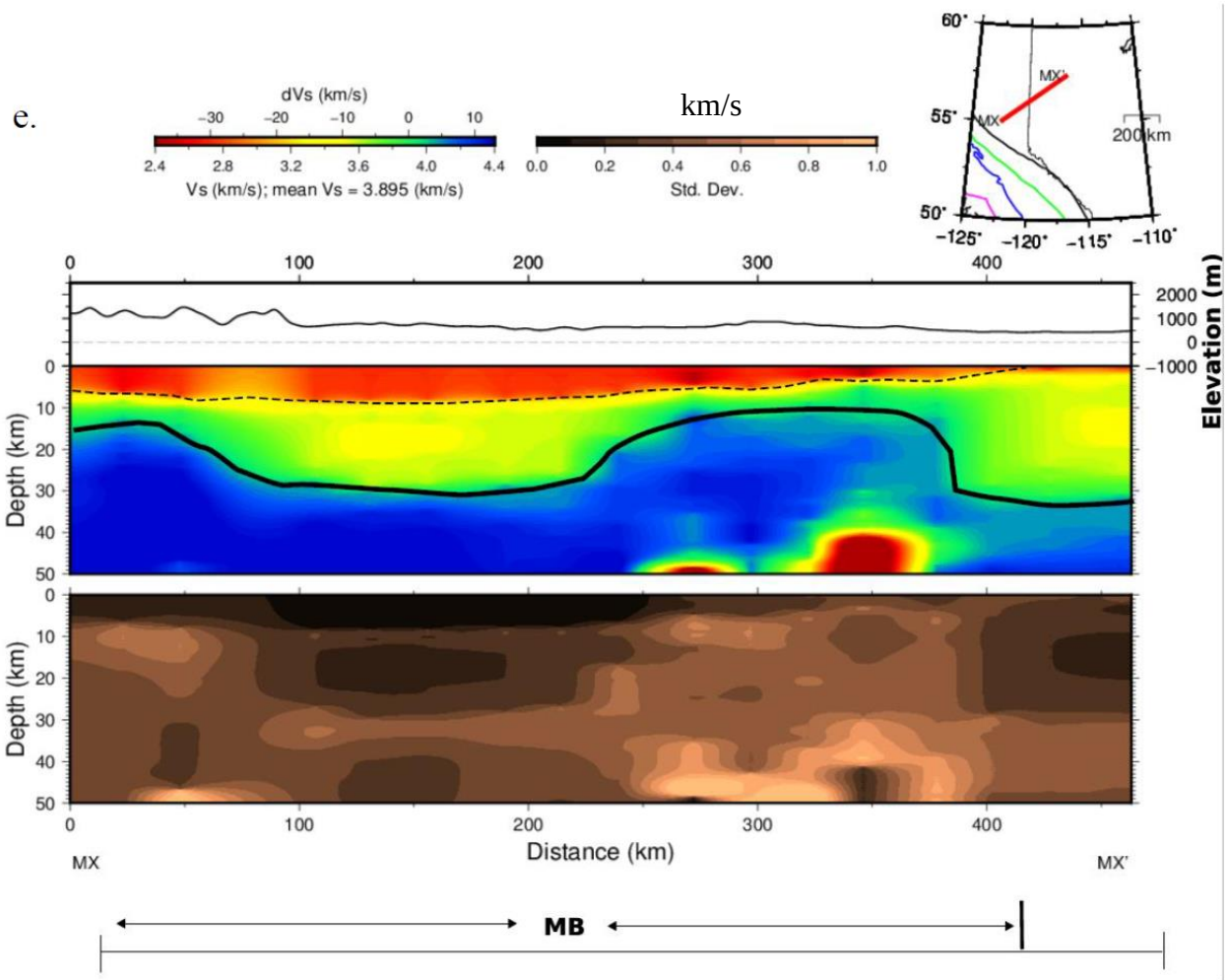

Figure 3.8 (continued).

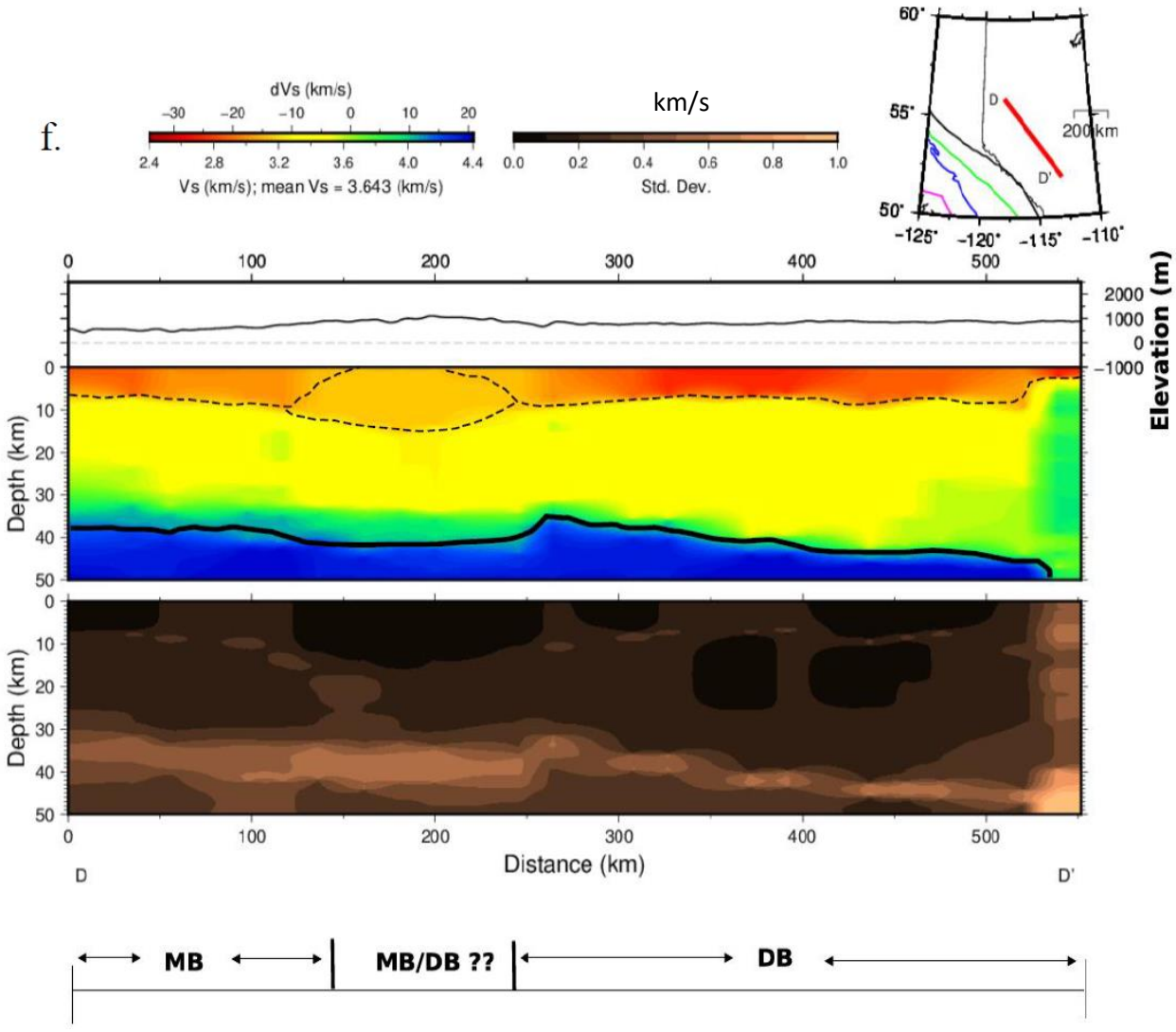

Figure 3.8 (continued).

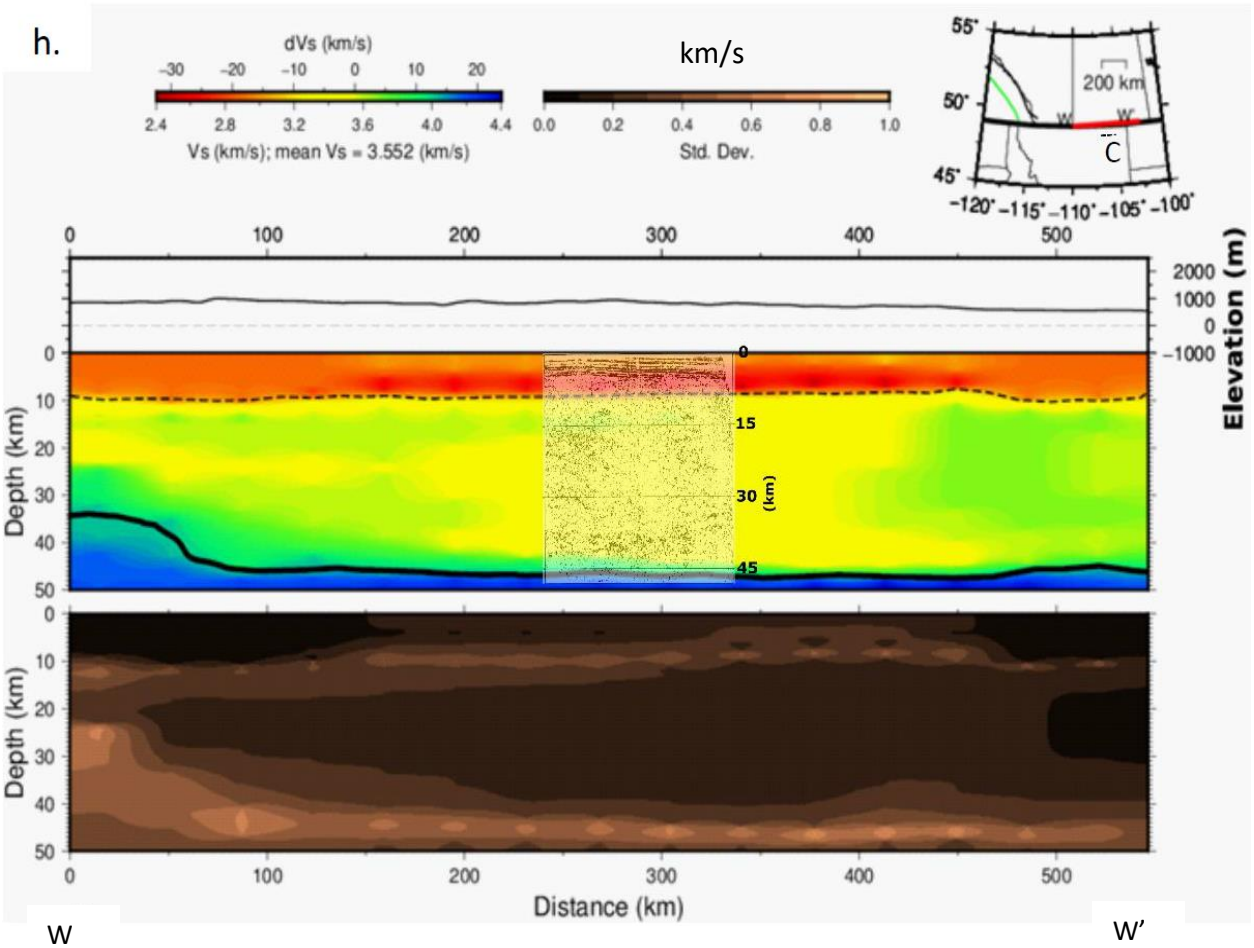

Figure 3.8 (continued).

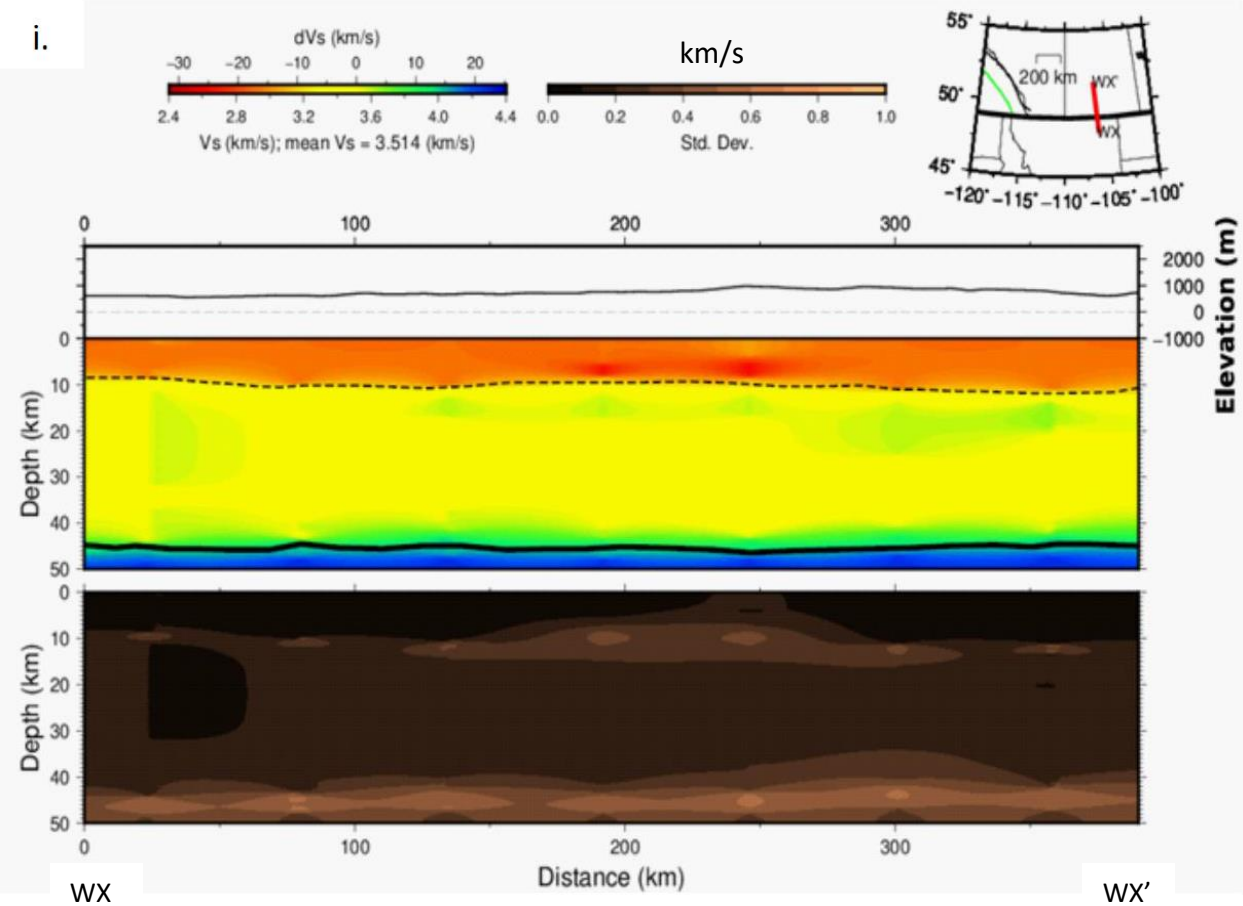

The low *Vs* anomalies in the upper 10 km along LH-LH' and LHX-LHX' correspond to sedimentary rocks of the Liard/Horn River basins deposited between Late Devonian and Jurassic (Figure 3.8b and c). These include the Besa assemblage and Muskwa formation of the Liard and Horn River basins, respectively (Gordey et al., 1991; Walsh et al., 2005). The results for the basins at shallow depths are well constrained as shown by the corresponding low uncertainty estimates. Uncertainties are observed to increase with depth along LHX-LHX (Figure 3.9c), especially in the SW edge and beneath the basin at the NE edge. The base of the sedimentary rocks has a maximum depth of ~10 km near the southern part of LH-LH' (Figure 3.9b). The thicker column of relatively low *Vs* (~3.05 km/s), overlain by a veneer of low *Vs* (at distances >300 km), corresponds to a deeper segment of the HRB's Paleozoic rocks. On LHX-LHX' (Figure 3.9b), the low-*Vs* structure thickens eastward into Northwest Territories (NWT). The Moho beneath LH-LH' is clearly constrained at ~34 and 42 km in the north and south, respectively, through a step-like drop near the distance of 100 km. Along LHX-LHX', the Moho depth is at 46 km in the southwest, but shallows beneath the thickest part of the basin (distance > 350 km), suggesting a severe extensional process in the basin history (Gordey et al., 1991; Wilson, 2019). In the absence of previous crustal-scale seismic studies in this area, we rely on the uncertainty estimates associated with the *Vs* results to constrain our interpretation. The shallow Moho at distances greater than 350 km along LHX-LHX' occurs at an area of relatively high uncertainty (~0.5 km/s), which could change the location of the Moho in that segment.

South of Horn River, cross-sections M-M' (Figure 3.8d) and MX-MX' (Figure 3.8e) image the Montney basin. Three distinct low-*Vs* sequences separated by crustal *Vs* are observed at shallow depths on M-M'. The first is a thin layer with a maximum depth of ~2 km, located in the distance range of 0 – 100 km near the northwestern edge of the M-M'. It is separated from the

main Montney basin and therefore probably belongs to the northern HRB. At distances between ~150 and 500 km, there is a thick layer of low-*Vs* anomaly with a maximum depth of ~10 km on both ends. This location is near the southeastern edge of M-M' and corresponds to the Duvernay/Alberta Deep basin. The Montney basin is ~10 km deep and located at the distance of ~200 – 400 km in the middle of M-M'. The edges of the basin are deeper, with maximum depths of ~12 and ~14 km at distances of 150 and ~530 km, respectively. Finally, a low-*Vs* anomaly that extends to >10 km depth is located at distances >600 km. At depth, an asymmetric dome-shaped high-*Vs* anomaly with the shallowest depth of ~20 km at the distance of ~210 km on the cross-section underlies the low *Vs* anomalies (Figure 3.8d). The top of the high *Vs* anomaly corresponds to the Moho discontinuity. It shallows to the depth of ~20 km beneath the northwestern edge of the basin and flattens toward the south (Figure 3.9c). The cross-section MX-MX' (Figure 3.8e) is characterized by a low-*Vs* anomaly in the uppermost ~10 km, which corresponds to the sedimentary basin. The basin is located at distances up to ~200 km but gradually tapers to the east. The top of the high *Vs* anomaly, which corresponds to the Moho discontinuity, is undulating but is the deepest (~33 km) at the easternmost edge of the cross-section. Two distinct low-*Vs* anomalies are observed at depth (>40 km) at the distance range between 250 and 400 km (Figure 3.8e). Mean *Vs* for the M-M' and MX-MX' cross-sections are 3.87 and 3.10 km/s, respectively, and uncertainty estimates are generally low and well constrained.

Cross-sections D-D' (Figure 3.8f) and DX-DX' (Figure 3.8g) image the Duvernay basin, and D-D' probably also images the southern part of the Montney Basin (Figure 3.8f). Low-*Vs* anomalies overlie the upper 10 km of the cross-section, with the two prominent segments separated by a less prominent one at the distance range between 150 and 250 km. A south-dipping layer of high-*Vs* anomaly is observed at the depths between 35 and 45 km. The mean *Vs* along D-D' is 3.74

km/s. In the E–W direction (DX-DX'), the top 10 km is dominated by low-*Vs* anomalies, with the less prominent anomaly near the western edge transitioning to a more prominent low-*Vs* anomaly at the distance of ~200 km that tapers eastward (Figure 3.8g). Beneath the low-*Vs* anomalies, crustal characteristics change to lower *Vs* at the distance of ~100 km and depths between 10 and 40 km. Transition to a west-dipping high-*Vs* anomaly occurs at the depth of ~42 km in the west and shallows to ~34 km in the east (Figure 3.9f). Mean *Vs* along D-D' and DX-DX' are 3.74 and 3.75 km/s, respectively, with low uncertainty estimates associated with both cross-sections.

The low *Vs* that overlies the upper 10 km in the southeastern segment of D-D' (distance > 230 km) correspond to the Duvernay basin (Figure 3.8d). The basin is filled with sediments deposited during a period of maximum flooding (Potma et al., 2001). The low-*Vs* structure continues to the north, in what could be the northwestern extension of the basin, a southeastern extension of the Montney or a part of the Alberta Deep basin. The low-*Vs* anomaly in the transition zone between the northwestern and southeastern segments reaches ~15-km depth but shallows toward the southeasternmost edge of D-D', where the underlying crust transitions to slightly higher *Vs*. At depth, transition to high *Vs* corresponds to the Moho, which appears gradational near the northwesternmost edge. The Moho depth is ~38 km near the northwestern edge and deepens to ~45 km in the southeast, but completely disappears at the southeastern-most edge where the crust thickens and the basin shallows. Along DX-DX' (Figure 3.9d), the maximum depth of the Duvernay basin is ~6 km at the distance of 200 – 250 km but appears to taper toward the northeastern where the Moho shallows accordingly. The low *Vs* in the southeastern segment likely corresponds to the Alberta Deep basin.

Finally, cross-sections W-W' and WX-WX' image the Williston basin in the E–W (Figure 3.8h) and N-S directions (Figure 3.8i), respectively. On both cross-sections, a prominent low-*Vs*

layer is observed within the upper 10 km but the *Vs* value transitions to the crustal range (3.2<*Vs* <3.7 km/s) at depths >10 km. On W-W', the *Vs* increase between 10 and 40 km in the middle segment appears to be very different from that toward the two ends. A transition to a high-*Vs* anomaly (*Vs* >4 km/s) occurs at the depth of ~35 km near the westernmost edge, but sharply drops to the depth of ~47 km at the distance of ~80 km along W-W'. Meanwhile for WX-WX', the transition to high-*Vs* anomaly occurs at the depth of ~47 km and remains flat across the cross-section. Mean *Vs* for W-W' and WX-WX' are 3.55 and 3.51 km/s, respectively, and both cross-sections are characterized by generally low uncertainty estimates, especially in the Williston basin.

To ground-truth the observations in the Williston basin, a nearby COCORP reflection seismic line (location marked "C" in Figure 3.8h) with an E–W orientation is overlain at the same scale on the corresponding segment of the W-W' cross-section. Strong reflections, which are horizontally aligned within the upper crust, are truncated at the depth of ~10 km, coinciding with the base of the low-*Vs* layer on W-W'. On both cross-sections, the shallow low *Vs* in the upper 10 km corresponds to the Paleozoic sediments, of which the Ordovician and Silurian strata of the plains are best preserved (Wright et al., 1994). This is consistent with previous studies (e.g. Anna et al, 2013), which estimated depths in parts of the basin to be in excess of 5 km. The sub-basin crust extends to the depths of 35 and 45 km near the western and eastern edge of W-W' respectively (Figure 3.8h). Meanwhile, strong sub-horizontal reflections are observed in the depth range of 35 – 45 km on the COCORP line. Transition to the high-*Vs* layer on W-W' coincides remarkably well with the base of the reflections and is thus interpreted as the Moho. This interpretation is consistent with previous studies (e.g. Latham et al., 1988; Morel-A-L'Huissier et al., 1987). A stepwise increase in the Moho depths from 35 to 45 km occurs at the distance of ~50 km on W-W', resulting

in an eastwardly thicker crust (Figure 3.8h). The Moho geometry along WX-WX' is flat at the depth of ~45 km in the N-S direction (Figure 3.8i).

3.2.6 Implication and Discussion

The westward growth of the ancestral North American continent involved multiple episodes of rifting, collision and accretion of exotic terranes near both the eastern and western edges. Present-day western Canada is formed by the accretion of Intermontane and Insular superterranes with suture zones at the Omineca and Coast Mountain belts respectively. These events led to the formation of sedimentary basins within, and variation of crustal thickness between, the terranes.

3.2.6.1 Structure of the Sedimentary Basins

The major sedimentary basins in western Canada, originally derived through geological mapping, are well constrained by our results (Figure 3.9). In the Insular terrane, our results beneath the GB correspond well with previous studies (England & Bustin, 1998; Zelt et al., 2001). We show that the basin is characterized by slightly higher *Vs* and a shallower sedimentary basement in the north than in the south, an observation consistent with the results of Zelt et al. (2001). The overall basin thickness is shown to be ~6 km, which is also consistent with previous studies. In contrast, the QCB shows a variable maximum depth of 7 – 10 km to the sedimentary basement. This is in agreement with previous studies based on seismic reflection and refraction methods (Hole et al., 1993; Rohr & Dietrich, 1990; Rohr & Dietrich, 1992; Spence & Asudeh, 1993). This basin depth makes the QCB one of the thickest basins in western Canada (Figure 3.9). We observe that the basin is shallower towards the southern tip of Alaska and thins out just north of VI. In addition to this, our *Vs* range corresponds to the *Vp* range reported by these studies when converted using a nominal *Vp/Vs* of 1.7 (Poisson's ratio = 0.25). Crustal thinning, such as is observed on the

flanks of Q-Q', supports the extensional history of the basin (Rohr & Dietrich, 1992; Spence & Asudeh, 1993; Yuan et al., 1992). The thicker crust in the middle of Q-Q', beneath the thickest sediments, and along QX-QX', may not be indicative of an extensional regime. The fault-block tectonic model (Lyatsky, 1993, 2006; Lyatsky & Haggart, 1993) however, does not necessarily require a thin crust and may thus be supported by the observation of thicker crusts along our QCB cross-sections.

The maximum depth of sedimentary basins within the IMB is moderate when compared with major basins in western Canada (Figure 3.9). The composite basin originates from the Cordillera accretion of the Intermontane superterrane (Calvert et al., 2011; Gabrielse & Yorath, 1991; Idowu et al., 2011; Stephenson et al., 2011). Smaller basins which form the northern extension of the IMB (e.g., the Whitehorse Trough) are also clearly expressed in northern BC and Yukon. Variable basin thickness of up to 6 km recorded for the BSB agrees well with previous studies (Cook et al., 2004; Evenchick et al., 2005; Welford et al., 2001). The basement depth is ~7 km at the center of the NB and thins to ~3 km to the south. This trend is also consistent with previous studies (Idowu et al., 2011; Stephenson et al., 2011).

In the WSCB, thick sediments are observed in the Liard/Horn River basin to the north, Duvernay, Montney and Alberta Deep basin in the middle, and the Williston basin to the south. The thickest sedimentary rocks occur in the Alberta Deep Basin, within which the largest oil field in Canada is located (Nielsen & Porter, 1984). The basin location and geometry marked by the dashed lines on Figure 3.9 are mostly derived through geological mapping.

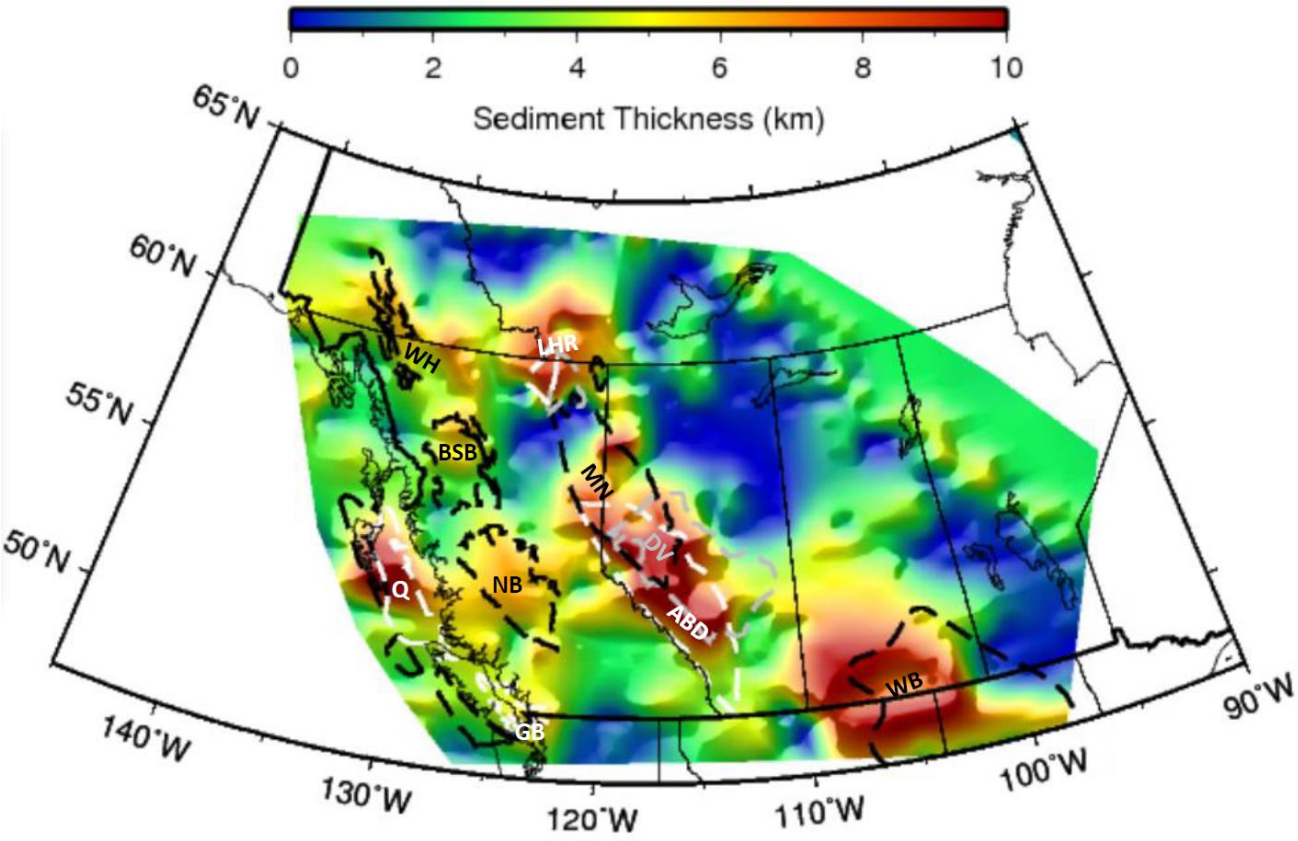

Figure 3. 9 3-D sediment thickness across western Canada. Thick sediments (red color) are shown to approximately correspond to locations of major sedimentary basins in western Canada, while locations with no sediments are shown in blue color. Lines: Locations of deep sedimentary basins derived through geological mapping are marked with dashed lines as: ABD – Alberta Deep Basin (white), WB – Williston Basin (black); Q – Queen Charlotte Basin (white); WH – White Horse Trough (black); BSB – Bowser/Sustut Basin (black); NB – Nechako Basin (black); DV – Duvernay Basin (gray); MN – Montney Basin (black); LHR – Liard/Horn River Basins (Liard – white, HR – gray); GB – Georgia Basin (white). Variation in dashed line colors are to show contrast with the background.

3.2.6.2 Characteristics of the Crust-Mantle Transition

Earlier studies represented the transition between the crust and mantle as an interface marked by a large velocity change (referred to as the Moho discontinuity*;* Mohorovicic, 1910). It has been shown that, for a given location, the Moho depth may vary depending on the adopted method of imaging (Cook et al., 2010). As a result, it is not uncommon to have prefixes attached to the term Moho – e.g. reflection-, refraction-, electric-Moho (Cook et al., 2010; Kao et al., 2013). ANT-derived Moho uses *Vs* derived from surface wave dispersion to constrain the depth. For example, Kao et al. (2013) showed that the crust-mantle transition varies in sharpness depending on the location within Canada. They further presented a novel method to characterize the transition and reasonably define the Moho based on the vertical *Vs* gradient. The actual Moho depth may be a boundary at the base of the crust, top of the mantle or may lie in-between (Figure 3.10).

Following their reasoning, we developed a Graphical User Interface (GUI) for picking the depths $Z_{0\%}$ and $Z_{100\%}$ corresponding to the base of the crust and the top of the mantle respectively (Figure 3.11). The *Vs* values $Vs_{0\%}$ and $Vs_{100\%}$, which are respectively associated with the base of the crust and the top of the mantle, are presented in Figure 3.12. The base of the crust is the deepest depth which marks either a sharp or gradational *Vs* increase to typical upper mantle velocities (4.13 – 4.55 km/s). The *Vs* values $Vs_{0\%}$ and $Vs_{100\%}$ for all the grids were selected using the GUI and they specifically correspond to depths $Z_{0\%}$ and $Z_{100\%}$, representing the depths where the *Vs* begins to increase ($Vs_{0\%}$) and the end of the *Vs* increase ($Vs_{100\%}$) respectively.

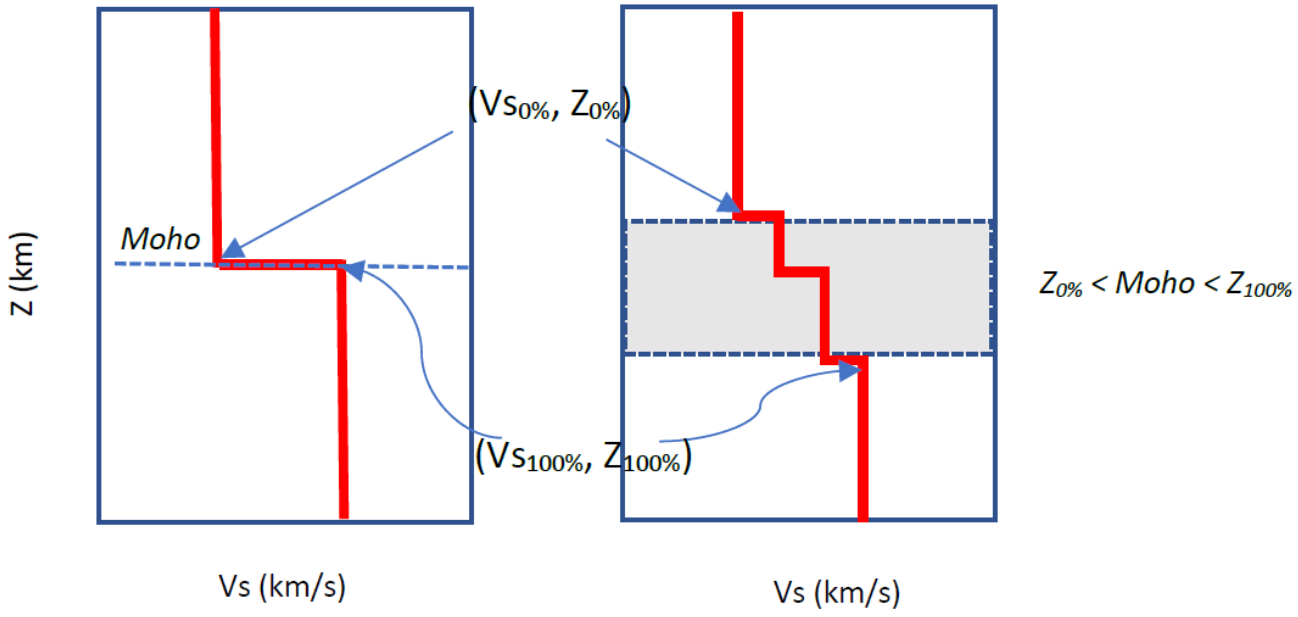

Figure 3. 10 Cartoon illustration of two velocity models showing the types of crust-mantle boundaries referenced in the text, Z and Vs are depth and velocity. Left panel indicates a sharp transition and Z0% = Z100%. The right panel shows gradational transition to the top of the mantle, where the Moho could lie anywhere within the shaded rectangle.

a.

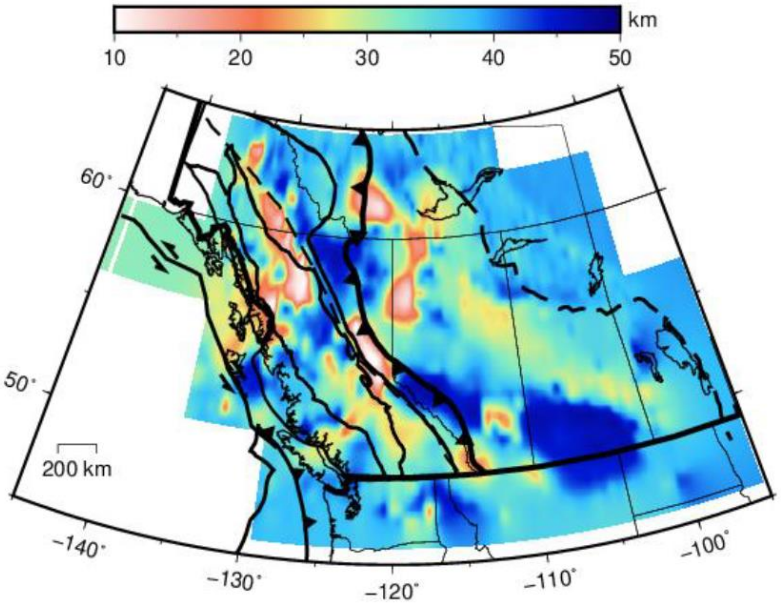

b.

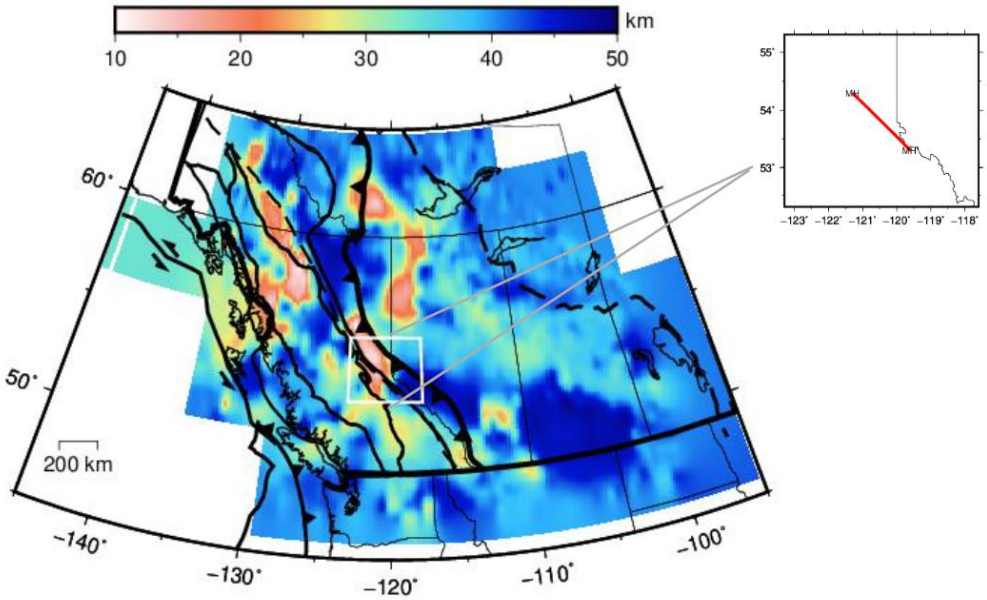

Figure 3. 11 Depth variation at (a) the base of the crust (referenced in the text as $Z_{0\%}$) and (b) the top of the mantle (referenced in the text as $Z_{100\%}$). The deepest depths lie near the Williston basin and parts of the cordillera deformation front. The inset marked by the white box is the location of line MH-MH' referenced in the text to show Moho depths and uncertainty.

$Z_{0\%}$ and $Z_{100\%}$ are both deepest beneath the Williston Basin and parts of the cordillera deformation front (Figure 3.11). Morel-à-l'Huissier et al. (1987) presented Moho depth estimates of 41 – 48 km and suggested a complex process in the lowermost crust beneath the center of the Williston Basin. This may be related to the phase change from gabbro to eclogite hinted at earlier by Fowler and Nisbet (1985) as the mechanism for the Phanerozoic basin subsidence. $Vs_{0\%}$ and $Vs_{100\%}$ vary as expected; they are generally higher near the edge of the exposed craton and the Platform, lower within the Platform and varying beneath the Cordillera (Figure 3.11). $Vs_{0\%}$ observed beneath the center of the Williston Basin is lower than the surrounding parts of the basin and may indicate a concentration of the complex phase change process (Fowler and Nisbet, 1985) in the middle of the basin (Figure 3.12a).

The depth (ΔZ) and velocity (ΔVs) changes from the base of the crust to the top of the mantle are presented in Figures 3.13. In most places, transition from $Z_{0\%}$ to $Z_{100\%}$ occurs over a depth range that is < 10% of $Z_{0\%}$ (blue color), except at specific locations, in the northern Cordillera, southern Alberta and near the eastern edge of the Platform bordering the exposed craton, where the transition depth is in excess of 20% of $Z_{0\%}$ (red color). Similarly, transition from $Vs_{0\%}$ to $Vs_{100\%}$ requires an increase of >10% of $Vs_{0\%}$ in most places. Prominent increases corresponding to >25% of $Vs_{0\%}$ occur at the edge of the craton, Williston basin and locations within the Cordillera. There is a higher spatial correlation between $Z_{100\%}$ (Figure 3.11b) and $Vs_{100\%}$ (Figure 3.12b) than between $Z_{0\%}$ (Figure 3.11a) and $Vs_{0\%}$ (Figure 3.12a)

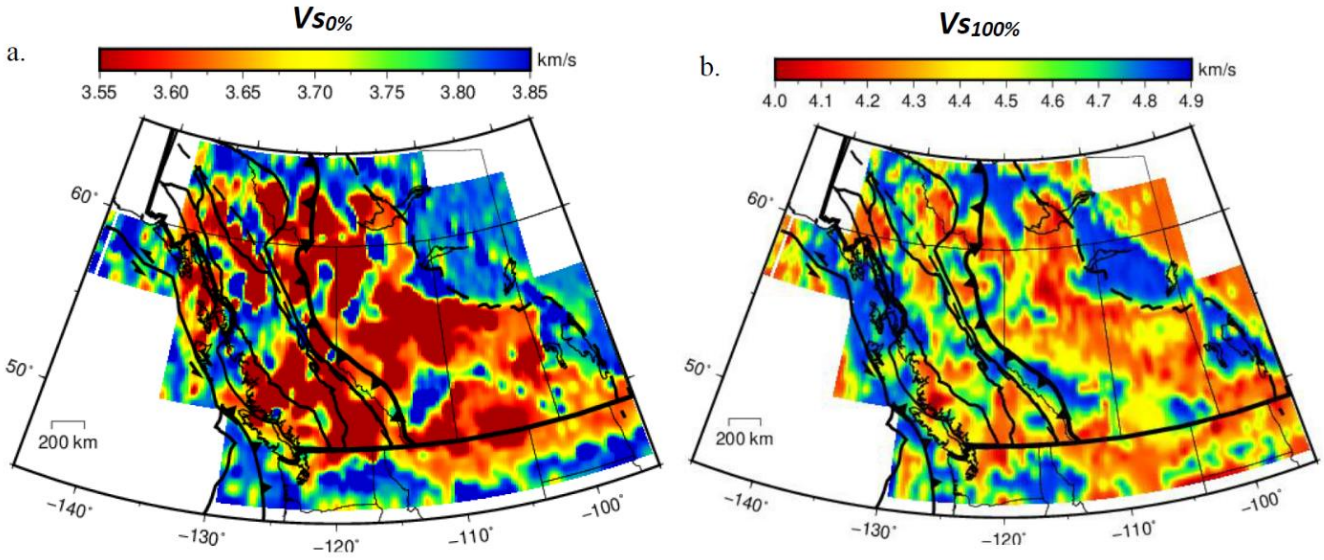

Figure 3. 12 Distribution of *Vs* at: (a) the base of the crust (referenced in the text as $V_{0\%}$); (b) the top of the mantle (referenced as $V_{100\%}$). *Vs* values are predominantly higher beneath the craton and lower beneath the Platform. The low *Vs* at the eastern edge of the Platform approximately follows the craton-Platform boundary.

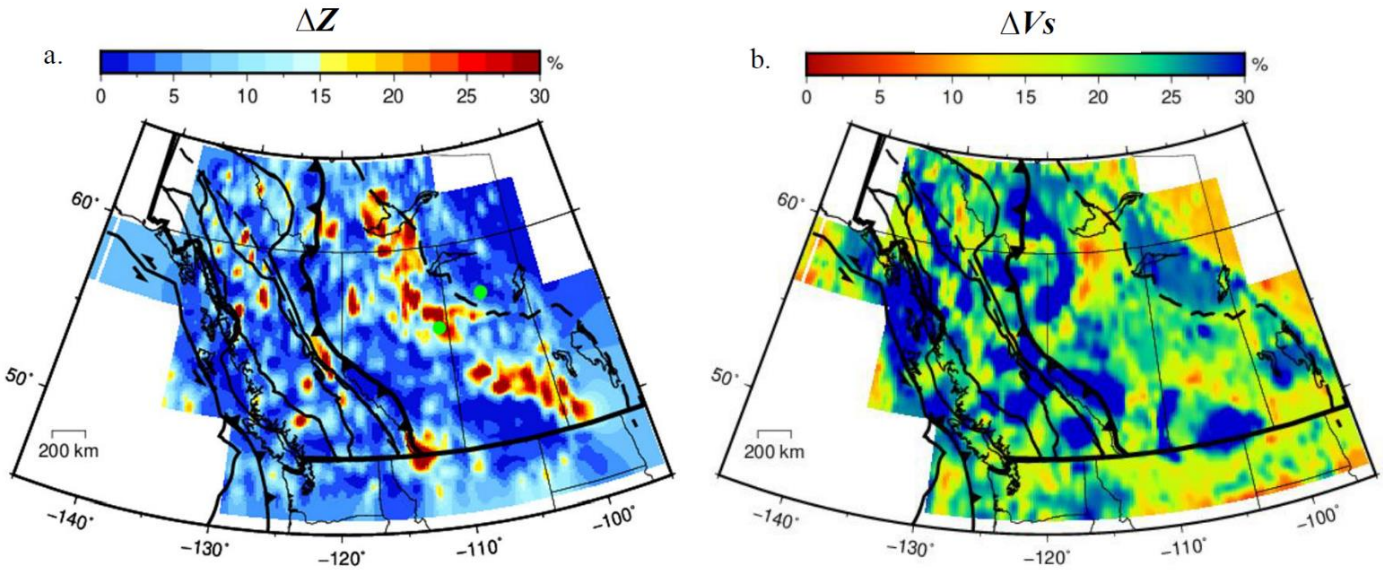

Figure 3. 13 Percentage change of depth (a) and *Vs* (b) from the base of the crust to the top of the mantle. A band of large change near the eastern edge of the platform indicates a zone where the crust-mantle transition occurs over a broad depth range. The two green dots located within the band on the Platform and on the craton indicate locations where 1-D *Vs* models are drawn to further analyze the feature.

3.2.6.3 Comparison with Existing Crustal Models

We compare our results with two published models of crustal thickness: Z_c (Figure 3.14) from CRUST1.0 (Laske et al., 2013), and Z_{k50} and Z_{k85} (defined as the intermediate depths between Z_0 and Z_{100} where the *Vs* change reaches 50% and 85%, respectively, Figure 3.15a-d) obtained from a Canada-wide ANT study (Kao et al., 2013). CRUST1.0 is a global model derived from a variety of datasets including active seismic, teleseismic, and gravity (for places where seismic constraints are unavailable). Both models have a 1^ox1^o resolution but are resampled to a finer grid in order to compare with our results.

For the CRUST1.0 model, we define the variance functions ΔZ_{0c} and ΔZ_{100c} as the differences between our results and Z_c (i.e., $\Delta Z_{0c} = Z_{0\%} - Z_c$ and $\Delta Z_{100c} = Z_{100\%} - Z_c$). In most places within our study region, both ΔZ_{0c} and ΔZ_{100c} are within the range of ±7.5 km, (colors yellow – cyan; Figure 3.14b and c), with Z_c observed to be generally larger over the Platform than both $Z_{0\%}$ and $Z_{100\%}$. The relative variation of ΔZ_{0c} and ΔZ_{100c} within the Cordillera depends on the location, however $|\Delta Z_{0c}|$ is larger than $|\Delta Z_{100c}|$ in most places.

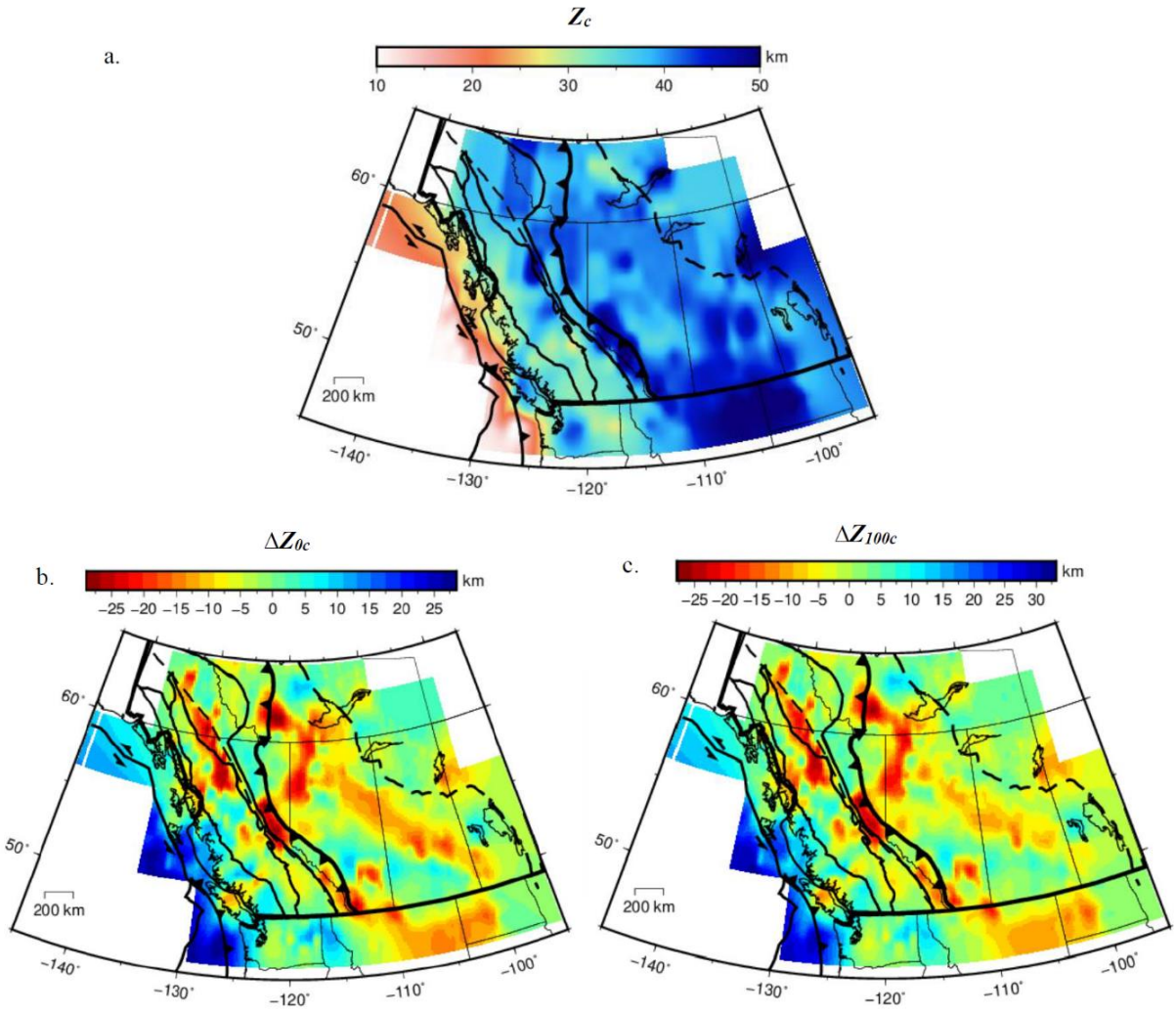

Figure 3. 14 Plot of CRUST1.0 Moho depths for western Canada (a) showing, deep Moho mostly beneath the Platform and predominantly shallower Moho beneath the Cordillera. The diffrence between CRUST1.0 Moho depths and depths to the base of the crust (b) and the top of the mantle (c) from this study.

In comparing our results to Z_{k50} and Z_{k85}, we define the variance functions $\Delta Z1$ and $\Delta Z2$ as follows:

$\Delta Z1 = Z_0 - Z_{k50}$ and

$\Delta Z2 = Z_{100} - Z_{k85}$

We compare $Z_{0\%}$ with Z_{k50} since Z_{k50} is the shallowest crust-mantle transition depth limit published by Kao et al., 2013. A similar reasoning applies to the comparison of $Z_{100\%}$ with Z_{k85}. Qualitatively, the patterns observed with $\Delta Z1$ and $\Delta Z2$ (Figure 3.15d) are similar to those of the ΔZ_{0c} and ΔZ_{100c} presented earlier (3.14c). Quantitatively, the variations are more dramatic with ΔZ_{100k} especially near the Williston basin and the Platform-craton boundary. Large (>10 km) variances (red color) which align with parts of the deformation front and the RMT emerge from the comparison of our results with both the CRUST1.0 and Kao et al. (2013) crustal models. These differences occur near the location of our cross-sections NB, NBX, BS and BSX. A possible explanation for the large differences is the mid-lower crustal high-*Vs* values observed along the cross-sections extend to these areas and presumably represent the extension of the NA craton buried beneath the cordillera terranes. It is also possible that the large depths are the result of large uncertainties arising from the complexity of the structure. If the former were the case, then the crust-mantle transition in the area may lie at or near the depths derived from the alternative interpretation of Figure 3.7a and b (white dashed lines). In this case, the variance falls within the nominal range ±7.5 km. Although there is no uncertainty estimation associated with the CRUST1.0 and Kao et al. models, a comparison of both models (Z_{k50} - Z_c; Figure 3.15c) shows relatively large variations at similar locations as we observe in the comparisons with our model. This is consistent with the relatively large uncertainties we obtained in our result and may be a further indication that the structures at those locations are indeed complex. To further analyze this, we draw a NW-SE *Vs* cross-section

with the corresponding uncertainties crossing a segment of the area with shallow high-*Vs* values toward the areas with the thickest crust (Figure 3.16). Relatively larger uncertainties (~0.5 km/s) are observed to coincide with the shallow high-*Vs* structure at distances up to ~76 km, with the uncertainty increasing with depth.

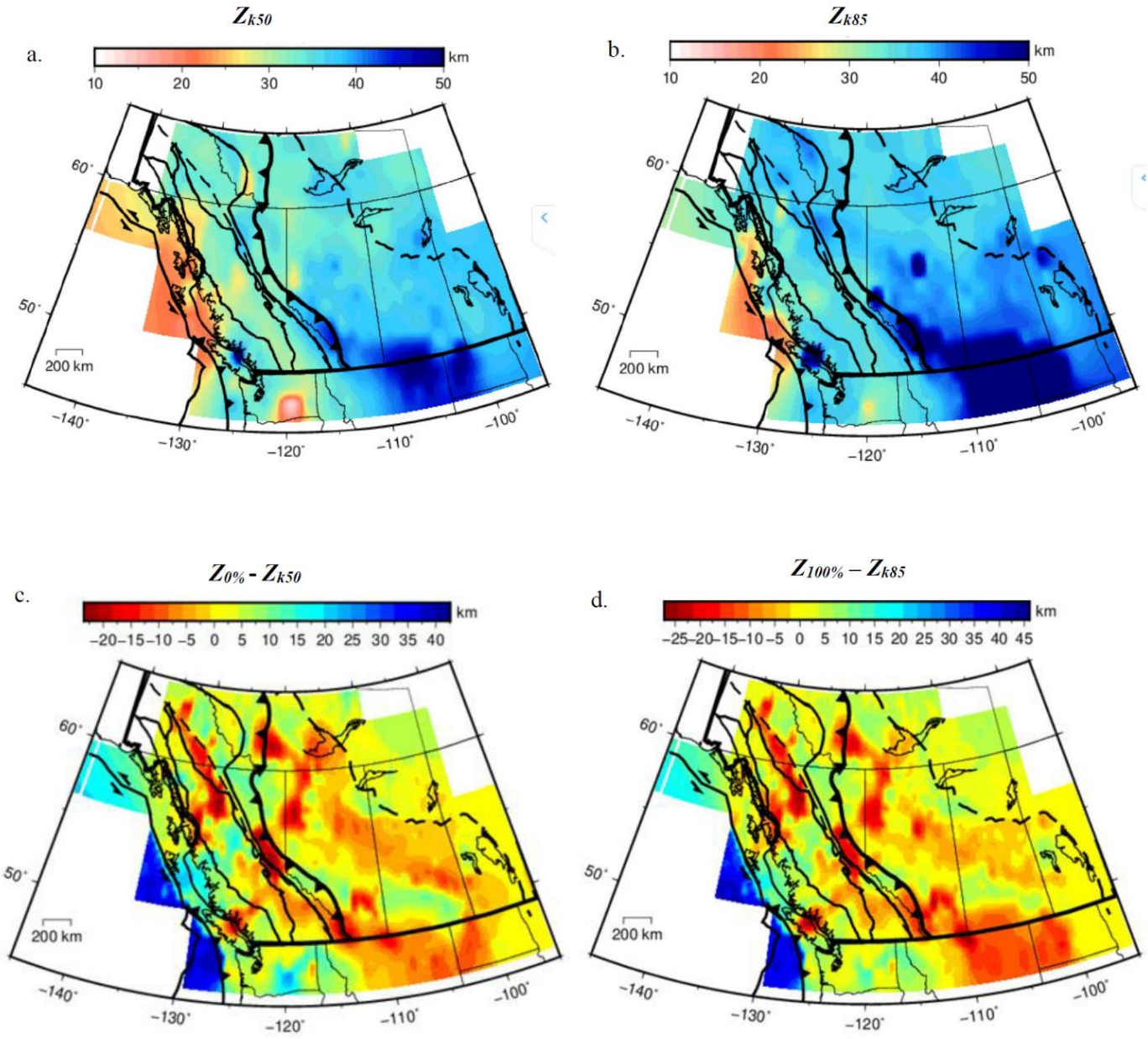

Figure 3. 15 Intermediate depths between base of the crust and the top of the mantle where the *Vs* change reaches (a) 50% (or Z_{k50}) and (b) 85% (or Z_{k85}) from Kao et al., 2013 model. Z_{k50} is compared with $Z_{0\%}$ (c), while Z_{k85} is compared with $Z_{100\%}$ (d). Finally, for a proper context in our comparisons, we compare Z_{k50} to Z_c from CRUST1.0 (e).

Figure 3.15 (continued).

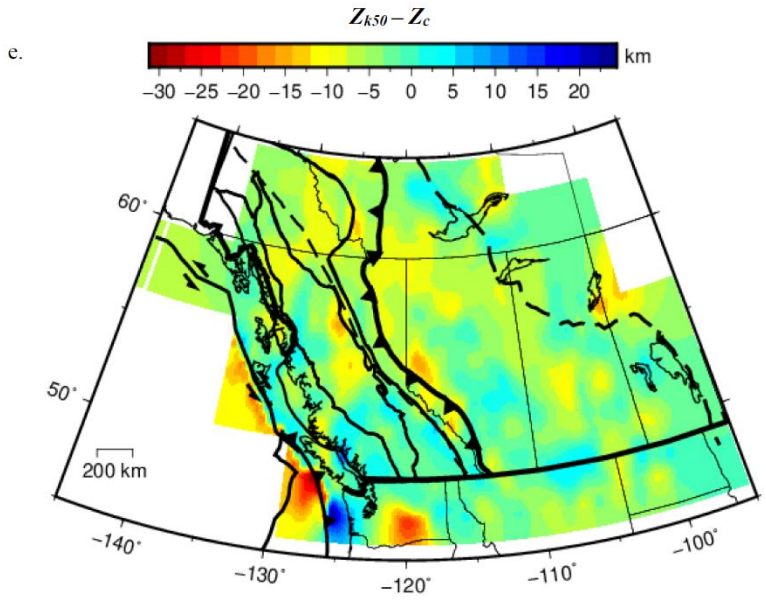

Another significant feature observed in comparing our results with the other models is the large depth variance observed for the crust-mantle transition immediately west of the craton-Platform boundary (Figure 3.13a). The feature is located in an area where the crust is thinner and the *Vs* at the top of the mantle is lower, relative to the surrounding (Figure 3.11 and 3.12b). The shape of the feature follows the curvature of the boundary. We draw two 1-D *Vs* models, one taken over the Platform (at the location of the feature) and the other over the craton (Figure 3.17). The 1-D models show a gradual crust-mantle transition from ~26 km to ~37 km near the eastern edge of the Platform, and a sharp crust-mantle transition from ~39 km to ~41 km near the western edge of the craton. The uncertainty estimates are reasonable for both models suggesting the feature could be real. Further investigation of this feature with adequate data constraint is an interesting future work. Based on the comparisons presented above, our results of crust-mantle transition depths are generally robust, except for the areas shaded on Figure 3.18 which are probably not well constrained due to structural complexity associated with proximal geological boundaries.

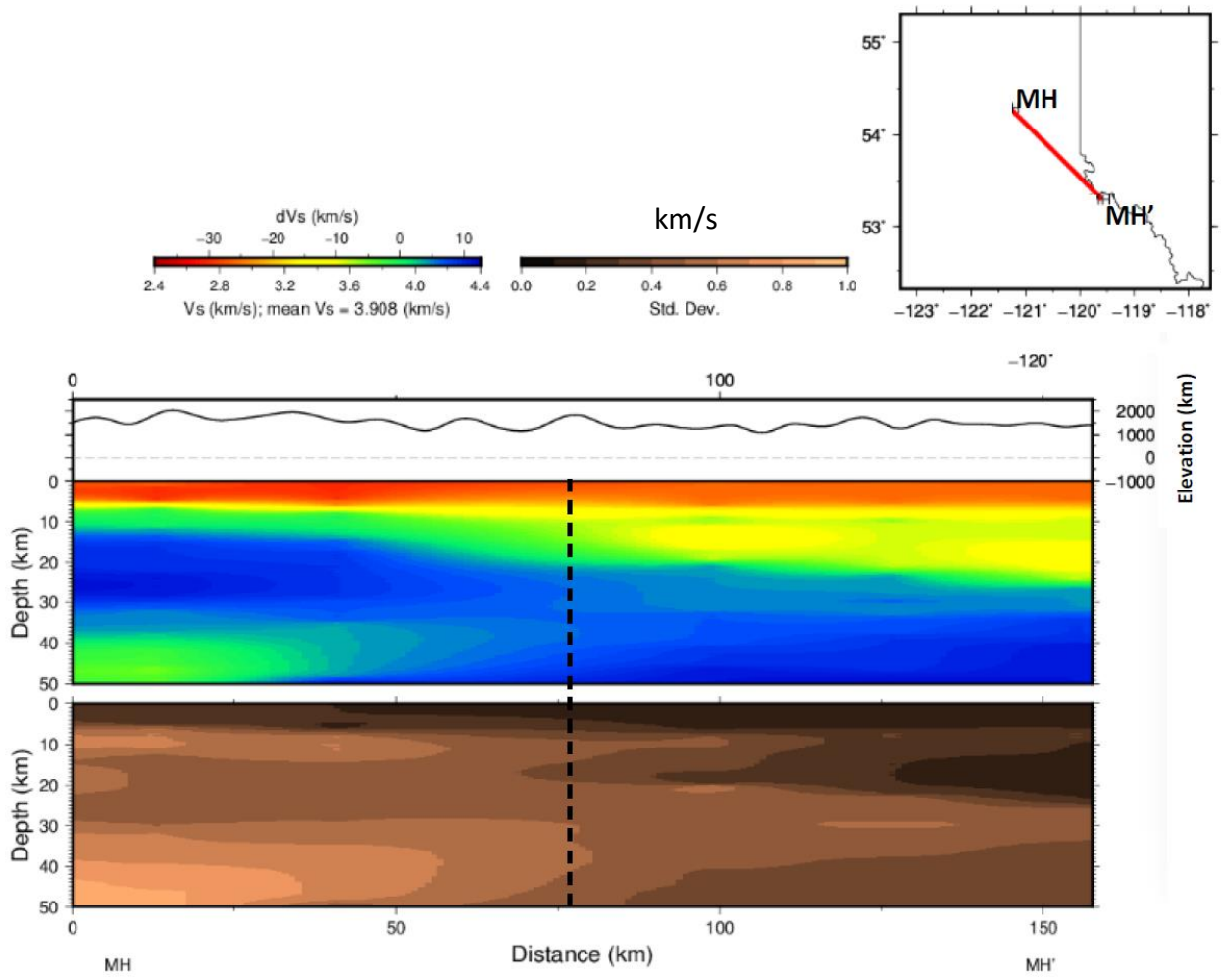

Figure 3. 16 *Vs* and uncertainty estimates across a segment of the shallow high-*Vs* structure (location shown in the inset and on Figure 3.12b). The top of the high-*Vs* structure dips in the SE direction, toward the thick crust (as shown in Figure 3.12b). At distances < 76 km (bounded by the black dashed line), the uncertainty becomes larger with depth.

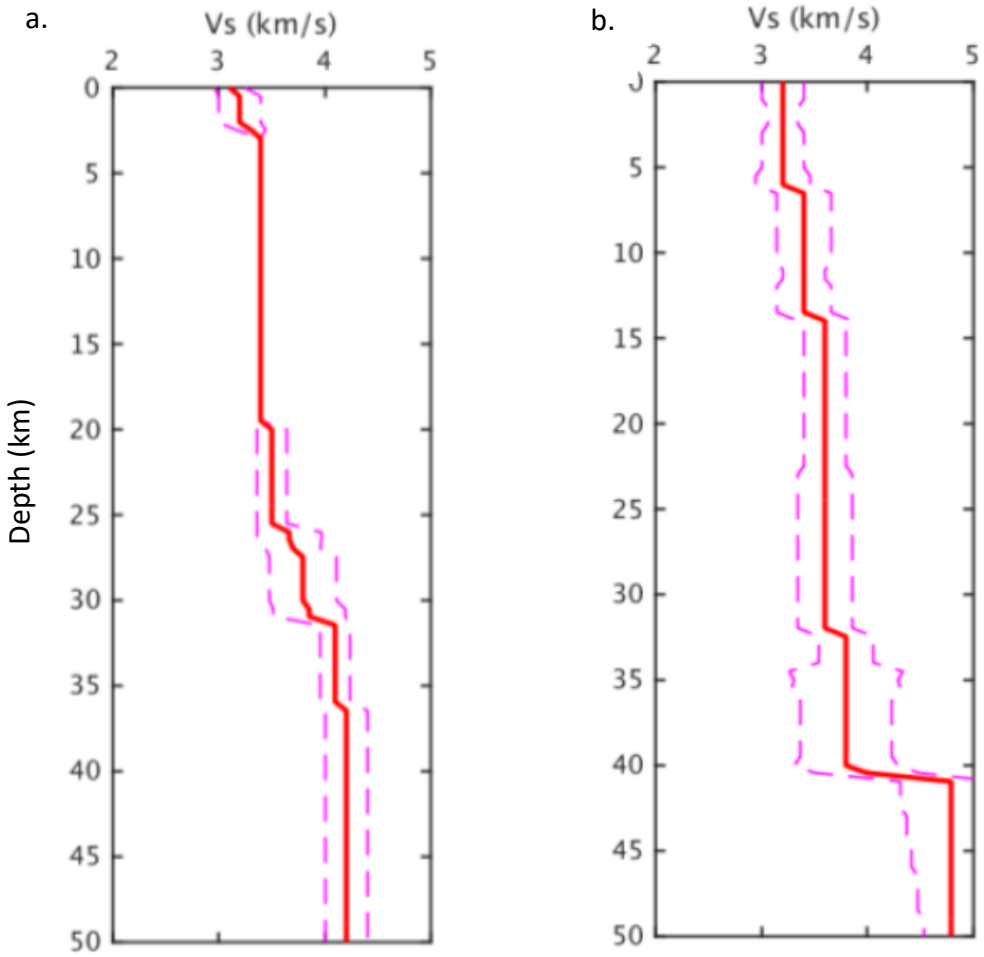

Figure 3. 17 1-D *Vs* model (solid red line) and associated uncertainty estimates (dashed magenta line) drawn near the eastern edge of the Platform (a) and the western edge of the craton (b). The location of both models are shown on Figure 3.12a. Transition from the base of the crust to the top of the mantle occurs gradually at depths from ~26 km to ~37 km on (a) and sharply on (b) at depths from ~39 km to ~41 km.

a

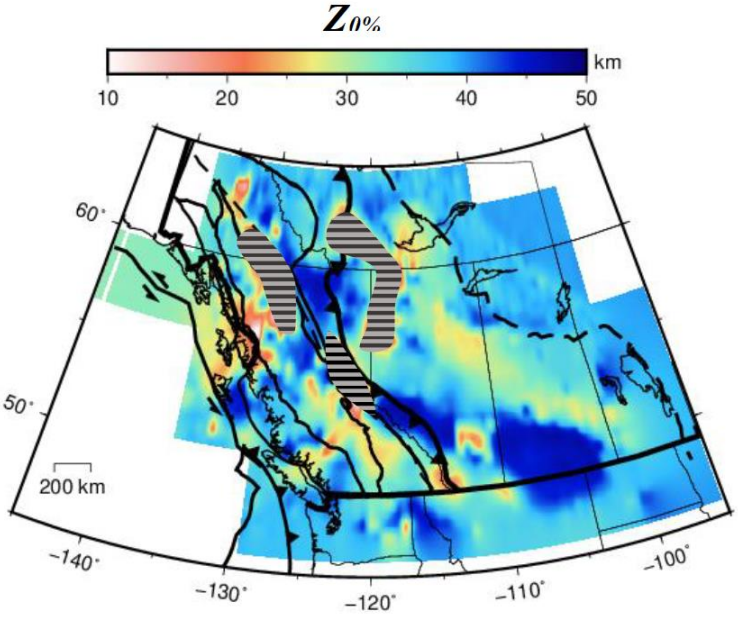

b.

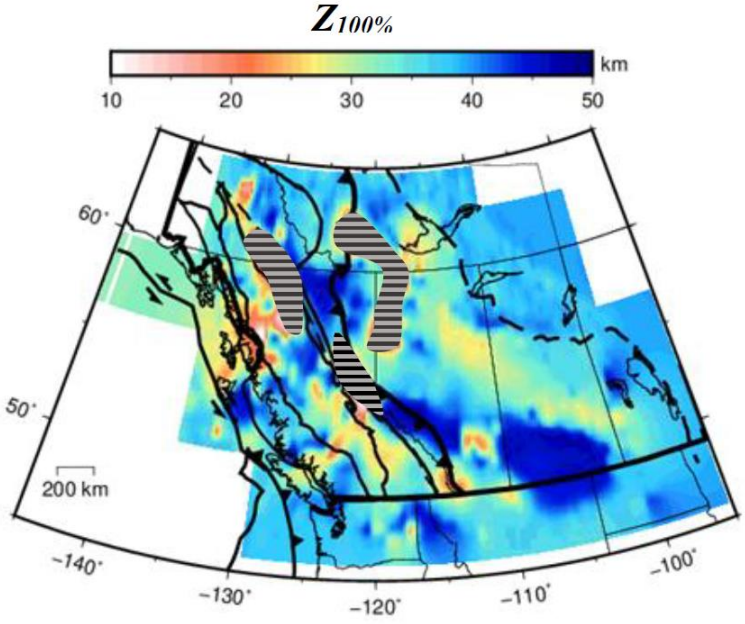

Figure 3. 18 Depths to the base of the crust (a) and the top of the mantle (b), similar to Figure 3.11, however, areas with unreliable estimates are covered by the gray and black dashed masks.

3.2.7 Summary and Conclusions

In this study, we present a comprehensive 3-D *Vs* model for western Canada with associated uncertainty estimates obtained by processing a total of 13 years of ambient seismic noise data recorded by 151 seismic stations in and adjacent to western Canada. The geometry of the major sedimentary basins in western Canada as well as the 3-D variations in the Moho beneath them are inferred from the results. The major results are summarized below:

1. The offshore basins imaged in this study are Queen Charlotte Basin (QCB) and Georgia Basin (GB). The basin depths vary to a maximum of 6 and 10 km beneath the GB and QCB respectively. Moho depths vary from 23 – 44 km respectively beneath the QCB, and 22 – 42 km beneath the GB, along our chosen cross-sections.

2. Within the Intermontane belt, the maximum basin depth of sediments is 7.5 and 7 km for Nechako and Bowser/Sustut basins respectively. A deeper but less prominent low *Vs* structure, possibly consisting of intercalated sediments and volcanics, lie at the southern edge of the basin.

3. Although Moho depths are contrained by the 1-D *Vs* models at specific locations in the north and south of the Intermontane and Omineca belts, they appear to be unreliable along some of our cross-sections. Large uncertainties associated with the *Vs* values at depth beneath the cross-section may be associated with structure complexity at the edge of an underthrust cratonic basement (Ross, 1991; Carr and Brown, 1990).

4. In the WCSB, the maximum basin depth for the Alberta basins is well in excess of 6 km and can be found immediately west of Montney and Duvernay basins, probably within the Alberta Deep Basin. Detailed stratigraphic analysis will provide further details of the

corresponding formations at depth. At depth, the Moho is observed to have a general southwest-ward dip, except for local variations beneath Montney basin.

5. The thickest sediments estimated in this study are found beneath QCB, Williston basin and the Alberta basins.

6. The deepest Moho estimated in this study underlies the Williston basin, parts of the QCB, Alberta Deep Basin, and northern BC.

7. Velocity at the base of the crust is the lowest at the center of the Williston basin.

8. A zone of low uppermost mantle velocity is located near the eastern edge of the Platform (immediately west of the craton-Platform boundary). The zone is also characterized by a broad crust-mantle transition zone.

3.2.8 Acknowledgements

We benefited from discussions with Dr. Roy D Hyndman (Emeritus). Heat flow measurements from previous research work were provided by Dr. Jacek Majorowicz. This research is partly supported by the Induced Seismicity Research Project of Natural Resources Canada (NRCan), Natural Sciences and Engineering Research Council (NSERC) of Canada grants to H. K., Seismic data were obtained from Canadian National Seismic Network (http://www.earthquakescanada.nrcan.gc.ca/stndon/CNSN-RNSC/stnbook-cahierstn/index-en.php) and Incorporated Research Institution for Seismology (IRIS; http://ds.iris.edu/mda) data centers. Most of the figures were plotted by the Generic Mapping Tools (GMT).

3.3 Supplemental Materials

1. ***Preambles:***

   Time for project planning and requirement gathering: 1 month

2. ***Data:***

   Minimum number of days of data: 180

   Date range: 2003: 2016

   Effective number of years: 3

   Full day SAC size: 14 MB

   Total daily file size for 151 stations: 2.31 TB

3. ***Cross-correlation Processing (From Data Download to Stacking):***

   No of station pairs: 11,250

   Total number of daily paired SAC files: 12,318,750

   Cross correlation processing time: 5,133 hours (~7 months)

   - *40 nodes (parallel processing)*
   - *1 minute/pair (multi-threaded)*

   Size per file: 1.4 MB

   Total file size: 17 TB

   Total no of stacked/symmetrized file: 5,246

   Total size of symmetric file: 7.3 KB

4. ***Dispersion Measurement and Surface Wave Tomography:***

   Dispersion (FTAN): 5 min/pair x 5246 pairs = ~437 hours (~18 days)

   Step 1 (inversion) and step 2 (resolution test): ~20 days

5. ***TransD Inversion Processing:***

   Total number of grids: 5,246

   Number of samples drawn per grid: 500,000

   Total number of samples: 2.62 billion

   Inversion time: >2 months

   Time to process raw results into plots: variable (continuous processing until final plots are acceptable)

6. ***Time for 2D and 3D Imaging***

   - *Variable (continuous processing until the selected models were achieved) – several months.*

Steps 2 – 4 were done thrice and step 5 was done twice due to multiple failures of the storage drives.

Chapter 4. Combining Measurements from Ambient Seismic Noise with Earthquake Datasets for Imaging Crustal and Mantle Structures

4.1 Article Information

4.1.1 Author and Coauthor Contributions

The article presented in this Chapter will be submitted for publication. The author of this dissertation, APK, carried out the data preprocessing and cross-correlations, signal-to-noise ratio analysis and ambient noise dispersion measurements. APK wrote the manuscript under the supervision of HK. The research was jointly designed by APK and HK. FD provided the earthquake dispersion measurements. JFC and GS contributed to the writing style and pre-submission reviews. All coauthors contributed to the thorough review of the manuscript before submission.

4.1.2 Citation

Ayodeji Paul Kuponiyi[1, 2*], Honn Kao[1, 2], John F. Cassidy[1,2], Fiona Darbyshire[3] and George Spence[1], Construction of Broadband Dispersion Curves by Reconciling Ambient Seismic Noise and Earthquake Surface Wave Data, manuscript in preparation.

4.1.3 Author's Names and Affiliations

Ayodeji Paul Kuponiyi[1, 2*], Honn Kao[1, 2], John F. Cassidy[1,2], Fiona Darbyshire[3] and George Spence[1]

[1]School of Earth and Ocean Sciences, University of Victoria, Victoria, BC V8P 5C2, Canada
[2]Geological Survey of Canada, Pacific Geoscience Centre, Sidney, BC V8L 4B2, Canada
[3]Centre de Recherche GEOTOP, Université du Québec à Montréal, Montréal, Québec, Canada

* Corresponding Author: ayodejik@uvic.ca; ayodeji.kuponiyi@gmail.com

4.1.4 Article Format

The text and figures are included in a manuscript draft being re-purposed to be submitted for publication. Figures and tables in the draft manuscript have been renumbered to conform with the dissertation style. References cited in the draft are included in the bibliography of this dissertation.

4.1.5 Data and Resources

We thank Canadian Hazard Information Service for providing CNSN data from Canadian National Seismic Network data center (http://www.earthquakescanada.nrcan.gc.ca/stndon/CNSN-RNSC/stnbook-cahierstn/index-en.php). USArray data were obtained from the Incorporated Research Institutions for Seismology Data Management Center. Some of the computations were carried out using the ObsPy libraries (https://github.com/obspy). Most of the figures were plotted using the Generic Mapping Tools (GMT) software (Wessel & Smith, 1995), other by the Python module "Matplotlib".

4.2 Construction of Broadband Dispersion Curves by Reconciling Ambient Seismic Noise and Earthquake Surface Wave Data

4.2.1 Abstract

Deep lithospheric structures have been traditionally constrained by inverting long-period dispersion curves measured from surface waves of distant earthquakes recorded by station pairs. In the last decade, the development of ambient seismic noise (ASN) correlation methods has provided the opportunity to routinely extract short-period dispersion curves, suitable for constraining crustal structures. These developments present the possibility to efficiently study the entire lithosphere by combining long-period earthquake dispersion data with short-period ASN dispersion for co-incident station pairs to obtain dispersion curves with as broad a spectrum as possible. Constructing broadband dispersion curves following this method is theoretically possible but practically challenging in many cases due to potential discrepancies between the datasets at overlapping frequencies. In this study, we investigate the causes of the discrepancies between phase velocity dispersion curves from earthquake and ASN data using seismic waveforms from the Canadian National Seismograph Network. We find that estimating the low frequency limits of ASN dispersion based only on the wavelength-interstation distance relation could, in some cases, lead to selecting an incorrect branch of the ASN phase velocity dispersion curve, making it inconsistent with the conjugate curve derived from earthquake data. We introduce a method which identifies a reliable spectral window based on period-dependent signal-to-noise ratio analyses and propose a framework for constructing broadband dispersion curves. Our framework places more weight on data quality than on the traditional interstation distance-wavelength relation. We further demonstrate that the method could improve the quality and quantity of empirical Green's

functions, and thus contribute to better data processing and selection for ASN tomography inversion.

4.2.2 Introduction

Surface wave dispersion measurements were traditionally made from seismic waves generated by distant earthquakes (Brune & Dorman, 1963; Knopoff, 1972). However, the high-frequency components of the wave trains are already lost at the recording site due to intrinsic attenuation and geometric spreading over a long propagation distance. As a result, shallow structures beneath the recording stations, which are specifically sampled by high-frequency surface waves, are either poorly or never constrained.

The discovery over a decade ago that the Earth's response function can be extracted from continuous seismic noise records has motivated a deluge of ambient seismic noise studies, both in theoretical aspects (e.g. Lobkis & Weaver, 2001; Derode et al., 2003; Wapenaar, 2004) and applications (e.g Shapiro & Campillo, 2004; Kao et al., 2013; Kuponiyi et al., 2017). Typically, the Earth's natural vibrations are dominated by several modes of high-frequency surface waves traveling as ambient seismic noise (Kimman et al., 2012; Yao et al., 2011). Thus, the empirical Green's function (EGF) extracted from the ambient seismic noise inherits the intrinsic dispersive characteristics of high-frequency surface waves.

The prospect of constructing dispersion curves with a spectrum as broad as possible becomes achievable by combining measurements from relatively high-frequency (2 – 30 s) ambient seismic noise and low-frequency (30 – 200 s) surface wave data from distant earthquakes. A truly "broadband" dispersion curve can then be constructed and inverted to resolve full-scale lithospheric velocity structures. Although ambient noise tomography (ANT) has been used to

image the Earth's velocity structure at different scales, fewer studies compared (e.g. Bao et al., 2014; Zeng et al., 2015) or combined (e.g. Yao et al., 2006; McLellan et al., 2018) their dispersion results with path-averaged dispersion measurements from earthquake data.

In theory, collinear surface wave dispersion measurements derived from ambient noise and earthquake data should be consistent for the frequency band where the two spectra overlap. In reality, however, this is not always the case. While some studies showed that the two dispersion curves, derived independently from earthquakes and ambient noise over the same spectral band and along coincident paths, are consistent within acceptable error limits (e.g. Shapiro & Campillo 2004; Yao et al., 2006; Bao et al., 2014), others reported considerable variations between the two phase velocity dispersion data sets for some station pairs (e.g. Kao et al., 2013, McLellan et al,. 2018).

In this study, we have three specific objectives. First, we investigate the potential causes of discrepancies between dispersion curves derived from ambient seismic noise data and those derived from earthquake surface waves. Second, we develop a data-consistent method to determine the optimal corner periods of ambient noise derived EGF, within which reliable phase velocity dispersion curves can be measured. Third, we propose a systematic framework to construct a truly broadband dispersion curve with periods ranging from ~2 to ~200 s. Finally, we include data from a subset of the EarthScope USArray to demonstrate the benefits of following the proposed framework.

4.2.3 Discrepancies Between Dispersion Curves Derived from Earthquake and Ambient Noise Data

To demonstrate the cause of the discrepancy between dispersion curves derived from earthquake and ambient noise data, we use data from 16 Canadian National Seismograph Network (CNSN) seismic stations (Figure 4.1). These are a subset of stations used in earlier studies within the Canadian shield (Darbyshire et al., 2013), in which Rayleigh wave phase velocity dispersion curves from teleseismic earthquakes were measured. The stations also form part of a Canada-wide ambient noise tomography study (Kao et al., 2013), in which the large-scale velocity structure of Canada was constrained using Rayleigh wave group and phase velocities.

The process to extract dispersion curves from earthquake surface waves has been well developed over the years. Following different processing routines, several studies (e.g. Bensen et al., 2007; Arroucau et al., 2010; Kimman et al., 2012) have shown that group and phase velocity dispersion measurements can be extracted from ambient seismic noise correlation functions (NCFs). To obtain reliable dispersion curves using ambient noise NCFs, previous studies suggested an empirical relationship between the interstation distance (Δ) and the wavelength (λ), and by inference, period (T). For example, Bensen et al. (2007) suggested that reliable group velocity dispersion curves can only be measured when $\Delta > 3\lambda$. Other studies extended the application to phase velocity dispersion measurements and relaxed the condition to $\Delta > 2\lambda$ (e.g. Brandmayr et al., 2016) or $\Delta > \lambda$ (e.g. Wang et al., 2017). For a crustal phase velocity of 4 km/s, these criteria place the resolvable period limits (T_{max}) at $\Delta/12$, $\Delta/8$ and $\Delta/4$ respectively. Thus, the maximum depth sampled by surface waves is constrained by these criteria.

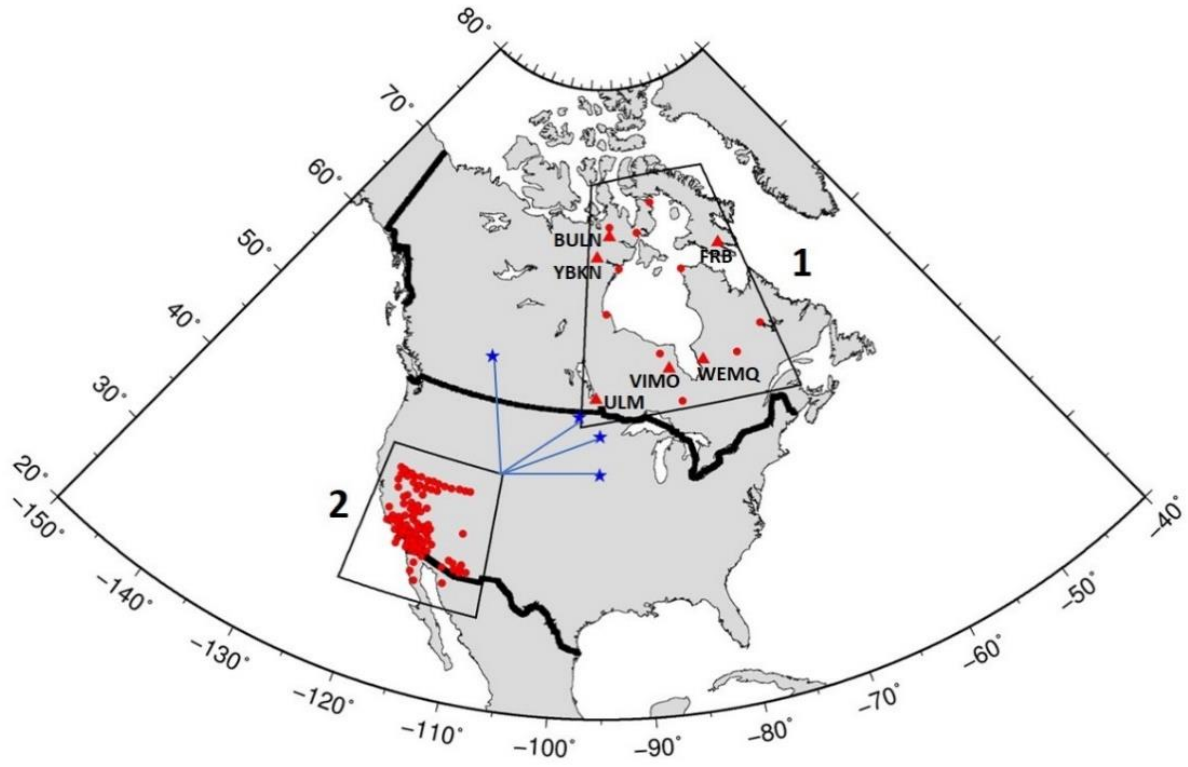

Figure 4. 1 Map showing the seismic stations used in this study. Canadian National Seismograph Network (CNSN) broadband seismic stations used in this study are represented by symbols within the polygon labeled “1”; triangles represent named stations referenced in the text. A subset of the USArray stations in western US is used for the statistical analyses and is represented by symbols within the polygon labeled “2”. The blue stars with lines connecting to polygon 2 show data from the stations that were cross-correlated with the western stations within polygon 2, to obtain large offset empirical Green’s functions (EGFs).

As shown in Chapters 2 and 3 of this dissertation, measuring the fundamental mode of group velocity is often associated with little to no measurement ambiguity but suffers from slightly lower structural resolution when compared to phase velocity. Despite phase velocity measurements generally possess lower uncertainties than group velocity measurements, they are sometimes affected by incorrect cycle/curve selection due to cycle skipping and poor signal resolution (Bensen et al., 2007; Luo et al., 2015). During automated processing, a typical solution to this problem is to guide the curve selection with a suitable regional reference curve calculated from earthquake data at long periods, often within the period limit (T_{max}) defined by the interstation distance. The selected branch is then traced from the long period edge of the ambient noise data back to shorter periods. This scheme works in many cases but fails in cases of severe cycle skipping and signal deterioration at long periods – leading to the determination of incorrect phase velocity dispersion curves. Two examples of this scenario are presented in Figure 4.2 for station pairs VIMO-YBKN and BULN-FRB. The selected phase velocity dispersion curve could be under- or over-estimated by one branch with respect to the true curve (Figure 4.2a and 5.2b). The failed cases are often unnoticed since the process is automated and the curves are rarely compared to collinear earthquake dispersion curves for each pair.

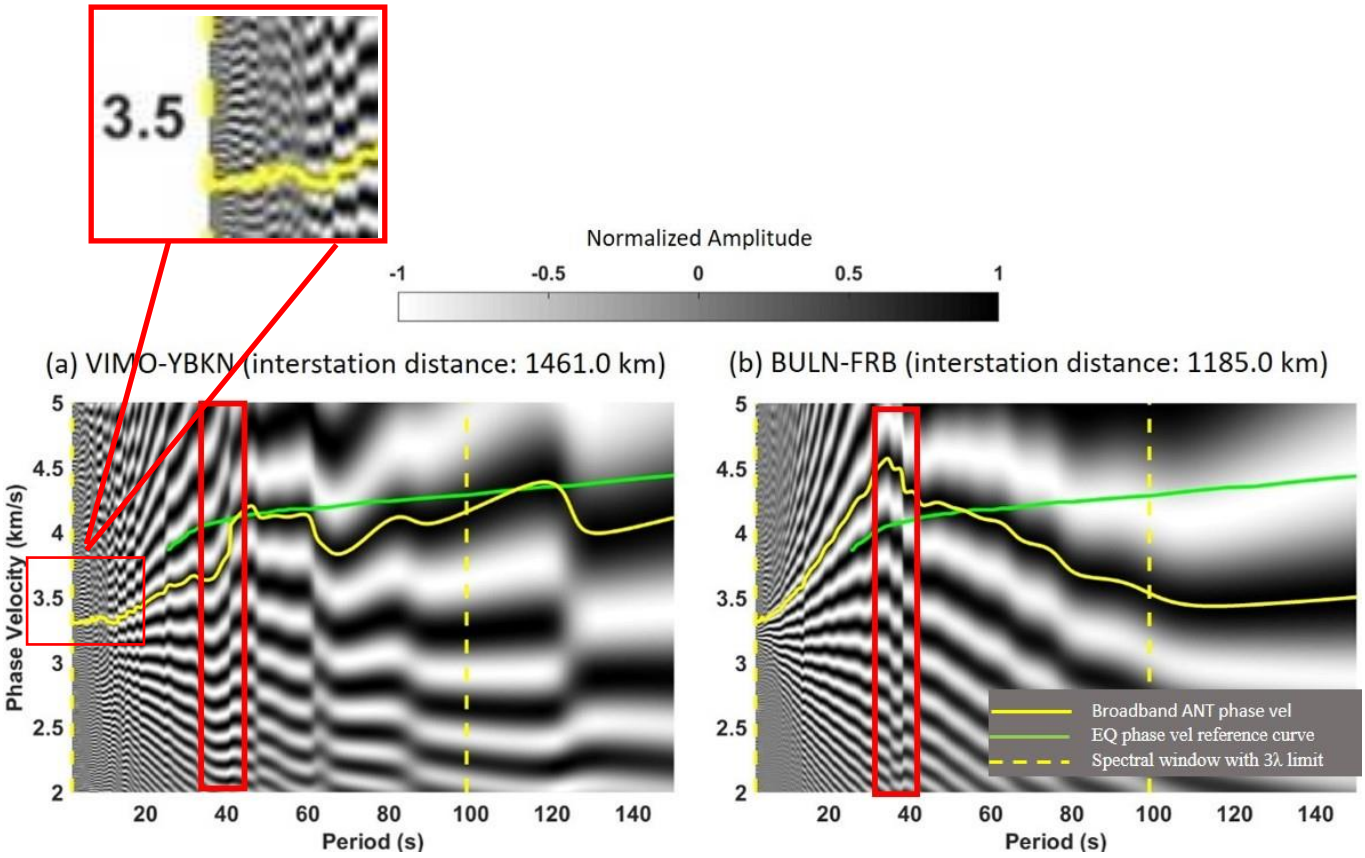

Figure 4. 2 Results of time-frequency analysis of two representative station pairs VIMO-YBKN (a) and BULN-FRB (b). Ambient noise phase velocity dispersion curves (solid yellow lines) are determined by tracking the amplitude ridges (black bands) closest to the regional phase velocity dispersion curve derived from earthquake data (green lines) at long periods (e.g. >40 s). Signal deterioration near 40 s (highlighted within solid red rectangles) results in discrepancies between the ambient noise and earthquake phase velocity dispersion curves. This leads to systematic under- and over-estimation of the phase velocity at periods <40 s for (a) and (b), respectively. Dashed yellow lines are the frequency boundaries corresponding to the three-wavelength criterion (i.e., interstation distance > 3 wavelengths). Zoomed in figure shows an example of incoherent short period portion of the phase velocity dispersion.

Another important parameter in ANT processing is the maximum frequency or minimum period – T_{min} (Campillo, 2006; James et al., 2017). Figure 4.2a shows severe distortions in the short period range (2–5 s) for the station pair VIMO-YBKN. The optimal T_{min} depends on the spectral resolution of surface wave cycles in the short period range. Many previous studies have attempted to obtain reliable phase velocity dispersion measurements by choosing an optimal Tmax without much emphasis on T_{min}. Theoretically, the Nyquist frequency is the maximum allowable limit of any digital filters used in ANT processing. However, setting the upper limit at the Nyquist frequency could produce waveforms with severe contamination from incoherent high-frequency sources. Typically, T_{min} is chosen in a somewhat ad hoc way without clear justification.

4.2.4 A Framework for the Construction of Broadband Dispersion Curves

In this section, we present a framework with specific steps toward the construction of broadband phase velocity dispersion curves from the combination of earthquake and ambient noise datasets. There are four major steps in this framework, as summarized in Figure 4.3: (i) preprocessing earthquake and ambient seismic noise data, (ii) dispersion measurements for earthquake data, (iii) dispersion measurements for ASN data with optimal corner periods, and (iv) combining dispersion measurements from ambient seismic noise and earthquake datasets. The key to success is in step (iii) where the range of resolvable periods must be carefully determined by signal-to-noise ratio (SNR) analysis of the ambient seismic noise data. Each step represents a set of procedures to manipulate data for optimal resolution. The flexibility in this framework makes it possible to be applied to existing or previously processed EGFs, without having to re-compute the station-pair cross-correlations.

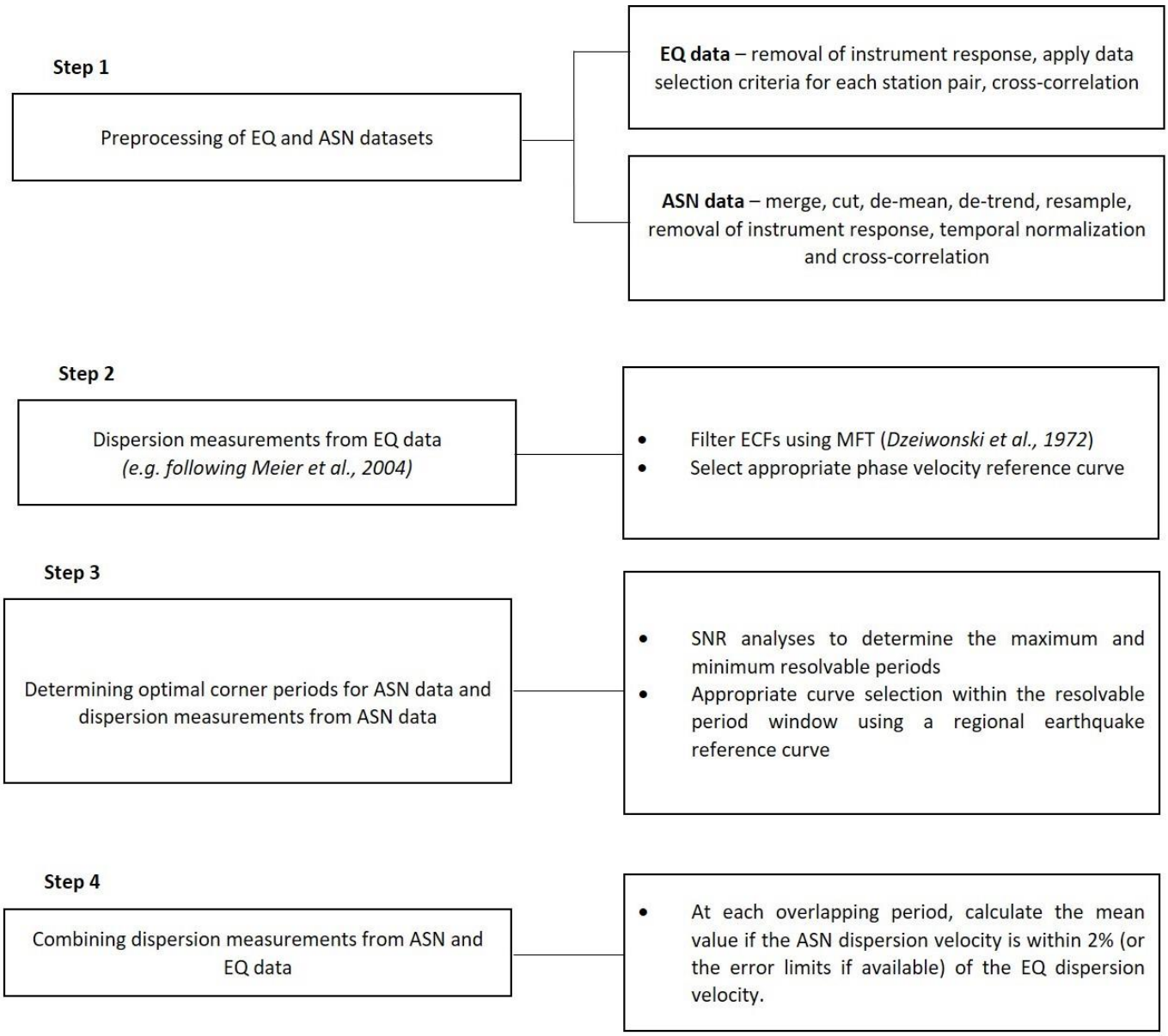

Figure 4. 3 Schematic summary of data processing steps to construct a broadband dispersion curve as discussed in Section 4.3. ASN: ambient seismic noise; EQ: earthquake; ECFs: earthquake correlation functions; MFT: multiple filtering technique.

4.2.4.1 Preprocessing Earthquake and Ambient Seismic Noise Datasets

We followed the steps described in detail by Darbyshire & Eaton (2010) to process earthquake data. Basically, only teleseismic events with magnitude ≥ 5.5 lying within ±5^{o} of the inter-station great-circle path were used for this study. Following the conventional two-station method (Knopoff, 1972; Meier et al., 2004; Sato, 1955), the earthquake waveforms were first filtered between 20 and 200 s and visually inspected for high SNR. Waveforms of a specific earthquake with a great-circle path within ±5^{o} of that of a recording station-pair are cross-correlated to give the earthquake correlation functions (ECFs).

The ambient noise data, retrieved from the CNSN database, comprises continuous vertical component seismic waveforms recorded between 2009 and 2012 at 16 CNSN seismic stations in eastern Canada. The data were processed to obtain NCFs, following similar techniques to those described by Bensen et al. (2007). The process consists of converting raw data from mini-SEED to SAC format, then merging and cutting them into one-day long segments. Gaps in the time series are zero-padded after the removal of the data mean and trend. Subsequently, each trace is resampled to 1 sample per second and converted to ground velocity by removing the instrument response. After that, temporal normalization is applied to the waveform to reduce the effect of high amplitude transients from seismic events. No significant difference was observed between applying the one-bit and the running-absolute-mean temporal normalization methods (Bensen et al., 2007). Due to its strongly non-linear nature, spectral normalization should be considered with caution because it can potentially alter the original spectral characteristics of noise waveforms (Pierre Arroucau et al., 2010; Brandmayr et al., 2016a). To ensure that subsequent processing steps are efficient, and the signal spectral information is optimized, the normalized waveform is bandpassed between 2 and 150 s. Simultaneously recorded waveforms from station pairs are then

cross-correlated to obtain the NCFs. The NCF for each station pair is stacked and symmetric components are obtained by averaging the negative and positive branches of the stack. The final NCF for each station pair is the symmetric component.

4.2.4.2 Dispersion Measurements for Earthquake Data (ECFs)

As described in Darbyshire & Eaton (2010), phase velocity dispersion measurements were estimated from earthquake data following the two-station method and multiple-filter technique (Dziewonski et al., 1972; Meier et al., 2004; Sato, 1955). The phase velocity (c) of the surface waves propagating between the station pair is estimated from the complex phase of the ECF ($\Phi(\omega)$) following the equation (Meier et al., 2004):

$$c(\omega) = \frac{\omega \Delta}{\eta(\omega)} \quad (1)$$

and

$$\eta(\omega) = \arctan\{\mathrm{Im}(\Phi(\omega))/\mathrm{Re}(\Phi(\omega))\} + 2\pi n \quad (2)$$

The $2\pi n$ term gives rise to an ambiguity typically encountered in phase velocity determination from ECFs and EGF. The solution to the equation is non-unique, resulting in multiple branches of dispersion curves for $n \in N$, with the branches well-spaced out at longer periods. Variations in the Earth's velocity structure are deemed minimal at longer periods due to comparatively smaller structural heterogeneity at depth. The phase is unwrapped using a regional/Earth reference model. The desired curve is the solution that minimizes the velocity variation when compared with the reference model at longer periods. To improve the accuracy of the dispersion curve obtained from earthquake data, the process is repeated multiple times using events along the same great-circle path. This produces multiple dispersion curves, and the final

solution is the mean of the curves, while the uncertainty is estimated as the standard deviation at each period.

4.2.4.3 Dispersion Measurements for the Ambient Seismic Noise Dataset

Phase velocity dispersion measurements from ambient noise EGFs are extracted following the image transformation technique (Yao et al., 2006). The EGF is defined as the negative time derivative of the NCF (Derode et al., 2003; Lobkis & Weaver, 2001a; Sabra et al., 2005; Snieder, 2004). The resulting image consists of several cycles/branches, consistent with phase velocity measurements using other methods (e.g. the spectral method (Aki, 1957; Ekström et al., 2009) or FTAN (Bensen et al., 2007; Yao et al., 2006)).

4.2.5 Main Drawbacks of Traditional ANT Phase Velocity Dispersion Measurement

Traditionally, phase velocity is measured within a spectral window defined by the interstation distance of station pairs. The window is bounded by T_{max} and T_{min} that are often chosen without clear justification. The interstation distance criterion suggested by Bensen et al. (2007) imposes the strictest penalty on T_{max}. Figure 4.2 shows the phase velocity images from station pairs VIMO-YBKN and BULN-FRB, located within the Canadian Shield, with interstation separations of 1461 and 1185 km respectively. Applying the interstation distance criterion, T_{max} is ~122 s for VIMO-YBKN and ~99 s for BULN-FRB (marked with yellow dashed lines). The selection of the phase velocity curve (yellow solid line) within the period windows 2–100 s (VIMO–YBKN) and 2–99 s (BULN–FRB) is then guided by the reference dispersion curve derived from earthquake data for the region (green solid curve) at the long period edge of the ambient noise spectra. For each pair, the cycle corresponding to the reference dispersion curve was

selected at long periods (>40–100 s). Severe signal degradation results in cycle skipping of the selected phase branch near 40 s (marked by the solid red box), causing the ambient noise phase velocity curve to be underestimated for VIMO-YBKN and overestimated for BULN-FRB. In addition, while the phase spectrum in the short period range is well-resolved for BULN-FRB, the resolution is poor at periods < 15 s for VIMO-YBKN.

4.2.6 Determining the Optimal Corner Periods for Phase Velocity Dispersion Measurement Using SNR Analyses

It has been shown that the spectral characteristics of EGFs depend on the spatiotemporal propagation parameters of surface waves (Dahlen & Tromp 1998, Yao et al. 2006). However, surface wave signals may suffer spectral contamination that obscures quality dispersion measurements (Yang & Ritzwoller, 2008). Furthermore, both experimental results (Derode et al., 2003) and numerical simulations (Yang & Ritzwoller, 2008) show that the signal quality of EGFs is more important in the accuracy of dispersion measurements than the distribution pattern of the seismic noise sources. To determine the optimal corner periods (T_{min} and T_{max}) within which reliable phase velocity dispersion could be measured, a period-dependent SNR analysis of each stacked NCF is carried out. SNR is here defined to be the ratio of the peak amplitude within the signal window to the root-mean-square of amplitude in the noise window. The signal window is defined within group velocity intervals of 2–5 km/s. Several studies (e.g. Luo et al. 2015, Tian & Ritzwoller 2015) only consider the trailing segment of the signal window to estimate the SNR, however the ability to clearly identify the signal may also be impaired by spurious preceding arrivals. Thus, we define the noise window as the segments preceding and trailing the signal window. SNR thresholds are established to determine T_{min} and T_{max}. After processing a large

amount of data, we find optimal SNR thresholds of 3 and 5 for T_{min} and T_{max}, respectively. In other words, given the SNR values corresponding to a set of periods, the shortest period with SNR value ≥3 is T_{min}; while the longest period with SNR ≥ 5 is T_{max}. A reliable spectral window (RSW) bounded by T_{min} and T_{max} is then established. Outside the RSW, the resolution of dispersion measurements is mostly unreliable. Taking the two station pairs shown in Figure 4.2 as examples, the RSW for VIMO-YBKN and BULN-FRB are 10–33 s and 2–37 s respectively (Figure 4.4). Because the contamination from random, incoherent noise is insignificant within the RSW, phase velocity dispersion curves measured within this period range are continuous and always consistent when compared with the reference earthquake-derived dispersion curve (Figure 4.5).

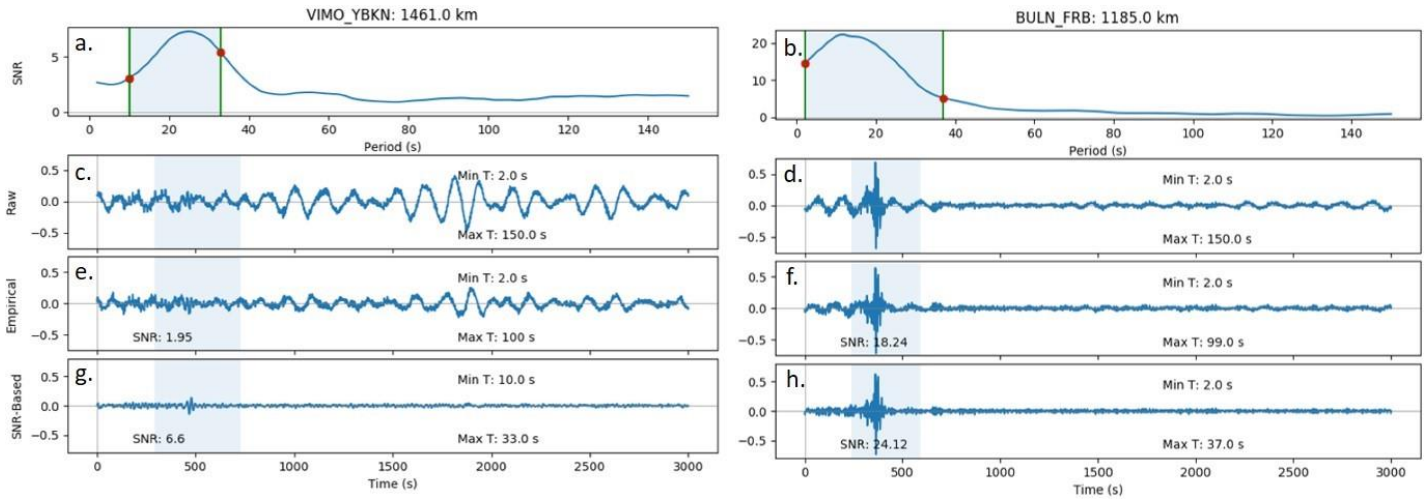

Figure 4. 4 Two representative examples showing the determination of minimum and maximum resolvable periods (red dots) with the SNR thresholds of 3 and 5, respectively. SNR as a function of period are plotted in (a) and (b). Original broadband waveforms (periods between 2 and 150 s) are shown in (c) and (d). Bandpass filtered waveforms with corner frequencies determined from interstation distances are shown in (e) and (f). Bandpass filtered waveforms with corner frequencies determined from (a) and (b) are shown in (g) and (h). Proper selection of corner frequencies results in significantly higher overall SNR.

4.2.7 Combining Dispersion Measurements from Ambient Seismic Noise and Earthquake Datasets to Construct a Broadband Phase Velocity Dispersion Curve

After extracting reliable phase velocity dispersion curves from EGFs and ECFs for corresponding station pairs, broadband dispersion curves are constructed by merging them. Theoretically, both curves should be consistent and continuous; in reality, inconsistencies often arise (e.g. Yao et al., 2006; Kao et al., 2013; McLellan et al., 2018). Slight variations between the two curves may be caused by computational rounding errors, minor temporal variations in velocity structure or GF approximations due to non-symmetric distribution of noise sources. In contrast, larger variations could arise from including frequencies outside the resolution limits of the data, significant processing errors, and/or potential signal degradation from local or instrument noise. Other equally likely sources of significant variations include signal contamination from other modes or phases of seismic waves and perhaps selecting the wrong branch of the phase velocity solution (as demonstrated in Figure 4.2). Figure 4.6 shows the combined dispersion curves for station pairs VIMO-YBKN and BULN-FRB. For slight variations between EGF- and ECF-estimated dispersion measurements at overlapping periods, only EGF measurements that fall within 2% of ECF dispersion or those within the uncertainty limits of ECF dispersion estimates, if available, are accepted. By averaging dispersion measurements from EGF and ECF at overlapping periods, the representative velocities at those periods are derived and a broadband curve is obtained. Significant mismatch between dispersion curves from both datasets had prevented earlier workers from combining the datasets for several station pairs in this region, including the ones shown here (Kao et al., 2013). The results obtained here show remarkable consistency between the

earthquake- and ambient noise-derived dispersion measurements for the previously inconsistent station pairs.

4.2.8 Broader Advantage of Band-pass Filtering Based on Period-dependent SNR

An important factor for resolving structures in surface wave tomography studies is the number of path-averaged dispersion measurements that cross individual grids at successive periods. The quality of dispersion measurements used in ANT studies is often improved by selecting EGFs with SNR greater than a specified threshold. The SNR used for this purpose is estimated using the full EGF waveforms and therefore is different from the SNR defined in our processing framework (Figure 4.3). The selection threshold is typically set at 5, but it can be increased to 7 or 10 depending on the amount of available data and the required data quality (e.g. Arroucau et al. 2010, Wang et al. 2017, Li et al. 2018). EGFs with SNRs below the threshold are excluded from the surface wave tomography, consequently reducing the resolution of structures across all periods.

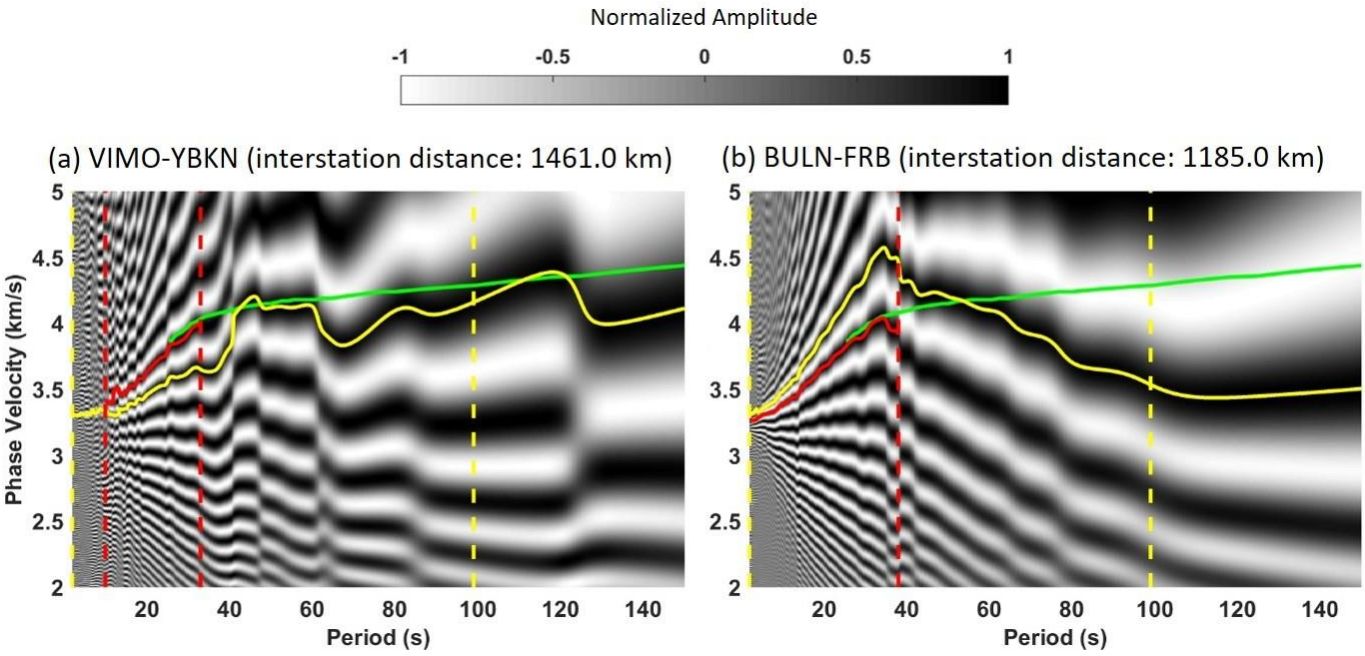

Figure 4. 5 Phase velocity curves correctly determined within the optimal threshold window for station pairs shown in Figure 4.2: (a) VIMO-YBKN and (b) BULN-FRB; red dashed lines are the boundaries of the Reliable Spectral Window (RSW), within which, reliable and consistent ambient noise phase velocity dispersion (red solid line) can be measured. Other features of these figures are described in Figure 4.2.

Improvement in the SNR of EGF

A clear benefit of applying a SNR-based band-pass filter (as described in Section 4.3) is to increase the number of available EGFs for ANT. Figure 4.7 shows an example of EGF corresponding to the station pair ULM-WEMQ. The optimal minimum and maximum periods are obtained by applying the period-dependent SNR analysis (Figure 4.7a) on the raw EGF (Figure 4.7b). The EGF bandpass-filtered in the period range of 2–100 s, which is consistent with the empirical interstation distance criteria, has a SNR of 6.6 (Figure 4.7c). Applying filters with corner periods obtained using our proposed method results in an improvement of SNR from 6.6 to 15.37 (Figure 4.7d). Such improvement allows this EGF to be included in the subsequent dispersion measurement and tomography steps, which would otherwise have been discarded due to poor SNR. The station pair VIMO-YBKN is another example, as shown in Section 4.2.6 (Figure 4.4g).

Interstation Distance Effect

To further examine the applicability of the proposed method in different regions and on a larger scale, we analyze seismic data from a subset of the USArray stations in the western United States in addition to all CNSN stations. We first process the datasets using the traditional method with a bandpass filter determined from the interstation distance only, and the results are used as references. We then process the same datasets using the method described in Section 4.3 with corner frequencies determined from period-dependent SNR analysis. Figure 4.8 shows the improvement obtained by applying the SNR-based method to the CNSN (left panel) and USArray (right panel) datasets. The SNR change is obtained by comparing SNR estimates from the traditional processing method with our method (expressed as a percentage, 0% means no improvement). The histogram plot (top rows) shows the number (count) of station pairs associated

with a specific SNR change, while the scatter plot (bottom rows) shows the SNR change with interstation distance. The analyses show that 92% of the entire CNSN dataset can be improved, with a maximum SNR improvement of over 200% across the full range of interstation distances (Figure 4.8a i-ii). About 71% of the USArray dataset shows improvement, with a maximum SNR improvement of greater than 100% (Figure 4.8a iii-iv). When examining the results in more detail, we notice that all CNSN and about 93% of USArray datasets can be improved if the interstation distance (Δ) is over 1000 km (Figure 4.8b). As the interstation distance decreases, the improvement becomes less impressive. For example, only 95% of CNSN data and ~74% of USArray data can be improved if Δ is between 350 and 1000 km (Figure 4.8c). No improvement can be observed for CNSN data if Δ is <350 km. The corresponding improvement rate for the USArray dataset is only ~57% (Figure 4.8d).

Luo et al. (2015) show that uncertainties in the measurement of ambient seismic noise phase velocity measurements increase slightly with decreasing interstation distances. As summarized in Table 4.1, our analysis demonstrates that the improvement in the signal quality becomes marginal with decreasing interstation distance.

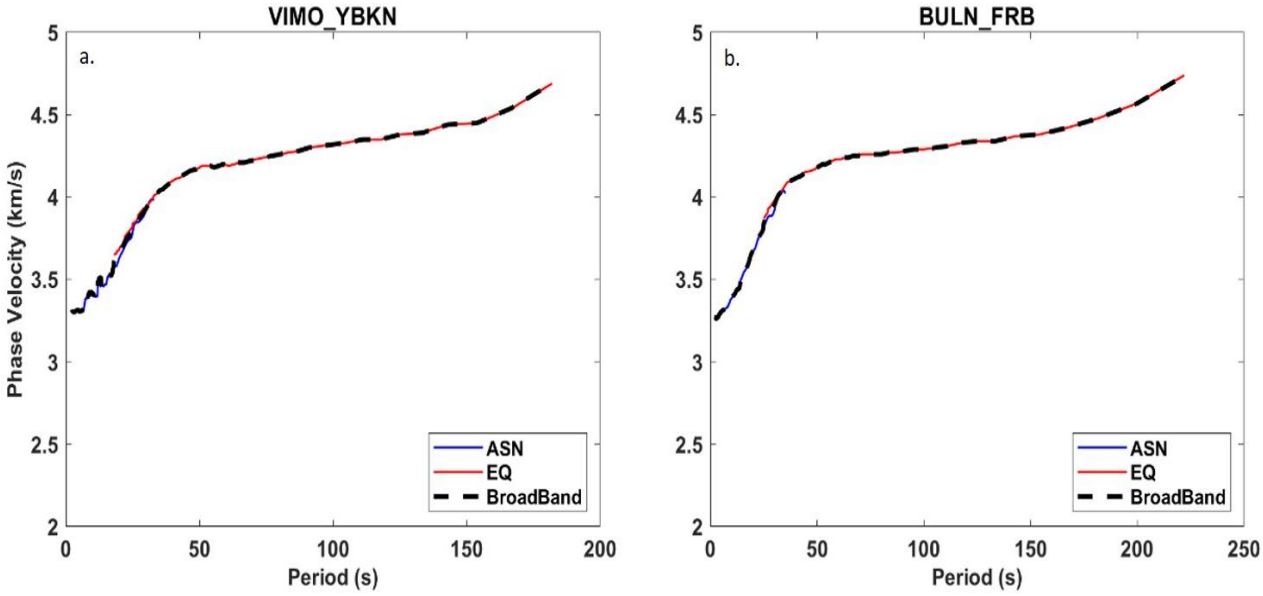

Figure 4. 6 Broadband phase velocity curves (dashed black line) for station pairs (a) VIMO-YBKN and (b) BULN-FRB, obtained by combining earthquake (EQ; solid red line) with correctly determined ambient seismic noise (ASN; solid blue line) phase velocity curves.

4.2.9 Discussion and Conclusion

This paper proposes a reliable method for constructing a broadband phase velocity dispersion curve by combining ambient seismic noise EGFs, which lie mainly in the relatively short-period frequency band, with the predominantly long-period earthquake dispersion measurements. We have demonstrated that, for some station pairs, inconsistencies may exist between ambient noise and earthquake phase velocity dispersion curves, typically due to cycle-skipping from poor signal quality at the long-period end of the ambient noise phase velocity dispersion curve. EGFs which satisfy the conventional interstation distance criterion could still produce phase velocity dispersion curves that are out-of-phase with earthquake data. Thus, the spatial dependency of surface wave propagation, which for ambient seismic noise studies is governed by the interstation distance, may be a necessary but insufficient criterion for obtaining reliable phase velocity dispersion measurements from ambient noise EGFs. By implication, the interstation-distance criterion places a constraint on the EGF which may not always be satisfied by the spectral quality of the data.

Table 4. 1 Percentage of Station Pairs with Improvement in Waveform Signal-to-Noise Ratio

Interstation distance (km)	**CNSN[1] Stations (%)**	**USArray[2] Stations (%)**
Short (< 350)	0	57
Medium (350 - 1000)	95	74
Large (≥ 1000)	100	93

[1] Canadian National Seismograph Network

[2] Transportable Array of the USArray Project (www.usarray.org).

SNR analysis is a common step in many seismological methods, including ambient noise processing. Specifically in this study, we explore the optimal way of applying SNR analysis to obtain reliable, data-consistent phase velocity dispersion curves. By setting adequate thresholds in a period-dependent SNR analysis of NCFs, the minimum and maximum resolvable period limits are determined. Broadband phase velocity dispersion curves are then obtained by averaging the phase velocities from ambient seismic noise and earthquake data in the overlapping frequency band with a difference of no more than 2%.

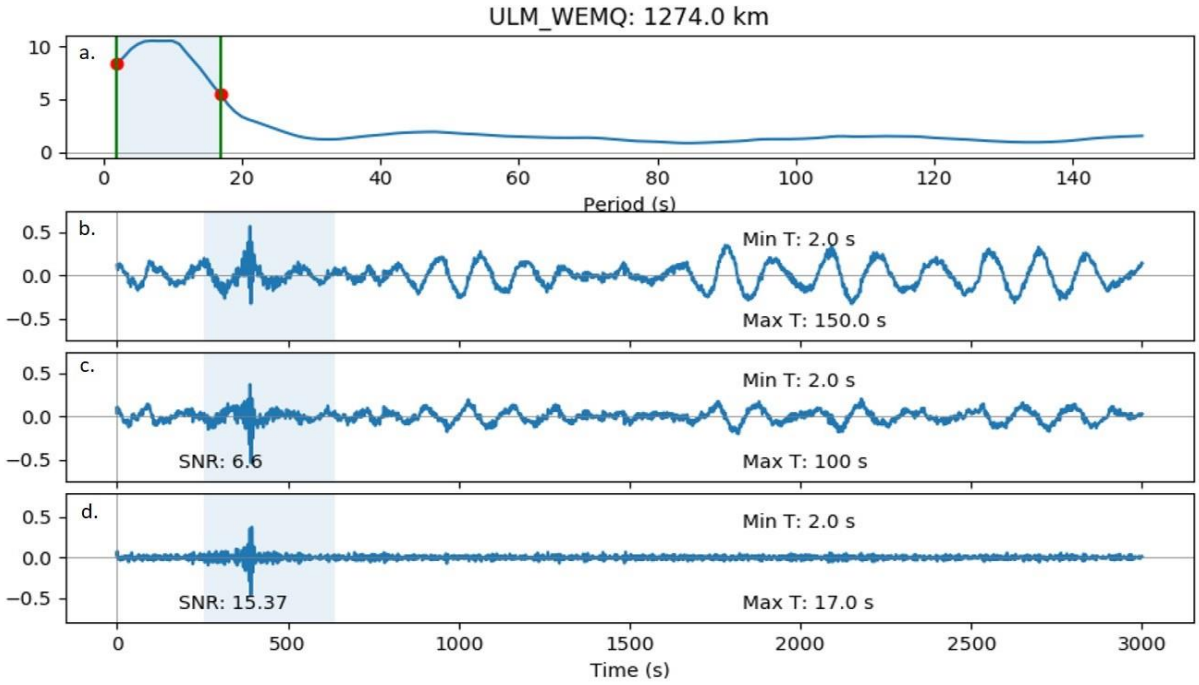

Figure 4. 7 Example showing SNR improvement above typical dispersion quality thresholds of 7 and 10 for the station pair ULM-WEMQ. (a) SNR as a function of period, showing the determination of minimum and maximum resolvable periods (red dots) with the SNR thresholds of 3 and 5, within the RSW (shaded blue patch bounded by solid green lines) respectively. (b) Original broadband waveform (periods between 2 and 150 s). (c) Bandpass filtered waveform with corner frequencies determined from interstation distances > 3 wavelengths. (d) Bandpass filtered waveform with corner frequencies determined from (a). Notice that proper selection of corner frequencies results in significantly higher overall SNR.

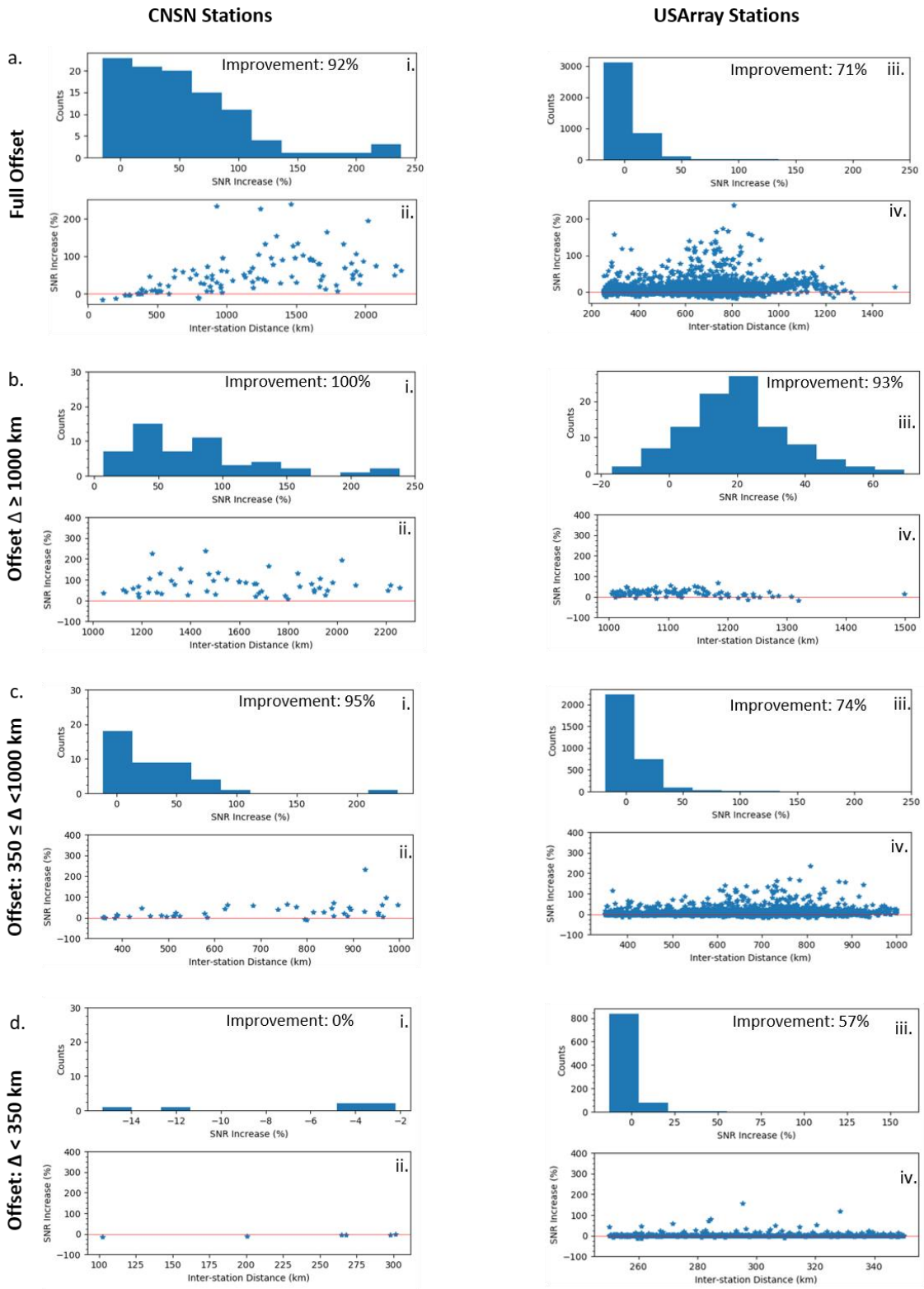

Figure 4. 8 Analyses of SNR improvement for CNSN (i and ii) and USArray (iii and iv) stations with interstation distances at: (a) full offset, (b) 1000 km and greater, (c) from 350 to less than 1000 km, (d) less than 350 km.

Figure 4.8 (continued).

The upper panels (i and iii) are histograms representing the count of pairs with specific percentage improvement. The lower panels (ii and iv) show the improvements (as a percentage) over several inter-station distances. Δ denotes offset or inter-station distance; red horizontal line is the zero mark; full offset refers to the range of all interstation distances used for the analysis.

Robust statistical analyses show that the application of our method can lead to a significant improvement in the signal quality of the ambient noise-derived EGFs over the traditional methods. Such improvement can consequently contribute to an increase in the number of high-quality phase velocity dispersion measurements used in surface wave tomography inversion, resulting in a better resolution of velocity structures. Results of our experiments indicate that the improvement of applying variable band-pass filters based on period-dependent SNR analysis is most impressive when the interstation distance is over 1000 km. The improvement becomes less significant with decreasing interstation distance, and appears to be marginal when the interstation distance is <350 km.

4.2.10 Acknowledgements

This study benefits from discussions with Andrew Schaeffer and Stan Dosso. This research is supported by the Natural Resources Canada (NRCan)'s Induced Seismicity Research Project and Natural Sciences and Engineering Research Council (NSERC) of Canada Discovery Grants (H. K., J.F.C., G.D.S., and F.D.).

Chapter 5. Temporal Variation in Cultural Seismic Noise and Noise Correlation Functions During COVID-19 Lockdown in Canada

5.1 Article Information

5.1.1 Author and Coauthor Contributions

The article presented in this Chapter has been published. The author of this dissertation, APK, carried out the data preprocessing and cross-correlations, seismic power, probabilistic power spectral density and signal-to-noise ratio analysis of seismic noise. APK wrote the manuscript under the supervision of HK. The research was jointly designed by APK and HK. FD. All authors contributed to the thorough review of the manuscript before submission.

5.1.2 Citation

Ayodeji Paul Kuponiyi, Honn Kao; Temporal Variation in Cultural Seismic Noise and Noise Correlation Functions during COVID-19 Lockdown in Canada. *Seismological Research Letters* 2021; doi: https://doi.org/10.1785/0220200330

5.1.3 Author's Names and Affiliations

Ayodeji Paul Kuponiyi[1, 2*], Honn Kao[1, 2]

[1]School of Earth and Ocean Sciences, University of Victoria, Victoria, BC V8P 5C2, Canada

[2]Geological Survey of Canada, Pacific Geoscience Centre, Sidney, BC V8L 4B2, Canada

* Corresponding Author: ayodejik@uvic.ca; ayodeji.kuponiyi@gmail.com

5.1.4 Article Format

The text and figures are included in a manuscript draft first submitted to *Seismological Research Letters* for publication in September 2020, revised in December 2020 and published in April 2021. Figures and Tables in the draft manuscript have been renumbered to conform with the dissertation style. References cited in the manuscript are included in the bibliography of this dissertation.

5.1.5 Data and Resources

This research is partly supported by the Induced Seismicity Research Project of Natural Resources Canada (NRCan), Natural Sciences and Engineering Research Council (NSERC) of Canada grants to H. K., Seismic data were obtained from Canadian National Seismic Network (http://www.earthquakescanada.nrcan.gc.ca/stndon/CNSN-RNSC/stnbook-cahierstn/index-en.php) data center. The Observational Seismology Python module (Obspy, Beyreuther *et al.*, 2010) is used for data processing. Some figures are generated by the Generic Mapping Tool (Wessel et al., 2013), others by the Python plotting module “Matplotlib” .

5.2 Temporal Variation in Cultural Seismic Noise and Noise Correlation Functions During COVID-19 Lockdown in Canada

5.2.1 Abstract

The COVID-19 pandemic of 2020 led to a widespread lockdown that restricted human activities, particularly land, air and maritime traffic. The "quietness" on land/ocean that followed presents an opportunity to measure an unprecedented reduction in human-related seismic activities and study its effect on the short-period range of ambient noise cross-correlation functions (NCFs). We document the variations in seismic power levels and signal quality of short-period (1 – 10 s) NCFs measured by four seismographs located near Canadian cities across the pandemic-defined timeline. Significant drops in seismic power levels are observed at all the locations around mid-March. These drops coincide with lockdown announcements by the various Canadian provinces where the stations are located. Mean seismic power reductions of ~24% and ~17% are observed near Montreal and Ottawa respectively, in eastern Canada. Similar reductions, of ~27% and 17% are recorded in western Canada near Victoria and Sidney, respectively. None of the locations show full recovery in seismic power back to the pre-lockdown levels by the end of June, when the provinces moved into gradual reopening. The overall levels of seismic noise during lockdown are a factor of 5–10 lower at our study locations in western Canada, relative to the east. Signal quality of NCF measured in the secondary microseism frequency band (4 – 8 s) for the station-pair in western Canada is maximum before lockdown (late February–early March), minimum during lockdown (mid–late March) and increased to intermediate levels in the reopening phase (late May). A similar pattern was observed for the signal quality of the eastern Canada station-pair, except for an increase in levels at similar periods during the lockdown phase. The signal quality of NCF

within the secondary microseism band is further shown to be the lowest for the western Canada station-pair during the 2020 lockdown phase, when compared to similar time-windows in 2018 and 2019.

5.2.2 Introduction

The rapid spread of a novel Coronavirus (also known as COVID-19), first identified in 2019, has led to a global lockdown since early 2020. By the third week of March 2020, many countries, including Canada, had imposed heavy restrictions on most human activities (especially air, land and maritime travel). Different provinces in Canada responded to the COVID-19 pandemic with different measures, including slightly different starting dates in the implementation of lockdown and re-opening. Most of the initial narratives on the impacts of COVID-19 were driven by traditional and social media reports. Seismologists around the world observed a significant drop in the level of background seismic noise (Gibney, 2020), especially at seismic stations located near city centers (e.g., *Asia*: Pandey *et al.*, 2020; Xiao *et al.*, 2020; *Europe*: Cannata *et al.*, 2020; Piccinini *et al.*, 2020; Poli *et al.*, 2020; *North America*: Lindsey *et al.*, 2020; *Global*: Gibney, 2020; Lecocq *et al.*, 2020). Reduction in human-related maritime activities also led to the suggestion of a "quiet ocean" during the lockdown (e.g., Thomson and Barclay, 2020). Studies have shown that ship noise is broadband (e.g., Erbe *et al.*, 2019) and can contribute to the seismic noise spectrum. Although intuitively the overall reduction of background seismic noise is considered a positive effect that improves the detection of small earthquakes (Lecocq et al., 2020; McNamara & Buland, 2004), it is unclear whether it can have a negative impact on seismological studies that depend on ambient seismic noise (e.g., Shapiro and Campillo, 2004; Bensen et al., 2007; Ritzwoller et al., 2011; Kao et al., 2013; Kuponiyi *et al.*, 2017).

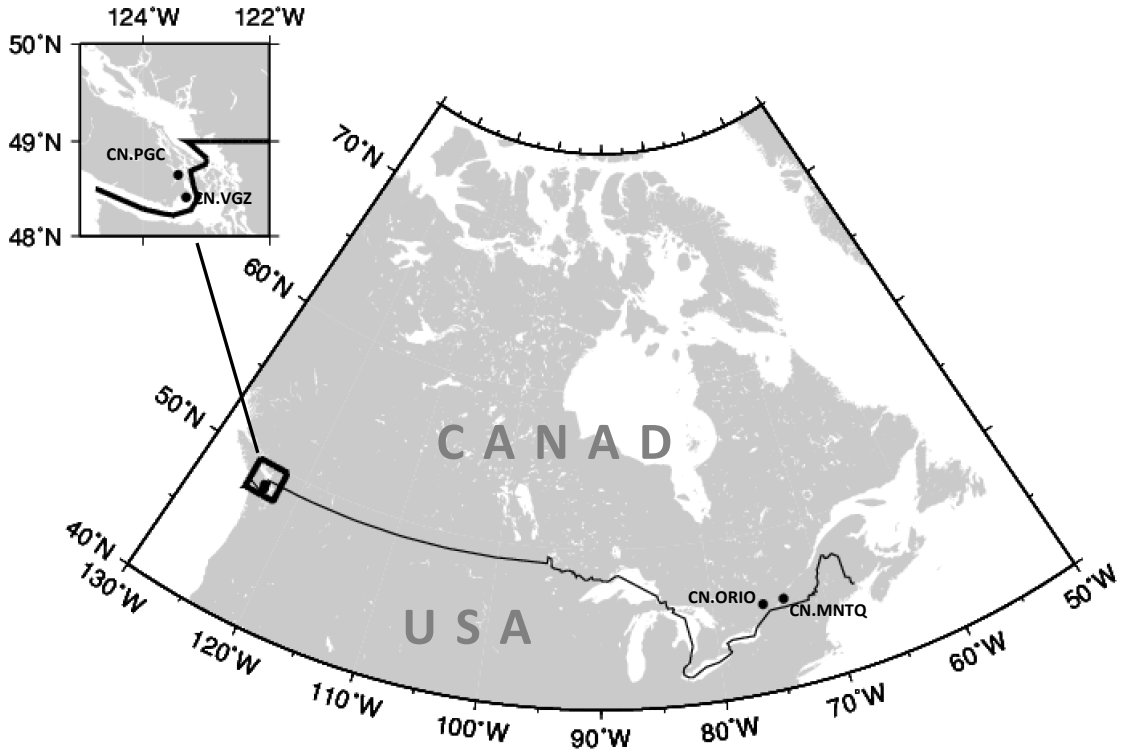

Figure 5. 1 Map showing CNSN seismic stations used in this study. MNTQ and ORIO are two stations located in Montreal (Quebec) and Ottawa (Ontario) respectively in eastern Canada, while PGC and VGZ are located in Victoria and Sidney (British Columbia) respectively in western Canada. Inset: enlarged map showing locations of PGC and VGZ.

In general, the ambient noise spectrum is dominated by a number of different physical phenomena, each with unique spectral characteristics. At short periods up to 1 s (i.e., frequencies ≥1 Hz), it mainly corresponds to cultural noise from anthropogenic sources. Within this band, spectral signatures of vehicular traffic are found at periods ≤ 0.1 s (i.e., ≥ 10 Hz). Earthquake body waves and ocean microseisms dominate the spectrum from 1 to 20 s. While primary microseisms are typically generated by ocean interactions in coastal waters and typically peak at 8 – 16 s, secondary microseisms are generated by standing gravity waves that are formed from the superposition of ocean waves of equal frequencies traveling in opposite directions. They are often characterized by double peaks typically from 4 to 8 s (McNamara & Buland, 2004; Peterson, 1993). At periods longer than 20 s, the seismic noise spectrum is mainly controlled by longer period surface waves, referred to as earth hum (McNamara & Buland, 2004; Rhie & Romanowicz, 2004; Suda, 1998). Unsurprisingly, the seismic response to the lockdown is most visible in the frequency range typically dominated by cultural noise from anthropogenic sources (Dias et al., 2020; Lecocq et al., 2020; Poli et al., 2020).

Since its introduction as a seismic imaging method over a decade ago, ambient noise tomography (ANT) has become an important tool in seismology (e.g., Lobkis and Weaver, 2001; Bensen *et al.*, 2007; Kuponiyi *et al.*, 2017). The method relies on the empirical Green's functions (EGF) derived by cross-correlating continuous waveforms simultaneously recorded by a pair of seismic stations (Shapiro & Campillo, 2004b). An important advantage of ANT is that it does not depend on the distribution of active seismic sources or earthquakes to obtain a noise cross-correlation function (NCF). This merit makes ANT a very popular choice to image the spatial distribution of seismic velocity at different scales from local (e.g. Idowu *et al.*, 2011; Brandmayr *et al.*, 2016), regional (e.g., Arroucau *et al.*, 2010; Kuponiyi *et al.*, 2017; Li *et al.*, 2018), to

continental (e.g., Bensen *et al.*, 2008; Saygin and Kennett, 2010; Kao *et al.*, 2013). The ANT method is a particularly viable option for seismic velocity structure studies near city centers, where the application of active seismic sources may be difficult due to safety and environmental concerns. While the traditional ambient seismic noise (ASN) processing procedure is intrinsically designed to reduce incoherent noise and improve the signal-to-noise ratio (SNR) of NCFs (Bensen et al., 2007; Sabra et al., 2005), exactly how a significant change in the overall level of background noise affects the SNR of NCFs remains unexplored.

The focus of most ASN enhancement studies is on improving the processing routine (Bensen et al., 2007; Ping et al., 2020) to achieve better SNR. Relatively high frequency cultural noise from anthropogenic sources make up a large portion of the seismic noise generated in city centers (Diaz et al., 2020; Díaz et al., 2017), while lower frequency microseisms are sourced primarily from the ocean. The COVID-19 lockdown, accompanied by land/ocean 'quietness', represents a rare opportunity to observe a dramatic reduction in human activities and its effect on the short period range of NCFs. In this study, we focus on three key points. The first is to document and analyze the temporal variation of the power of seismic noise at four broadband seismograph stations located near city centers in three Canadian provinces before, during, and after the COVID-19 lockdown period (Figure 5.1). The second is to investigate the corresponding spectral characteristics of the background seismic noise as a result of the lockdown. The third, which is probably more scientifically important, is to examine the temporal variation of the signal quality of NCF across the COVID-19 timeline.

5.2.3 Data and Analysis

For this study, we use continuous vertical component seismic waveform data from four broadband seismograph stations of the Canadian National Seismograph Network (CNSN, Figure 5.1) (Geological Survey Of Canada, 1989). We acknowledge that the number of CNSN stations at or near city centers is generally limited, mainly to avoid the negative effect of anthropogenic noise on routine earthquake monitoring. In eastern Canada, we process data obtained from stations ORIO (located in Ottawa, Ontario) and MNTQ (Montreal, Quebec). In western Canada, we use a station located in Victoria, British Columbia (VGZ). Station PGC, located in a rural area near Sidney, British Columbia (PGC), is included as a reference site for comparison.

Table 5.1 COVID-19 Timeline for Canadian Provinces and Seismograph Stations used in this Study.

	Province	**Station**	**Starting Date of Lockdown as Announced by the Provincial Government**	**Starting Date of the Reopening Phase**
1.	British Columbia	PGC and VGZ	March 16, 2020	May 19, 2020
2.	Ontario	ORIO	March 12 – 17, 2020	May 16, 2020
3.	Quebec	MNTQ	March 12 – 13, 2020	May 20, 2020

In most parts of Canada, as with most places around the world, the lockdown started around March 15, 2020. Table 5.1 lists the official starting dates of the public lockdown announced by the three relevant Canadian provinces (British Columbia, Ontario and Quebec). Accordingly, we define three temporal windows corresponding to the pre-lockdown phase (February 27 – March 9), the lockdown phase (March 20 – 31, 2020) and the reopening phase (May 19 – 30, 2020). The data processing is divided into three parts. The first one entails processing the entire timeseries to obtain the temporal variation of the power of seismic signals across the defined time windows. The second part involves computing the Probabilistic Power Spectral Density (PPSD) functions of seismic noise records by following the steps described in McNamara and Buland (2004). In order to highlight the lockdown effect for the first and second parts of the processing, we include timeseries from February 1 to June 30, 2020. The last part involves following the ASN pre-processing steps described in Kuponiyi *et al.* (2017) to obtain NCFs corresponding to the pre-, during, and post- lockdown temporal windows. Frequency- (period-) dependent signal quality calculations are subsequently carried out on the NCFs.

Specifically in the first part, we estimate the seismic power for each station by taking the square of the amplitude of the vertical-component ground displacement. The ground displacement measurements at each station were first obtained by removing the corresponding instrument response from raw records. The resulting waveforms were then cut into daily segments, down-sampled to 25 samples per second (sps), band-pass filtered between 2 and 12 Hz, and merged into monthly segments. In total, there are 326,160,000 data points (86400 seconds ***** 25 sps ***** 151 days) to process. As data reduction is necessary to improve computational efficiency, we adopt a data processing scheme with a moving window of 12 hours and no overlap. For each 12-hour window, the median value is used to represent the temporal seismic power (gray lines in Figure 5.2). We

also apply a 48-hour moving window to better visualize the longer trends of seismic power over the duration of the study for each station. The 48-hour values are smoothed by first-order spline interpolation at 30-minute intervals (black lines plotted over gray lines in Figure 5.2).

In the second part, we compute PPSDs following the method described in McNamara and Buland (2004). To estimate the power spectral density (PSD), continuous data from each station record are preprocessed by first dividing the waveforms into one-hour long records with 50% overlap. Each one-hour record is then divided into 13 segments with each segment overlapping by 75%. Data in each segment are truncated to the next lowest power of 2, demeaned and detrended. Each segment is then transformed to the frequency domain with a 10% cosine taper applied to its ends. PSDs are subsequently estimated as the square of the amplitude spectrum multiplied by a factor determined as $2\Delta t/N$, where Δt is the time interval between each sample and N is the number of samples in each segment. A correction of 1.142857 is applied to each segment's PSD to account for the 10% cosine taper previously applied, followed by the removal of the corresponding instrument response. Finally, the PSD for each hour is determined by averaging the PSDs for the constituent 13 segments. PPSDs are computed by generating probability density functions from all available hour-long PSDs. In our case, PPSDs are computed for the entire duration of investigation (February 1 – June 30, 2020, Figure 5.3), as well as for the individual time windows defined in accordance to the timeline presented in Table 5.1 (Figure 5.4). Readers who are interested in the construction of PPSD are referred to McNamara and Buland (2004) for more technical details.

The third part of processing involves estimating spectral SNRs for NCFs calculated in each defined temporal window. In this context, daily seismic data files are processed following the ASN routine described in Kuponiyi et al. (2017). For each temporal window, 12 daily files for each

station pair are processed by cutting them into equal lengths. Data gaps are filled by linear interpolation if necessary. Data mean, linear trends and instrument response are removed from the data. The waveforms are band-pass filtered between 1 and 20 s and normalized in the time-domain by applying one-bit normalization. The waveform pair for each day is then cross-correlated to obtain the daily NCF. The daily NCFs within each defined temporal window are stacked and symmetrized to give the final NCF (Figure 5.5). The period-dependent SNR is subsequently estimated for each symmetrized waveform to quantify its signal quality (Figure 5.6). Specifically, we first apply a narrow-band frequency filter on the NCFs around individual periods from 1 to 10 s. The maximum amplitude within the signal window is divided by the root-mean-square value of the noise window for each frequency band to give the corresponding period-dependent SNR. We define the signal window by arrivals corresponding to velocities between 2 and 5 km/s, respectively, while a 300-s trailing noise window is taken 50 s after the end of the signal. The 50-s gap is necessary to prevent the leakage of parts of the signal into the noise window, especially at longer periods.

5.2.4 Results

Variations in the lockdown and reopening dates across individual Canadian provinces are taken into consideration in our analysis. Most provinces implemented the lockdown in or near the week of March 15. We present our results in three different forms. The first is the time series of the ASN power for the four stations from February to June 2020 (Figure 5.2). This time range spans across the pre-lockdown, lockdown and reopening phases. The second is the collection of PPSDs computed for the four stations. The spectral characteristics for the entire time span (i.e., February–June 2020) are presented in Figure 5.3, whereas results corresponding to the 3 temporal windows are shown in Figure 5.4. Finally, we present period-dependent assessment of the signal

quality of NCFs for station pairs located in eastern (ORIO-MNTQ) and western (PGC-VGZ) Canada (Figures 5.5 and 5.6).

The mean seismic power values observed before lockdown at MNTQ (Montreal) and ORIO (Ottawa) are 0.878 and 0.678 nm^2, respectively (Figures 5.2a and b). A sharp transition to lower levels is observed in both eastern Canada locations after the declaration of city-wide lockdown on March 13. During lockdown, the mean seismic power dropped to 0.665 and 0.564 nm^2 at MNTQ and ORIO, respectively, corresponding to a dramatic reduction of 24.2% and 16.8%. In the reopening phase, the mean seismic power in Montreal (MNTQ) reached 0.708 nm^2, representing an 80.6% recovery compared to the pre-lockdown level. In contrast, Ottawa (ORIO) showed no clear sign of recovery with a mean seismic power of 0.541nm^2 during reopening (Figures 5.2a and b).

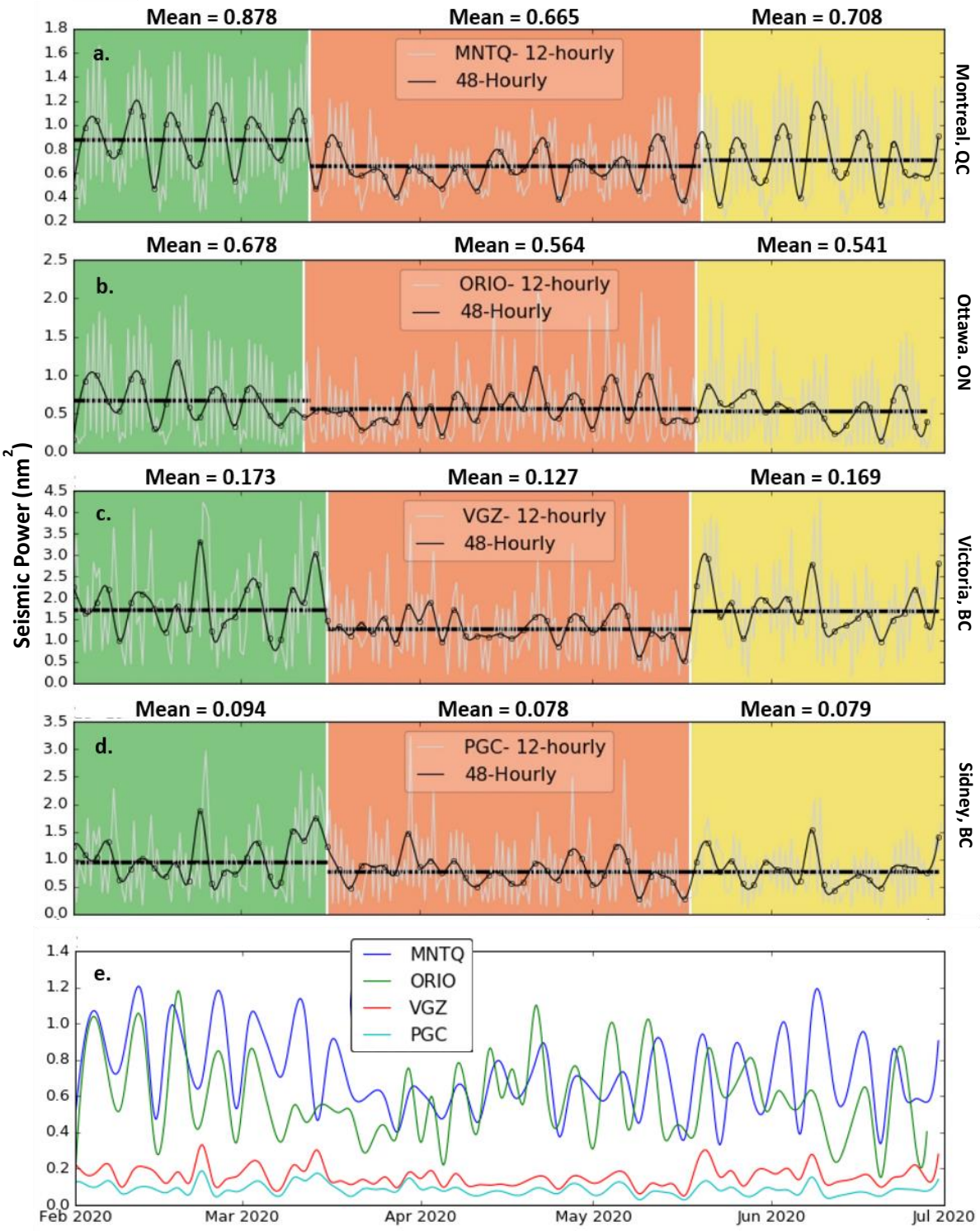

Figure 5. 2 Seismic power calculated over 12-hour (gray solid lines) and 48-hour (black open circles) moving windows for stations MNTQ (a), ORIO (b), VGZ (c), and PGC (d). Waveforms are band-pass filtered between 2 and 12 Hz.

Figure 5.2 (continued).

The black open circles are connected by a smoothed black line for a better visual effect. Green background indicates the pre-lockdown phase, red and yellow backgrounds indicate official lockdown and reopening phases respectively, for the provinces where the stations are located (details in Table 5.1). The thick horizontal black lines are the mean seismic power computed for each temporal window. (e) The smoothed 48-hour moving window seismic power curves of all four stations are plotted on the same scale. This shows clear differences in seismic power amplitudes between stations located in the eastern Canadian provinces and those in the west.

In western Canada, the mean seismic power changed from 0.173 to 0.127 nm^2 at VGZ (Victoria) and from 0.094 to 0.078 nm^2 at PGC (Sidney) after entering the lockdown phase (Figures 5.2c and d). These changes correspond to drops of 26.6% and 17%, respectively. In the reopening phase, the mean seismic power bounced back to 0.169 and 0.079 nm^2, representing a significant recovery of the background seismic noise that is comparable to the pre-lockdown level (Figures 5.2c and d).

The PPSDs of the ASN calculated in the timeline of this study show single-peaked curves centered near 4 s at ORIO and MNTQ (Figures 5.3a and b). In contrast, the curves are broader, asymmetrical and peaked near 6 s at PGC and VGZ (Figures 5.3c and d). When examined in detail for the three temporal windows, we observe distinct differences of the observed spectral power in the frequency range of cultural noise (i.e., period ≤1 s) for eastern Canada stations (ORIO and MNTQ, Figures 5.4a and b), i.e., the highest amplitude was observed before the lockdown (A_{pl}), the lowest during the lockdown (A_{ld}), and intermediate after the reopening started (A_{ro}). This tripartite pattern of $A_{pl} > A_{ro} > A_{ld}$, however, is not observed for western Canada stations (PGC and VGZ; Figures 5.4 c and d).

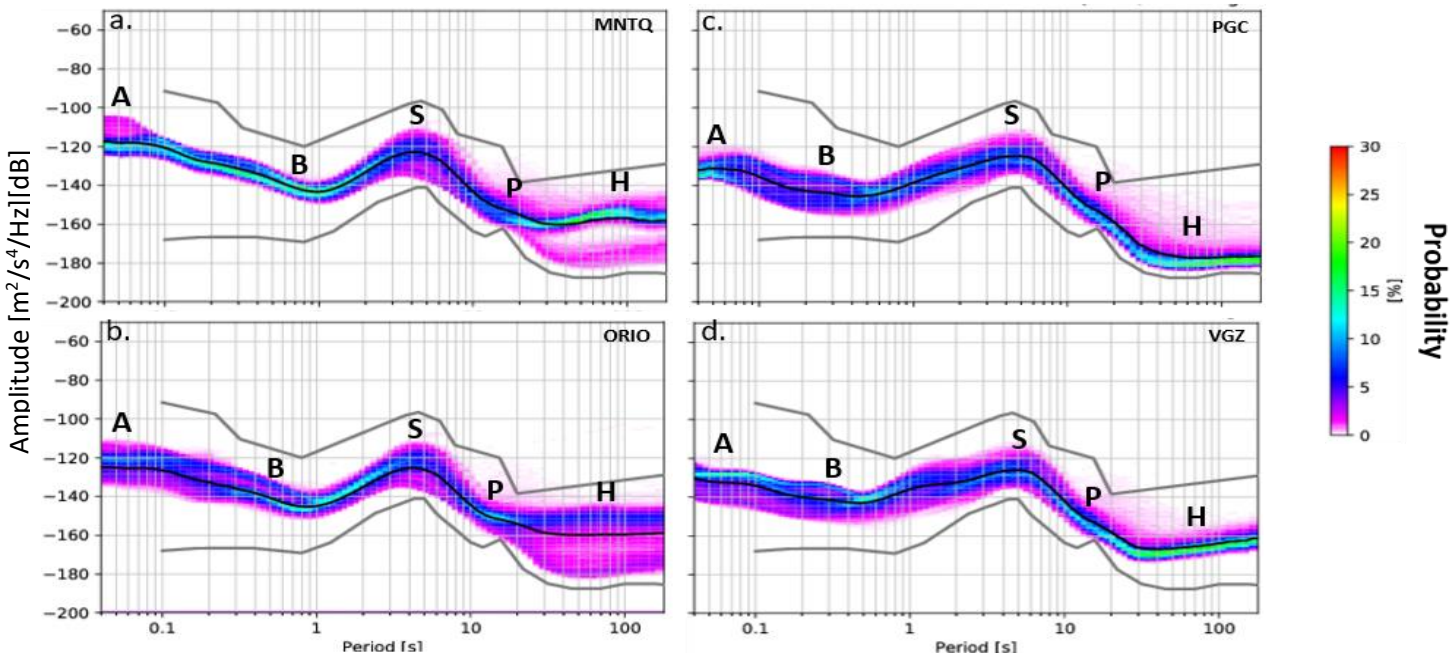

Figure 5. 3 Probability density functions of seismic noise for stations MNTQ (a), ORIO (b), PGC (c), and VGZ (d) – each constructed with 7247 segments. Colors represent seismic power probability within a frequency- (period-) bin. The two gray bounding lines are the New Low Noise Model (NLNM) and New High Noise Model (NHNM) by Peterson (1993). Station data are available from February – June 2020. Alphabet labels (A, B, S, P and H) mark components of seismic noise spectrum: A – anthropogenic, B – body waves, S – secondary microseism, P – primary microseism, H – Earth hum. The black line tracking the distribution is the mean PSD.

For the period range of 1–20 s (the frequency band dominated by ocean microseisms associated with seasonal storms), our results also show a tripartite pattern but the relative strength during the three temporal windows is clearly different from that in the cultural noise band (Figure 5.4). Instead of the $A_{pl} > A_{ro} > A_{ld}$ pattern, we observe a monotonic decrease of the power of seismic noise with time from the pre-lockdown phase to the reopening phase (i.e., $A_{pl} > A_{ld} > A_{ro}$) at all stations. This pattern implies a controlling factor that is more consistent with seasonal changes (transition from winter to summer), than anthropogenic activities at periods >1 s.

NCFs for both eastern and western Canada station pairs generally show clear emerging signals across all three temporal windows (Figure 5.5). A much earlier signal arrival for the PGC-VGZ pair (Figure 5.5a), relative to ORIO-MNTQ (Figure 5.5b), is as expected due to the shorter interstation offset (Figure 5.1). The spectral SNRs measured for each temporal window across the COVID-19 timeline show several interesting features (Figure 5.6a). First, for both station pairs, the SNR curves corresponding to the pre-lockdown and reopening phases have similar shapes, albeit different amplitudes. We observe minimally varying SNR levels at the shortest periods (< 4 s) for all three temporal windows. At periods longer than 4 s, the SNR curves of the two station pairs have different peaks during the lockdown (ORIO-MNTQ: ~5.5 s vs. PGC-VGZ: ~7 s). Such a difference is consistent with the different PPSD distributions observed at the constituent stations (Figure 5.4). Another interesting characteristic of the SNR curves is that the portion with high SNR values is much narrower during the lockdown (Figure 5.6a). For instance, the spectral range with a SNR of ≥15 is 5.5–8 s for PGC-VGZ during the lockdown, but 5–9 s and 5.2–9 s during the pre-lockdown and reopening phases, respectively (upper panel, Figure 5.6a). Similarly, for ORIO-MNTQ, the high-SNR portion (SNR ≥15) spans between 4.2 and 7 s during the lockdown. In contrast, the pre-lockdown curve has a high SNR between 3.8 and 9.5 s, while the range is slightly

narrower during the reopening (4.7–9.3 s, lower panel of Figure 5.6a). Finally, we point out the general trend of having the highest SNR during the pre-lockdown phase, followed by the reopening and the lockdown, except for the period range of 3–9 s in which the ORIO-MNTQ curve shows a clear jump during the lockdown phase (Figure 5.6).

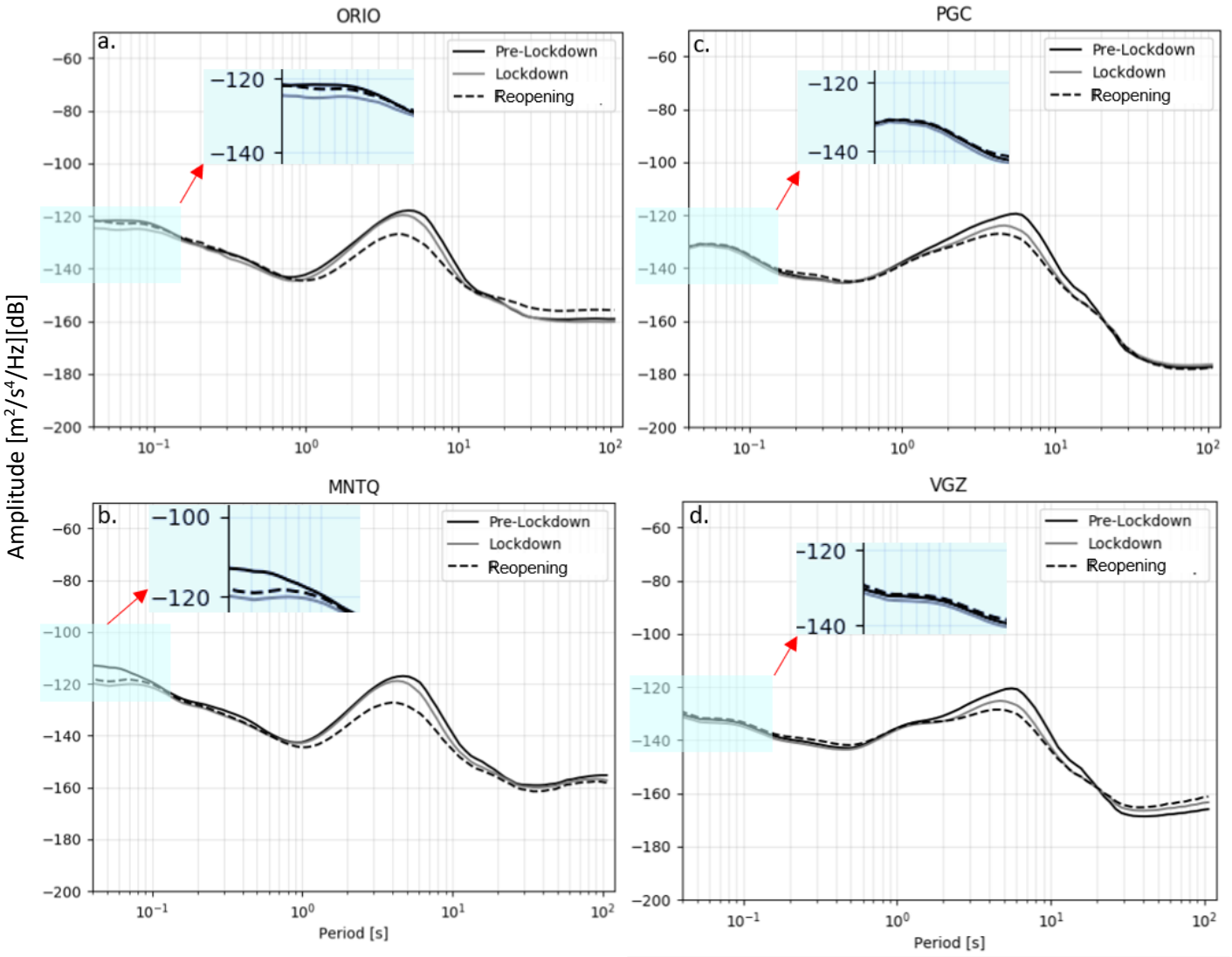

Figure 5. 4 Mean of seismic noise in the three temporal windows under consideration for stations ORIO (a), MNTQ (b), PGC (c), and VGZ (d). Notice that a three-way split is observed at periods ≤ 0.1 s in (a) and (b) but not in (c) and (d). Zoomed-in images show the high-frequency portion of the plot in greater detail.

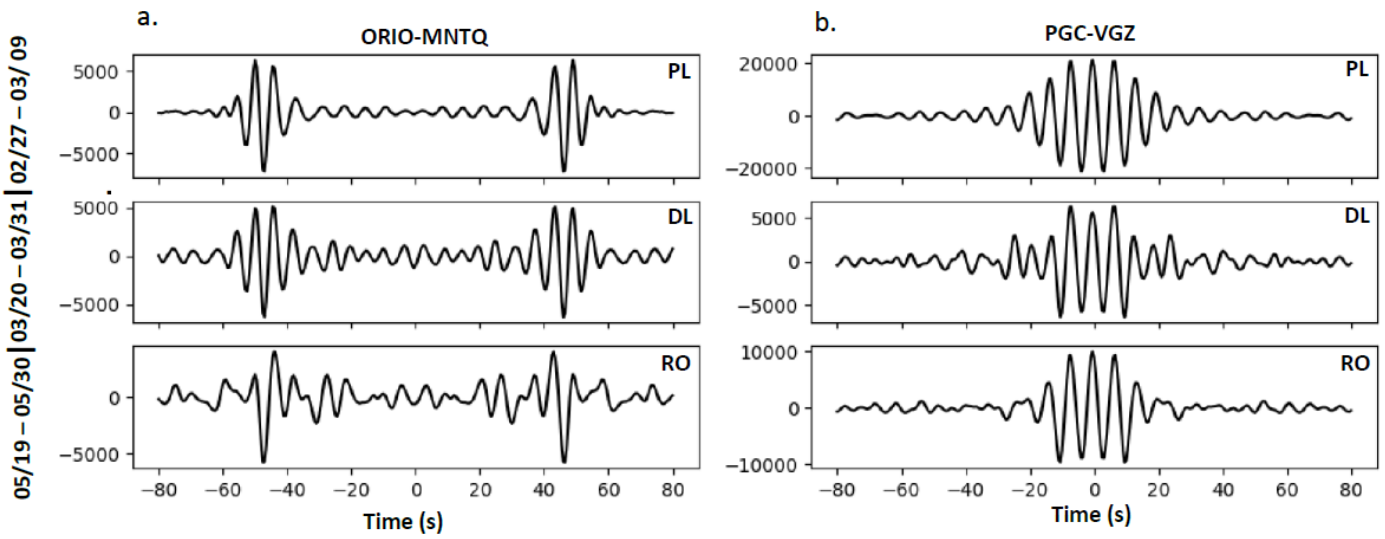

Figure 5. 5 Symmetric ambient noise cross-correlation functions for station-pairs ORIO-MNTQ (a) and PGC-VGZ (b) stacked over three date ranges representing the pre-lockdown (02/27 – 03/09; top row as marked by PL), during lockdown (03/20 – 03/31; middle row as marked by DL) and reopening (05/19 – 05/30; bottom row as marked by RO) phases.

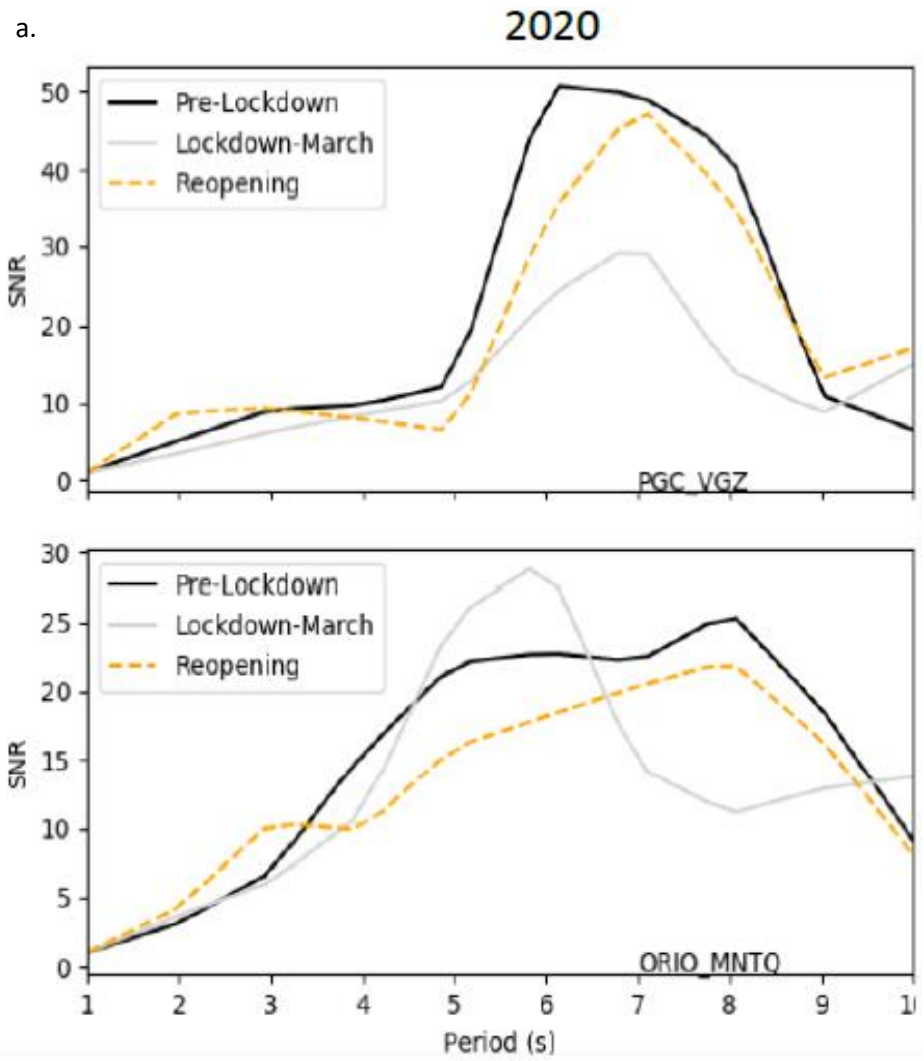

Figure 5. 6 Spectral SNR for the period band of 1-10 s calculated from noise cross-correlation functions of the two station pairs. (a) Different temporal windows in 2020 are marked by lines in different style. The upper and lower panels correspond to different station pairs. (b) For the station pair ORIO-MNTQ, the three panels correspond to different date ranges (PL: pre-lockdown; DL: during lockdown; RO: reopening), while different colors represent different years. (c) Same as (b) except for the station pair PGC-VGZ.

Figure 5.6 (continued).

b.

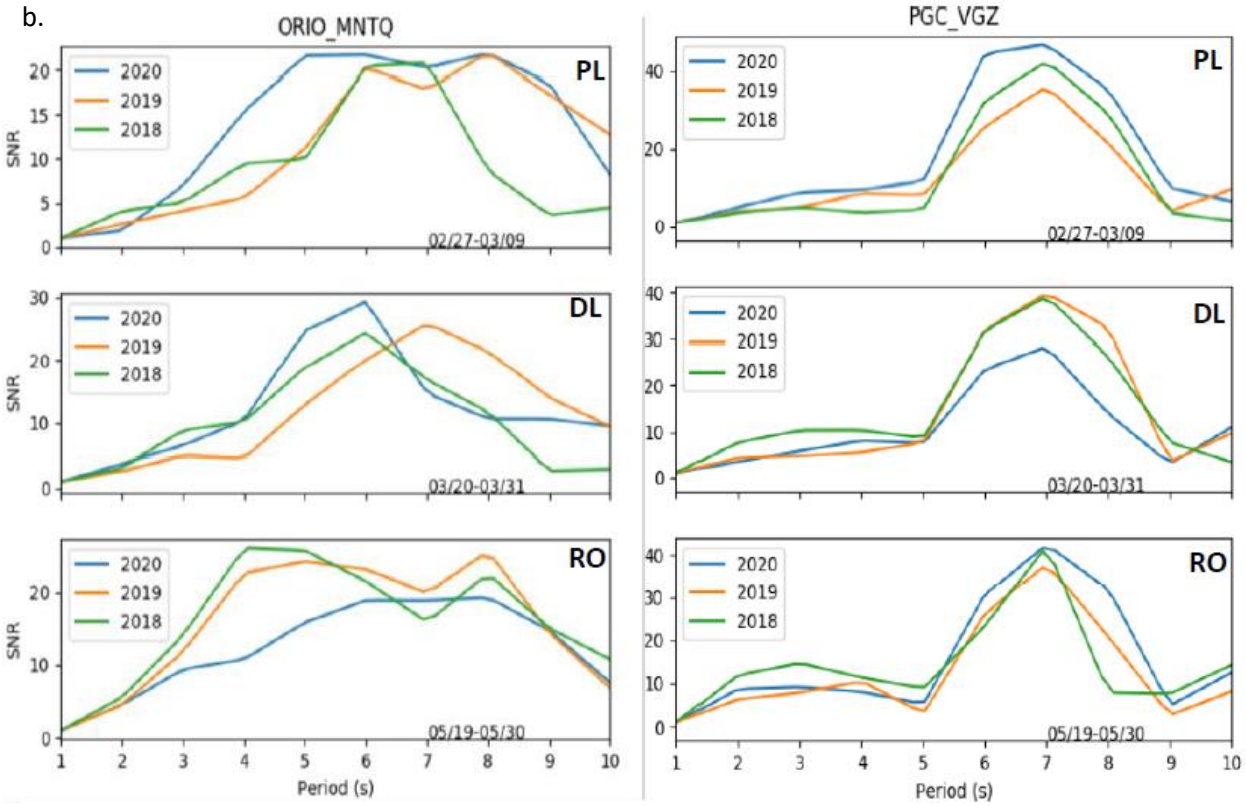

To evaluate how the observed temporal variations in 2020 might be linked to the unique COVID-19 situation, we compare the period-dependent SNR curves of the NCFs for the same three temporal windows in 2018 and 2019, and the results are shown in Figure 5.6b and 5.6c for ORIO-MNTQ and PGC-VGZ, respectively. In general, both station pairs have similar SNR levels at the shorter periods regardless of the year (e.g., <3 s for ORIO-MNTQ and <5 s for PGC-VGZ, Figure 5.6). In the secondary microseism band (4–8 s), on the other hand, the two station pairs appear to have very different SNR patterns. For PGC-VGZ, the 2020 curves have overall higher SNR during late February – early March (i.e., the pre-lockdown window, SNR_{pl}) and mid – late May (the reopening phase, SNR_{ro}), while the SNR is the lowest during the lockdown (SNR_{ld}). In contrast, the 2020 curves of ORIO-MNTQ can be either above or below the 2018 and 2019 curves depending on the specific temporal window and period (Figure 5.6b).

5.2.5 Discussion and Conclusion

Larger drops in the mean seismic power level than what we present in this study were reported by the news and social media in late March for Montreal and Ottawa (e.g., CBC news, https://www.cbc.ca/news/technology/noise-earthquakes-1.5531375; social media, https://www.linkedin.com/posts/activity-6655366886873800704-3dtI; both last accessed 11 September 2020), but these early assessments were based on observations within a short window immediately after the lockdown. The mean seismic power observed during the first two weeks of the lockdown is lower than the later weeks, suggesting that the mean drop is sharper in the earlier stage of the lockdown and becomes milder as the lockdown continues. For instance, while we observe a mean drop of ~17% at the Ottawa station (ORIO) between the pre-lockdown and lockdown windows, the drop is actually double in the first few days immediately after the Province's lockdown announcement (Figure 5.2b). A change in the level of low-magnitude local seismicity, which is prevalent in the <1 s period band (McNamara & Buland, 2004), could be responsible for the relatively high late-stage noise levels (Thouvenot & Bouchon, 2008). This possibility cannot be ruled out especially in the Charlevoix seismic zone of eastern Canada where intraplate seismicity is not uncommon (e.g., Adams and Basham, 1989; Mazzotti and Adams, 2005). Our attempt to verify this proposition was restricted by the detection threshold of the regional seismograph network, as there were only 2 events with Mn ranging between 0 and 1 in the Ottawa–Montreal area from March 12 to May 20, 2020 in NRCan's Canadian National Earthquake Database (http://earthquakescanada.nrcan.gc.ca/stndon/NEDB-BNDS/bulletin-en.php, last accessed on November 27, 2020). An alternative explanation is that, people's response to the lockdown was better during the initial weeks. Either way, it is clear that the drop of mean seismic power is not uniform across the lockdown phase.

The absence of double peaks in the secondary microseism band (i.e., periods of 4–8 s), together with the weak amplitude in the primary microseism band (i.e., 8–16 s) can be explained by the fact that our data are predominantly outside of the winter storm season. Within the cultural noise band, vehicular traffic dominates the band of periods ≤0.1 s (frequency ≥10 Hz, McNamara and Buland, 2004). The tripartite pattern obtained within this band in the PPSD analysis of the two eastern Canada stations (ORIO and MNTQ, Figure 5.4a and b), clearly shows a significant drop in vehicular traffic in the vicinity of the two stations during the lockdown and gradual reopening. For ORIO, when compared to the pre-lockdown level, a drop of ~5% and 1.5% is estimated for the lockdown and reopening phases, respectively. Similarly, for MNTQ, the drop is estimated to be ~8% and ~5% for the lockdown and reopening phases, respectively. The absence of a tripartite pattern in the corresponding band of the PPSD results of the two western stations (PGC and VGZ, Figure 5.4c and d), however, is perhaps due to both stations being located away from significant vehicular traffic.

As the effect of the lockdown is most apparent in the cultural noise band (Figure 5.4), we would expect a similar effect on the quality of NCFs. Obtaining NCFs for periods <1 s, however, requires ASN data from closely spaced seismograph arrays – a configuration very different from CNSN's. Instead, we focus our NCF quality analysis on the period range of 1–10 s, including the secondary microseism band, mainly because it is widely used by previous ANT studies as the most effective spectral band to map the uppermost crustal structures (e.g., Brandmayr *et al.*, 2016).

The tripartite pattern of $A_{pl} > A_{ld} > A_{ro}$ observed in the PPSDs for PGC and VGZ in the secondary microseism band (4–8 s, Figure 5.4c and d) is inconsistent with that of $SNR_{pl} > SNR_{ro} > SNR_{ld}$ in the period-dependent SNR results (upper panel, Figure 5.6a). This is somewhat surprising because a first-order correlation between the quality of NCF and the spectral

characteristics of microseisms measured at the constituent stations should be expected (Lepore & Grad, 2018). In this specific case, the corresponding SNR seems to be more correlated with the lockdown rather than the microseism activity. The coincidence of the lowest SNR with the timing of COVID-19 lockdown is further evident in the results of the multi-year comparison, i.e., the SNR during the 2020 COVID-19 lockdown has the lowest level relative to previous years (Figure 5.6c). We also note that the SNR is actually higher during the reopening phase, when the microseism energy is trending toward the lowest levels (Figure 5.4c and d). Given these observations, we infer that the period-dependent SNR of NCF may not be controlled by the seasonal variation in the ocean microseism alone. Further investigation into effects from other natural processes with meteorological and marine data in western Canada is probably needed.

For the eastern pair (ORIO-MNTQ), the SNR in the microseism band before the lockdown is also higher than that during the reopening (lower panel, Figure 5.6a), an observation similar to the PGC-VGZ result. It is unclear however, why the observed SNR is particularly high in the period band of 4–7 s during the lockdown. Nonetheless, this puzzling observation once again confirms our inference that the seasonal variation in the level of ocean microseisms is not the only controlling factor for the signal quality of NCF.

The mean values of ASN power shown in Figure 5.2 are based on averages within the temporal windows defined by the dates of official announcements. When examined in more detail, we notice that the overall levels of background seismic noise over the lockdown window are a factor of 5–10 lower at PGC and VGZ, which are located in western Canada, relative to MNTQ and ORIO in the east (Figure 5.2e). It is common to observe variations in the level of background seismic noise from one region to another, and they have been attributed to factors such as seasonal variability, site conditions and cultural activities (e.g. Given, 1990; Ali *et al.*, 2004). While the

COVID-19 lockdown should not be the source of the observed variations in the level of background noise between stations in eastern and western Canada, it has provided a unique opportunity to register the natural level of regional background noise with little or no influence from the anthropogenic factors. In our case, we infer that the generally higher levels of background seismic noise at MNTQ and ORIO, relative to that at PGC and VGZ, should not be solely attributed to the big difference in city size and population. Instead, we speculate that the significant difference in the tectonic settings from east to west may play the most important role. Studies have shown that seismic waves are more attenuated in the tectonically active western North America than the stable Canadian shield (Bao et al., 2016; Bowden et al., 2017). Therefore, the generally higher seismic attenuation in western Canada may have contributed to the low levels of ASN power observed in Sidney and Victoria. While this topic may be interesting, we note that it is beyond the main scope of this study.

Finally, we point out that including data from time-windows after the first wave of the pandemic (March – June, 2020) may not offer better results than what we have presented in this study. This is due to the asynchronized schedules of lockdown and re-opening adopted by various provinces during the subsequent waves compared to the first. We acknowledge that studying the temporal variation of NCFs due to the COVID-19 lockdown in the high-frequency band (> 1 Hz) is limited by the number of CNSN stations near Canadian city centers. A more detailed analysis of the ASN wavefield to determine the corresponding source locations and strength using data from closely-spaced array of seismic stations may provide better insight into the controlling factor(s) of the signal quality of NCF, especially in the high-frequency band (> 1 Hz). This is, however, very challenging with the current station density and network configuration. A possible solution, as a natural next step, is to expand the ASN dataset by including privately owned/operated

seismograph networks, in particular dense broadband seismic arrays established by the industry and individually owned Raspberry Shake sensors (typically with an effective frequency range of 0.7–44 Hz). It is probably helpful as well to conduct a systematic Canada-wide study of the detailed 3D distribution of seismic attenuation structures, similar to the ANT studies of Kao *et al.* (2013), to improve interpretations of our results.

5.2.6 Acknowledgements

We thank Stephen Hicks and three anonymous reviewers for their constructive comments. We benefit from discussions with John Cassidy, Andrew Schaeffer, Adebayo Ojo, and Allison Bent. This study is partially supported by a NSERC Discovery grant (HK) and the NRCan Environmental Geoscience Program. NRCan contribution number 20200572.

Chapter 6. Conclusions

6.1 Summary

For the first time, we apply a systematic approach to sudy the crustal structure of large portions of Canada (Appalachian-craton-Cordillera), at a resolution higher than previous surface wave studies in the regions. This PhD dissertation is thus the culmination of a uniquely broad, multi-scale and multi-purpose application of seismic noise analysis that spans Canada. The work comprises an extensive development and use of computer codes to process a massive volume of seismic data that spans the east and west of Canada and the neighbouring parts of the United States of America. It combines three topics spread over four chapters, based on manuscripts that are published, or being prepared. The topics covered are: (1) Imaging of sedimentary basins and sub-basin structures in eastern and western Canada using ambient seismic noise. (2) Combining measurements from ambient seismic noise with earthquake datasets for imaging crustal and mantle structures. (3) Temporal variation of seismic power spectra across the COVID-19 timeline and the potential impacts of COVID-19 lockdown on ambient noise correlation functions (NCFs). The main scientific contributions of this dissertation are summarized below.

The focus of Chapters 2 and 3 is to obtain the geometry and infer the evolution of the structure beneath the Gulf of St. Lawrence (GSL)'s Maritime basin in eastern Canada as well as the major sedimentary basins in western Canada, using shear wave velocities (*Vs*) derived from Rayleigh wave group velocities of ambient seismic NCFs.

In Chapter 2, I present the results of ambient noise tomography of the GSL in eastern Canada, obtained by processing 3 years of data recorded by 24 seismic stations. The major

contributions of this Chapter are derived from the 3-D *Vs* model we obtained for the GSL. From the model, we infer exactly how the sediment thickness varies across the composite Maritime basins, the geometry and location of Appalachian structural wedge and of the successive Appalachian terranes at depth. First-order order features from our results correspond well with the results of previous studies along collocated cross-sections. In general, the Grenville Province to the northwest, comprising of rocks of ancestral North America, and the Appalachian terranes to the southeast comprising mostly of exotic rocks, both have high *Vs*, a feature that is characteristic of their provenance. They are, however, separated in the middle by prominently low *Vs* to depths of at least 10 km, a feature that is characteristic of sedimentary basins. The 10-km estimate is based on the maximum depth measured on the cross-sections analyzed from our 3-D model. The basins were formed in response to the rifting and collision cycles that led to the accretion of multiple terranes in eastern Canada. The transition between the Grenville Province and the younger rocks of the basin and terranes occurs along the Appalachian Structural Front (ASF). As an interesting finding from this work, we show that although the location of the ASF from our results is largely consistent with the conventional location, it is offset by up to 200 km near the middle of the GSL. We also show that the Grenville Province is wedged out at depth along the Red Indian Line, which is known as the major suture zone between the rocks of Peri-Laurentia and Peri-Gondwana. One of the most interesting discoveries of this work is that the upper crust of the Peri-Gondwanan terranes that accreted onto North America as Avalon and Meguma is seismically distinct and detached from its basement. We interpret the basement as a remnant of the leading edge of the western African craton that was under-thrust beneath Meguma during the Alleghenian continent-continent collision and left behind during Mesozoic post-orogenic rifting associated with the opening of the Atlantic Ocean (Hutchinson et al., 1988; Keen et al., 1991; van Staal & Barr, 2012).

In Chapter 3, I present the results of ambient noise tomography of western Canada, obtained by processing 13 years of ambient seismic noise data recorded by 151 seismic stations. The major contributions of this Chapter are derived from the 3-D *Vs* model we obtained for western Canada. The model shows variations of the sediment thicknesses in all the major basins in western Canada. Within the Insular belt, the depths of both the basin and Moho is deepest beneath parts of the Queen Charlotte basin (QCB). Basin and Moho depths are at least 10 and 44 km respectively for the QCB, 6 and 40 km respectively for the Georgia Basin, along our studied cross-sections within the offshore basins. In the Intermontane belt, basin depths are at least 7 km within the Nechako and Bowser/Sustut basins. The Moho depths in the north and south of Intermontane belt, derived from the 1-D *Vs* models are 34 and 33 km respectively. In the Western Canada Sedimentary Basin (WCSB), the maximum depths are in excess of 6 and 10 km within the Alberta Deep basin and the Williston basin respectively. From our studied cross-sections, the Moho beneath the basin is shown to have a general southwest-ward dip except for the local variation beneath Montney basin. The thickest sediments estimated in this study are found beneath the QCB, Williston and Alberta basins. The deepest Moho depths estimated in this study underlie the Williston basin, parts of the QCB, the Alberta Deep basin and northern BC.

Although Chapters 2 and 3 are based on Rayleigh waves group velocity measurements, phase velocity offers better measurement uncertainties and structural resolution. However unlike group velocity, phase velocity measurements are sometimes affected by incorrect cycle/curve selection due to cycle skipping and poor signal resolution. In Chapter 4, I present a method to resolve this issue. The main objective of the new method is to combine short-period ambient seismic noise (ASN) dispersion curves with earthquake-derived dispersion curves along colinear paths. Theoretically, ASN dispersion curves derived from empirical Green functions (EGFs) in the

short period range should be continuous with earthquake-derived dispersion curves in the long-period range. This is not the case in many instances. Conventionally, an interstation distance criterion is applied to ensure quality ASN dispersion curves are derived. However, some dispersion curves obtained even after applying the criterion are still inconsistent with earthquake dispersion measurements from corresponding station pairs. In this work, we show that the conventional interstation distance criterion may be necessary, but insufficient to obtain reliable ambient noise phase velocity dispersion curve and propose a method to obtain reliable ASN dispersion curves that are consistent with colinear earthquake measurements. To address this, our method places more weight on the spectral quality to obtain data-consistent ASN phase velocity dispersion measurements that are compatible with earthquake data. We show that ASN dispersion curves derived using this method are consistent with earthquake-derived dispersion measurements. Furthermore, robust statistical analysis shows the method can significantly improve the quantity and the signal quality of EGFs selected for dispersion measurements and the surface wave tomography step over the traditional methods. The analysis also shows the spatial correlation of signal quality improvement and interstation distance. The method shows that the signal quality improvement is remarkable for larger interstation offsets but marginal for shorter interstation offsets.

Finally in Chapter 5, I present the temporal variation of seismic power spectra across the COVID-19 lockdown timeline in Canada, and quantify the potential impacts of the lockdown on ambient noise correlation functions (NCFs). The COVID-19 related lockdown that started in the first quarter of 2020, now referred to as the first wave, presented an unprecedented opportunity to observe and document a “quiet” earth and ocean, resulting from reduced global human activities (including air, land and maritime traffic). This article quantifies changes in the seismic power and

NCFs in response to the reduction in human activities related to the first wave of the COVID-19 pandemic in four Canadian cities – Ottawa and Quebec, in eastern Canada; Victoria and Sidney in western Canada. The contributions of this work are in three parts. In the first part, we find that changes in the seismic power measured at the seismic stations near the cities correspond to changes in the official lockdown announcements. The seismic power was maximum before the lockdown and minimum during lockdown. In the early reopening stage, seismic power in all the cities was at intermediate levels, in all the cities, indicating a gradual resumption of human related activities. This pattern is consistent with the spectral amplitude variations observed in the probabilistic power spectral density. Secondly, we show that nominal seismic power levels are orders of magnitude more in eastern Canada than the west. This could easily be discarded on the basis that cities in eastern Canada are much larger than the west, however, this pattern is sustained regardless of the lockdown status. In this case, we attribute the pattern to a combination of city/population size and attenuation differences in the east versus the west. Our interpretation is supported by previous North American attenuation models, which estimate higher attenuation for the younger western North American orogen than on the ancestral North American craton. The final contribution assesses the changes in the NCFs when compared within the COVID-19 timeframe and at corresponding timeframes across multiple years. We find that for the station pair in western Canada, NCF signal quality in the microseism spectral band was maximum before the lockdown, minimum during the lockdown and at intermediate levels during the reopening stages. This is consistent with the earlier mentioned pattern of seismic power variation across the same timeframe. The signal quality of NCFs in the microseism band is often linked to the level of ocean microseism energy generated from storms, which are strongest in winter and spring seasons. The lowest levels of signal quality observed for the western Canada station pair occurred over the

lockdown time window, which coincides with intermediate levels of microseism energy (near the end of winter season) observed for the same period. It therefore follows, that this level of microseism energy should correspond to an intermediate level of signal quality. Since this not the case, it is then possible that the reduction in signal quality is related to factors other than seasonal variation. To highlight this, the multi-year comparison shows that signal quality of NCF of the western station pair in the microseism band during the 2020 COVID-19 lockdown time window is the lowest when compared to those within the corresponding time windows in 2018 and 2019. In other words, taken together, both the multi-season and multi-year analyses show that there is a NCF signal degradation over the COVID-19 lockdown for the coastal station pair in western Canada, while the multi-season analysis shows that, there may be other factors affecting the signal quality of NCFs other than microseism energy from seasonal variation.

6.2 Recommendations for Future Work

The studies included in this dissertation demonstrate the power of the ASN methods in seismic imaging and monitoring over a large area. The method however depends on the quality and quantity of seismic data, as well as the station distribution relative to the structure being imaged. In western Canada, we had previously attempted to image the offshore basin and the shallow depths of the cascadia megathrust fault using ASN methods. Our attempt was hampered by the inadequate and poor quality ASN data recorded by the short-period ocean bottom seismometers (OBS) used in the study. This remains an interesting area of future research, which should be undertaken using adequately spaced broadband OBS.

In some parts of the cordillera, relativity high uncertainty estimates reduce the relaibilty of our results in contraining the western limits of the Canadian craton beneath the terranes. Future

ASN studies could focus on obtaining data with better coverage beneath the cordillera, perhaps taking advantage of new stations deployments in western Canada (e.g., part of the CN, C8 and PQ network). Another interesting area of future research is near the craton-Platform boundary, where we observed a large crust-mantle transition zone, thinner crust, and low-uppermost mantle *Vs*, should be further investigated using a combination of seismic methods.

In eastern Canada, our observation of a seismically distinct lower-crust beneath Avalon and Meguma terranes of Nova Scotia, interpreted here as a vestige of western African craton, opens up a window of future research opportunity. Seismic anisotropy studies could provide futher insights on the structural fabric beneath these terranes.

A practical application of ASN methods in public safety is in its use for monitoring seismic hazards. By combining ASN data with other datasets, monitoring of seismic hazards such as earthquakes and volcanoes is an interesting area of research, especially in western Canada, where relative seismic hazard probability is high.

Bibliography

Adams, J., & Basham, P. (1989). The Seismicity and Seismotectonics of Canada East of the Cordillera. *Geoscience Canada*. Retrieved from http://journals.lib.unb.ca/index.php/GC/article/view/3585

Aki, K. (1957). Space and time spectra of stationary stochastic waves, with special reference to microtremors. *Bull. Earthq. Res. Inst.*, *35*, 415–456.

Alabi, A. O., Camfield, P. A., & Gough, D. I. (1975). The North American Central Plains Conductivity Anomaly. *Geophysical Journal of the Royal Astronomical Society*, *43*(3), 815–833. https://doi.org/10.1111/j.1365-246X.1975.tb06197.x

Ali, J., Daud, M. D., Qaisar, M., & Ali, Z. (2004). Variation In Seismic Noise At Seismic Stations With Implications For Event Detection. *Pakistan Journal of Meteorology*, *1*(1). Retrieved from http://pjm.pmd.gov.pk/index.php/pjm/article/view/81

Anderson, R. G. (1993). A Mesozoic Stratigraphic and Plutonic Framework for Northwestern Stikinia (Iskut River Area), Northwestern British Columbia, Canada, 477–494.

Anna, L.O., Pollastro, R., and Gaswirth, S.B. (2013). Williston Basin Province—Stratigraphic and structural framework to a geologic assessment of undiscovered oil and gas resources, chap. 2 of U.S. Geological Survey Williston Basin Province Assessment Team, Assessment of undiscovered oil and gas resources of the Williston Basin Province of North Dakota, Montana, and South Dakota, 2010 (ver. 1.1, November 2013): U.S. Geological Survey Digital Data Series 69–W, 17 p.

Armstrong, R.L. (1988). Mesozoic and early Cenozoic magmatic evolution of the Canadian Cordillera. In Processes in continental lithospheric deformation. Edited by S. P. Clark, Jr.,

B. C. Burchfiel, and J. Suppe. Geological Society of America, Special Paper 218, pp. 55-92.

Arroucau, P., Rawlinson, N., & Sambridge, M. (2010). New insight into Cainozoic sedimentary basins and Palaeozoic suture zones in southeast Australia from ambient noise surface wave tomography. Geophysical Research Letters, 37(7). https://doi.org/10.1029/2009GL041974

Audet, P., Schutt, D. L., Schaeffer, A. J., Estève, C., Aster, R. C., & Cubley, J. F. (2020). Moho Variations across the Northern Canadian Cordillera. *Seismological Research Letters*. https://doi.org/10.1785/0220200166

Baird, D. J., Knapp, J. H., Steer, D. N., Brown, L. D., & Nelson, K. D. (1995). Upper-mantle reflectivity beneath the Williston basin, phase-change Moho, and the origin of intracratonic basins. *Geology*, *23*(5), 431–434. https://doi.org/10.1130/0091-7613(1995)023<0431:UMRBTW>2.3.CO;2

Bao, F., Ni, S., Xie, J., Zeng, X., Li, Z., & Li, Z. (2014). Validating Accuracy of Rayleigh-Wave Dispersion Extracted from Ambient Seismic Noise Via Comparison with Data from a Ground-Truth Earthquake. *Bulletin of the Seismological Society of America*, *104*(4), 2133–2141.

Bao, X., Dalton, C. A., Jin, G., Gaherty, J. B., & Shen, Y. (2016). Imaging Rayleigh wave attenuation with USArray. *Geophysical Journal International*, *206*(1), 241–259. https://doi.org/10.1093/gji/ggw151

Barr, S. M., Brisebois, D., & Macdonald, A. S. (1985). Carboniferous volcanic rocks of the Magdalen Islands, Gulf of St. Lawrence. *Canadian Journal of Earth Sciences*, *22*(11), 1679–1688. Retrieved from http://www.nrcresearchpress.com/doi/abs/10.1139/e85-176

Bastow, I. D., Thompson, D. A., Wookey, J., Kendall, J.-M., Helffrich, G., Snyder, D. B., et al. (2011). Precambrian plate tectonics: Seismic evidence from northern Hudson Bay, Canada. *Geology*, *39*(1), 91–94. https://doi.org/10.1130/G31396.1

Bensen, G. D., Ritzwoller, M. H., Barmin, M. P., Levshin, A. L., Lin, F., Moschetti, M. P., et al. (2007a). Processing seismic ambient noise data to obtain reliable broad-band surface wave dispersion measurements. *Geophysical Journal International*, *169*(3), 1239–1260. https://doi.org/10.1111/j.1365-246X.2007.03374.x

Bensen, G. D., Ritzwoller, M. H., & Shapiro, N. M. (2008). Broadband ambient noise surface wave tomography across the United States. *Journal of Geophysical Research: Solid Earth*, *113*(B5). https://doi.org/10.1029/2007JB005248

Beyreuther, M., Barsch, R., Krischer, L., Megies, T., Behr, Y., & Wassermann, J. (2010). ObsPy: A Python toolbox for seismology. *Seismological Research Letters*, *81*(3), 530–533.

Bodin, T., Sambridge, M., Tkalčić, H., Arroucau, P., Gallagher, K., & Rawlinson, N. (2012). Transdimensional inversion of receiver functions and surface wave dispersion. *Journal of Geophysical Research: Solid Earth*, *117*(B02301). Retrieved from http://onlinelibrary.wiley.com/doi/10.1029/2011JB008560/full

Bouzidi, Y. , Schmitt, D.R. , Burwash, R.A., and Kanasewich, E.R. (2002) Depth migration of deep seismic reflection profiles: crustal thickness variations in Alberta. Canadian Journal of Earth Sciences . 39 (3): 331-350.https://doi.org/10.1139/e01-080

Bowden, D. C., Tsai, V. C., & Lin, F.-C. (2017). Amplification and Attenuation Across USArray Using Ambient Noise Wavefront Tracking. Journal of Geophysical Research: Solid Earth, 122(12), 10,086-10,101. https://doi.org/10.1002/2017JB014804

Boyce, A., Bastow, I. D., Darbyshire, F. A., Ellwood, A. G., Gilligan, A., Levin, V., & Menke, W. (2016). Subduction beneath Laurentia modified the eastern North American cratonic edge: Evidence from P wave and S wave tomography. Journal of Geophysical Research: Solid Earth, 121(7), 5013–5030. Retrieved from http://onlinelibrary.wiley.com/doi/10.1002/2016JB012838/full

Brandmayr, E., Kuponiyi, A. P., Arroucau, P., & Vlahovic, G. (2016). Group velocity tomography of the upper crust in the eastern Tennessee seismic zone from ambient noise data. Tectonophysics, 688, 148–156. https://doi.org/10.1016/j.tecto.2016.09.035

Brown, D. A., Logan, J. M., Gunning, M. H., Orchard, M. J., & Bamber, W. E. (1991). Stratigraphic evolution of the Paleozoic Stikine assemblage in the Stikine and Iskut rivers area, northwestern British Columbia. Canadian Journal of Earth Sciences, 28(6), 958–972. https://doi.org/10.1139/e91-087

Brune, J., & Dorman, J. (1963). Seismic waves and earth structure in the Canadian shield. Bulletin of the Seismological Society of America, 53(1), 167–209.

Calvert A.J, Hayward N.E, Spratt J.E, & Craven J.A. (2011). Seismic reflection constraints on upper crustal structures in the volcanic-covered central Nechako basin, British Columbia. Canadian Journal of Earth Sciences. https://doi.org/10.1139/e10-097

Campillo, M. (2006). Phase and Correlation inRandom'Seismic Fields and the Reconstruction of the Green Function. Pure and Applied Geophysics, 163(2), 475–502.

Campillo, M., & Paul, A. (2003). Long-range correlations in the diffuse seismic coda. Science, 299(5606), 547–549. Retrieved from http://science.sciencemag.org/content/299/5606/547.short

Cannata, A., Cannavò, F., Di Grazia, G., Aliotta, M., Cassisi, C., De Plaen, R. S. M., et al. (2020). Seismic evidences of the COVID-19 lockdown measures: Eastern Sicily case of study (preprint). The evolving Earth surface/Seismics, seismology, geoelectrics, and electromagnetics/Seismology. https://doi.org/10.5194/se-2020-136

Carr, S. D. (1995). The southern Omineca Belt, British Columbia: new perspectives from the Lithoprobe Geoscience Program. Canadian Journal of Earth Sciences, 32(10), 1720–1739. https://doi.org/10.1139/e95-135

Carr, S. D., and Brown, R. L. (1990). Southern Cordilleran Lithoprobe transect lines 6 to 10: crustal structure and tectonic chronology. Southern Canadian Cordillera Transect Workshop, March 34, University of Calgary, Calgary, Alta., pp. 10-18.

Cassidy, J. F. (1995). Review: Receiver function studies in the southern Canadian Cordillera. Canadian Journal of Earth Sciences, 32(10), 1514–1519. https://doi.org/10.1139/e95-123

Cheraghi, S., Craven, J. A., & Bellefleur, G. (2015). Feasibility of virtual source reflection seismology using interferometry for mineral exploration: A test study in the Lalor Lake volcanogenic massive sulphide mining area, Manitoba, Canada. Geophysical Prospecting, 63(4), 833–848. Retrieved from http://onlinelibrary.wiley.com/doi/10.1111/1365-2478.12244/full

Clowes, R., Cook, F., Hajnal, Z., Hall, J., Lewry, J., Lucas, S., & Wardle, R. (1999). Canada's LITHOPROBE Project (Collaborative, multidisciplinary geoscience research leads to new understanding of continental evolution). Episodes, 22. https://doi.org/10.18814/epiiugs/1999/v22i1/002

Clowes, R. M., Zelt, C. A., Amor, J. R., & Ellis, R. M. (1995). Lithospheric structure in the southern Canadian Cordillera from a network of seismic refraction lines. Canadian Journal of Earth Sciences. https://doi.org/10.1139/e95-122

Clowes, R. M., Hammer, P. T., Fernández-Viejo, G., & Welford, J. K. (2005). Lithospheric structure in northwestern Canada from Lithoprobe seismic refraction and related studies: a synthesis. Canadian Journal of Earth Sciences, 42(6), 1277–1293.

Constable, S. C., Parker, R. L., & Constable, C. G. (1987). Occam's inversion: A practical algorithm for generating smooth models from electromagnetic sounding data. Geophysics, 52(3), 289–300. Retrieved from http://library.seg.org/doi/abs/10.1190/1.1442303

Cook , F.A., Green, A.G., Simony, P.S., Price, R.A., Parrish, R.R., Milkereit, B., Gordy, P.L., Brown, R.L., Coflin, K.C., and Patenaude, C. (1988). Lithoprobe seismic reflection structure of the southeastern Canadian Cordillera: Initial results: Tectonics , v. 7 p. 157-180.

Cook, F. A., Varsek, J. L., Clowes, R. M., Kanasewich, E. R., Spencer, C. S., Parrish, R. R., Brown, R. L., Carr, S. D., Johnson, B. J., and Price, R. A. (1992), Lithoprobe crustal reflection cross section of the southern Canadian Cordillera, 1, Foreland thrust and fold belt to Fraser River Fault, Tectonics, 11(1), 12– 35, doi:10.1029/91TC02332.

Cook, F. A. (1995) The reflection Moho beneath the southern Canadian Cordillera. Canadian Journal of Earth Sciences 1995;; 32 (10): 1520–1530. doi: https://doi.org/10.1139/e95-124

Cook, F. A., Varsek, J. L., & Thurston, J. B. (1995). Tectonic significance of gravity and magnetic variations along the Lithoprobe Southern Canadian Cordillera Transect. Canadian Journal of Earth Sciences, 32(10), 1584–1610. https://doi.org/10.1139/e95-128

Cook, F. A., Clowes, R. M., Snyder, D. B., Velden, A. J. van der, Hall, K. W., Erdmer, P., & Evenchick, C. A. (2004). Precambrian crust beneath the Mesozoic northern Canadian Cordillera discovered by Lithoprobe seismic reflection profiling. Tectonics, 23(2). https://doi.org/10.1029/2002TC001412

Cook, F. A., White, D. J., Jones, A. G., Eaton, D. W. S., Hall, J., & Clowes, R. M. (2010). How the crust meets the mantle: Lithoprobe perspectives on the Mohorovičić discontinuity and crust–mantle transitionThis article is one of a series of papers published in this Special Issue on the theme Lithoprobe — parameters, processes, and the evolution of a continent . Canadian Journal of Earth Sciences, 47(4), 315–351. https://doi.org/10.1139/E09-076

Creaser, B., & Spence, G. (2005). Crustal structure across the northern Cordillera, Yukon Territory, from seismic wide-angle studies: Omineca Belt to Intermontane Belt. Canadian Journal of Earth Sciences. 42(6): 1187-1203. https://doi.org/10.1139/e04-093

Dahlen, F. A., & Tromp, J. (1998). Theoretical global seismology. Princeton University Press.

Dalton, C. A., Gaherty, J. B., & Courtier, A. M. (2011). Crustal VS structure in northwestern Canada: Imaging the Cordillera-craton transition with ambient noise tomography. Journal of Geophysical Research: Solid Earth, 116(B12). https://doi.org/10.1029/2011JB008499

Darbyshire, F. A., & Eaton, D. W. (2010). The lithospheric root beneath Hudson Bay, Canada from Rayleigh wave dispersion: No clear seismological distinction between Archean and Proterozoic mantle. Lithos, 120(1–2), 144–159.

Darbyshire, F. A., Eaton, D. W., & Bastow, I. D. (2013). Seismic imaging of the lithosphere beneath Hudson Bay: Episodic growth of the Laurentian mantle keel. Earth and Planetary Science Letters, 373, 179–193.

Davis, E. E., & Riddihough, R. P. (1982). The Winona Basin: structure and tectonics. Canadian Journal of Earth Sciences, 19(4), 767–788. https://doi.org/10.1139/e82-065

Dehler, S. A., & Roest, W. (1998). Gravity anomaly map, Atlantic region, Canada. Geological Survey of Canada, Open File, (3658), http://geogratis.gc.ca/api/en/nrcan-rncan/ess-sst/0dedda44-ec1b-5d1b-9f7f-f67004f9e710.html. Retrieved from http://geogratis.gc.ca/api/en/nrcan-rncan/ess-sst/0dedda44-ec1b-5d1b-9f7f-f67004f9e710.html

DeMets, C., & Dixon, T. H. (1999). New kinematic models for Pacific-North America motion from 3 Ma to present, I: Evidence for steady motion and biases in the NUVEL-1A Model. Geophysical Research Letters, 26(13), 1921–1924. https://doi.org/10.1029/1999GL900405

Derode, A., Larose, E., Tanter, M., De Rosny, J., Tourin, A., Campillo, M., & Fink, M. (2003). Recovering the Green's function from field-field correlations in an open scattering medium (L). The Journal of the Acoustical Society of America, 113(6), 2973–2976.

Dettmer, J., Dosso, S. E., & Holland, C. W. (2010). Trans-dimensional geoacoustic inversion. The Journal of the Acoustical Society of America, 128(6), 3393–3405. Retrieved from http://scitation.aip.org/content/asa/journal/jasa/128/6/10.1121/1.3500674

Dias, F. L., Assumpção, M., Peixoto, P. S., Bianchi, M. B., Collaço, B., & Calhau, J. (2020). Using Seismic Noise Levels to Monitor Social Isolation: An Example From Rio de Janeiro, Brazil. Geophysical Research Letters, 47(16), e2020GL088748. https://doi.org/10.1029/2020GL088748

Díaz, J., Ruiz, M., Sánchez-Pastor, P. S., & Romero, P. (2017). Urban Seismology: on the origin of earth vibrations within a city. Scientific Reports, 7. https://doi.org/10.1038/s41598-017-15499-y

Diaz, J., Schimmel, M., Ruiz, M., & Carbonell, R. (2020). Seismometers Within Cities: A Tool to Connect Earth Sciences and Society. Frontiers in Earth Science, 8. https://doi.org/10.3389/feart.2020.00009

Dietrich, J., Lavoie, D., Hannigan, P., Pinet, N., Castonguay, S., Giles, P., & Hamblin, A. (2011). Geological setting and resource potential of conventional petroleum plays in Paleozoic basins in eastern Canada. Bulletin of Canadian Petroleum Geology, 59(1), 54–84. Retrieved from http://archives.datapages.com/data/cspg/data/059/059001/54_cspg590054.htm

Dosso, S. E., Holland, C. W., & Sambridge, M. (2012). Parallel tempering for strongly nonlinear geoacoustic inversion. The Journal of the Acoustical Society of America, 132(5), 3030–3040. Retrieved from http://scitation.aip.org/content/asa/journal/jasa/132/5/10.1121/1.4757639

Dosso, S. E., Dettmer, J., Steininger, G., & Holland, C. W. (2014). Efficient trans-dimensional Bayesian inversion for geoacoustic profile estimation. Inverse Problems, 30(11), 114018(29pp). Retrieved from http://iopscience.iop.org/article/10.1088/0266-5611/30/11/114018/meta

Dziewonski, A., Bloch, S., & Landisman, M. (1969). A technique for the analysis of transient seismic signals. Bulletin of the Seismological Society of America, 59(1), 427–444. Retrieved from http://www.bssaonline.org/content/59/1/427.short

Dziewonski, A. M., Hales, A. L., & Bolt, B. A. (1972). Numerical analysis of dispersed seismic waves. Seismology: Surface Waves and Earth Oscillations, 11, 39–84.

Eaton, D. W., Ross, G. M., & Clowes, R. M. (1999). Seismic-reflection and potential-field studies of the Vulcan structure, western Canada: A Paleoproterozoic Pyrenees? Journal of Geophysical Research: Solid Earth, 104(B10), 23255–23269. https://doi.org/10.1029/1999JB900204

Eberz, G. W., Clarke, D. B., Chatterjee, A. K., & Giles, P. S. (1991). Chemical and isotopic composition of the lower crust beneath the Meguma Lithotectonic Zone, Nova Scotia: evidence from granulite facies xenoliths. Contributions to Mineralogy and Petrology, 109(1), 69–88. Retrieved from http://www.springerlink.com/index/K1TQ018RPVT38W25.pdf

Edwards, B. R., & Russell, J. K. (1999). Northern Cordilleran volcanic province: A northern Basin and Range? Geology, 27(3), 243–246. https://doi.org/10.1130/0091-7613(1999)027<0243:NCVPAN>2.3.CO;2

Edwards, B. R., & Russell, J. K. (2000). Distribution, nature, and origin of Neogene–Quaternary magmatism in the northern Cordilleran volcanic province, Canada. GSA Bulletin, 112(8), 1280–1295. https://doi.org/10.1130/0016-7606(2000)112<1280:DNAOON>2.0.CO;2

Ekström, G., Abers, G. A., & Webb, S. C. (2009). Determination of surface-wave phase velocities across USArray from noise and Aki's spectral formulation. Geophysical Research Letters, 36(18). https://doi.org/10.1029/2009GL039131

England, T. D. J., & Bustin, R. M. (1998). Architecture of the Georgia Basin southwestern British Columbia. Bulletin of Canadian Petroleum Geology, 46(2), 288–320. https://doi.org/10.35767/gscpgbull.46.2.288

Erbe, C., Dähne, M., Gordon, J., Herata, H., Houser, D. S., Koschinski, S., et al. (2019). Managing the Effects of Noise From Ship Traffic, Seismic Surveying and Construction on Marine Mammals in Antarctica. Frontiers in Marine Science, 6. https://doi.org/10.3389/fmars.2019.00647

Ermert, L., Villaseñor, A., & Fichtner, A. (2016). Cross-correlation imaging of ambient noise sources. Geophysical Journal International, 204(1), 347–364. https://doi.org/10.1093/gji/ggv460

Evenchick, C. A. (1991). Geometry, evolution, and tectonic framework of the Skeena Fold Belt, north central British Columbia. Tectonics, 10(3), 527–546. https://doi.org/10.1029/90TC02680

Evenchick, C. A., Gabrielse, H., & Snyder, D. (2005). Crustal structure and lithology of the northern Canadian Cordillera: alternative interpretations of SNORCLE seismic reflection lines 2a and 2b,. Canadian Journal of Earth Sciences, 42(6), 1149–1161. https://doi.org/10.1139/e05-009

Fountain, D. M., & Christensen, N. I. (1989). Composition of the continental crust and upper mantle; a review. Geological Society of America Memoirs, 172, 711–742. Retrieved from http://memoirs.gsapubs.org/content/172/711.short

Fowler, C. M. R., & Nisbet, E. G. (1985). The subsidence of the Williston Basin. Canadian Journal of Earth Sciences, 22(3), 408–415. https://doi.org/10.1139/e85-039

Gabrielse, H., & Yorath, C. J. (1991). Geology of the Cordilleran Orogen in Canada. Geological Society of America. https://doi.org/10.1130/DNAG-GNA-G2

Gabrielse, H., Monger, J., Wheeler, J., & Yorath, C. (1991). Morphological belts, tectonic assemblages, and terranes, Part A. Geology of the Cordilleran Orogen of Canada. Edited by H. Gabrielse and CJ Yorath. Geological Survey of Canada, (4), 329–371.

Gehrmann, R. A., Dettmer, J., Schwalenberg, K., Engels, M., Dosso, S. E., & Özmaral, A. (2015). Trans-dimensional Bayesian inversion of controlled-source electromagnetic data in the German North Sea. Geophysical Prospecting, 63(6), 1314–1333. Retrieved from http://onlinelibrary.wiley.com/doi/10.1111/1365-2478.12308/full

Geological Survey Of Canada. (1989). Canadian National Seismograph Network. International Federation of Digital Seismograph Networks. https://doi.org/10.7914/SN/CN

Gibling, M. R., Culshaw, N., Rygel, M. C., & Pascucci, V. (2008). Chapter 6 The Maritimes Basin of Atlantic Canada: Basin Creation and Destruction in the Collisional Zone of Pangea. In Sedimentary Basins of the World (Vol. 5, pp. 211–244). Elsevier. Retrieved from http://linkinghub.elsevier.com/retrieve/pii/S1874599708000063

Gibney, E. (2020). Coronavirus lockdowns have changed the way Earth moves. Nature, 580(7802), 176–177.

Giles, P. S. (2009). Windsor Group (Late Mississippian) stratigraphy, Magdalen Islands, Quebec: a rare eastern Canadian record of late Visean basaltic volcanism. Atlantic Geology, 167–185. http://dx.doi.org/10.4138/5932

Given, H. K. (1990). Variations in broadband seismic noise at IRIS/IDA stations in the USSR with implications for event detection. Bulletin of the Seismological Society of America, 80(6B), 2072–2088.

Gordey, S. P., Geldsetzer, H. H. J., Morrow, D. W., Bamber, E. W., Henderson, C. M., Richards, B. C., et al. (1991). Upper Devonian to Middle Jurassic Assemblages. In H. Gabrielse &

C. J. Yorath, Geology of the Cordilleran Orogen in Canada. Geological Society of America. https://doi.org/10.1130/DNAG-GNA-G2.219

Green, A. C., Hajnal, Z., & Weber, W. (1985). An evolutionary model of the western churchill province and western margin of the superior province in Canada and the North-Central United States. Tectonophysics, 116(3–4), 281–322. https://doi.org/10.1016/0040-1951(85)90212-4

Green, P. J. (1995). Reversible jump Markov chain Monte Carlo computation and Bayesian model determination. Biometrika, 82(4), 711–732. Retrieved from http://biomet.oxfordjournals.org/content/82/4/711.short

Gu, Y. J., & Shen, L. (2015). Noise correlation tomography of Southwest Western Canada Sedimentary Basin. Geophysical Journal International, 202(1), 142–162. https://doi.org/10.1093/gji/ggv100

Gu, Y. J., Chen, Y., Dokht, R. M. H., & Wang, R. (2018). Precambrian Tectonic Discontinuities in Western Laurentia: Broadband Seismological Perspectives on the Snowbird and Great Falls Tectonic Zones. Tectonics, 37(5), 1411–1434. https://doi.org/10.1029/2017TC004843

Gunning, M. H. (1998). Definition and interpretation of Paleozoic volcanic domains, northwestern Stikinia, Iskut River Area, British Columbia., 1.

Hall, J., Wardle, R. J., Gower, C. F., Kerr, A., Coflin, K., Keen, C. E., & Carroll, P. (1995). Proterozoic orogens of the northeastern Canadian Shield: new information from the Lithoprobe ECSOOT crustal reflection seismic survey. Canadian Journal of Earth Sciences, 32(8), 1119–1131. Retrieved from http://www.nrcresearchpress.com/doi/abs/10.1139/e95-093

Hall, J., Marillier, F., & Dehler, S. (1998). Geophysical studies of the structure of the Appalachian orogen in the Atlantic borderlands of Canada. Canadian Journal of Earth Sciences, 35(11), 1205–1221. Retrieved from http://www.nrcresearchpress.com/doi/abs/10.1139/e98-075

Hammer, P. T. C., & Clowes, R. M. (2004). Accreted terranes of northwestern British Columbia, Canada: Lithospheric velocity structure and tectonics. Journal of Geophysical Research: Solid Earth, 109(B6). https://doi.org/10.1029/2003JB002749

Hannigan, P. K., Dietrich, J. R., Lee, P. J., & Osadetz, K. G. (2001). Petroleum resource potential of sedimentary basins on the Pacific margin of Canada. Retrieved from https://www.osti.gov/etdeweb/biblio/20196558

Haworth, R. T. (1978). Interpretation of geophysical data in the northern Gulf of St. Lawrence and its relevance to lower Paleozoic geology. Geological Society of America Bulletin, 89(7), 1091–1110. Retrieved from http://gsabulletin.gsapubs.org/content/89/7/1091.short

Hayward, N., Dehler, S. A., & Oakey, G. N. (2001). The structure of the northeastern Gulf of St. Lawrence, Canada: new insight from geophysical data analysis. Canadian Journal of Earth Sciences, 38(11), 1495–1516. https://doi.org/10.1139/cjes-38-11-1495

Herrmann, R. B. (2013) Computer programs in seismology: An evolving tool for instruction and research, *Seism. Res. Lettr.* 84, 1081-1088, doi:10.1785/0220110096

Hibbard, J. P., van Staal, C. R., Rankin, D. W., & Williams, H. (2006). Lithotectonic map of the Appalachian Orogen. Canada–United States of America: Geological Survey of Canada Map A, 2096, 2.

Higgs, R. (1991). Sedimentology, basin-fill architecture and petroleum geology of the Tertiary Queen Charlotte Basin, British Columbia, Canada. Geological Survey of Canada Paper 90-10, Edited by G.J. Woodsworth, 90–10, 337–371.

Hoffman, P. F. (1988). United Plates of America, The Birth of a Craton: Early Proterozoic Assembly and Growth of Laurentia. Annual Review of Earth and Planetary Sciences, 16(1), 543–603. https://doi.org/10.1146/annurev.ea.16.050188.002551

Holdsworth, R. E. (1994). Structural evolution of the Gander-Avalon terrane boundary: a reactivated transpression zone in the NE Newfoundland Appalachians. Journal of the Geological Society, 151(4), 629–646. Retrieved from http://jgs.lyellcollection.org/content/151/4/629.short

Hole, J. A., Clowes, R. M., & Ellis, R. M. (1993). Interpretation of three-dimensional seismic refraction data from western Hecate Strait, British Columbia: structure of the Queen Charlotte Basin. Canadian Journal of Earth Sciences, 30(7), 1427–1439. https://doi.org/10.1139/e93-123

Hole, J. A., Clowes R. M., & Ellis, R. M. (1993). Interpretation of three-dimensional seismic refraction data from western Hecate Strait, British Columbia: structure of the crust. Canadian Journal of Earth Sciences. 30(7): 1440-1452. https://doi.org/10.1139/e93-124

Hope, J., Eaton, D. W., & Ross, G. M. (1999). Lithoprobe seismic transect of the Alberta Basin: Compilation and overview. Bulletin of Canadian Petroleum Geology, 47(4), 331–345. https://doi.org/10.35767/gscpgbull.47.4.331

Howie, R. D. (1988). Upper Paleozoic evaporites of southeastern Canada, 1(380), 1–120. https://doi.org/doi:10.4095/126314

Hughes, S., Hall, J., & Luetgert, J. H. (1994). The seismic velocity structure of the Newfoundland Appalachian orogen. Journal of Geophysical Research: Solid Earth, 99(B7), 13633–13653. Retrieved from http://onlinelibrary.wiley.com/doi/10.1029/94JB00653/full

Hutchinson, D. R., Klitgord, K. D., Lee, M. W., & Trehu, A. M. (1988). US Geological Survey deep seismic reflection profile across the Gulf of Maine. Geological Society of America Bulletin, 100(2), 172–184. Retrieved from http://gsabulletin.gsapubs.org/content/100/2/172.short

Hyndman, R. D. (2010). The consequences of Canadian Cordillera thermal regime in recent tectonics and elevation: a reviewThis article is one of a series of papers published in this Special Issue on the theme Lithoprobe — parameters, processes, and the evolution of a continent .Geological Survey of Canada Contribution 20090195. Canadian Journal of Earth Sciences, 47(5), 621–632. https://doi.org/10.1139/E10-016

Hyndman, R. D., Lewis, T. J., Wright, J. A., Burgess, M., Chapman, D. S., & Yamano, M. (1982). Queen Charlotte fault zone: heat flow measurements. Canadian Journal of Earth Sciences, 19(8), 1657–1669. https://doi.org/10.1139/e82-141

Hyndman, Roy D., & Hamilton, T. S. (1990). Cenozoic relative plate motions along the northeastern Pacific margin and their association with Queen Charlotte area tectonics and volcanism. Pacific Geoscience Centre, Geological Survey of Canada.

Hyndman, Roy D, Flück, P., Mazzotti, S., Lewis, T. J., Ristau, J., & Leonard, L. (2005). Current tectonics of the northern Canadian Cordillera1, 2, 42, 20.

Idowu, O. A., Frederiksen, A. W., Cassidy, J. F., & Mareschal, J.-C. (2011a). Imaging the Nechako Basin, British Columbia, using ambient seismic noise. Canadian Journal of Earth Sciences, 48(6), 1038–1049. https://doi.org/10.1139/e11-007

Jackson, H. R. (2002). Seismic refraction profiles in the Gulf of Saint Lawrence and implications for extent of continuous Grenville lower crust. Canadian Journal of Earth Sciences, 39(1), 1–17. https://doi.org/10.1139/e01-054

Jackson, H. R., Marillier, F., & Hall, J. (1998). Seismic refraction data in the Gulf of Saint Lawrence: implications for the lower-crustal blocks. Canadian Journal of Earth Sciences, 35(11), 1222–1237. Retrieved from http://www.nrcresearchpress.com/doi/abs/10.1139/e98-043

James, S. R., Screaton, E. J., Russo, R. M., Panning, M. P., Bremner, P. M., Stanciu, A. C., et al. (2017). Hydrostratigraphy characterization of the Floridan aquifer system using ambient seismic noise. Geophysical Journal International, 209(2), 876–889.

Kao, H., Behr, Y., Currie, C. A., Hyndman, R., Townend, J., Lin, F.-C., et al. (2013a). Ambient seismic noise tomography of Canada and adjacent regions: Part I. Crustal structures. Journal of Geophysical Research: Solid Earth, 118(11), 5865–5887. https://doi.org/10.1002/2013JB010535

Katnick, D. C., & Mustard, P. S. (2003). Geology of Denman and Hornby islands, British Columbia: implications for Nanaimo Basin evolution and formal definition of the Geoffrey and Spray formations, Upper Cretaceous Nanaimo Group. Canadian Journal of Earth Sciences, 40(3), 375–393. https://doi.org/10.1139/e03-005

Keen, C. E., Keen, M. J., Nichols, B., Reid, I., Stockmal, G. S., Colman-Sadd, S. P., et al. (1986). Deep seismic reflection profile across the northern Appalachians. Geology, 14(2), 141–145. Retrieved from http://geology.gsapubs.org/content/14/2/141.short

Keen, C. E., Stockmal, G. S., Welsink, H., Quinlan, G., & Mudford, B. (1987). Deep crustal structure and evolution of the rifted margin northeast of Newfoundland: results from LITHOPROBE East. Canadian Journal of Earth Sciences, 24(8), 1537–1549. Retrieved from http://www.nrcresearchpress.com/doi/abs/10.1139/e87-150

Keen, C. E., MacLean, B. C., & Kay, W. A. (1991). A deep seismic reflection profile across the Nova Scotia continental margin, offshore eastern Canada. Canadian Journal of Earth Sciences, 28(7), 1112–1120. Retrieved from http://www.nrcresearchpress.com/doi/abs/10.1139/e91-100

Keen, M. J., & Williams, G. L. (1990). Geology of the continental margin of eastern Canada. Geological Survey of Canada.

Kennett, B. L. N., Sambridge, M. S., & Williamson, P. R. (1988). Subspace methods for large inverse problems with multiple parameter classes. Geophysical Journal International, 94(2), 237–247. Retrieved from http://gji.oxfordjournals.org/content/94/2/237.short

Kimman, W. P., Campman, X., & Trampert, J. (2012). Characteristics of seismic noise: fundamental and higher mode energy observed in the northeast of the Netherlands. Bulletin of the Seismological Society of America, 102(4), 1388–1399.

King, M. S., & Barr, S. M. (2004). Magnetic and gravity models across terrane boundaries in southern New Brunswick, Canada. Canadian Journal of Earth Sciences, 41(9), 1027–1047. Retrieved from http://www.nrcresearchpress.com/doi/abs/10.1139/e04-046

Klitgord, K., and H. Schouten (1986), Plate kinematics of the central Atlantic, Geol. N. Am., 1000, 351–378.

Knopoff, L. (1972). Observation and inversion of surface-wave dispersion. Tectonophysics, 13(1–4), 497–519.

Kuponiyi, A. P., Kao, H. (2021). Temporal Variation in Cultural Seismic Noise and Noise Correlation Functions during COVID-19 Lockdown in Canada. Seismological Research Letters. 0895-0695. doi: https://doi.org/10.1785/0220200330

Kuponiyi, A. P., Kao, H., van Staal, C. R., Dosso, S. E., Cassidy, J. F., & Spence, G. D. (2017). Upper crustal investigation of the Gulf of Saint Lawrence region, eastern Canada using ambient noise tomography. Journal of Geophysical Research: Solid Earth, 122(7), 5208–5227. https://doi.org/10.1002/2016JB013865

Landing, E. (2004). Precambrian–Cambrian boundary interval deposition and the marginal platform of the Avalon microcontinent. Journal of Geodynamics, 37(3), 411–435. Retrieved from http://www.sciencedirect.com/science/article/pii/S0264370704000158

Latham, T. S., Best, J., Chaimov, T., Oliver, J., Brown, L., & Kaufman, S. (1988). COCORP profiles from the Montana plains: The Archean cratonic crust and a lower crustal anomaly beneath the Williston basin. Geology, 16(12), 1073–1076. https://doi.org/10.1130/0091-7613(1988)016<1073:CPFTMP>2.3.CO;2

Lecocq, T., Hicks, S. P., Noten, K. V., Wijk, K. van, Koelemeijer, P., Plaen, R. S. M. D., et al. (2020). Global quieting of high-frequency seismic noise due to COVID-19 pandemic lockdown measures. Science. https://doi.org/10.1126/science.abd2438

Lefort, J. P., & Haworth, R. T. (1978). Geophysical study of basement fractures on the western European and eastern Canadian shelves: transatlantic correlations, and late Hercynian movements. Canadian Journal of Earth Sciences, 15(3), 397–404. Retrieved from http://www.nrcresearchpress.com/doi/abs/10.1139/e78-044

Leonard, L. J., Hyndman, R. D., Mazzotti, S., Nykolaishen, L., Schmidt, M., & Hippchen, S. (2007). Current deformation in the northern Canadian Cordillera inferred from GPS measurements. Journal of Geophysical Research: Solid Earth, 112(B11). https://doi.org/10.1029/2007JB005061

Lepore, S., & Grad, M. (2018). Analysis of the primary and secondary microseisms in the wavefield of the ambient noise recorded in northern Poland. Acta Geophysica, 66(5), 915–929. https://doi.org/10.1007/s11600-018-0194-2

Li, C., Chen, C., Dong, D., Kuponiyi, A. P., Dosso, S. E., & Su, D. (2018). Ambient noise tomography of the Shandong province and its implication for Cenozoic intraplate volcanism in Eastern China. Geochemistry, Geophysics, Geosystems, 19(9), 3286–3301. https://doi.org/10.1029/2018GC007515

Lin, F.-C., Ritzwoller, M. H., Townend, J., Bannister, S., & Savage, M. K. (2007). Ambient noise Rayleigh wave tomography of New Zealand. Geophysical Journal International, 170(2), 649–666. Retrieved from http://gji.oxfordjournals.org/content/170/2/649.short

Lindsey, N. J., Yuan, S., Lellouch, A., Gualtieri, L., Lecocq, T., & Biondi, B. (2020). City-Scale Dark Fiber DAS Measurements of Infrastructure Use During the COVID-19 Pandemic. Geophysical Research Letters, 47(16), e2020GL089931. https://doi.org/10.1029/2020GL089931

Lobkis, O. I., & Weaver, R. L. (2001a). On the emergence of the Green's function in the correlations of a diffuse field. The Journal of the Acoustical Society of America, 110(6), 3011–3017.

Lobkis, O. I., & Weaver, R. L. (2001b). On the emergence of the Green's function in the correlations of a diffuse field. The Journal of the Acoustical Society of America, 110(6), 3011–3017.

Luo, Y., Yang, Y., Xu, Y., Xu, H., Zhao, K., & Wang, K. (2015). On the limitations of interstation distances in ambient noise tomography. Geophysical Journal International, 201(2), 652–661.

Lyatsky, H. V. (1993). Basement-controlled structure and evolution of the Queen Charlotte Basin, west coast of Canada. Tectonophysics, 228(1–2), 123–140. https://doi.org/10.1016/0040-1951(93)90217-8

Lyatsky, H. V. (2006). Continental-Crust Structures on the Continental Margin of Western North America. Springer.

Lyatsky, H. V., & Haggart, J. W. (1993). Petroleum exploration model for the Queen Charlotte Basin area, offshore British Columbia. Canadian Journal of Earth Sciences, 30(5), 918–927. https://doi.org/10.1139/e93-077

Malinverno, A. (2002). Parsimonious Bayesian Markov chain Monte Carlo inversion in a nonlinear geophysical problem. Geophysical Journal International, 151(3), 675–688. Retrieved from http://gji.oxfordjournals.org/content/151/3/675.short

Manthei, C. D., Ducea, M. N., Girardi, J. D., Patchett, P. J., & Gehrels, G. E. (2010). Isotopic and geochemical evidence for a recent transition in mantle chemistry beneath the western Canadian Cordillera. Journal of Geophysical Research: Solid Earth, 115(B2). https://doi.org/10.1029/2009JB006562

Marillier, Francois, & Verhoef, J. (1989). Crustal thickness under the Gulf of St. Lawrence, northern Appalachians, from gravity and deep seismic data. Canadian Journal of Earth Sciences, 26(8), 1517–1532. Retrieved from http://www.nrcresearchpress.com/doi/abs/10.1139/e89-130

Marillier, François, Keen, C. E., Stockmal, G. S., Quinlan, G., Williams, H., Colman-Sadd, S. P., & O'Brien, S. J. (1989). Crustal structure and surface zonation of the Canadian Appalachians: implications of deep seismic reflection data. Canadian Journal of Earth

Sciences, 26(2), 305–321. Retrieved from http://www.nrcresearchpress.com/doi/abs/10.1139/e89-025

Mazzotti, S., & Adams, J. (2005). Rates and uncertainties on seismic moment and deformation in eastern Canada. Journal of Geophysical Research: Solid Earth, 110(B9). https://doi.org/10.1029/2004JB003510

McCrory, P. A., Blair, J. L., Oppenheimer, D. H., & Walter, S. R. (2006). Depth to the Juan de Fuca Slab Beneath the Cascadia Subduction Margin— A 3-D Model for Sorting Earthquakes. U.S. Geological Survey, 1.2, 13.

McLellan, M., Schaeffer, A. J., & Audet, P. (2018a). Structure and fabric of the crust and uppermost mantle in the northern Canadian Cordillera from Rayleigh-wave tomography. Tectonophysics, 724–725, 28–41. https://doi.org/10.1016/j.tecto.2018.01.011

McLellan, M., Schaeffer, A. J., & Audet, P. (2018b). Structure and fabric of the crust and uppermost mantle in the northern Canadian Cordillera from Rayleigh-wave tomography. Tectonophysics, 724, 28–41.

McNamara, D. E., & Buland, R. P. (2004). Ambient Noise Levels in the Continental United States. Bulletin of the Seismological Society of America, 94(4), 1517–1527. https://doi.org/10.1785/012003001

Meier, T., Dietrich, K., Stöckhert, B., & Harjes, H.-P. (2004). One-dimensional models of shear wave velocity for the eastern Mediterranean obtained from the inversion of Rayleigh wave phase velocities and tectonic implications. Geophysical Journal International, 156(1), 45–58.

Mercier, J.-P., Bostock, M. G., Cassidy, J. F., Dueker, K., Gaherty, J. B., Garnero, E. J., et al. (2009). Body-wave tomography of western Canada. Tectonophysics, 475(3), 480–492. https://doi.org/10.1016/j.tecto.2009.05.030

Mohorovicic, A. (1910), Das Beben Vom 8. x. 1909, in Jahrbuch Meterologie Observatorie Zagrab, vol. 9, pp. 1–63, ZagrebUniversity, Zagreb,Yugoslavia.

Monger, J. W. H., & Price, R. A. (1979). Geodynamic evolution of the Canadian Cordillera — progress and problems. Canadian Journal of Earth Sciences, 16(3), 770–791. https://doi.org/10.1139/e79-069

Monger, J. W. H., Price, R. A., & Tempelman-Kluit, D. J. (1982). Tectonic accretion and the origin of the two major metamorphic and plutonic welts in the Canadian Cordillera. Geology, 10(2), 70–75.

Morel-à-l'Huissier, P., Green, A. G., & Pike, C. J. (1987). Crustal refraction surveys across the Trans-Hudson Orogen/Williston Basin of south central Canada. Journal of Geophysical Research: Solid Earth, 92(B7), 6403–6420. https://doi.org/10.1029/JB092iB07p06403

Morel-A-L'Huissier, P., Green, A. G., Jones, A. G., Latham, T., Majorowicz, J. A., Drury, M. J., & Thomas, M. D. (1987). The Crust Beneath The Intracratonic Williston Basin From Geophysical Data, 92(B7), 6403–6420. https://doi.org/10.1029/JB092iB07p06403

Muller, J. E. (1977). Evolution of the Pacific Margin, Vancouver Island, and adjacent regions. Canadian Journal of Earth Sciences, 14(9), 2062–2085. https://doi.org/10.1139/e77-176

Murthy, G. S., & Rao, K. V. (1976). Paleomagnetism of Steel Mountain and Indian head anorthosites from western Newfoundland. Canadian Journal of Earth Sciences, 13(1), 75–83. Retrieved from http://www.nrcresearchpress.com/doi/abs/10.1139/e76-007

Musacchio, G., Mooney, W. D., Luetgert, J. H., & Christensen, N. I. (1997). Composition of the crust in the Grenville and Appalachian Provinces of North America inferred from Vp/Vs ratios. Journal of Geophysical Research: Solid Earth, 102(B7), 15225–15241. Retrieved from http://onlinelibrary.wiley.com/doi/10.1029/96JB03737/full

Mustard, P. (1994). The Upper Cretaceous Nanaimo Group, Georgia Basin. https://doi.org/10.4095/203246

Nelson, K. D., Baird, D. J., Walters, J. J., Hauck, M., & Brown, L. D. (1993). Trans-Hudson orogen and Williston basin in Montana and North Dakota: New COCORP deep-profiling results, 4.

Nielsen, A. R., & Porter, J. W. (1984). Pembina Oil Field — In Retrospect, 1–13.

Oakey, G. N., & Dehler, S. A. (1998). Magnetic anomaly map, Atlantic region, Canada (Geological Survey of Canada Open File 3659, scale 1 : 3 000 000 No. 3659). Retrieved from http://geoscan.nrcan.gc.ca/starweb/geoscan/servlet.starweb?path=geoscan/fulle.web&search1=R=209979

O'Brien, S. J., O'Brien, B. H., Dunning, G. R., & Tucker, R. D. (1996). Late Neoproterozoic Avalonian and related peri-Gondwanan rocks of the Newfoundland Appalachians. Special Papers-Geological Society Of America, 9–28. Retrieved from https://books.google.com/books?hl=en&lr=&id=xjOESSpelNsC&oi=fnd&pg=PA9&dq=late+neoproterozoic+avalonia&ots=R_cZemEVjj&sig=kQYpsR5YXEp_CihManKCIePZFe8

O'Leary, D. M., Clowes R. M., and Ellis R. M. (1993) Crustal velocity structure in the southern Coast Belt, British Columbia. Canadian Journal of Earth Sciences. 30(12): 2389-2403. https://doi.org/10.1139/e93-207

Pandey, A. P., Singh, A. P., Bansal, B. K., Suresh, G., & Prajapati, S. K. (2020). Appraisal of seismic noise scenario at national seismological network of India in COVID-19 lockdown situation. Geomatics, Natural Hazards and Risk, 11(1), 2095–2122. https://doi.org/10.1080/19475705.2020.1830187

Pawlak, A., Eaton, D. W., Bastow, I. D., Kendall, J.-M., Helffrich, G., Wookey, J., & Snyder, D. (2011). Crustal structure beneath Hudson Bay from ambient-noise tomography: implications for basin formation: Crustal structure beneath Hudson Bay from ANT. Geophysical Journal International, 184(1), 65–82. https://doi.org/10.1111/j.1365-246X.2010.04828.x

Peterson, J. (1993). Observation and Modelling of Seismic Background Noise, Open-File Report 93-322. https://doi.org/10.3133/ofr93322

Petrescu, L., Bastow, I. D., Darbyshire, F. A., Gilligan, A., Bodin, T., Menke, W., & Levin, V. (2016). Three billion years of crustal evolution in eastern Canada: Constraints from receiver functions. Journal of Geophysical Research: Solid Earth. Retrieved from http://onlinelibrary.wiley.com/doi/10.1002/2015JB012348/pdf

Piccinini, D., Giunchi, C., Olivieri, M., Frattini, F., Di Giovanni, M., Prodi, G., & Chiarabba, C. (2020). COVID-19 lockdown and its latency in Northern Italy: seismic evidence and socio-economic interpretation. Scientific Reports, 10(1), 16487. https://doi.org/10.1038/s41598-020-73102-3

Pilia, S., Rawlinson, N., Direen, N. G., Reading, A. M., Cayley, R., Pryer, L., et al. (2015). Linking mainland Australia and Tasmania using ambient seismic noise tomography: Implications for the tectonic evolution of the east Gondwana margin. Gondwana Research, 28(3), 1212–1227. https://doi.org/10.1016/j.gr.2014.09.014

Pinet, N. (2013). Gaspé Belt subsurface geometry in the northern Québec Appalachians as revealed by an integrated geophysical and geological study: 2—Seismic interpretation and potential field modelling results. Tectonophysics, 588, 100–117. Retrieved from http://www.sciencedirect.com/science/article/pii/S0040195112007743

Pinet, N., Lavoie, D., Keating, P., & Duchesne, M. (2014). The St Lawrence Platform and Appalachian deformation front in the St Lawrence Estuary and adjacent areas (Quebec, Canada): structural complexity revealed by magnetic and seismic imaging. Geological Magazine, 151(06), 996–1012. https://doi.org/10.1017/S0016756813001015

Ping, P., Chu, R., Zhang, Y., & Xie, J. (2020). Enhancing Signal-to-Noise Ratios of High-Frequency Rayleigh Waves Extracted from Ambient Seismic Noises in Topographic Region. Bulletin of the Seismological Society of America, 110(2), 793–802.

Plafker, G., & Berg, H. C. (Eds.). (1994). Geology of the southern Alaska margin. In The Geology of Alaska (pp. 389–449). Boulder, Colorado: Geological Society of America. https://doi.org/10.1130/DNAG-GNA-G1.389

Poli, P., Boaga, J., Molinari, I., Cascone, V., & Boschi, L. (2020). The 2020 coronavirus lockdown and seismic monitoring of anthropic activities in Northern Italy. Scientific Reports, 10(1), 9404. https://doi.org/10.1038/s41598-020-66368-0

Porter, J. W., Price, R. A., & McCrossan, R. G. (1982). The Western Canada Sedimentary Basin. Philosophical Transactions of the Royal Society of London. Series A, Mathematical and Physical Sciences, 305(1489), 169–192.

Potma, K., Weissenberger, J. A. W., Wong, P. K., & Gilhooly, M. G. (2001). Toward a sequence stratigraphic framework for the Frasnian of the Western Canada Basin. Bulletin of Canadian Petroleum Geology, 49(1), 37–85. https://doi.org/10.2113/49.1.37

Price, R. A. (1981). The Cordilleran foreland thrust and fold belt in the southern Canadian Rocky Mountains. In Thrust and nappe tectonics. Edited by K. R. Clay and N. J. Price. Geological Society of London, Special Publication 9, pp. 427-448.

Price, R. (1994). Cordilleran tectonics and the evolution of the Western Canada sedimentary basin (pp. 13–24).

Ramachandran, K., Hyndman, R. D., & Brocher, T. M. (2006). Regional P wave velocity structure of the Northern Cascadia Subduction Zone. Journal of Geophysical Research: Solid Earth, 111(B12). https://doi.org/10.1029/2005JB004108

Rawlinson, N., & Sambridge, M. (2003). Seismic traveltime tomography of the crust and lithosphere. Advances in Geophysics, 46, 81–199. Retrieved from https://books.google.ca/books?hl=en&lr=&id=ikFcqh1u1Q0C&oi=fnd&pg=PA81&dq=Seismic+traveltime+tomography+of+the+crust+and+lithosphere&ots=VCWm9qtVbC&sig=1h2qI1g3pOiCszQdvynCB9Bnclk

Reusch, D. N., & van Staal, C. R. (2011). The Dog Bay–Liberty Line and its significance for Silurian tectonics of the northern Appalachian orogen 1 2 1 This article is one of a series of papers published in this CJES Special Issue: In honour of Ward Neale on the theme of Appalachian and Grenvillian geology. 2 Geological Survey of Canada Contribution

20100257. Canadian Journal of Earth Sciences, 49(1), 239–258. Retrieved from http://www.nrcresearchpress.com/doi/abs/10.1139/e11-024

Rhie, J., & Romanowicz, B. (2004). Excitation of Earth's continuous free oscillations by atmosphere–ocean–seafloor coupling. Nature, 431(7008), 552–556. https://doi.org/10.1038/nature02942

Ricketts, B. (2008). Chapter 10 Cordilleran Sedimentary Basins of Western Canada Record 180 Million Years of Terrane Accretion. Sedimentary Basins of the World, 5, 363–394. https://doi.org/10.1016/S1874-5997(08)00010-5

Riddihough, R. (1984). Recent movements of the Juan de Fuca Plate System. Journal of Geophysical Research: Solid Earth, 89(B8), 6980–6994. https://doi.org/10.1029/JB089iB08p06980

Ritzwoller, M. H., Shapiro, N. M., Pasyanos, M. E., Bensen, G. D., & Yang, Y. (2005). Short period surface wave dispersion measurements from ambient seismic noise in North Africa, the Middle East, and Central Asia. Proceedings of the 27th Seismic Research Review: Ground-Based Nuclear Explosion Monitoring, 20–22. Retrieved from http://l2a.ucsd.edu/local/Meetings/2005_SRR/PAPERS/01-18.PDF

Rivers, T. (1997). Lithotectonic elements of the Grenville Province: review and tectonic implications. Precambrian Research, 86(3), 117–154. Retrieved from http://www.sciencedirect.com/science/article/pii/S0301926897000387

Rivers, T. (2008). Assembly and preservation of lower, mid, and upper orogenic crust in the Grenville Province—Implications for the evolution of large hot long-duration orogens. Precambrian Research, 167(3), 237–259. Retrieved from http://www.sciencedirect.com/science/article/pii/S0301926808001745

Rogers, G., & Dragert, H. (2003). Episodic Tremor and Slip on the Cascadia Subduction Zone: The Chatter of Silent Slip. Science, 300(5627), 1942–1943. https://doi.org/10.1126/science.1084783

Rohr, K., & Dietrich, J. (1990). Deep seismic reflection survey of Queen Charlotte basin. AAPG Bulletin (American Association of Petroleum Geologists); (USA), 74:5. Retrieved from https://www.osti.gov/biblio/6642967

Rohr, K. M. M., & Dietrich, J. R. (1992). Strike-slip tectonics and development of the Tertiary Queen Charlotte Basin, offshore western Canada: evidence from seismic reflection data. Basin Research, 4(1), 1–20. https://doi.org/10.1111/j.1365-2117.1992.tb00039.x

Ross, G. M. (1991). Precambrian basement in the Canadian Cordillera: an introduction. Canadian Journal of Earth Sciences, 28(8), 1133-1139.

Sabra, K. G., Gerstoft, P., Roux, P., Kuperman, W. A., & Fehler, M. C. (2005b). Extracting time-domain Green's function estimates from ambient seismic noise. Geophysical Research Letters, 32(3). https://doi.org/10.1029/2004GL021862

Sahabi, M., Aslanian, D., & Olivet, J. -L. (2004). Un nouveau point de départ pour l'histoire de l'Atlantique central, C. R. Geosci., 336, 1041–1052, doi:10.1016/j.crte.2004.03.017.

Sambridge, M., Gallagher, K., Jackson, A., & Rickwood, P. (2006). Trans-dimensional inverse problems, model comparison and the evidence. Geophysical Journal International, 167(2), 528–542. https://doi.org/10.1111/j.1365-246X.2006.03155.x

Sambridge, M. S. (1990). Non-linear arrival time inversion: constraining velocity anomalies by seeking smooth models in 3-D. Geophysical Journal International, 102(3), 653–677. Retrieved from http://gji.oxfordjournals.org/content/102/3/653.short

Sambridge, Malcolm. (2014). A parallel tempering algorithm for probabilistic sampling and multimodal optimization. Geophysical Journal International, 196(1), 357–374. https://doi.org/10.1093/gji/ggt342

Sato, Y. (1955). Analysis of Dispersed Surface Waves by means of Fourier Transform I. Bull. Earthq. Res. Inst., Univ. Tokyo, 33, 33–48.

Saygin, E., & Kennett, B. L. N. (2010). Ambient seismic noise tomography of Australian continent. Tectonophysics, 481(1), 116–125. https://doi.org/10.1016/j.tecto.2008.11.013

Schaeffer, A. J., & Lebedev, S. (2014). Imaging the North American continent using waveform inversion of global and USArray data. Earth and Planetary Science Letters, 402, 26–41. https://doi.org/10.1016/j.epsl.2014.05.014

Sethian, J. A., & Popovici, A. M. (1999). 3-D traveltime computation using the fast marching method. Geophysics, 64(2), 516–523. Retrieved from http://library.seg.org/doi/abs/10.1190/1.1444558

Shapiro, N. M., & Campillo, M. (2004b). Emergence of broadband Rayleigh waves from correlations of the ambient seismic noise. Geophysical Research Letters, 31(7).

Shapiro, N. M., Campillo, M., Stehly, L., & Ritzwoller, M. H. (2005). High-resolution surface-wave tomography from ambient seismic noise. Science, 307(5715), 1615–1618. Retrieved from http://science.sciencemag.org/content/307/5715/1615.short

Snieder, R. (2004). Extracting the Green's function from the correlation of coda waves: A derivation based on stationary phase. Physical Review E, 69(4), 046610.

Spence, G.D., & Asudeh, I. (1993). Seismic velocity structure of the Queen Charlotte basin beneath Hecate Strait. Canadian Journal of Earth Sciences, 30(4), 787–805.

Spence, George D., & McLean, N. A. (1998). Crustal seismic velocity and density structure of the Intermontane and Coast belts, southwestern Cordillera. Canadian Journal of Earth Sciences, 35(12), 1362–1379. https://doi.org/10.1139/e98-070

Spencer, C., Green, A., Milkereit, B., Luetgert, J., Stewart, D., Unger, J., et al. (1989). The extension of Grenville Basement beneath the northern Appalachians: Results from the Quebec-Maine seismic reflection and refraction surveys. Tectonics, 8(4), 677–696. Retrieved from http://onlinelibrary.wiley.com/doi/10.1029/TC008i004p00677/fullvan Staal, C. R. (1987). Tectonic setting of the Tetagouche group in northern New Brunswick: Implications for plate tectonic models of the northern Appalachians. Canadian Journal of Earth Sciences, 24(7), 1329–1351. Retrieved from http://www.nrcresearchpress.com/doi/abs/10.1139/e87-128

Spratt, J., & Craven, J. (2011). Near-surface and crustal-scale images of the Nechako basin, British Columbia, Canada, from magnetotelluric investigations. Canadian Journal of Earth Sciences, 48(6), 987-999.

van Staal, C. R. (1994). Brunswick subduction complex in the Canadian Appalachians: Record of the Late Ordovician to Late Silurian collision between Laurentia and the Gander margin of Avalon. Tectonics, 13(4), 946–962. Retrieved from http://onlinelibrary.wiley.com/doi/10.1029/93TC03604/full

van Staal, C. R., & Barr, S. M. (2012). Lithospheric architecture and tectonic evolution of the Canadian Appalachians and associated Atlantic margin. Tectonic Styles in Canada: The Lithoprobe Perspective: Geological Association of Canada Special Paper, 49, 55. Retrieved from http://eps.harvard.edu/files/eps/files/chapter2_12may2012watermark.pdf

van Staal, C. R., Sullivan, R. W., & Whalen, J. B. (1996). Provenance and tectonic history of the Gander Zone in the Caledonian/Appalachian orogen: Implications for the origin and assembly of Avalon. Special Papers-Geological Society Of America, 347–368. Retrieved from https://books.google.com/books?hl=en&lr=&id=xjOESSpelNsC&oi=fnd&pg=PA347&dq=provenance+and+tectonic+history+of+the+gander&ots=R_cZemAXho&sig=eoeTkEwvo_aRDT6GDsJQpx0krsE

van Staal, C. R., Dewey, J. F., Mac Niocaill, C., & McKerrow, W. S. (1998). The Cambrian-Silurian tectonic evolution of the northern Appalachians and British Caledonides: history of a complex, west and southwest Pacific-type segment of Iapetus. Geological Society, London, Special Publications, 143(1), 197–242. Retrieved from http://sp.lyellcollection.org/content/143/1/197.short

van Staal, C. R., Whalen, J. B., McNicoll, V. J., Pehrsson, S., Lissenberg, C. J., Zagorevski, A., et al. (2007). The Notre Dame arc and the Taconic orogeny in Newfoundland. Geological Society of America Memoirs, 200, 511–552. Retrieved from http://memoirs.gsapubs.org/content/200/511.short

van Staal, C. R., Currie, K. L., Rowbotham, G., Goodfellow, W., & Rogers, N. (2008). PT paths and exhumation of Late Ordovician-Early Silurian blueschists and associated metamorphic nappes of the Salinic Brunswick subduction complex, northern Appalachians. Geological Society of America Bulletin, 120, 1455–1477.

van Staal, C. R., Whalen, J. B., Valverde-Vaquero, P., Zagorevski, A., & Rogers, N. (2009). Pre-Carboniferous, episodic accretion-related, orogenesis along the Laurentian margin of the

northern Appalachians. Geological Society, London, Special Publications, 327(1), 271–316. Retrieved from http://sp.lyellcollection.org/content/327/1/271.short

Stacey, R. A. (1973). Gravity Anomalies, Crustal Structure, and Plate Tectonics in the Canadian Cordillera. Canadian Journal of Earth Sciences, 10(5), 615–628. https://doi.org/10.1139/e73-062

Steininger, G., Dettmer, J., Dosso, S. E., & Holland, C. W. (2013). Trans-dimensional joint inversion of seabed scattering and reflection data. The Journal of the Acoustical Society of America, 133(3), 1347–1357. Retrieved from http://scitation.aip.org/content/asa/journal/jasa/133/3/10.1121/1.4789930

Stephenson, A.L., Spence, G.D., Wang, K., Hole, J.A., Miller, K.C., Clowes, R.M., Harder, S.H., & Kaip, G.M. (2011). Crustal velocity structure of the southern Nechako basin, British Columbia, from wide-angle seismic traveltime inversion. Canadian Journal of Earth Sciences. 48(6): 1050-1063. https://doi.org/10.1139/e11-006

Stephenson, R. A., Zelt, C. A., Ellis, R. M., Hajnal, Z., Morel-À-L'Huissier, P., Mereu, R. F., et al. (1989). Crust and Upper Mantle Structure and the Origin of the Peace River Arch. Bulletin of Canadian Petroleum Geology, 37(2), 224–235. https://doi.org/10.35767/gscpgbull.37.2.224

Stewart, D. B., Wright, B. E., Unger, J. D., Phillips, J. D., & Hutchinson, D. R. (1993). Global Geoscience Transect 8: Quebec-Maine-Gulf of Maine Transect, Southeastern Canada, Northeastern United States of America. Retrieved from http://pubs.usgs.gov/imap/2329/report.pdf

Struik, L. (1992). Eastern Canadian Cordillera : Implications of a balanced basement (Mason R: Basement Tectonics 7. Proceedings of the International Conferences on Basement

Tectonics, Vol. 1). Springer, Dordrecht. Retrieved from https://link-springer-com.ezproxy.library.uvic.ca/chapter/10.1007/978-94-017-0833-3_21

Suda, N. (1998). Earth's Background Free Oscillations. Science, 279(5359), 2089–2091. https://doi.org/10.1126/science.279.5359.2089

Teskey, D. J., Dods, S. D., & Hood, P. J. (1982). Compilation techniques for the 1: 1 million magnetic anomaly map series. Geological Survey of Canada, Paper, 351–358.

Thompson, D. A., Bastow, I. D., Helffrich, G., Kendall, J.-M., Wookey, J., Snyder, D. B., & Eaton, D. W. (2010). Precambrian crustal evolution: Seismic constraints from the Canadian Shield. Earth and Planetary Science Letters, 297(3), 655–666. https://doi.org/10.1016/j.epsl.2010.07.021

Thomson, D. J. M., & Barclay, D. R. (2020). Real-time observations of the impact of COVID-19 on underwater noise. The Journal of the Acoustical Society of America, 147(5), 3390–3396. https://doi.org/10.1121/10.0001271

Thouvenot, F., & Bouchon, M. (2008). What is the Lowest Magnitude Threshold at Which an Earthquakecan be Felt or Heard, or Objects Thrown into the Air? In J. Fréchet, M. Meghraoui, & M. Stucchi (Eds.), Historical Seismology: Interdisciplinary Studies of Past and Recent Earthquakes (pp. 313–326). Dordrecht: Springer Netherlands. https://doi.org/10.1007/978-1-4020-8222-1_15

Tian, Y., & Ritzwoller, M. H. (2015). Directionality of ambient noise on the Juan de Fuca plate: Implications for source locations of the primary and secondary microseisms. Geophysical Journal International, 201(1), 429–443.

Tollo, R. P., Corriveau, L., McLelland, J., & Bartholomew, M. J. (2004). Proterozoic tectonic evolution of the Grenville orogen in North America: An introduction. Geological Society

of America Memoirs, 197, 1–18. Retrieved from http://memoirs.gsapubs.org/content/197/1.full

Unsworth, M. (2015). Magnetotelluric studies of lithospheric structure beneath Western Canada: insights into plate tecton. Retrieved October 10, 2020, from https://www.csegrecorder.com/articles/view/magnetotelluric-studies-of-lithospheric-structure-beneath-western-canada

Varsek, J. L., Cook, F. A., Clowes, R. M., Journeay, J. M., Monger, J. W. H., Parrish, R. R., et al. (1993). Lithoprobe crustal reflection structure of the Southern Canadian Cordillera 2: Coast mountains transect. Tectonics, 12(2), 334–360. https://doi.org/10.1029/92TC00598

van der Velden, A. J., van Staal, C. R., & Cook, F. A. (2004). Crustal structure, fossil subduction, and the tectonic evolution of the Newfoundland Appalachians: Evidence from a reprocessed seismic reflection survey. Geological Society of America Bulletin, 116(11–12), 1485–1498. Retrieved from http://gsabulletin.gsapubs.org/content/116/11-12/1485.short

Voogd, B., & Keen, C. E. (1987). Lithoprobe east: results from reflection profiling of the continental margin: Grand Banks Region. Geophysical Journal International, 89(1), 195–200. Retrieved from http://gji.oxfordjournals.org/content/89/1/195.short

Wade, J. A., Brown, D. E., Traverse, A., & Fensome, R. A. (1996). The Triassic-Jurassic Fundy Basin, eastern Canada: regional setting, stratigraphy and hydrocarbon potential. Atlantic Geology, 32, 189–231. Retrieved from http://archives.datapages.com/data/atlantic-geology-journal/data/032/032003/pdfs/189.pdf

Waldron, J. W., & van Staal, C. R. (2001). Taconian orogeny and the accretion of the Dashwoods block: A peri-Laurentian microcontinent in the Iapetus Ocean. Geology, 29(9), 811–814. Retrieved from http://geology.gsapubs.org/content/29/9/811.short

Waldron, J. W., & Stockmal, G. S. (1994). Structural and tectonic evolution of the Humber Zone, western Newfoundland 2. A regional model for Acadian thrust tectonics. Tectonics, 13(6), 1498–1513. Retrieved from http://onlinelibrary.wiley.com/doi/10.1029/94TC01505/full

Waldron, J. W. F., Barr, S. M., Park, A. F., White, C. E., & Hibbard, J. (2015). Late Paleozoic strike-slip faults in Maritime Canada and their role in the reconfiguration of the northern Appalachian orogen. Tectonics, 34(8), 2015TC003882. https://doi.org/10.1002/2015TC003882

Walsh, W., Salad Hersi, O., & Hayes, M. (2005). LIARD BASIN - MIDDLE DEVONIAN EXPLORATION.

Wang, Y., Lin, F.-C., Schmandt, B., & Farrell, J. (2017). Ambient noise tomography across Mount St. Helens using a dense seismic array. Journal of Geophysical Research: Solid Earth, 122(6), 4492–4508.

Wapenaar, K. (2004). Retrieving the elastodynamic Green's function of an arbitrary inhomogeneous medium by cross correlation. Physical Review Letters, 93(25), 254301.

Welford, J. K., Clowes, R. M., Ellis, R. M., Spence, G. D., Asudeh, I., & Hajnal, Z. (2001). Lithospheric structure across the craton–Cordilleran transition of northeastern British Columbia. Canadian Journal of Earth Sciences, 38(8), 1169–1189. https://doi.org/10.1139/e01-020

Welford J. K., Clowes R. M. (2006). Three-dimensional seismic reflection investigation of the upper crustal Winagami sill complex of northwestern Alberta, Canada, Geophysical

Journal International, Volume 166, Issue 1, July 2006, Pages 155–169, https://doi-org.ezproxy.library.uvic.ca/10.1111/j.1365-246X.2006.02805.x

Wessel, P., & Smith, W. H. (1995). New version of the generic mapping tools. Eos, Transactions American Geophysical Union, 76(33), 329–329.

Wessel, P., Smith, W. H., Scharroo, R., Luis, J., & Wobbe, F. (2013). Generic mapping tools: improved version released. Eos, Transactions American Geophysical Union, 94(45), 409–410.

Wiener, R. W., McLelland, J. M., Isachsen, Y. W., & Hall, L. M. (1984). Stratigraphy and structural geology of the Adirondack Mountains, New York: Review and synthesis. Geological Society of America Special Papers, 194, 1–56. Retrieved from http://specialpapers.gsapubs.org/content/194/1.abstract

Williams, H., & St. Julien, P. (1982). The Baie Verte-Brompton Line: early Paleozoic continent-ocean interface in the Canadian Appalachians. Geological Association of Canada, Special Paper, 24, 177–208.

Williams, H., Currie, K. L., & Piasecki, M. A. J. (1993). The Dog Bay Line: a major Silurian tectonic boundary in northeast Newfoundland. Canadian Journal of Earth Sciences, 30(12), 2481–2494. Retrieved from http://www.nrcresearchpress.com/doi/abs/10.1139/e93-215

Williams, Harold. (1979). Appalachian orogen in Canada. Canadian Journal of Earth Sciences, 16(3), 792–807. Retrieved from http://www.nrcresearchpress.com/doi/abs/10.1139/e79-070

Williams, Harold. (1995). Geology of the Appalachian—Caledonian Orogen in Canada and Greenland. Geological Society of America. Retrieved from https://books.google.com/books?hl=en&lr=&id=0N-

lBQAAQBAJ&oi=fnd&pg=PP1&dq=williams+appalachian+geology&ots=fIRhHUZUyP&sig=jzrId-olvZtAw86XvC4LOs9XJ9o

Williams, Harold, & Piasecki, M. A. J. (1990). The Cold Spring Melange and a possible model for Dunnage–Gander zone interaction in central Newfoundland. Canadian Journal of Earth Sciences, 27(8), 1126–1134. Retrieved from http://www.nrcresearchpress.com/doi/abs/10.1139/e90-117

Williams, Harold, Colman-Sadd, S. P., & Swinden, H. S. (1988). Tectonic-stratigraphic subdivisions of central Newfoundland. Current Research, Part B. Geological Survey of Canada, Paper, 88, 91–98.

Wilson, R. A., Burden, E. T., Bertrand, R., Asselin, E., & McCracken, A. D. (2004). Stratigraphy and tectono-sedimentary evolution of the Late Ordovician to Middle Devonian Gaspé Belt in northern New Brunswick: evidence from the Restigouche area. Canadian Journal of Earth Sciences, 41(5), 527–551. Retrieved from http://www.nrcresearchpress.com/doi/abs/10.1139/e04-011

Wilson, T. (2019). Unconventional petroleum systems analysis of upper Devonian organic-rich shales in the Horn River and Liard Basins, and adjacent Western Canadian Sedimentary Basin. University of British Columbia. https://doi.org/10.14288/1.0384918

Wright, G., McMechan, M., Potter, D., & Holter, M. (1994). Structure and architecture of the Western Canada sedimentary basin. Geological Atlas of the Western Canada Sedimentary Basin, 4, 25–40.

Xiao, H., Eilon, Z. C., Ji, C., & Tanimoto, T. (2020). COVID-19 Societal Response Captured by Seismic Noise in China and Italy. Seismological Research Letters, 91(5), 2757–2768. https://doi.org/10.1785/0220200147

Yang, Y., & Ritzwoller, M. H. (2008). Characteristics of ambient seismic noise as a source for surface wave tomography. Geochemistry, Geophysics, Geosystems, 9(2)(2). https://doi.org/10.1029/2007GC001814

Yao, H., van der Hilst, R. D., & de Hoop, M. V. (2006). Surface-wave array tomography in SE Tibet from ambient seismic noise and two-station analysis - I. Phase velocity maps. Geophysical Journal International, 166(2), 732–744. https://doi.org/10.1111/j.1365-246X.2006.03028.x

Yao, H., Gouedard, P., Collins, J. A., McGuire, J. J., & van der Hilst, R. D. (2011). Structure of young East Pacific Rise lithosphere from ambient noise correlation analysis of fundamental-and higher-mode Scholte-Rayleigh waves. Comptes Rendus Geoscience, 343(8), 571–583.

Yorath, C. J. (1980). The Apollo structure in Tofino Basin, Canadian Pacific continental shelf. Canadian Journal of Earth Sciences, 17(6), 758–775. https://doi.org/10.1139/e80-072

Yorath, C. J., Green, A. G., Clowes, R. M., Brown, A. S., Brandon, M. T., Kanasewich, E. R., Hyndman, R. D., & Spencer, C. (1985). Lithoprobe, southern Vancouver Island: Seismic reflection sees through Wrangellia to the Juan de Fuca plate. Geology, 13(11), 759-762. https://doi.org/10.1130/0091-7613(1985)13<759:LSVISR>2.0.CO;2

Yorath, C. J. (1991). Upper Jurassic to Paleogene Assemblages. In H. Gabrielse & C. J. Yorath, Geology of the Cordilleran Orogen in Canada. Geological Society of America. https://doi.org/10.1130/DNAG-GNA-G2.329

Yorath, C. J., Gordy, P. L., Williams, G. K., Bustin, R. M., Bell, R. T., Souther, J. G., & Halstead, E. C. (1991). Energy and Groundwater Resources of the Canadian Cordillera. In H.

Gabrielse & C. J. Yorath, Geology of the Cordilleran Orogen in Canada. Geological Society of America. https://doi.org/10.1130/DNAG-GNA-G2.769

Yuan, T., Spence, G. D., & Hyndman, R. D. (1992). Structure beneath Queen Charlotte Sound from seismic-refraction and gravity interpretations. Canadian Journal of Earth Sciences, 29(7), 1509–1529.

Zagorevski, A., & van Staal, C. R. (2011). The record of Ordovician arc–arc and arc–continent collisions in the Canadian Appalachians during the closure of Iapetus. In Arc-Continent Collision (pp. 341–371). Springer. Retrieved from http://link.springer.com/chapter/10.1007/978-3-540-88558-0_12

Zagorevski, A., van Staal, C. R., McNicoll, V., & Rogers, N. (2007). Upper Cambrian to Upper Ordovician peri-Gondwanan island arc activity in the Victoria Lake Supergroup, Central Newfoundland: Tectonic development of the northern Ganderian margin. American Journal of Science, 307(2), 339–370. Retrieved from http://www.ajsonline.org/content/307/2/339.short

Zagorevski, Alexandre, van Staal, C. R., McNicoll, V., Rogers, N., & Valverde-Vaquero, P. (2008). Tectonic architecture of an arc-arc collision zone, Newfoundland Appalachians. Geological Society of America Special Papers, 436, 309–333. Retrieved from http://specialpapers.gsapubs.org/content/436/309.full

Zaporozan, T., Frederiksen, A. W., Bryksin, A., & Darbyshire, F. (2018). Surface-wave images of western Canada: lithospheric variations across the Cordillera–craton boundary. Canadian Journal of Earth Sciences, 55(8), 887–896. https://doi.org/10.1139/cjes-2017-0277

Zelt, B. C., Ellis, R. M., Zelt, C. A., Hyndman, R. D., Lowe, C., Spence, G. D., & Fisher, M. A. (2001). Three-dimensional crustal velocity structure beneath the Strait of Georgia, British

Columbia. Geophysical Journal International, 144(3), 695–712. https://doi.org/10.1046/j.0956-540X.2000.01364.x

Zelt B. C., Ellis R. M., & Clowes R. M. (1993) Crustal velocity structure in the eastern Insular and southernmost Coast belts, Canadian Cordillera. Canadian Journal of Earth Sciences. 30(5): 1014-1027. https://doi.org/10.1139/e93-085

Zeng, X., Xie, J., & Ni, S. (2015). Ground truth location of earthquakes by use of ambient seismic noise from a sparse seismic network: A case study in Western Australia. Pure and Applied Geophysics, 172(6), 1397–1407.